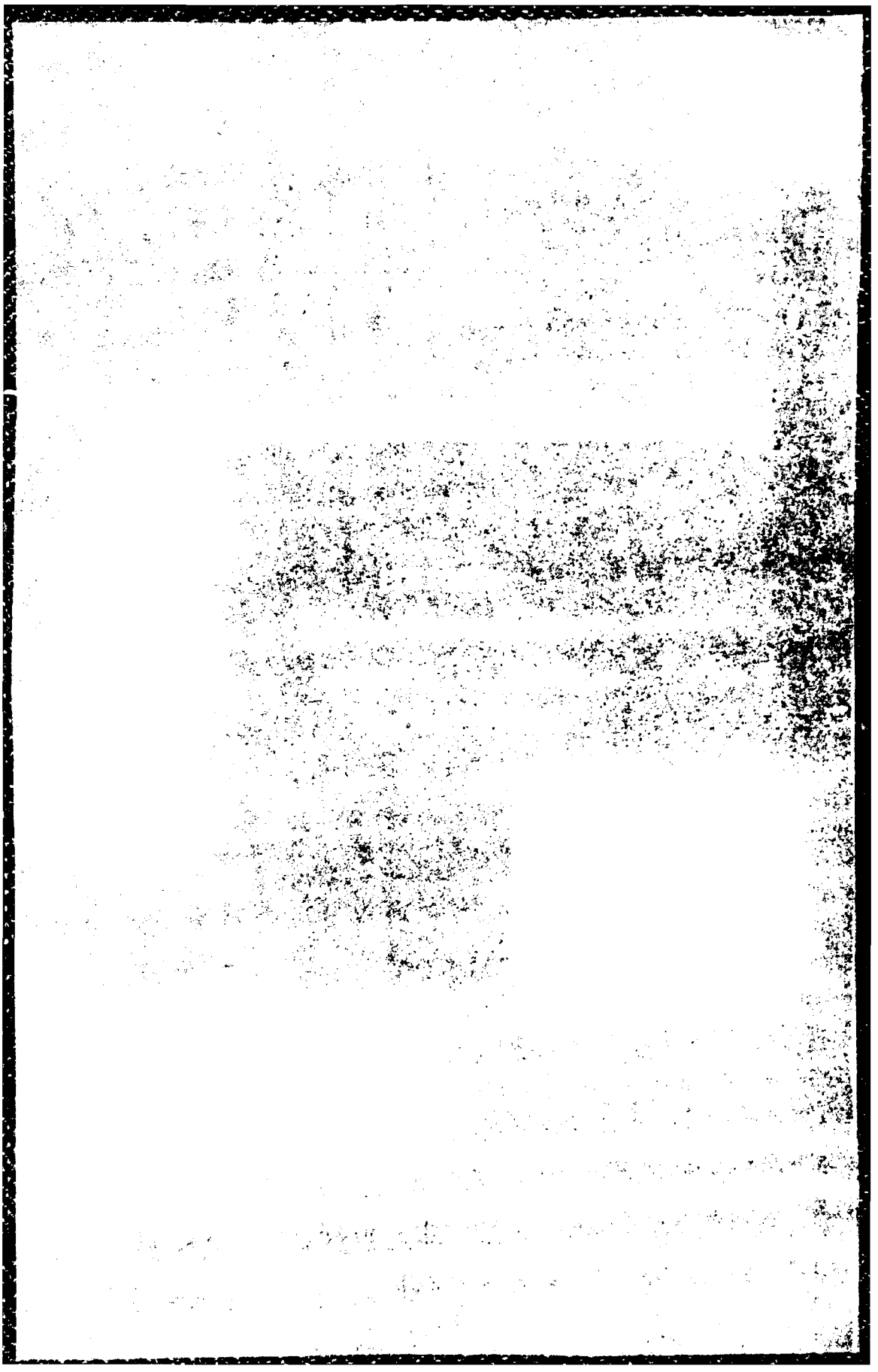

Biomolecular Materials

MATERIALS RESEARCH SOCIETY SYMPOSIUM PROCEEDINGS VOLUME 292

Biomolecular Materials

Symposium held December 1-3, 1992, Boston, Massachusetts, U.S.A.

EDITORS:

Christopher Viney
Center for Bioengineering
University of Washington
Seattle, Washington, U.S.A.

Steven T. Case
Department of Biochemistry
University of Mississippi Medical Center
Jackson, Mississippi, U.S.A.

J. Herbert Waite
College of Marine Studies
University of Delaware
Lewes, Delaware, U.S.A.

93-13201

MRS
MATERIALS RESEARCH SOCIETY
Pittsburgh, Pennsylvania

93 6 14 027

This work was supported in part by the Office of Naval Research under Grant Number N00014-93-1-0120. The United States Government has a royalty-free license throughout the world in all copyrightable material contained herein.

Single article reprints from this publication are available through University Microfilms Inc., 300 North Zeeb Road, Ann Arbor, Michigan 48106

CODEN: MRSPDH

Copyright 1993 by Materials Research Society.
All rights reserved.

This book has been registered with Copyright Clearance Center, Inc. For further information, please contact the Copyright Clearance Center, Salem, Massachusetts.

Published by:

Materials Research Society
9800 McKnight Road
Pittsburgh, Pennsylvania 15237
Telephone (412) 367-3003
Fax (412) 367-4373

Library of Congress Cataloging in Publication Data

Biomolecular materials / editors, Christopher Viney, Steven T. Case, J. Herbert Waite
p. cm.—(Materials Research Society symposium proceedings,
ISSN 0272-9172 ; v. 292)
Includes bibliographical references and index.
ISBN 1-55899-187-5
1. Biopolymers—Congresses. 2. Biomedical materials—Congresses.
3. Biomedical engineering—Congresses. I. Viney, Christopher II. Case, Steven T., 1949- . III. Waite, J. Herbert IV. Series: Materials Research Society symposium proceedings ; v. 292.
QP801.B69B55 1993 93-12846
574.19'2—dc20 CIP

Manufactured in the United States of America

Contents

*Invited Paper

DTIC QUALITY INSPECTED 8

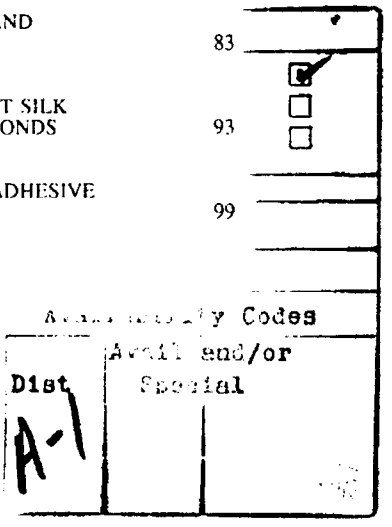

PART III: NON-CELLULAR SYNTHESIS

PART IV: STRUCTURAL AND MECHANICAL PROPERTIES

*Invited Paper

*Invited Paper

Preface

Biological materials are naturally occurring substances produced and utilized internally or externally by living organisms. In contrast, biomolecular materials are partial, complete or modified replicas of biological materials whose synthesis and utilization may be unrelated to their original biological source. Whether the objective is to replicate the properties of a biological material, or to produce derivatives with novel properties, the ultimate goal is to attain biomolecular materials that have industrial, medical, or agricultural applications.

This symposium, held at the 1992 Fall Meeting of the Materials Research Society, brought together an interdisciplinary group of scientists (zoologists, molecular biologists, biochemists, inorganic and organic chemists, materials scientists, mathematicians) that are directly or indirectly involved in some aspect of biomolecular materials research.

The diversity of biological (Nature's) materials was amply demonstrated: cockroach elastin, mussel adhesives, trematode and avian eggshells, spider and midge silks, abalone shell, rhinoceros horn, algal pigments, a bacterial hemolytic protein, and nut shells! Descriptions of these biological systems ranged from the relatively unknown to detailed information regarding the structure, composition, processing and physical properties of the biological material.

In several instances, particularly for protein-based polymers, biomolecular materials have been obtained by cellular synthesis through biotechnology. Bacterial cells have been engineered to synthesize discrete portions of insect silk and mussel adhesive proteins, multifunctional proteins with a unique combination of multiple binding sites, and recombinant proteins with specific combinations of functional groups that lead to ordered assembly into supramolecular complexes.

Numerous examples were presented whereby the synthesis and assembly of materials and microstructures was achieved in the absence of a living organism. Cast and Langmuir-Blodgett monolayer and multilayer films have been obtained from inorganic and organic materials such as tin oxide, cadmium arachidate, octadecyltrichlorosilane, polydiacetylene, gelatin, and copolymers of polythiophene and phenol/aniline derivatives. Films have also been obtained from proteins such as poly(γ-benzyl-*L*-glutamate), a modified cytochrome, regenerated silk, and actin. Phospholipase and antibody films have been achieved at the interface of lipid biomembranes. Non-cellular synthesis can also yield higher-order structures, including three-dimensional lattices of DNA, liquid crystals of proteins, hydroxyapatite-ZnO-polyacrylate composites, and magnetite and protein fibers.

While biochemical techniques provide insight about the biological material, biophysical and materials science techniques have been used to study the ultrastructure and mechanical properties of the biomolecular materials. In addition to those mentioned above, specific data were presented for abalone nacre (a ceramic-polymer composite), avian eggshell, algal pigment proteins, homopolymeric and repeated periodic peptides, magnetite fibers, and membranes based on hyaluronic acid. The applicable techniques include microscopy (optical, scanning electron, transmission electron, atomic force), spectroscopy (visible light, ultraviolet light, circular dichroism, laser Raman, Fourier transform infrared, angular resolved electron), ellipsometry, solid state nuclear magnetic resonance imaging, x-ray diffraction and computational modelling.

Finally, some biomolecular materials have attained the applications stage. For example, biologically produced composites have been used to establish new approaches to synthesis, processing and design for ceramic matrix composites. A bacterial protein that normally lysis red blood cells can self-assemble, insert into lipid bilayers and form a pore capable of interconversion between either of two conductance states. Both a

cross-linked elastomeric matrix of a viscoelastic polypeptide and a hyaluronic acid-based membrane have been shown to prevent post-operative adhesions. The elastomeric protein, in particular, has undergone extensive testing for adhesion prevention in model mammalian peritoneal and eye surgeries.

Though few biomolecular materials have reached the applications stage, many more have the potential to do so. The probability of success will, to a large degree, depend upon continued interactions and increased collaborations between interdisciplinary teams of scientists such as those who enthusiastically participated in this stimulating symposium.

Steven T. Case
Christopher Viney
J. Herbert Waite

February 1993

Acknowledgments

The many participants' fervor and cooperation as speakers, authors and reviewers made the organizers' tasks enjoyable and worthwhile. For this we are most grateful. We look forward to future endeavors, and to following the scientific progress of our many new colleagues.

The organizers were ably assisted by three additional session chairs, to whom we extend our thanks:

Viola Vogel
Center for Bioengineering
University of Washington
Seattle, Washington, U.S.A.

Hagan Bayley
Worcester Foundation for Experimental Biology
Shrewsbury, Massachusetts, U.S.A.

Julian Vincent
Centre for Biomimetics
The University
Reading, United Kingdom

We wish also to thank the support staff of the Materials Research Society for organizational and logistical assistance, particularly with the press conference.

Our symposium could not have taken place without financial support. We are delighted to acknowledge our gratitude to:

The Office of Naval Research
Johnson and Johnson
E.I. du Pont de Nemours & Co., Inc.

Volume 258—Amorphous Silicon Technology—1992, M.J. Thompson, Y. Hamakawa, P.G. LeComber, A. Madan, E. Schiff, 1992, ISBN: 1-55899-153-0

Volume 259—Chemical Surface Preparation, Passivation and Cleaning for Semiconductor Growth and Processing, R.J. Nemanich, C.R. Helms, M. Hirose, G.W. Rubloff, 1992, ISBN: 1-55899-154-9

Volume 260—Advanced Metallization and Processing for Semiconductor Devices and Circuits II, A. Katz, Y.I. Nissim, S.P. Murarka, J.M.E. Harper, 1992, ISBN: 1-55899-155-7

Volume 261—Photo-Induced Space Charge Effects in Semiconductors: Electro-optics, Photoconductivity, and the Photorefractive Effect, D.D. Nolte, N.M. Haegel, K.W. Goossen, 1992, ISBN: 1-55899-156-5

Volume 262—Defect Engineering in Semiconductor Growth, Processing and Device Technology, S. Ashok, J. Chevallier, K. Sumino, E. Weber, 1992, ISBN: 1-55899-157-3

Volume 263—Mechanisms of Heteroepitaxial Growth, M.F. Chisholm, B.J. Garrison, R. Hull, L.J. Schowalter, 1992, ISBN: 1-55899-158-1

Volume 264—Electronic Packaging Materials Science VI, P.S. Ho, K.A. Jackson, C-Y. Li, G.F. Lipscomb, 1992, ISBN: 1-55899-159-X

Volume 265—Materials Reliability in Microelectronics II, C.V. Thompson, J.R. Lloyd, 1992, ISBN: 1-55899-160-3

Volume 266—Materials Interactions Relevant to Recycling of Wood-Based Materials, R.M. Rowell, T.L. Laufenberg, J.K. Rowell, 1992, ISBN: 1-55899-161-1

Volume 267—Materials Issues in Art and Archaeology III, J.R. Druzik, P.B. Vandiver, G.S. Wheeler, I. Freestone, 1992, ISBN: 1-55899-162-X

Volume 268—Materials Modification by Energetic Atoms and Ions, K.S. Grabowski, S.A. Barnett, S.M. Rossnagel, K. Wasa, 1992, ISBN: 1-55899-163-8

Volume 269—Microwave Processing of Materials III, R.L. Beatty, W.H. Sutton, M.F. Iskander, 1992, ISBN: 1-55899-164-6

Volume 270—Novel Forms of Carbon, C.L. Renschler, J. Pouch, D. Cox, 1992, ISBN: 1-55899-165-4

Volume 271—Better Ceramics Through Chemistry V, M.J. Hampden-Smith, W.G. Klemperer, C.J. Brinker, 1992, ISBN: 1-55899-166-2

Volume 272—Chemical Processes in Inorganic Materials: Metal and Semiconductor Clusters and Colloids, P.D. Persans, J.S. Bradley, R.R. Chianelli, G. Schmid, 1992, ISBN: 1-55899-167-0

Volume 273—Intermetallic Matrix Composites II, D. Miracle, J. Graves, D. Anton, 1992, ISBN: 1-55899-168-9

Volume 274—Submicron Multiphase Materials, R. Baney, L. Gilliom, S.-I. Hirano, H. Schmidt, 1992, ISBN: 1-55899-169-7

Volume 275—Layered Superconductors: Fabrication, Properties and Applications, D.T. Shaw, C.C. Tsuei, T.R. Schneider, Y. Shiohara, 1992, ISBN: 1-55899-170-0

Volume 276—Materials for Smart Devices and Micro-Electro-Mechanical Systems, A.P. Jardine, G.C. Johnson, A. Crowson, M. Allen, 1992, ISBN: 1-55899-171-9

Volume 277—Macromolecular Host-Guest Complexes: Optical, Optoelectronic, and Photorefractive Properties and Applications, S.A. Jenekhe, 1992, ISBN: 1-55899-172-7

Volume 278—Computational Methods in Materials Science, J.E. Mark, M.E. Glicksman, S.P. Marsh, 1992, ISBN: 1-55899-173-5

MATERIALS RESEARCH SOCIETY SYMPOSIUM PROCEEDINGS

Volume 279—Beam-Solid Interactions—Fundamentals and Applications, M.A. Nastasi, N. Herbots, L.R. Harriott, R.S. Averback, 1993, ISBN: 1-55899-174-3

Volume 280—Evolution of Surface and Thin Film Microstructure, H.A. Atwater, E. Chason, M. Grabow, M. Lagally, 1993, ISBN: 1-55899-175-1

Volume 281—Semiconductor Heterostructures for Photonic and Electronic Applications D.C. Houghton, C.W. Tu, R.T. Tung, 1993, ISBN: 1-55899-176-X

Volume 282—Chemical Perspectives of Microelectronic Materials III, C.R. Abernathy, C.W. Bates, D.A. Bohling, W.S. Hobson, 1993, ISBN: 1-55899-177-8

Volume 283—Microcrystalline Semiconductors—Materials Science & Devices, Y. Aoyagi, L.T. Canham, P.M. Fauchet, I. Shimizu, C.C. Tsai, 1993, ISBN: 1-55899-178-6

Volume 284—Amorphous Insulating Thin Films, J. Kanicki, R.A.B. Devine, W.L. Warren, M. Matsumura, 1993, ISBN: 1-55899-179-4

Volume 285—Laser Ablation in Materials Processing—Fundamentals and Applications, B. Braren, J. Dubowski, D. Norton, 1993, ISBN: 1-55899-180-8

Volume 286—Nanophase and Nanocomposite Materials, S. Komarneni, J.C. Parker, G.J. Thomas, 1993, ISBN: 1-55899-181-6

Volume 287—Silicon Nitride Ceramics—Scientific and Technological Advances, I-W. Chen, P.F. Becher, M. Mitomo, G. Petzow, T.S. Yen, 1993, ISBN: 1-55899-182-4

Volume 288—High Temperature Ordered Intermetallic Alloys V, I. Baker, J.D. Whittenberger, R. Darolia, M.H. Yoo, 1993, ISBN: 1-55899-183-2

Volume 289—Flow and Microstructure of Dense Suspensions, L.J. Struble, C.F. Zukoski, G. Maitland, 1993, ISBN: 1-55899-184-0

Volume 290—Dynamics in Small Confining Systems, J.M. Drake, D.D. Awschalom, J. Klafter, R. Kopelman, 1993, ISBN: 1-55899-185-9

Volume 291—Materials Theory and Modelling, P.D. Bristowe, J. Broughton, J.M. Newsam, 1993, ISBN: 1-55899-186-7

Volume 292—Biomolecular Materials, S.T. Case, J.H. Waite, C. Viney, 1993, ISBN: 1-55899-187-5

Volume 293—Solid State Ionics III, G-A. Nazri, J-M. Tarascon, M. Armand, 1993, ISBN: 1-55899-188-3

Volume 294—Scientific Basis for Nuclear Waste Management XVI, C.G. Interrante, R.T. Pabalan, 1993, ISBN: 1-55899-189-1

Volume 295—Atomic Scale Imaging of Surfaces and Interfaces, D.K. Biegelsen, D.S.Y. Tong, D.J. Smith, 1993, ISBN: 1-55899-190-5

Volume 296—Structure and Properties of Energetic Materials, R.W. Armstrong, J.J. Gilman, 1993, ISBN: 1-55899-191-3

Prior Materials Research Society Symposium Proceedings available by contacting Materials Research Society

PART I

Lessons from Nature

PRELIMINARY CHARACTERIZATION OF RESILIN ISOLATED FROM THE COCKROACH, *PERIPLANETA AMERICANA*

ELIZABETH CRAIG LOMBARDI AND DAVID L. KAPLAN
Biotechnology Division
U.S. Army Natick Research Development and Engineering Center
Natick, Massachusetts 01760-5020

ABSTRACT

We would like to mimic the mechanical properties of animal systems for the development of novel materials. Insect cuticle serves as one source of inspiration for the design of these materials. Cuticle is composed of chitin embedded in a protein matrix which may also contain plasticizers, fillers, crosslinkers, and minerals. The specific properties of the cuticle depend on the type, amount and interactions between each component. We are renewing the investigation of the elastic cuticle, resilin. Resilin, a protein-based elastomer first described in the early 1960s, has properties which have been reported to be most like those of ideal rubbers. We have examined resilin isolated from the prealar arms of the cockroach, *Periplaneta americana*. The results of amino acid analysis are in good agreement with earlier data reported for resilin. A series of tryptic fragments have been isolated and sequenced. These peptides have been used for the design of oligonucleotide probes for the identification of the gene(s) from a teneral cockroach cDNA library. A biopolymer, based on one tryptic fragment, has been designed and synthesized. We are continuing to treat resilin with residue specific proteases in order to map the resilin protein.

INTRODUCTION

Certain areas of the exoskeleton in many insects exhibit long-range, reversible rubber-like elasticity. This rubber-like cuticle is composed of small chitin lamellae embedded in a protein matrix. The protein, resilin, is responsible for the elastomeric properties of this cuticle. Resilin was first described in 1960 [1]. This protein was initially identified in the flight [2] and jumping mechanisms [3] of insects, but has since been found in other structures of various arthropods [4,5,6,7]. The elastic tendon from the dragonfly, *Aeshna juncea*, has been used to demonstrate that the elastomeric properties of resilin arise from the entropic force associated with protein deformation [8]. Loaded elastic tendon did not exhibit any creep over a period of days or weeks. The tendon also displayed complete elastic recovery with no observed hysteresis [9]. Resilin has been viewed by X-ray diffraction and electron microscopy and no fine ultrastructure has been observed [10]. Resilin is not soluble in any solvent that does not degrade peptide bonds. This insolubility has been attributed to the nature of the protein's crosslinks. Although resilin is reportedly loosely crosslinked, the crosslinks are formed as a result of a post-translational free radical reaction involving the tyrosyl residues [11]. Advances in molecular biology and protein chemistry have allowed for the renewed investigation of this biomaterial.

MATERIALS AND METHODS

Amino acid composition

The prealar arms from adult *Periplaneta americana* (US Army, Aberdeen, MD) and *Blaberus craniifer* (gift from L. Roth, Harvard University) were dissected and stored in 70% ethanol according to a procedure outlined by Bailey and Weis-Fogh [12]. Whole prealar arms were hydrolyzed in constant boiling 6N HCl (0.2 ml) at 112°C for 22 hours on a Water's Pico Tag workstation. The hydrolysate was analyzed for amino acid content on a Waters Pico Tag column (15cm) following the standard recommended procedure. All analyses were performed in triplicate.

Mat. Res. Soc. Symp. Proc. Vol. 292. © 1993 Materials Research Society

Tryptic digestion
The prealar arms of 50 adult *P. americana* (1.47mg) were dissected and transferred into a 200ml working volume tissue grinder (Kontes). All subsequent reactions were carried out in this vial. After the arms were ground, a small amount (10ml) of 6N guanidine HCl, 50mM Tris-HCl pH7.7, was added to the ground arms and homogenization continued. Additional guanidine solution was added to bring the final volume to 200ml. The digestion mixture was incubated at room temperature for 24 hours. The resulting mixture was centrifuged and the supernatant discarded. The precipitate was washed twice with 200mM ammonium bicarbonate to remove any residual denaturant, then resuspended in 100ml of ammonium bicarbonate solution. Approximately 20 BAEE units of trypsin (Sigma, EC 3.4.31.4) were added and then incubated at 37°C for 24 hours. The reaction was centrifuged and the supernatant collected and dried.

Isolation and analysis of peptides
The dried digested material was resuspended in 0.2 ml of 0.09% trifluoroacetic acid/water then filtered. Samples (25µl) were injected onto a narrow bore HPLC column (Waters Delta Pak C18, 300Å, 2x150 mm, 5mm) equilibrated with 95% 0.09% trifluoroacetic acid/5% acetonitrile. The fragments were eluted over a linear gradient running from 5-25% organic phase (acetonitrile). The UV absorbance was monitored on a Waters 991 photodiode array detector at 210 and 280nm. Fractions were collected and dried under vacuum.

Sequencing
The fractions were analyzed for their amino acid content then sequenced via automated Edman degradation using an ABI 470A gas phase peptide sequencer at the Analytical and Synthetic Facility at Cornell University.

Biopolymer synthesis and characterization
The peptide, N-(AGPHGAFYKGFGSG)$_4$-C, was assembled in a stepwise synthesis using N-Fmoc (9-Fluorenylmethloxycarbonyl) protected amino acids and TBTU (2-(1H-Benzotriazole-1-yl)-1,1,3,3-tetramethyluronium tetrafloroborate) activation on a MilliGen 9050 continuous flow synthesizer. Purification was by reverse phase HPLC using an acetonitrile-water gradient containing 0.05% TFA and an ODS-AQ column (YMC, Morris Heights, NJ). The positive ion electrospray mass spectrum showed M+3H through M+9H ions of the expected masses. Amino acid analysis (Waters Pico-Tag) confirmed that the product had the correct composition. The peptide content of the lyophilized product was determined to be 86% by quantitative amino acid analysis, the balance being bound water and TFA counter-ions. Circular dichroism (CD) spectra were recorded in the wavelength range of 240-190 nm on an AVIV 60DS solid state CD spectrophotometer (AVV. Associates, Lakewood, NJ). The instrument was calibrated using +d-10-camphorsulfonic acid and also with benzene vapor in a long pathlength (10 cm) cell. Secondary structure determination was made using a program supplied by AVIV which is based on the work of Yang et al. [13]. Thermogravimetric analysis (TGA) was performed in a nitrogen atmosphere on a TA Instruments Hi-Res TGA 2950 Thermogravimetric Analyzer. Calorimetric measurements were taken at a rate of 10°C/min on a Du Pont Instruments 912 Differential Scanning Calorimeter (DSC).

RESULTS

The results of the amino acid analysis are presented in tabular form in Table 1. The tryptic fragments were separated by reverse-phase HPLC, then sequenced. The results are found in Table 2.

Previous studies have shown resilin to have no significant secondary structure [10]. Computer generated secondary structure predictions based on the sequence data reported here (DNASTAR, Inc., Madison, WI) suggest that the fragments contains a high degree of ß-turn. CD analysis of the resilin-like peptide (Figure 1) reveals that the ß-structure accounts for approximately 2/3 of the secondary conformation with 39.0% and 27.8%, ß-sheet and ß-turn respectively. Alpha helix accounts for 15.2% of the secondary structure and random coil

18.0%. This may reflect localized areas of ordered conformation. TGA shows four discernible decomposition events, at 171°C, 238°C, 336°C and 387°C. The residue at 600°C accounts for 39±4% of the starting weight; comparable to that found for *Bombyx mori* silk. The residue disappears when the purge gas is changed from nitrogen to air. The DSC first-heating scan shows one endothermic peak, with a peak temperature of 83°C and a ΔH of 83 J/g. Subsequent cooling and heating scans show no event other than decomposition.

Table 1. Amino acid composition analysis of resilin (in mole percent). All samples were taken from the prealar arms of the organisms.

Amino Acid	Cockroach (*Blaberus* sp.)	Cockroach (*Periplaneta americana*)	Locust[1] (*Schistocerca gregaria*)
Asx	6.6	6.8	11.3
Glx	5.8	6.3	3.8
Ser	9.9	9.0	7.5
Gly	37.0	34.9	39.7
His	2.4	2.2	1.1
Arg	2.6	2.2	3.8
Thr	2.6	2.5	3.1
Ala	11.2	13.3	11.2
Pro	8.3	8.7	7.7
Tyr	3.5	3.9	2.9
Val	4.1	4.1	2.5
Met	--	--	--
Cys	--	--	--
Ile	0.9	0.8	1.4
Leu	1.3	1.7	2.8
Phe	3.0	2.8	2.4
Lys	0.4	0.5	0.5
Totals	99.6%	99.7%	100.0%

[1][15]

DISCUSSION

The amino acid composition of resilin isolated from the cockroach, *P. americana*, has been established and compares well to that reported for resilin present in other insects. Our results show glycine (34.9%), alanine (13.3%), serine (9.0%) and proline (8.7%) as the major components of this protein. Tyrosine is present at 4.1%. Although the data are in good agreement with the results previously published, slight variations are apparent as would be expected from different organisms. Bailey and Weis-Fogh [12] used the wing hinge ligaments and prealar arms from the locust, *S. gregaria*, and the elastic tendon of the dragonfly, *A. juncea*, to determine the amino acid composition of resilin. The results for these samples did not vary significantly and therefore were averaged by the investigators. Their analyses found the major components of resilin to be glycine (38%), alanine (11%), aspartic acid (10%), serine (8%), and proline (7.8%). There were no sulfur-containing amino acids and only trace amounts of tryptophan [14]. These data were later reexamined by Andersen [15]. He found no differences from the amino acid data published earlier. Also included were data for resilin from other insects. The major difference between the cockroach resilin and that of other resilins is in the amount of asx and glx residues. Interestingly, the combined percentage of these residues is approximately the same with the exception of the abdominal spring of *Oryctes rhinoceros*, which has an unusually high amount of aspartic acid.

Table 2. Sequences of peptide fragments from tryptic digests of resilin isolated from the prealar arms of *P. americana*.. The two columns represent sequence data collected from different digests and starred sequences were found in both preparations.

APSSTY	GDQESR
DGDVAQGSY*	KPEIR
SAPAVGYT	DGDVAQGSY*
LDGSSQED	GAPGGGQ
VAPEVAQ	NVLLPDGR*
NVLLPDGR*	NINVVE
GFGSGAGPHGSFYK	EFSYDVNDASTGTEF*
EFSYDVNDASTGTEF*	
QQGDSGGPV	
VLDYD	
SSGTSYPDV	
YDVNDASA	
GFGSGAGPHGAF	

In addition to resilin, several other rubber-like proteins have been identified, abductin and elastin. Resilin, elastin and abductin perform similar functions in the different organisms in which they are present but each has a noticeably different amino acid composition [16,17]. These proteins are all rich in glycine. Small side chain amino acids (glycine, alanine, serine) account for 55% to 70% of the total residues for these elastomeric proteins. These residues also comprise over 85% of the structural protein, silk fibroin from *B. mori* [18]. Therefore, one would not expect these amino acids themselves to be responsible for the elastomeric properties. These proteins are crosslinked via significantly different processes.

The physical properties, structure and amino acid composition of resilin have been thoroughly investigated; however, no sequence data have been previously reported. Bailey and Weis-Fogh [12] suggested that glycine, which accounts for one third of the amino acid composition, is present at every third residue. The limited sequence data reported here does not support this suggestion. Only one fragment isolated to date has a significant amount of glycine present in any repetitious manner. There is not enough sequence information to suggest any regularly occurring repeating subunits or ultrastructure.

The sequence data have allowed us to design and synthesize oligonucleotide probes for use in screening a cDNA library. The degeneracy of the genetic code along with the unknown codon preference for cockroaches creates ambiguity in the design of these probes. We have eliminated the number of probes created as a result of mixed sites through the use of inosine. This will allow hybridization to mixed sites. The use of multiple probes should allow for the identification of resilin-encoding clones.

A short biopolymer, N-$(AGPHGAFYKGFGSG)_4$-C, with a confirmed molecular mass of 5355.09 amu, has also been designed and synthesized based on this sequence data. The physical characterization of the peptide indicates significant ß-structure (Figure 1). These data support the computer-generated secondary structure predicted for this peptide. Thermal characterization of the resilin-like biopolymer indicates no melt transition but significant thermal stability (up to about 40%) when heated to 600°C in a nitrogen atmosphere. Initially we were

Figure 1. CD analysis of the synthetic peptide. The y-axis is in mean residue ellipticity (divide by 110 for milli-degrees).

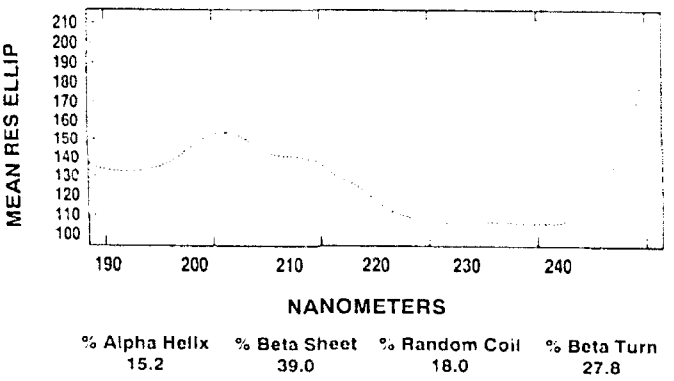

concerned about the presence of contaminating salt. A quantitative amino acid analysis accounted for all but 16% of the mass of the starting material; the remainder is believed to reflect the water content. This material decomposes in the presence of air, possibly indicating a stable carbon backbone. We have started crosslinking studies to compare the properties of the uncrosslinked polymer to that of the crosslinked state. One significant difference will be the crosslink density as natural resilin is approximately 4% whereas the synthetic polypeptide is 7%. This will also serve to increase the molecular weight of the material.

ACKNOWLEDGEMENTS

We would like to express our appreciation to Louis M. Roth, Museum of Comparative Zoology, Harvard University, for the generous gift of *Blaberus*, John Walker, Wayne Muller, and Peter Stenhouse of our laboratory, and Ted Thannhauser at Cornell University for various contributions to this work.

REFERENCES

1. T. Weis-Fogh, J. Exp. Biol. 37, 889-907 (1960).
2. M. Jensen and T. Weis-Fogh, Phil. Trans. Roy. Soc. Ser. B 245, 137-169 (1962).
3. H. C. Bennet-Clark and E. C. A. Lucey, J. Exp. Biol. 47, 59-76 (1967).
4. H. A. Edwards, J. Exp. Biol. 105, 407-409 (1983).
5. S. Govindarajan and G. S. Rajulu, Experientia 30, 908-909 (1974).
6. H. R. Hermann and D. E. Willer, Int. J. Insect Morphol. and Embryol. 15, 107-114 (1986).
7. J. A. Scott, The Pan-Pacific Entomologist 46, 225-231 (1970).
8. T. Weis-Fogh, J. Mol. Biol. 3, 648-667 (1961).
9. T. Weis-Fogh, J. Mol. Biol. 3, 520-531 (1961).
10. G. F. Elliott, A. F. Huxley, and T. Weis-Fogh, J. Mol. Biol. 13, 791-795 (1965).
11. S. O. Andersen, Acta Physiol. Scand. 66, 9-81 (1966).
12. K. Bailey and T. Weis-Fogh, Biochim Biophys Acta 48, 452-459 (1961).
13. J. T. Yang, C.-S. C. Wu, and H. M. Martinez, Meth. in Enz. 130, 208-269 (1986).
14. S. O. Andersen and T. Weis-Fogh, Adv. Insect Physiol. 2, 1-65 (1964).
15. S. O. Andersen, in *Comprehensive Biochemistry* (ed. Florkin, M. and Stotz, E. H.) Elsevier, Amsterdam (1971).
16. G. A. Kahler, F. M. Fisher, and R. L. Sass, Biol. Bull. 151, 161-181 (1976).
17. E. H. Sage and W. R. Gray, in *Elastin and Elastic Tissue* (ed. Sandberg, L. B., Gray, W.R. and Franzblau, C.) Plenum Press, New York (1976).
18. F. Lucas, J. T. B. Shaw, and S. G. Smith, Advanc. Protein Chem. 13, 107 (1958).

THE ADHESIVE GLYCOPROTEIN OF THE ORB WEB OF *ARGIOPE AURANTIA* (ARANEAE, ARANEIDAE)

EDWARD K. TILLINGHAST*, MARK A. TOWNLEY*, THOMAS N. WIGHT**, GERHARD UHLENBRUCK*** AND EVELINE JANSSEN***
*University of New Hampshire, Department of Zoology, Durham, NH 03824 USA
**University of Washington, Department of Pathology, Seattle, WA 98195 USA
***Universität zu Köln, Institut für Immunbiologie, Kerpener Straße 15, D-5000 Köln 41, Germany.

ABSTRACT

A phosphorylated, glycoprotein preparation has been obtained from orb webs of the araneid spider *Argiope aurantia*. This preparation probably contains proteins from more than one gland type, but resolution of these proteins has not yet been achieved. Nevertheless, a major component appears to be the adhesive glycoprotein(s) from the adhesive spiral. A product of the aggregate glands[2,6], this glycoprotein(s) occurs as discrete nodules along the core fibers of the adhesive spiral, within the viscid, aqueous droplets[11,12].

The glycoprotein preparation has a high apparent molecular weight (> 200 kDa) and is polydisperse. The only monosaccharide constituent identified by gas-liquid chromatography or in lectin studies is *N*-acetylgalactosamine and this is at least primarily *O*-linked to threonine. By electron microscopy, linear, unbranched and apparently flexible filaments are observed. Phosphorylated serine and threonine residues are present in the preparation and glycine, proline and threonine together account for about 57 mole % of the preparation's amino acid content. Thus, in some, but not all, respects, this glycoprotein preparation is reminiscent of a secretory mucin.

INTRODUCTION

The orb webs of araneid spiders are composed of elements from several types of glands. Major ampullate silk glands (principally) give rise to various nonadhesive fibers in the web, including, but not limited to, frame lines, the hub spiral and the spoke-like radii[1-3]. Pyriform glands produce attachment disks[1,2,4] and, likely, the cements which occur at junctions between ampullate fibers[1,3,5] (e.g. at hub spiral/radius junctions). (Cements at adhesive spiral/radius junctions are of unknown origin.) Flagelliform glands produce the core fibers of the adhesive spiral while aggregate glands produce the viscid solution which envelops these core fibers[2,6]. It is with the viscid coating of the adhesive spiral that this paper is largely concerned.

The aqueous solution that emerges from the aggregate gland spigots contains organic and inorganic low molecular weight components (< 200 Da) in high concentration[7-10], as well as protein. After it is applied to the core fibers, this solution takes the form of a series of droplets connected by narrow liquid bridges. If adhesive spiral segments are examined microscopically, one or two discrete nodules can usually be observed surrounding the core fibers within each droplet[11,12]. These nodules are composed, at least in part, of glycoprotein.

Mat. Res. Soc. Symp. Proc. Vol. 292. © 1993 Materials Research Society

Guanidine hydrochloride extracts of orb webs built by *Argiope aurantia* have yielded a glycoprotein preparation which appears to originate in part with the nodules. A preliminary characterization of this glycoprotein preparation follows.

MATERIALS AND METHODS

Web Collection

Adult and late juvenile female *Argiope aurantia* Lucas were collected in New Hampshire, Maine and Massachusetts. Uncontaminated orb webs were obtained by maintaining spiders individually in cages for up to one week without feeding. Spiders were given water daily. Webs were collected daily on glass rods and stored at -20°C until analyzed. As an aid in locating orb web components following separation by chromatographic and electrophoretic procedures, some spiders were fed 10 μCi D-[^{14}C(U)]-glucose (NEN Research Products, Boston, MA) and their webs were added to nonradioactive web collections. The occurrence of phosphorus in the glycoprotein preparation was examined by feeding each of 30 spiders an average of 27 μCi [^{32}P]-Na_2HPO_4 (NEN). Isotopes were offered to spiders in aqueous solution from the tips of 10 μL Hamilton syringes.

Web Extraction and Fractionation

Collection rods coated with web were extracted in batches of about 50-70 webs with 3 mL filtered 6 M guanidine HCl, 0.7 M 2-mercaptoethanol, 0.2 M Na_2HPO_4. Extraction was allowed to proceed for 1 day with occasional low-speed vortexing. The solvent used does not solubilize all web components. In an effort to determine which web elements are solubilized by this solution, droplets of solvent were directly applied to selected areas of webs which had been collected on glass plates[13]. The results were observed by light microscopy using a Zeiss RA 38 microscope.

Web extracts were fractionated by size-exclusion chromatography on 90 cm x 2 cm^2 columns of Sephacryl S-400 HR (Pharmacia LKB, Piscataway, NJ) using the aforementioned guanidine solution for equilibration and elution of columns. Flow rates were typically about 10 mL/h and 2.5 - 3.2 mL fractions were collected (LKB-Bromma 2212 Helirac). Radioactivity and O.D. 280 of each fraction were determined using a LKB-Wallac 1214 Rackbeta Excel liquid scintillation counter and a Beckman DB-GT grating spectrophotometer, respectively. Pooled fractions were dialyzed against distilled water (Spectrum Spectra/Por 6 membranes, mol. wt. cutoff 2000 Da) and lyophilized (Labconco Freeze Dryer 4.5). Lyophilized material was often desiccated in vacuo over P_2O_5 and weighed (Perkin-Elmer AD-2 autobalance or Mettler AE 163 or H10Tw balances). The 'glycoprotein preparation' used in the analyses described below consisted of the earliest eluting material off the Sephacryl columns (Fig. 1).

Since inorganic phosphate is one of the solutes in the viscid coating of the adhesive spiral[7,8], the ^{32}P-labeled web was washed with water before being

extracted with the guanidine solution. This was done by gently immersing the web-coated collection rod in 20 mL distilled water for 1 h four times (with no vortexing). Radioactivity in extracts and fractions was measured by Cherenkov counting.

Sodium Dodecyl Sulfate Polyacrylamide Gel Electrophoresis (SDS-PAGE)

Dialyzed and lyophilized guanidine extracts or fractions thereof were examined by SDS-PAGE on 3.75% or 14% uniform concentration or 5-20% linear gradient acrylamide gels using the discontinuous system of Laemmli[14], with AcrylAide (FMC BioProducts, Rockland, ME) used as crosslinker in place of N,N'-methylenebisacrylamide. Gels were polymerized on GelBond PAG film (FMC). Electrophoresis was performed at 25 mA, requiring about 5 h. After electrophoresis, proteins were fixed and stained overnight in a solution of 2-propanol/glacial acetic acid/water (25/10/65, v/v/v) containing 0.1% Coomassie brilliant blue R-250 (BRL, Gaithersburg, MD). The same solution, without dye but with 3% glycerol added, was used for destaining. After rinsing with distilled water, gels were air dried and photographed using Kodak Electrophoresis Duplicating Paper. In the case of radioactive samples, Kodak SB-5 film was used to prepare autoradiograms from dried gels. Molecular weight standards were products of BRL.

Chemical Composition of Glycoprotein Preparation

1. *Amino acid composition.* Amino acid analyses were performed at the Instrumentation Center of the University of New Hampshire (UNH) and at AAA Laboratory (Mercer Island, Washington). At both locations, amino acid analyzers employing ion-exchange/ninhydrin methodology[15] were used. Samples analyzed at UNH were hydrolyzed in 6 N HCl under vacuum at 110°C for 24 h and then dried in vacuo over NaOH pellets. Analyses were performed on a Beckman 118CL amino acid analyzer coupled to a Varian LSD III integrator. Samples analyzed at AAA Laboratory were hydrolyzed under vacuum (50 mtorr) for 20 h at 115°C in 6 N HCl, 0.05% 2-mercaptoethanol, to which one crystal of phenol was added. Hydrolysates were dried in vacuo using a Buchler Evapo-Mix and analyzed on either a Dionex D550 amino acid analyzer (with a PDP 8/L computer operating with Dionex MK II software) or a Beckman 6300 amino acid analyzer upgraded to a 7300 (with a Northgate PC computer operating with Beckman System Gold software). Buffer systems and operating conditions for the analyzers followed the manufacturers' recommendations. In all analyses, the destruction during hydrolysis of 10% of the serine and 5% of the threonine was assumed[15,16] and compensated for in calculating amino acid composition.

Cystine/2 was determined at AAA Laboratory by the performic acid oxidation method described by Moore[17], except that oxidation took place at 50°C for 15 min. Following oxidation, acid hydrolysis was performed as described above for this facility and the hydrolysates were analyzed on the Beckman 7300 amino acid analyzer. The molar percentage of cysteic acid was calculated by reference to aspartic acid.

2. *Phosphate linkage.* Portions of the ^{32}P-labeled glycoprotein preparation were hydrolyzed in 6 N HCl at 110°C for 1 h or 4 h[18,19] and then dried on a Savant Speed-Vac concentrator. The air was not evacuated from the hydrolysis tubes before they were sealed. Aliquots of hydrolysate resulting from 0.5-1.5 mg of unhydrolyzed glycoprotein preparation were electrophoresed at 3000 V on 23 x 57 cm sheets of Whatman 3MM chromatography paper. Standard phosphoserine (P-Ser), phosphothreonine (P-Thr) and phosphotyrosine (P-Tyr) (Sigma Chemical, St. Louis, MO) were co-electrophoresed and their positions used to identify their radioactive counterparts in the hydrolysates. A given portion of hydrolysate was either electrophoresed for 1 h using a formic acid/acetic acid/water electrolyte, pH 1.9[20], or electrophoresed for 45 min using a pyridine/acetic acid/water electrolyte, pH 3.5[19]. The current at the start of a run was typically 100 mA for the pH 1.9 electrolyte and 130 mA for the pH 3.5 electrolyte. Autoradiograms were prepared from the electrophoretograms as for SDS-PAGE gels, after which phosphoamino acids and other amines were visualized with ninhydrin/cadmium acetate[21]. Densitometry was performed on autoradiograms using an Elmo EV-308 visual presenter and a Macintosh II computer operating with Image version 1.22 software (by W. Rasband, Research Services Branch, NIMH).

3. *Carbohydrate composition.* Monosaccharide constituents of samples (0.12 - 0.69 mg) of the glycoprotein preparation were identified by gas-liquid chromatography (GLC) as their trimethylsilyl derivatives using a procedure published by Chaplin[22]. Methanolysis was performed by treating lyophilized samples with 0.63 N methanolic HCl for 4 h at 90°C. Following re-*N*-acetylation and subsequent trimethylsilylation using *N*-methyl-*N*-trimethylsilyl-trifluoroacetamide (Pierce Europe B.V., Oud-Beijerland, The Netherlands), the monosaccharide derivatives were separated on a fused silica capillary column (30 m) wall-coated with RSL 300 (Alltech, Unterhaching, FRG) using the following temperature program: 100°C to 130°C at 16°C/min, then up to 260°C at 4°C/min.

Hexosamine analyses, again using ion exchange/ninhydrin methodology[15], were performed at AAA Laboratory on 0.50-1.05 mg samples of the glycoprotein preparation. Samples were hydrolyzed under vacuum (50 mtorr) for 4 h at 115°C in 4 N HCl[mod. from 23], dried using a Buchler Evapo-Mix and analyzed on the Beckman 7300 amino acid analyzer optimized for resolving amino sugars.

Lectin affinities were examined by double diffusion tests[24] in plated gels consisting of 1% low melting point agarose (BRL) in 60 mM barbital buffer, pH 8.6, with 0.02% sodium azide. Lectins (Sigma Chemical) and the glycoprotein preparation were added to wells at a concentration of 1 mg/mL in the same buffer.

In addition, the presence of sialic acids in the orb web was investigated using the resorcinol method of Svennerholm[25]. Batches of up to six whole orb webs from adult females were assayed.

4. *Substituents O-linked to serine or threonine.* To estimate the extent of *O*-substitution (including, but not limited to, glycosylation and phosphorylation[26]) of serine/threonine residues, samples (about 0.7 mg each) of

the glycoprotein preparation were treated with 0.2 N NaOH at 45°C for 5, 10 or 24 h[mod from 27,28]. The reaction mixtures were then neutralized with 6 N HCl and dried under vacuum over P_2O_5. Acid hydrolysis and amino acid analysis were performed at AAA Laboratory as described above. By the alkaline pretreatment *O*-substituted serine and threonine residues are converted to 2-aminopropenoic acid and 2-amino-2-butenoic acid, respectively, as a result of a β-elimination reaction[26,29]. A reduction in the molar percentages of threonine and/or serine indicates the extent of *O*-substitution of these amino acids.

Electron Microscopy of Glycoprotein Preparation

Lyophilized samples of the glycoprotein preparation were prepared for electron microscopy using the spreading procedure of Kleinschmidt and Zahn[30], with modifications[31]. Samples were solubilized in 1 M ammonium acetate, pH 5.0, at a concentration of 25 μg/mL. Aliquots of 50 μL were mixed with 50 μL of 10 mM Tris, 1 mM EDTA, pH 8.5, and 2 μL cytochrome *c* (2.5 mg/mL 2 M Tris, 50 mM EDTA, pH 8.5). Using 0.15 M ammonium acetate, pH 7.0, as hypophase, the protein was layered down a ramp onto the hypophase surface. This was allowed to spread for 30 sec. Monolayer samples were picked up onto copper grids (300 mesh) coated with carbon-stabilized Parlodion. These were stained immediately with 5×10^{-5} M uranyl acetate in 90% ethanol for 30 sec, rinsed with 90% ethanol and air dried. The grids were rotary shadowed with a 15 mm platinum/palladium wire at low angles (6-10 degrees). Glycoproteins were observed in a JEOL 100B electron microscope and photographed. The photographs were enlarged to 55,100 X and glycoprotein contour lengths were measured in well spread preparations.

RESULTS

Size-Exclusion Chromatography and SDS-PAGE

The 'glycoprotein preparation' examined in this study was obtained by fractionating guanidine extracts of *A. aurantia* orb webs on Sephacryl S-400 HR and pooling the earliest eluting material. This high M_r material, not easily detected at 280 nm (at least while in the guanidine solution), begins eluting just after the void volume (Fig. 1B). Thus far, attempts to examine the heterogeneity of the material by SDS-PAGE have yielded results which are difficult to evaluate. When electrophoresed, a high molecular weight (> 200 kDa) is again indicated, but the preparation forms a diffuse smear rather than a distinct band or bands. Very poor staining with Coomassie blue is also characteristic of the material.

Later fractions off Sephacryl columns contained four to six major proteins of lower M_r (< 35 kDa) as well as about ten more minor proteins, all of which form discrete bands and show typical affinities for Coomassie blue (Fig. 2). For the chromatographic run presented in Figure 1, these lower molecular weight proteins began eluting at fractions 45-47 and could be observed by SDS-PAGE through fractions 69-71. The glycoprotein preparation included all material eluting in fractions 30-44 and gravimetrically accounted for 53% of

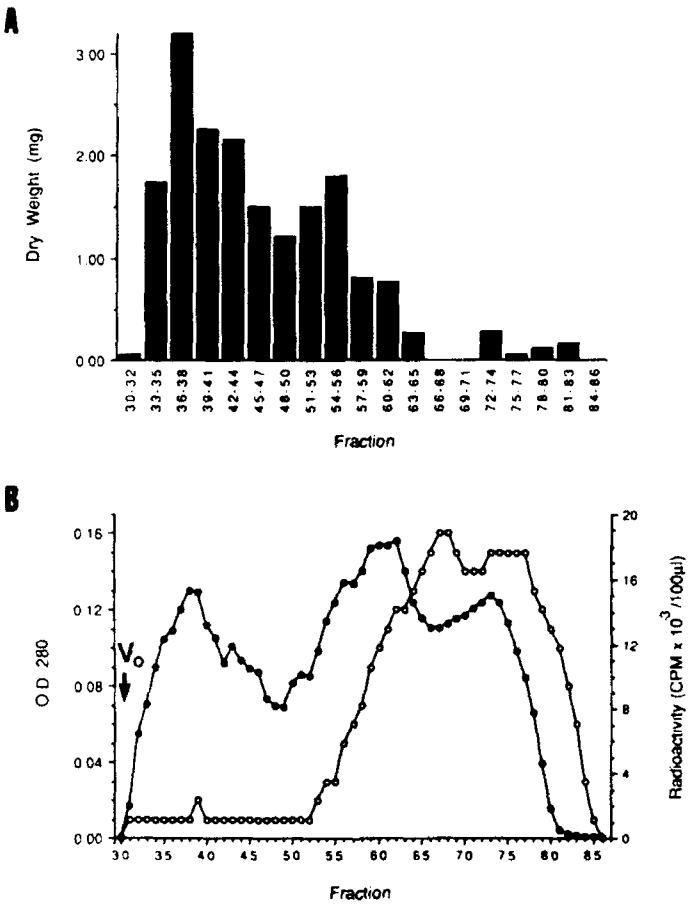

FIGURE 1. A representative fractionation on Sephacryl S-400 HR of guanidine-extracted components of ^{14}C-labeled *A. aurantia* orb webs. In this particular run, the glycoprotein preparation included material eluting in fractions 30-44. **(A)** Weight of material remaining in fractions (pooled in groups of three) after dialysis and lyophilization. **(B)** Absorbance at 280 nm (open circles) and radioactivity (solid circles) of fractions prior to dialysis. Flow rate was set at 10 mL/h and 2.5 mL fractions were collected. Blue dextran 2000 (Pharmacia LKB) was used to determine void volume (V_O). For additional details see text.

the guanidine-extracted material remaining after dialysis and lyophilization (Fig. 1A). Moreover, the presence of substantial quantities of protein in fractions 45-62, indistinguishable by SDS-PAGE from that in the glycoprotein preparation, indicates that the lower M_r, 'typical' proteins observed in fractions 45-71 account for only a small percentage of the protein in guanidine extracts.

The relatively high absorbance and radioactivity observed in fractions after 71 (Fig. 1B), which contain no protein as determined by SDS-PAGE, are probably due in large measure to the very low molecular weight solutes (< 200

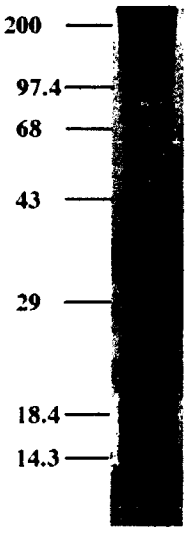

FIGURE 2. 14% SDS-polyacrylamide gel stained with Coomassie blue, showing the lower M_r, 'typical' proteins extracted from *A. aurantia* orb webs with the guanidine solution. These proteins were not included in the glycoprotein preparation. Positions of molecular weight standards (in kDa) are indicated on the left.

Da) known to be present in the adhesive spiral's viscid cover. (Of course, they undoubtedly begin eluting prior to fraction 72.) These compounds would be lost during dialysis and, hence, their presence is not reflected in the gravimetric weights (Fig. 1A).

The origin of the glycoprotein preparation was investigated by applying, to components of plated webs, the same guanidine solution used to extract webs. By this imperfect, but still useful, method the adhesive spiral core fibers appeared to be solubilized essentially immediately. However, 1 h after adding the solvent it was still possible to observe faint globules strewn along the path previously held by the core fibers. These globules were more irregularly spaced than the adhesive spiral nodules mentioned earlier. They were also, in some instances, larger than adhesive spiral nodules and irregularly shaped. Nevertheless, their appearance was most reminiscent of these nodules. Several other web components, namely the finest fibers in the stabilimentum, which are presumably of aciniform gland origin, and both types of junctional cements, seemed to be partially, even largely, solubilized by the guanidine solution, but were not completely solubilized after 1 h. Both major ampullate and minor ampullate fibers appeared to be resistant to this solvent.

Chemical Composition of Glycoprotein Preparation

The results obtained from amino acid analyses on the glycoprotein preparation are presented in Table I. Glycine, proline and threonine together account for about 57 mole % of the preparation's amino acid content. The lower molar percentage of glycine observed in samples analyzed at UNH may be due to diketopiperazine formation, resulting from the slow method used to dry hydrolysates (drying in vacuo over NaOH pellets)[32]. The effects of treating samples of the glycoprotein preparation with 0.2 N NaOH for various lengths of

TABLE I. Amino acid composition (in mole %) of samples of glycoprotein preparation analyzed at UNH or AAA Laboratory.

	UNH mean (SEM) n = 7	AAA mean (SEM) n = 3[a]
Asp	3.82 (0.191)	3.93 (0.087)
Thr	10.79 (0.335)	9.32 (0.505)
Ser	3.86 (0.074)	3.10 (0.049)
Glu	6.74 (0.038)	5.69 (0.114)
Pro	17.30 (0.255)	17.78 (0.179)
Gly	25.63 (0.572)	32.75 (1.539)
Ala	5.28 (0.286)	5.99 (0.293)
Cys/2	N.D.[b]	0.22 (0.022)
Val	4.96 (0.121)	5.55 (0.145)
Met	0.67 (0.062)	0.70 (0.058)
Ile	6.67 (0.310)	3.17 (0.252)
Leu	3.95 (0.237)	2.17 (0.260)
Tyr	2.59 (0.060)	2.61 (0.030)
Phe	2.28 (0.051)	2.11 (0.100)
His	1.13 (0.098)	0.46 (0.030)
Lys	3.81 (0.357)	4.04 (0.215)
Arg	0.52 (0.040)	0.41 (0.094)

[a] Includes the control data set presented in Table II.
[b] N.D. = not determined.

time prior to acid hydrolysis and amino acid analysis can be seen in Table II. Reductions in the molar percentages of threonine and serine indicate that about 80% and 45% of all threonine and serine residues, respectively, have *O*-linked substituents.

Carbohydrate analyses of the glycoprotein preparation using GLC indicate that *N*-acetylgalactosamine (GalNAc) is the predominant, if not sole, monosaccharide constituent (Fig. 3). No evidence for the presence of sialic acids was obtained either by GLC of monosaccharides released from the glycoprotein preparation or when whole orb webs were assayed by the resorcinol method. The results of double diffusion tests with several lectins were in agreement with the GLC findings (Table III). Only lectins with an affinity for GalNAc formed precipitates with the glycoprotein preparation. Estimates of the percentage by weight of GalNAc in the glycoprotein preparation were obtained from hexosamine analyses on an amino acid analyzer and, in one instance, by GLC. The former method gave a mean value of 8.6% (SEM 1.21%; n = 3) while 7.3% was obtained by the latter method. These data, however, assume that the glycoprotein preparation is fully dehydrated by the desiccant (P_2O_5) in vacuo at room temperature. Data from amino acid analyses indicate that it is not and, thus, that the percentage by weight of GalNAc is actually higher. Taking together data obtained from amino acid, hexosamine and GLC analyses, we estimate that the molar ratio of GalNAc/threonine is about 0.7.

TABLE II. Amino acid composition (in mole %) of glycoprotein preparation following treatment with 0.2 N NaOH.

	Length of alkaline treatment (h)			
	0	5	10	24
Asp	3.98	4.26	4.42	4.42
Thr	**10.23**	**4.12**	**3.29**	**2.27**
Ser	**3.14**	**2.25**	**2.10**	**1.88**
Glu	5.53	5.93	6.18	6.13
Pro	18.17	19.91	20.88	20.50
Gly	30.08	33.41	33.24	34.69
Ala	5.44	6.07	6.02	6.23
Val	5.85	5.74	5.83	5.72
Met	0.81	0.86	0.92	0.94
Ile	3.64	3.70	3.64	3.67
Leu	2.67	2.78	2.75	2.93
Tyr	2.67	2.75	2.88	2.88
Phe	2.31	2.44	2.52	2.52
His	0.51	0.54	0.56	0.53
Lys[a]	4.38	4.38	4.38	4.38
Arg	0.59	0.86	0.39	0.31

[a] A ninhydrin-positive compound which co-chromatographed with Lys was formed as a result of treating samples with NaOH prior to acid hydrolysis. Thus, Lys could not be quantitated in alkali-treated samples. As a reasonable estimate, the molar % of Lys in the control sample has been assigned to the alkali-treated samples.

Webs built by spiders fed ^{32}P yielded radioactive glycoprotein preparations. As a first step in examining the nature of the phosphate linkages, samples of the glycoprotein preparation were acid hydrolyzed for short periods of time and the hydrolysates were high-voltage electrophoresed. The distribution of isotope in the hydrolytic products, as quantitated by densitometry, is shown in Table IV. Using the pH 1.9 electrolyte, standard P-Ser and P-Thr were well resolved, but P-Thr and P-Tyr were not. All three phosphoamino acids were resolved using the pH 3.5 electrolyte, though spreading of individual compounds was such that the leading edge of P-Thr merged with the trailing edge of P-Ser. Consequently, having detected, at pH 3.5, no radioactive P-Tyr in hydrolysates, the relative quantities of radioactive P-Ser and P-Thr were estimated from autoradiograms prepared from pH 1.9 electrophoretograms. We should note that in an earlier ^{32}P-feeding experiment, performed in essentially the same manner as described above, the distribution of isotope in the phosphorylhydroxyamino acids was markedly different from the distribution presented in Table IV. After a 4 h hydrolysis, 88.0% of the radioactivity in the phosphoamino acids was in P-Ser, 12.0% in P-Thr.

With regard to the overall distribution of ^{32}P in the pooled collection of labeled orb webs, it is worth noting that 93.6% of radioactivity was extracted

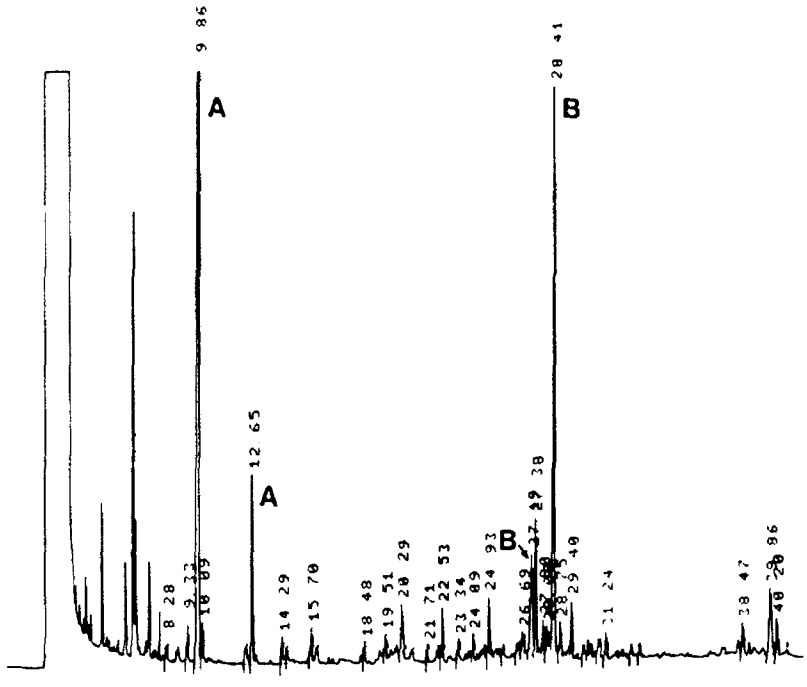

FIGURE 3. A representative GLC analysis of trimethylsilyl derivatives of methyl glycosides produced from the glycoprotein preparation. A, *iso*-erythritol (internal standard); B, *N*-acetylgalactosamine.

by gently immersing the web in distilled water and probably represents inorganic orthophosphate from the adhesive spiral's aqueous coating; 6.0% of radioactivity was extracted by the guanidine solution and largely represents the glycoprotein preparation; and 0.4% of radioactivity remained with the guanidine-insoluble fraction of the web.

Electron Microscopy of Glycoprotein Preparation

Electron microscopic examination of the glycoprotein preparation revealed polydisperse linear macromolecules exhibiting considerable flexibility (Fig. 4). Contour measurements of selected well spread preparations yielded values ranging from 900 nm to 2800 nm. If it is assumed that a single amino acid is 0.2 nm and has a molecular weight of 100 Da, then it is possible to calculate a nominal molecular weight range for the polypeptide component of this preparation as 450 to 1400 kDa assuming that the linear strands represent fully extended proteins.

TABLE III. Glycoprotein preparation - lectin interactions.

Lectin origin	Specificity[a]	Precipitation
Tetragonolobus purpureas (*Lotus tetragonolobus*) (asparagus pea)	α-Fuc	No
Lens culinaris (lentil)	α-Man > α-Glc, α-GlcNAc	No
Canavalia ensiformis (jack bean)	α-Man > α-Glc > α-GlcNAc	No
Glycine max (soybean)	α or β-GalNAc	Yes
Dolichos biflorus (horse gram)	α-GalNAc	No
Helix pomatia (edible snail)	α-GalNAc > β-GalNAc	Yes
Arachis hypogaea (peanut)	Gal (β1-3) GalNAc	No
Ptilota plumosa (red marine algae)	α-Fuc > α-Gal, α-Glc > α-GlcNAc	No

[a] *P. plumosa* specificity from Rogers et al[48]. *H. pomatia* specificity from Hammarström and Kabat[49] and Piller et al[50]. All others taken from review of Goldstein and Poretz[51].

DISCUSSION

Origin of the Glycoprotein Preparation

Observations made on plated webs indicate that guanidine extracts of whole *A. aurantia* orb webs contain products of the flagelliform, aggregate, aciniform and pyriform glands. While the glycoprotein preparation is free of the lower M_r, 'typical' proteins observed by SDS-PAGE (Fig. 2), it is still very likely that this preparation contains proteins from more than one type of gland. It is presently our view that the glycoprotein portion of this preparation (if, indeed, the glycoprotein preparation contains anything other than glycoproteins) is at least partially derived from the nodules on the adhesive spiral. These nodules, products of the aggregate glands, fluoresce intensely when incubated with FITC-labeled *Glycine max* (soybean) lectin[12], indicating the presence of terminal GalNAc residues. GalNAc was the only monosaccharide that was detected in the glycoprotein preparation by GLC (Fig. 3) and in double diffusion tests with lectins (Table III). Moreover, in several respects the glycoprotein preparation is reminiscent of a mucin (see below), and, from superficial considerations (e.g. the apparent high hydration of nodules[11] and the ability of nodules to be deformed into highly extended, filamentous strands[11,12]), nodules seem to be the most mucin-like structures in the web.

The inability of the guanidine solution to fully solubilize the adhesive spiral in plated webs within 1 h, specifically material which we presume was of nodular origin, may be at variance with the above supposition. However, it should be kept in mind that the solubilization occurring with plated web components after 1 h without agitation probably does not exactly reflect the

TABLE IV. Densitometric analysis of ^{32}P-labeled components of glycoprotein preparation following acid hydrolysis and high voltage paper electrophoresis.

Time of hydrolysis (h)	Distribution of ^{32}P in hydrolysates [Mean % of total radioactivity in hydrolysates (SEM)][a] P-AA	P-Pep[d]	Pi	n[e]	Distribution of ^{32}P in phosphoamino acids released by hydrolysis[b] [Mean % of total radioactivity in phosphoamino acids (SEM)][c] P-Ser	P-Thr	n[e]
1	16.3 (0.72)	60.4 (1.93)	23.3 (2.48)	5	61.4 (1.50)	38.6 (1.50)	2
4	19.1 (1.54)	40.8 (1.89)	40.1 (3.31)	6	51.8 (0.45)	48.2 (0.45)	2

Abbreviations: P-AA, phosphorylhydroxyamino acids; P-Pep, phosphopeptides; Pi, inorganic orthophosphate; P-Ser, phosphoserine; P-Thr, phosphothreonine

[a] Determined from runs made at pH 1.9 and 3.5.

[b] No phosphotyrosine was detected by the methods employed.

[c] Determined from runs made at pH 1.9.

[d] Includes radioactive material remaining near origin as well as at least three radioactive components which migrate toward the positive pole and at least one radioactive component which migrates toward the negative pole.

[e] n = The number of aliquots of a given hydrolysate that were analyzed by separate electrophoretic runs.

solubilization that occurs with rod-wound web after 24 h with agitation. Also, the plated webs used during this study had been collected several months previously and stored at room temperature. It may be that some web components, including adhesive spiral nodules, become more resistant to solvents with time under such conditions.

Comparison Between the Glycoprotein Preparation and Mucins

The glycoprotein preparation shares several characteristics with mammalian secretory mucins (see e.g. Refs. 33-37 for mucin reviews). By size-exclusion chromatography, SDS-PAGE and electron microscopy the glycoprotein preparation, like mucins, appears to be of high molecular weight and polydisperse. As with some mucins[38-40], it stains very poorly with Coomassie blue and absorbs poorly at 280nm. By electron microscopy, apparently flexible, unbranched, linear macromolecules are observed (Fig. 4), reminiscent of mucins[34-37]. Three amino acids that often occur in high molar percentage in mucins -- glycine, proline and threonine -- account for about 57 mole % of the glycoprotein preparation's amino acid composition (Table I).

In addition, it is a characteristic of mucins that most of their carbohydrate is *O*-linked to serine or threonine and the sugar directly bonded to these amino acids is GalNAc[33-37]. Indirect evidence reported herein indicates that this characteristic applies to the glycoprotein preparation as well. Decreases in the molar percentages of both threonine and serine were apparent in the amino acid compositions of samples of the glycoprotein preparation that had been exposed to alkali prior to amino acid analysis (Table II). However, since phosphoryl

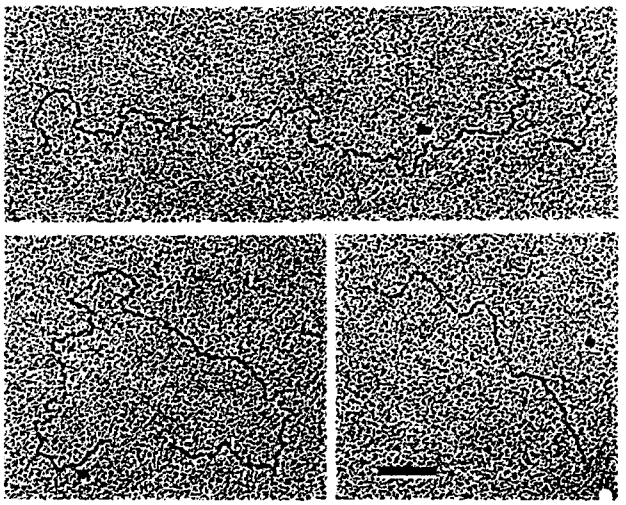

FIGURE 4. Electron micrographs of rotary-shadowed proteins from the glycoprotein preparation. Considerable flexibility is indicated. Examples from the high and low ends of a range of lengths are shown in the uppermost and lower right micrographs, respectively. All three micrographs are at the same magnification. Bar = 0.2 μm.

groups, as well as glycosyl groups, can undergo elimination by this procedure[26,41], and since P-Ser and P-Thr are present in the glycoprotein preparation, this result alone does not demonstrate the participation of serine and threonine residues in *O*-glycosidic linkages. But considering that there appears to be at least as much P-Ser in the glycoprotein preparation as P-Thr (Table IV), if not substantially more, and that the molar percentage of *O*-substituted threonine is considerably greater than the molar percentage of *O*-substituted serine (Table II), it is reasonable to suggest that the carbohydrate in the glycoprotein preparation is at least primarily *O*-linked. Moreover, these data indicate that at least much of the *O*-linked carbohydrate is bonded to threonine. Finally, as only GalNAc has been detected in the glycoprotein preparation (Fig. 3, Table III), it is the only candidate for linkage sugar.

The glycoprotein preparation also shows some important dissimilarities with mucins. For example, in mucins, threonine and serine together typically account for about 25-55 mole % of total amino acids[33,37-40,42], while in the glycoprotein preparation the corresponding value is about 13 mole % (Table I), with serine being especially low. This has a direct bearing on what is, perhaps, the most important difference between the two materials, namely, the large discrepancy in their total carbohydrate percentages. On a weight basis, from about 50 to 85% of a mucin is carbohydrate[34,36,37,42], whereas all data to date indicate that the glycoprotein preparation is <18% carbohydrate.

The presence of sialic acids, terminally positioned on some oligosaccharide chains, is also typical of mucins[33,35-37]. However, attempts to detect sialic acids in orb web constituents have yielded negative results, in both this study and previously[43,44]. Indeed, endogenous sialic acids appear to be largely, though not

entirely[45], absent in arthropods[46]. On the other hand, phosphorylated serine/threonine residues, present in the glycoprotein preparation, have not, to our knowledge, been reported in a mucin (though high molecular weight glycoproteins containing aminoethylphosphonic acid are present in mucus secreted by a sea anemone[47]). It should be recognized that if the glycoprotein preparation does contain products from more than one type of gland, then the individual components might appear more or less mucin-like in isolation.

We thank Stephanie Lara for preparing samples for electron microscopy and Susan F. Chase for excellent technical assistance. We are also very grateful to Lowell H. Eriesson and Nancy R. Eriesson (AAA Laboratory) for their carefully and expertly performed analyses. This work was supported by NIH area grant R15 GM44353-01A1, and HATCH (grant 352) and BRSG funds from the University of New Hampshire.

REFERENCES

1. C. Warburton, Quart. J. Microsc. Sci., N.S. **31**, 29 (1890).
2. H.M. Peters, Z. Naturforsch. **10b**, 395 (1955).
3. R.W. Work, Trans. Am. Microsc. Soc. **100**, 1 (1981).
4. C. Apstein, Arch. Naturgesch. **55**, 29 (1889).
5. E.J. Kavanagh and E.K. Tillinghast, J. Morph. **160**, 17 (1979).
6. K. Sekiguchi, Annot. Zool. Japon. **25**, 394 (1952).
7. F.G. Fischer and J. Brander, Hoppe-Seyler's Z. physiol. Chem. **320**, 92 (1960).
8. H. Schildknecht, P. Kunzelmann, D. Krauß, C. Kuhn, Naturwissenschaften **59**, 98 (1972).
9. F. Vollrath, W.J. Fairbrother, R.J.P. Williams, E.K. Tillinghast, D.T. Bernstein, K.S. Gallagher, M.A. Townley, Nature **345**, 526 (1990).
10. M.A. Townley, D.T. Bernstein, K.S. Gallagher, E.K. Tillinghast, J. Exp. Zool. **259**, 154 (1991).
11. G. Richter, Naturwissenschaften **43**, 23 (1956).
12. F. Vollrath and E.K. Tillinghast, Naturwissenschaften **78**, 557 (1991).
13. E.K. Tillinghast, E.J. Kavanagh, P.H. Kolbjornsen, J. Morph. **169**, 141 (1981).
14. U.K. Laemmli, Nature **227**, 680 (1970).
15. S. Moore and W.H. Stein, Meth. Enzymol. **6**, 819 (1963).
16. M.W. Rees, Biochem. J. **40**, 632 (1946).
17. S. Moore, J. Biol. Chem. **238**, 235 (1963).
18. D.B. Bylund and T.-S. Huang, Anal. Biochem. **73**, 477 (1976).
19. J.A. Cooper, B.M. Sefton, T. Hunter, Meth. Enzymol. **99**, 387 (1983).
20. G.N. Atfield and C.J.O.R. Morris, Biochem. J. **81**, 606 (1961).
21. J. Heilmann, J. Barrollier, E. Watzke, Hoppe-Seyler's Z. physiol. Chem. **309**, 219 (1957).
22. M.F. Chaplin, Anal. Biochem. **123**, 336 (1982).
23. B.J. Catley, S. Moore, W.H. Stein, J. Biol. Chem. **244**, 933 (1969).
24. O. Ouchterlony, Prog. Allergy **5**, 1 (1958).
25. L. Svennerholm, Biochim. Biophys. Acta **24**, 604 (1957).
26. R.G. Spiro, Adv. Prot. Chem. **27**, 349 (1973).
27. B. Anderson, P. Hoffman, K. Meyer, J. Biol. Chem. **240**, 156 (1965).
28. J. Montreuil, S. Bouquelet, H. Debray, B. Fournet, G. Spik, G. Strecker, in *Carbohydrate Analysis: A Practical Approach*, edited by M.F. Chaplin and J.F. Kennedy (IRL Press, Oxford, 1986), pp. 143-204.
29. A.B. Zinn, J.J. Plantner, D.M. Carlson, in *The Glycoconjugates, Vol. 1*, edited by M.I. Horowitz and W. Pigman (Academic Press, New York, 1977), pp. 69-85.
30. A. Kleinschmidt and R.K. Zahn, Z. Naturforsch. **14b**, 770 (1959).
31. L. Rosenberg, W. Hellmann, A.K. Kleinschmidt, J. Biol. Chem. **245**, 4123 (1970); J.H. Kimura, P. Osdoby, A.I. Caplan, V.C. Hascall, ibid., **253**, 4721 (1978).
32. L.H. Eriesson, AAA Laboratory, Mercer Island, WA (private communication).
33. W. Pigman, in *The Glycoconjugates, Vol. 1*, edited by M.I. Horowitz and W. Pigman (Academic Press, New York, 1977), pp. 137-152.
34. C.L. Laboisse, Biochimie **68**, 611 (1986).
35. P. Roussel, G. Lamblin, M. Lhermitte, N. Houdret, J.-J. Lafitte, J.-M. Perini, A. Klein, A.

Scharfman, Biochimie **70**, 1471 (1988).
36. S.E. Harding, Adv. Carbohyd. Chem. Biochem. **47**, 345 (1989).
37. G.J. Strous and J. Dekker, Crit. Rev. Biochem. Mol. Biol. **27**, 57 (1992).
38. T.F. Boat, P.W. Cheng, R.N. Iyer, D.M. Carlson, I. Polony, Arch. Biochem. Biophys. **177**, 95 (1976).
39. A.E. Eckhardt, C.S. Timpte, J.L. Abernethy, A. Toumadje, W.C. Johnson, Jr., R.L. Hill, J. Biol. Chem. **262**, 11339 (1987).
40. J.M. Creeth, B. Cooper, A.S.R. Donald, J.R. Clamp, Biochem. J. **211**, 323 (1983).
41. H. Juhl and T.R. Soderling, Meth. Enzymol. **99**, 37 (1983); J.E. Buss and J.T. Stull, ibid., **99**, 7 (1983).
42. S.A. Doehr, in *The Glycoconjugates, Vol. I*, edited by M.I. Horowitz and W. Pigman (Academic Press, New York, 1977), pp. 239-257.
43. K. Dreesbach, G. Uhlenbruck, E.K. Tillinghast, Insect Biochem. **13**, 627 (1983).
44. H. Sinohara and E.K. Tillinghast, Biochem. Int. **9**, 315 (1984).
45. J. Roth, A. Kempf, G. Reuter, R. Schauer, W.J. Gehring, Science **256**, 673 (1992).
46. A.P. Corfield and R. Schauer, in *Sialic Acids: Chemistry, Metabolism and Function*, edited by R. Schauer (Springer, Vienna, 1982), pp. 5-50.
47. T.A. Bunde, G.E. Dearlove, S.H. Bishop, J. Exp. Zool. **206**, 215 (1978).
48. D.J. Rogers, G. Blunden, P.R. Evans, Med. Lab. Sci. **34**, 193 (1977).
49. S. Hammarstrom and E.A. Kabat, Biochemistry **10**, 1684 (1971).
50. V. Piller, F. Piller, J.-P. Cartron, Eur. J. Biochem. **191**, 461 (1990).
51. I.J. Goldstein and R.D. Poretz, in *The Lectins: Properties, Functions, and Applications in Biology and Medicine*, edited by I.E. Liener, N. Sharon, I.J. Goldstein (Academic Press, Orlando, 1986), pp. 33-247.

SPIDER SILK PROTEINS

MIKE HINMAN, ZHENGYU DONG, MING XU and RANDOLPH V. LEWIS
Molecular Biology Department, U. of Wyoming, Box 3944 Laramie, WY 82071-3944

ABSTRACT

Dragline silk has been shown to consist of two proteins, Spidroins 1 and 2, which form this unique fiber. The cDNAs for these two proteins have been sequenced and a structure proposed which accounts for both the tensile strength and elasticity of dragline silk.

INTRODUCTION

Spiders are unique creatures due to the presence of glands in their abdomen producing silk. They are also unique in the use of silk throughout their life span and the nearly total dependence on silk for their evolutionary success. Although spiders have been studied since earliest man, the first papers using a scientific approach to spider webs and silk appeared in the 1800s. One of the earliest was by John Blackwell describing the construction of webs by spiders [1]. The following decades resulted in studies of the biology of the spiders and their anatomy, but little information was published about the silk itself. In 1907 Benton published one of the earliest studies describing properties of the silk [2]. In that same year Fischer demonstrated the protein nature of the silk by showing the predominant presence of amino acids [3]. There were periods of fairly intense study prior to World War II and in the late 1950s. However progress, especially when compared to silkworm silk, was relatively meager. Beginning in the 1970s the laboratories of Work, Gosline and Tillinghast revived interest in spider silk with several papers describing physical, mechanical and chemical properties of spider silks. Despite the efforts of these groups and others, the structure of the spider silk protein(s) remained unknown .

Spider webs are constructed from several different silks. Each of these silks is produced in a different gland. The glands occur as bilaterally symmetric paired sets. Although each of the glands has its own distinctive shape and size, their functional organization is similar. The majority of the gland serves as a reservoir for soluble silk protein which is synthesized in specialized cells at the distal end of the gland. The soluble silk is pulled down a narrow duct during which the physical and chemical changes occur which produce the solid silk fiber. There is a valve at the exit to the spinneret which can control the flow rate of the fiber and may control the fiber diameter to a small degree. The silk exits through the spinnerets, of which there are three pairs, anterior, median and posterior.

Due to their size and ease of study, the major ampullate glands have received the most attention. Thus, most of what is known about the synthesis of silk proteins is based on the study of that gland. However, morphological and histochemical studies of the other glands support the ideas developed for the major ampullate gland. The synthesis of the silk protein(s) takes place in specialized columnar epithelial cells [4] which appear to lack a Golgi apparatus. There appears to be at least two different types of cells producing protein [5] which correlates with our data on the composition of the silk from these glands. The newly synthesized protein appears within the cell as droplets which are secreted into the lumen of the gland via an

Mat. Res. Soc. Symp. Proc. Vol. 292, © 1993 Materials Research Society

unknown mechanism.

The state of the protein in the lumen of the gland is unknown but it must be in a state which prevents fiber formation as the fiber is not formed until passage down the duct. This is probably accomplished by a combination of protein structure and concentration which prevents aggregation in large protein arrays. It has been shown that the silk in the gland is not birefringent whereas the silk becomes birefringent as it passes down the duct [6]. Thus the ordering of protein seen in the final fiber is accomplished in the duct. This ordering appears to be due to the mechanical and frictional forces aligning the protein molecules and probably altering the secondary structure to the final fiber form. Experimental evidence for this has been the ability to draw silk fibers directly from the lumen of the major, minor and cylindrical glands (unpublished data) implying that the physical forces of drawing the solution are sufficient for fiber formation.

One of the features which attracted attention to spider silk was its unique properties. The spider must be able to use the minimum amount of silk in its web to catch prey in order to survive successfully. The web has to stop a rapidly flying insect nearly instantly in a manner that allows it to become entangled and trapped. To do this the web must absorb the energy of the insect without breaking and yet not act as a trampoline to send the insect back off the web. Gosline et al. [7] have reviewed several aspects of this and concluded that spider silk and the web are nearly optimally designed for each other.

As with any polymer, especially those made of protein, there are numerous factors which can affect the tensile strength and elasticity. These can include temperature, hydration state and rate of extension. Even with all those caveats, it is clear that dragline silk is a unique biomaterial. As seen in Table I dragline silk will absorb more energy prior to breaking than nearly any commonly used material. Thus, although it is not as strong as several of the current synthetic fibers, it can outperform them in many applications.

The composition of spider silks has been known to be predominantly protein since the early studies of Fischer [3]. In fact, except for the sticky spiral thread, no significant amounts of any substance other than protein have been detected, including sugars, minerals and lipids. The various silks have significantly different amino acid compositions as do the same silks from different spiders. In the major ampullate silks, the combination of Glu, Pro, Gly and Ala comprise 80% of the silk from each species. However, the proportion of Pro is significantly different in each. As will be discussed below these differences can be accounted for by different ratios of two proteins. The minor ampullate silks are more similar among species and differ from major ampullate silk in having significantly lower Pro values. Cylindrical (tubuliform) gland silk used for constructing egg cocoons is radically different from any of the other silks. The amount of Gly is reduced by nearly three quarters and Ser, in particular, has increased to compensate as have other amino acids to a much lesser extent. The coronate gland (swathing) silk is also very different in having a very high proportion of Pro in relation to the other amino acids.

There are two major reasons that virtually all of the biophysical data on spider silk has been obtained from major ampullate silk. First, it can be obtained easily since the spiders trail it along behind as they move. Second is the combination of mechanical properties of elasticity and high tensile strength, which will be discussed in detail below.

There were several early studies of silk fibers using X-ray diffraction which provided some information, much of which was interpreted based on the structure of silkworm silk [reviewed

TABLE I

Material	Strength ($N\ m^{-2}$)	Elasticity (%)	Energy to Break ($J\ kg^{-1}$)
Dragline silk	$1\text{-}2 \times 10^9$	35	1×10^5
KEVLAR	4×10^9	5	3×10^4
Rubber	1×10^6	600	8×10^4
Tendon	1×10^9	5	5×10^3

```
---------.....................G..
--------------------.........G..
------.......................S..
...---.......................S..
AGRGGLGGQGAGAAAAAAAGGAGQGGYGGLGNQG
...---...--.......-...........S..
.........-........-...........G..
--------------------.........S..
.........................---....G..
------A......S....-...........S..
...---..E.........-...........G..
--------------------.........S..
...............---.....---....G..
------A...........-...........S..
............V.................S..
...---............-.....R......N..
.............  ................N..
...---...--......--...........S..
...---............-V....E.IR---G..
--------------------.........S..
S................-.....---....G..
------A..........-..VR........S..
...---...........-...........G..
V..............---.........V.S-.
----------.S..S....
```

FIGURE 1

The Spidroin 1 amino acid sequence is shown organized to demonstrate the repeats; - is a deletion and . an identical residue at that position. This sequence is from a 2.4 kb cDNA clone with the non-repetitive regions and the 3' untranslated region not shown.

in 8]. These studies led to the classification of dragline silk as group beta 3, 4 or 5 depending on the species. These groups are distinguished by the intersheet distance between the beta sheets. The higher the number, the larger that spacing. It was also clear that much of the structure was not beta sheet and appeared to be random. However, it is clear from the amino acid compositions of the different silks that large bulky groups are present and must be accommodated either in the sheet or in the random regions. The amino acid sequences of the proteins from dragline silk put limits on what the structures can be and the X-ray data must be interpreted on that basis.

Using Fourier transform infrared spectroscopy (FTIR) Dong et al. [9] have probed the structure of the dragline silk fiber in the relaxed and extended states. The data confirm the presence of significant beta sheet-like structure which appears the same in both relaxed and extended forms. Dragline silk, which was dissolved in 4.7M $LiClO_4$, dialysed against water and dried to a film, also showed predominantly beta sheet-like conformation indicating this is a preferred secondary structure of the proteins in the solid state (unpublished data). However, in the extended state, the silk forms a helical structure which returns to the original form when the tension is released. The parallel polarized spectrum shows the orientation is parallel to the fiber axis. These same spectral features were observed for both *Nephila clavipes* and *Araneus gemmoides*. The helical regions appear to be coming from the random or non-oriented regions. However, minor ampullate silk, which exhibits very low elasticity, showed no such helix formation. These data suggest that helix formation is playing an important role in the elastic function of these proteins.

Another interesting characteristic of dragline silk is its ability to supercontract. When unrestrained dragline silk is placed in water it contracts to 50-60% of its original length. This contraction results in a 1000-fold decrease in the elastic modulus and a greatly increased extensibility [10]. Although several polymers exhibit this characteristic in organic solvents dragline silk will supercontract in water but not in organic solvents [11-14]. The data from X-ray diffraction suggest the beta sheet regions rotate within the fiber but otherwise are unchanged. Thus, the water must be altering the relationship of the sheet regions to the non-oriented regions. This supercontraction is reversible and repeatable and can be used to achieve mechanical work by the fibers.

With the proposed structure of dragline silk being crystalline regions interspersed with non-oriented regions, the question arises as to the mechanism of elasticity. In the supercontracted form, this appears to be predominantly an entropy driven process [10] with about 85% of the retractive force due to polymer chain conformational entropy. A later calculation estimates the average size of the random chains to be about 15 amino acids [7].

METHODS

Pure silk fibers

Much of the past research on spider silk relied on obtaining samples from webs or from the trailing fibers of the spider. It has become clear that many of these samples were composed of more than one silk type. Thus, Work and Emerson [15] designed an apparatus to forcibly silk spiders to obtain a single fiber type. Although the apparatus performed well, it was relatively complicated to construct and operate. We have designed a simple version of their instrument which consists of a variable speed drill which is connected to a sewing machine footpedal controller which regulates the drill speed. Forceps are used to take a single silk fiber, which is

wrapped around a spool, from a CO_2 anaesthetized spider whose legs have been taped down. The procedure is done with the aid of a microscope to insure that only a single fiber of the type desired is taken. While observing under the microscope, the silk is forcibly wound onto the spool. This method is applicable to both major and minor ampullate silk. In fact, both can be obtained simultaneously using two spools separated by 2 cm or more.

Occasionally it is possible to obtain swathing silk in the same manner but the success rate for this is relatively low in our experience. Swathing silk can be obtained from spiders fed frequently as they occasionally will wrap the prey for later use. This silk can be carefully removed from the prey for examination.

Cocoon silk has been obtained directly from fresh cocoons. However, in observing the cocoon construction by *Nephila clavipes*, it was seen that several fibers, probably eight, were laid down simultaneously. Thus, it is difficult to obtain single fibers, but it is possible. In addition, it was observed that after the eggs are laid, the viscous secretion that accompanies them is frequently smeared over the fibers which leads to erroneous amino acid compositions. The amino acid composition of this secretion is largely hydrophobic amino acids which are not present to a large degree in either the cylindrical gland or the carefully obtained single fibers.

Protein Sequence

Initial efforts to obtain protein sequence were directed at the silk fibers themselves. When the fibers were placed on the sequencer membrane, they were retained and sequence information could be obtained. The data clearly showed that no single amino terminus was present. In fact, the sequence data resembled the amino acid composition at nearly every step except for the occasional increase of Pro or Tyr. No useful information was obtained in this fashion.

The next approach was to solubilize the silk protein(s) and purify them by conventional means. As it was already known that these proteins were soluble only in highly chaotropic agents, we used LiSCN and $LiClO_4$. The latter is particularly useful due to its lack of UV absorbance at wavelengths used for protein detection. However, solubilization in these and several other reagents still did not allow for purification due to the lack of useful methods in the presence of such salts. We were unable to effectively utilize even size exclusion due to the very broad elution profiles of these proteins. In the end, we could find no useful method to solubilize and purify the proteins for sequence analysis.

The use of enzymatic cleavage to generate fragments of the protein for sequencing was hampered by the lack of a suitable agent in which the protein was soluble and the enzymes were active. Numerous combinations were tried, especially after solubilization in strong denaturants and attempts to dialyse into less harsh reagents, which all proved unsuccessful. Proteins denatured in the chaotropic agents were digested in the precipitated state with a wide variety of enzymes, but this approach also proved unsuccessful. It is easy to see why spider silks in nature are very resistant to normal degradative processes.

Attempts to use chemical cleavage were generally unsuccessful due to the lack of Met and Trp in these protein. However, later we were able to use N-bromosuccinimide (NBS) in formic acid with some success to cleave at Tyr for silks which were soluble in the concentrated acid.

Since the conventional approaches were unsuccessful, we returned to a technique employed in the early days of protein sequencing; partial acid hydrolysis. Even this generally

straightforward procedure was not without significant problems. The problems can be attributed to the repetitive nature of the proteins and the lack of significant diversity in the amino acids present. The result is peptide bonds which have very little difference in bond strength. Thus, once hydrolysis starts all bonds are cleaved at nearly identical rates. Trifluoroacetic acid proved to be an excellent hydrolysis reagent because the silk became soluble prior to hydrolysis. However, under conditions in which hydrolysis occurred the amino terminus of all isolated peptides was blocked to Edman degradation and no sequence information could be obtained. This led to a procedure [16] in which the silk was hydrolysed in 6N HCl for 3-4 min at 155°C. This resulted in nearly all of the solid silk disappearing but peptides were present. One minute longer resulted in complete hydrolysis and one minute less no cleavage at all. Other temperatures and acids were used, but none gave results that were better than these conditions. The peptides obtained were sequenced and were generally quite short. However, there was enough sequence to create a DNA probe for cloning studies.

Cloning

Completely degenerate oligonucleotide probes were synthesized based on the peptide sequences. In addition, the same probes were synthesized in four pools with one quarter the total degeneracy in each pool. The cDNA libraries were constructed using RNA from the major ampullate glands of *Nephila clavipes*. In order to insure a maximum level of silk protein mRNA, the spiders were forcibly silked to remove as much silk as possible. After four hours, at which time they should be maximally producing silk in the gland, they were sacrificed and the silk glands removed. Standard cDNA library construction methods were used as described in Xu and Lewis [16].

With the anticipation that the silk mRNA would comprise a significant proportion of the total mRNA of the gland we decided to use isolated colony screening instead of the standard plate screening used for less abundant messages. Therefore, 960 colonies were picked and grown in 96 well plates which were then dotted on filter paper. Standard screening methods were used and the positive colonies were clearly evident. In fact, overnight and 2 hour autoradiographic exposures gave such large spots that it was not possible to tell which colony was positive. It was necessary to use a 15 minute exposure to clearly decide which colony was the correct one. Initial screening gave 36 positives which were then analysed by Southern blotting. We found 21 hybridization positive plasmids with the largest indicating a 4 kb insert. Each of these was grown separately, the plasmids isolated and restriction digested to release the insert prior to another Southern blot. At this stage there were 12 positive inserts with the largest being 2.5 kb. The largest two of these were chosen for sequencing (2.1 kb and 1.8 kb).

It was disturbing that the large number of initial positive colonies was reduced to such a small number but, as was later found, this is a characteristic of all the silk cDNAs we have examined. They are unstable in all plasmids and cell lines we have tested. Some plasmids and cells have greater stability than others, but all have a significant deletion rate which can lead to problems if it is not taken into account. It is also clear that the larger the insert the higher the deletion rate although there appear to be islands of stable sizes which accounts for our finding the two larger colonies. We have transiently observed larger inserts in several libraries but have been unable to maintain them long enough to sequence them. In fact, this deletion rate can be seen in the colonies where initially white colonies containing plasmid

inserts start to turn blue from loss of inserts with time. We have even used this as a marker during initial screening to identify likely silk cDNA containing colonies.

DNA sequencing

As might be expected the problem with insert deletion led to numerous problems with sequencing as well. Unfortunately, this only became clear in retrospect after completion of the sequence of the first protein. Due to the likely repetitive nature of the DNA, we felt random fragmentation and sequencing might not be the most efficient approach. We therefore chose to create nested deletions to obtain the total sequence. This choice has proven to be the correct one as there were regions of over 200 bases which were identical between repeats. These large regions of identity also led to the need to have a large number of overlapping sequences to insure the correct placement of each fragment.

The problem with insert deletions manifested itself in the presence of only a few stable sizes of inserts no matter what time point of exonuclease digestion was used. As we found on the second protein, the solution was to examine a very large number (24-48) of colonies from each time point and choose a wide variety of insert sizes to insure adequate coverage of the region. We also observed compression regions which led to problems with accurate sequencing. Only with careful analysis of both strands could these be resolved [17].

RESULTS AND DISCUSSION

Spidroin 1

The sequence of Protein 1 is presented in Fig. 1, arranged to show the repeating units more clearly. The first obvious feature is the very low number of substitutions in the repeats. Another interesting feature is the large number of deletions from the consensus sequence. These deletions are almost all in multiples of three for currently unknown reasons. We have broken the sequence into three segments. The first nine amino acids are conserved in sequence, but the number of deletions is very high in this segment. The second segment is the $GAG(A)_n$ segment. This region is highly conserved with few substitutions and some variation in the number of Ala residues present. The third segment is the last 15 amino acids which is very highly conserved in sequence with virtually no substitutions and very few deletions. The only position showing any variation is the antepenultimate residue which can be Gly, Ser or Asn but no others. The sequence can be thought of as a $(GGX)_n(A)_n$ repeat or alternatively a $(GXG)_n(A)_n$ with X being Gln, Tyr or Leu. A search of the protein sequence database found no matching sequences to any six amino acids in the sequence except the $(Ala)_n$ region. Thus it appears these are, to date, unique combinations of amino acids.

Spidroin 2

From Fig. 1 it can be seen that no Pro is present in this sequence, yet the silk is 3.5% Pro and we isolated a major Pro containing peptide from the silk. We synthesized a new probe based on the Pro containing peptide and used it to rescreen our initial library. Over 20 positives were detected and following the same procedure as for Protein 1 we sequenced the largest which was about 2.1 kb. The sequence has been arranged to highlight the repetitive segments in Fig. 2. The repeat sequence of Protein 2 can be broken into three segments as

```
GPGQQGPGGYGPGQQGP--SGPGSAAAAAAAAAA----GPGGYGPGQQGPGGY
........R.....................----....-----.S........
..R.........................S...S.ESGQQ..............
.............................S--....-----..........
.............................S--....------.........
...............L.............---....--------------
.................................-....----------.....
....................A.........---....-----......L...
................GGY.....S......--....--------------
.............  ............S............----------.....
..........A.............S............----------.....
..........A.....................-....----------.....
```

FIGURE 2

The Spidroin 2 amino acid sequence is shown organized to demonstrate the repeats, - is a deletion and . an identical residue at that position. The sequence is from a 2.1 kb cDNA clone with the non-repetitive region and 3' untranslated regions not shown.

well. In this case the first segment, the first twenty amino acids is very highly conserved with only a couple of substitutions and one insertion. The second segment, the polyalanine region, is longer than in Protein 1 and has substitutions of Ser only. There is some difference in the number of Ala residues but less than was seen for Protein 1. The final fifteen amino acids are characterized by very few substitutions, but a large number of deletions. Interestingly the deletions are virtually all in multiples of five instead of three. This reflects the repeat which could be written as (GPGQQ)(GPGGY)GP (SGPGS)$(A)_n$(GPGGY)(GPGQQ)(GPGGY). The reason for the pentamer deletions may be more clear as discussed below in the predicted structure of this protein. The sequence database again shows no identical protein sequences for these peptide segments, although some similar groups of amino acids were detected as discussed in more detail below.

Codon usage

There is an incredible codon usage bias in both of these proteins. The skew is away from using C or G in the wobble base. This is particularly seen in Gln and Gly where there is over 90% use of A and T in the third position. This is probably not overly surprising since the majority of codons already have C and G in the first two bases. In order to prevent long stretches of Cs and Gs resulting in stem-loop formations which would be unstable, the wobble base is restricted to A or T. This is in contrast to the silkworm silk DNA which shows no strong codon bias like this [18].

Proposed Structure

It is always with trepidation that one tries to predict the structure of any protein without X-ray or 2-D NMR data but with proteins which show no sequence homology to other proteins it is even more difficult. To further complicate the situation with dragline silk there are two proteins, not one, and they exist in an environment of low water, a situation which has not been explored by protein structural research to any large degree. Finally, the data to date on the proteins is somewhat contradictory as to the secondary structure of the basic protein repeat elements. Despite these factors we will propose a structure based on available data and on analogies to proteins showing some similarity to the silk sequences. There are testable elements to this structure which we hope to examine to determine if it is correct.

Protein 1 seems to have little tendency to form a single thermodynamically stable structure (unpublished data). Rather it can assume a variety of secondary structures based other extrinsic factors. Thus we turned to Protein 2 to establish a preliminary structure. In view of the large number and spacing of Pro residues there is no chance the protein can assume either a helical or a typical sheet structure. Since the repeat distance of the Pro is 5 residues it cannot form a cross beta structure either since that would require an even number of residues.

When other high Pro proteins are examined there are two that have some similarity in sequence and spacing of Pro residues to silk protein 2. The first is gluten, an insoluble protein from wheat, which is thought to be responsible for the elasticity of dough [19]. The other is synaptophysin, an integral membrane protein of synaptic vesicles which can bind calcium [20]. Gluten has some repeat sequences which are Pro-Gly-Gln-Gly-Gln-Gln and synaptophysin is Tyr-Gly-Pro-Gln-Gly. Both of these proteins are thought to form beta-turn helices or a beta spiral. In addition, when the prediction of beta turn is examined in more detail [21], the prediction table gives the sequence Gly-Pro-Gly-Gln one of the highest

possible scores for a beta turn with Gly-Pro-Gly-Gly just slightly below that score. These are both for type II turns.

The poly-Ala region can clearly form an alpha-helix as we showed with the CD studies and others have noted as well [22]. However, these studies are all done in presence of water of hydration. The structure of these types of peptides in the absence of substantial water has been shown to be beta-sheets which is consistent both with fiber X-ray diffraction studies and with bound water determination for the silk fibers (unpublished data) [23].

Thus the poly Ala regions for Spidroins 1 and 2 form the beta-sheet regions seen by the various biophysical techniques. The Gly rich regions are likely to form beta-turns (possibly type 2'). Under tension the turns can open up sufficiently to allow for the observed elasticity. The driving force for the return to the turn structure probably involves an unfavorable bond angle for Pro as well as other forces. Current efforts are directed toward confirming these structures and mechanism.

Acknowledgement: This work was sponsored by the Army Office of Research.

References

1) Blackwell J (1830) Zool Journ V:181-188
2) Benton JR (1907) Amer Jour Sci xxiv: 75-78
3) Fischer E (1907) Hoppe-Seyler's Z Physiol Chem 53: 440-450
4) Bell AL, Peakall DB (1969) J Cell Biol 42:284-295
5) Kovoor J (1972) Ann Sci Nat Zool Biol Anim 14:1-40
6) Work RW (1977) Text Res J 47:650-662
7) Gosline JM, DeMont ME, Denny MW (1986) Endeavour 10:37-43
8) Fraser RDB, MacRae TP (1973) Academic Press, New York, London Chapter 13
9) Dong Z, Lewis RV and Middaugh CR (1991) Arch Biochem Biophys 284:53-57
10) Gosline JM, Denny MW, DeMont ME (1984) Nature 309:551-552
11) Work RW (1981) J. Arachnol 9:299-308
12) Work RW (1985) J Exp Biol 118:379-404
13) Work RW, Morosoff N (1982) Test Res J 52:349-356
14) Fornes RE, Work RW, Morosoff N (1983) J Polym Sci 21:1163-172
15) Work RW, Emerson PD (1982) J Arachnol 10:1-10
16) Xu M, Lewis RV (1990) Proc Natl Acad Sci USA 87: 7120-7124
17) Hinman M, Lewis RV (1991) J Biol Chem 267:19320-19324
18) Mita K, Ichimura S, Zarne M, Jones TC (1988) J Mol Biol 203:917-925
19) Field M, Tatham AS, Shewry PR (1987) Biochem J 247:215-221
20) Buckley KM, Floor E, Kelly RB (1987) J Cell Biol 105:2447-2456
21) Wilmot CM, Thornton JM (1988) J Mol Biol 203:221-232
22) Marqusee S, Robbins VH, Baldwin RW (1989) Proc Natl Acad Sci USA 86:5286-5290
23) Hempel A, Camerman N, Camerman A (1991) Biopolymers 31: 187-192

NUTS*

JULIAN F. V. VINCENT
Centre for Biomimetics, The University, Reading, RG6 2AT, UK

1 Abstract

The shell (pericarp) of nuts protects the seed from being eaten before it can germinate. It is presumably designed to resist fracture by external forces, and evolution will have optimised its design for this purpose. It appears that the material of larger shells, which will tend to be structurally more brittle, is tougher. However, the fracture mechanics theory for shells in compression is not available, nor the information on the biological selection pressures.

2 Introduction

Fracture mechanics theory tells us that the fracture strength of an object is dependent not only on material and structure but also on size. In general, smaller objects appear tougher since there is relatively less volume (a term in length cubed) for the storage of strain energy to feed to the advancing fracture (whose area is a function in length squared). So in small objects the strain energy density has to be higher in order to get a crack to propagate. Also, since the length of a critical Griffith crack remains the same, being a property of the material, a smaller object will be less likely to contain a critical crack of this length and therefore be safer at the same loads. This will also allow the smaller object to sustain the higher loads. Ultimately an object can be small enough not to fail in a brittle manner and will undergo plastic deformation. This general rule of materials science can be tested on natural structures; one of the most suitable is seeds.

A plant may produce a few large seeds, usually protected by a hard shell or pericarp, or a large number of small seeds which do not have such protection and may even have large amounts of edible material associated with them (loosely known as a fruit although it can have a variety of developmental origins) which will encourage the attentions of an animal. The large seeds are commonly known as nuts which may be produced either singly (hazel nut, walnut, acorn, macadamia nut, coconut, etc.) or several contained within a pod (Brazil nut, ngali nut, etc.). In this preliminary study I have concentrated on single nuts since these are more or less spherical allowing relatively easy analysis of both structure and material, and have used hazel nuts, walnuts and macadamia nuts. Since, by and large, the ecology of these structures is based on their mechanical properties, I have also considered the ways in which structural and mechanical properties interact to affect the ecology of the nut.

*This title is taken from a remark made by Brig. Gen. Anthony McAuliffe, then commanding the 101st Airborne Division, on Dec 22nd 1944 when invited to surrender to the German forces at Bastogne.

Mat. Res. Soc. Symp. Proc. Vol. 292. © 1993 Materials Research Society

3 Materials and Methods

Whole nuts were tested in slow compression in a universal testing machine (Instron 4202) until they fractured. In nearly every instance the fractured nut shell still supported a load; with walnut and macadamia nut (less commonly with hazel nut) the shell was incompletely fractured. The deduction can therefore be made that, since fracture is driven by elastic strain energy stored in the shell, when the stress level within the shell falls below the fracture stress there will be some strain energy remaining. Thus if the shell is then unloaded at the same rate as it was loaded (about 1 mm/min), the remaining strain energy is discounted and only the strain energy used to propagate the fracture (apparent fracture energy) is measured (figure 1). In some instances the shell was loaded further after the main fracture, and unloaded again before any further fracture occurred. In all such cases the shell showed complete elasticity (i.e. no hysteresis). The length of fracture and the mean thickness of the shell were then measured allowing the apparent fracture energy to be normalised to the area cleaved. The mean diameter of the nut was then estimated from the diameter measured in the x, y and z directions. If the strain energy available for fracture is proportional to the volume of the shell and the energy required for fracture is proportional to the surface area of that fracture, then simple geometry shows that the apparent fracture energy (R_{app}) is related to the amount of available strain energy (U) by:

$$R_{app} = krU$$

where k is a constant and r is the radius of the nut. This relationship ignores values of the thickness of the shell raised to powers of 2 or more; the radius of the hazel nut is about 10 times the thickness of the shell; the figure is nearer 30 in walnuts.

The mathematics of loading a shell in compression with the load concentrated in a small area have been documented [1]:

$$d = \frac{-2APr\sqrt{1-\nu^2}}{Et}$$

where d is the deflection of the shell, P is the force exerted, ν is the Poisson ratio (assumed to be about 0.3), E is the stiffness of the shell material and t is the thickness of the shell. A is a constant, calculated as about 0.4.

Fracture surfaces of small pieces of hazel nut and walnut shell were photographed in a scanning electron microscope following standard preparation procedures.

4 Results and Discussion

Electron and light microscopy show that in all three nuts the inner and outer layers of the shell are different (figures 2 and 3). The tendency is for the outer layer to be composed of cells (sclerids) which are apparently full of material, presumably lignin. The fracture surface looks like a loosely bonded concrete-like material which fractures relatively easily between the particles (= cells; figures 4 and 5). This material is obviously not good at resisting tension, but may well resist compression. It will also have to resist the cutting action of insect mandibles as when a weevil bores in to the nut. This will not involve strain energy storage but will rely upon the nut being locally hard. In the macadamia nut (which is dried at high temperature during cooking) the outer surface of the shell is covered with a large number of shallow cracks, presumably due to the contraction of the shell on drying. The inner layer of the hazel is very thin (figure 2), but is similar to that of the walnut in that it is comprised of cells which are well stuck together and

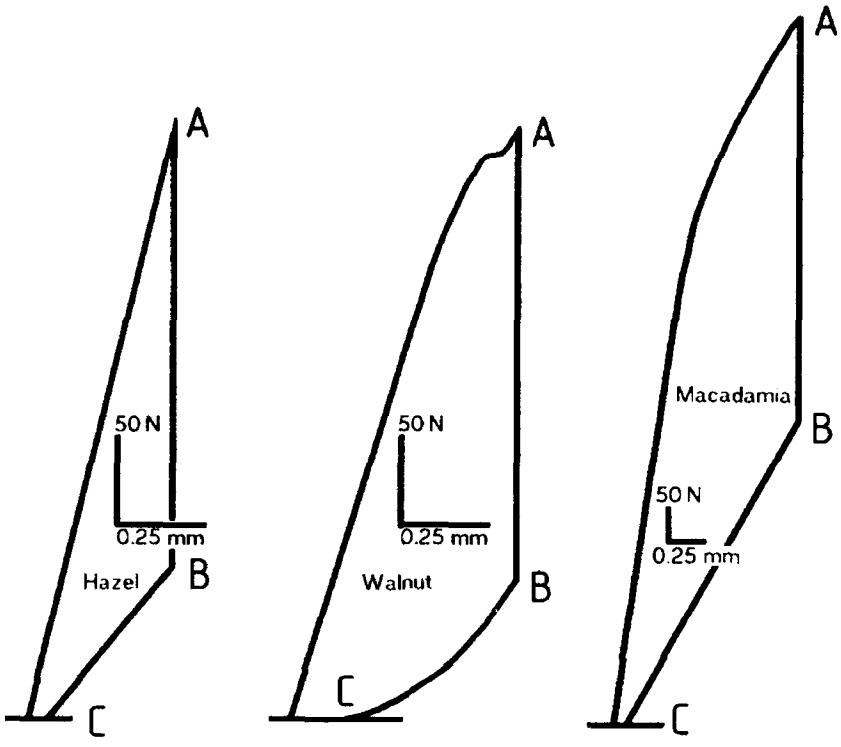

Fig. 1 Loading/unloading curve for whole nuts. The nut cracks longitudinally from pole to pole at the maximum load (A) and the load drops suddenly to B. The sample is unloaded at the same rate as it was loaded to C, thus accounting for elastic strain energy which was not used for fracture.

TABLE I
SOME MECHANICAL PROPERTIES OF WHOLE NUT SHELLS

	Hazel nut	Walnut	Macadamia nut	Coconut
Stiffness (GPa)	1.46 (0.374)	2.85 (1.058)	4.185 (2.518)	3 - 5
Work-to-fracture (kJ/m^2)	1.61 (0.54)	2.97 (1.20)	5.65 (2.04)	1.8
Strength (MPa)	147 (49.6)	221 (55.4)	338 (219)	
Strength / Stiffness	0.1	0.07	0.08	

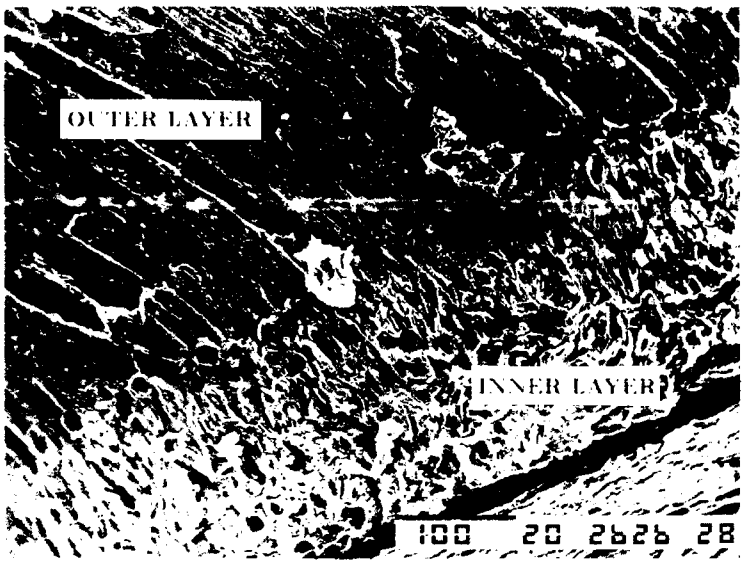

Fig. 2 Fracture surface of hazel nut shell showing the inner layer and part of the outer layer.

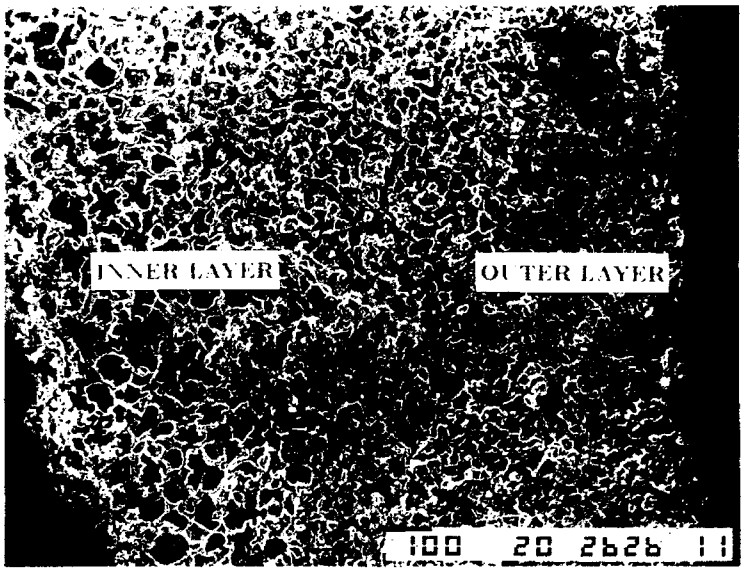

Fig. 3. Fracture surface of walnut shell showing inner and outer layers.

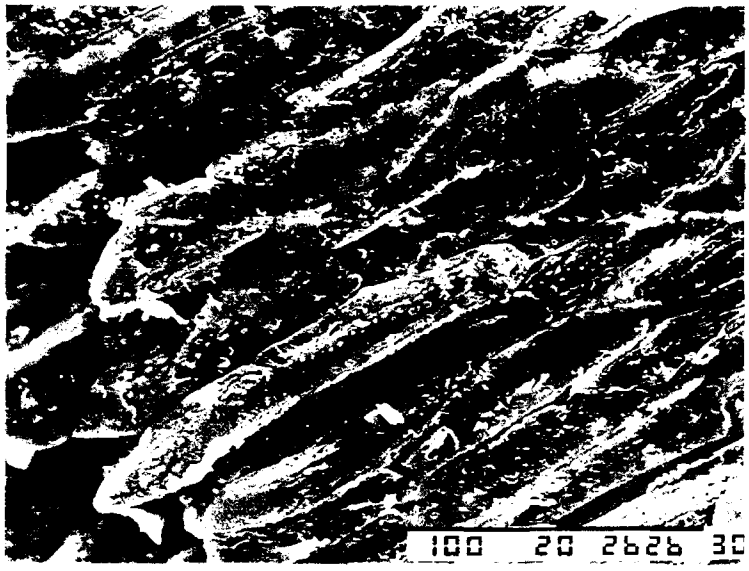

Fig. 4. Fracture surface of the outer layer of hazel nut shell. The cells can be elongated like these or more nearly isometric. The fracture passes between the cells.

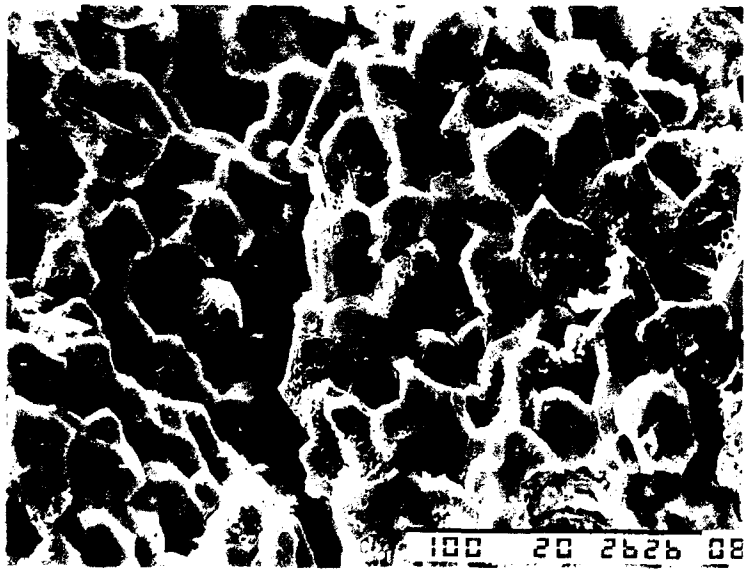

Fig. 5. Fracture surface of the outer layer of walnut shell. The cells are all isometric. A typical fracture can be seen, passing between the cells.

empty. In the walnut the fracture path goes through these cells, revealing the cell walls as multilayered and very fibrous (figure 6). This material could well be tougher in tension, and occurs to a greater extent in the tougher shell of the walnut (figure 3). In the shell of the macadamia nut this layer is composed of long sinuous fibres which pull out on fracture.

Apparent fracture energy is inversely proportional to mean diameter with both hazel nut and walnut (figure 7a, b); there are too few results from macadamia nuts to say whether this is true of these nuts as well. Stiffness, fracture energy and strength (P/t^2) were calculated from the measurements on whole shells and shown in Table I: data from previous work on the coconut are appended [2].

The values in brackets are standard deviations of the population: these are apparently high since the number of samples was about 20 for hazel and walnut, though only 6 for macadamia nut. However, this scatter is due to the influence of size on the results, at least for the fracture energy and for strength (figure 8). No variation of stiffness with size could be detected. This is in accord with the theory of fracture mechanics (see above) and confirms that, for a given morphology of the shell, the larger nut will be easier to break. Values for fracture energy of hazel were confirmed by compliance calibration of the strain release rate.

The data for macadamia nut are at variance with the results of Jennings and Macmillan [3] who quoted fracture values only a fifth of those reported here. Although it is not easy to measure fracture properties of nut shells due to the speed at which fracture propagates, and Jennings and Macmillan could not account for stored elastic strain energy

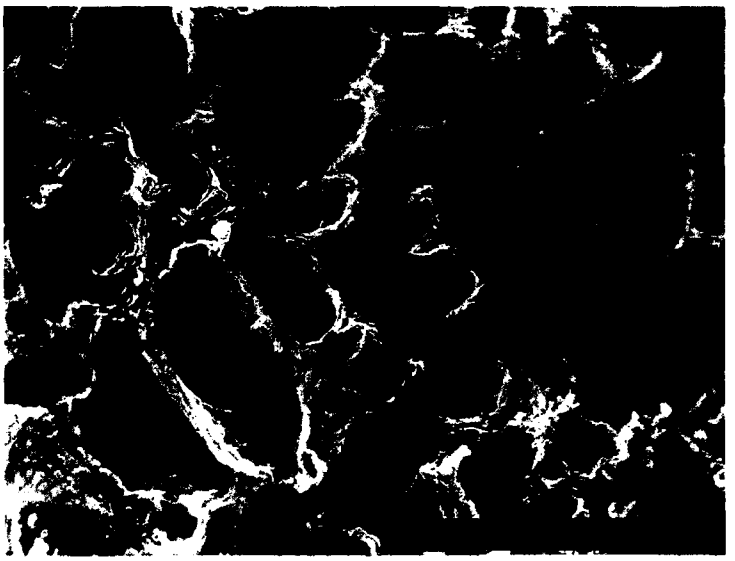

Fig. 6. Fracture surface of the inner layer of walnut shell. Typically the cells are fractured. The cells walls are multilayered and fibrous.

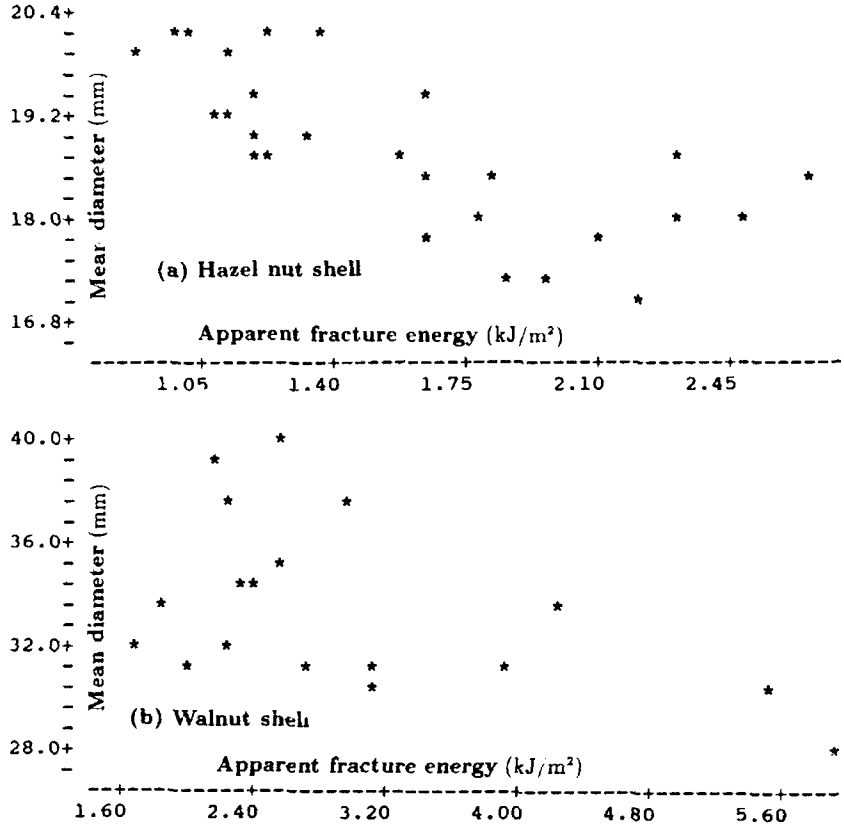

Fig. 7. Apparent fracture energy (calculated from traces like figure 1) plotted against the radius of the nut for hazel (a) and walnut (b).

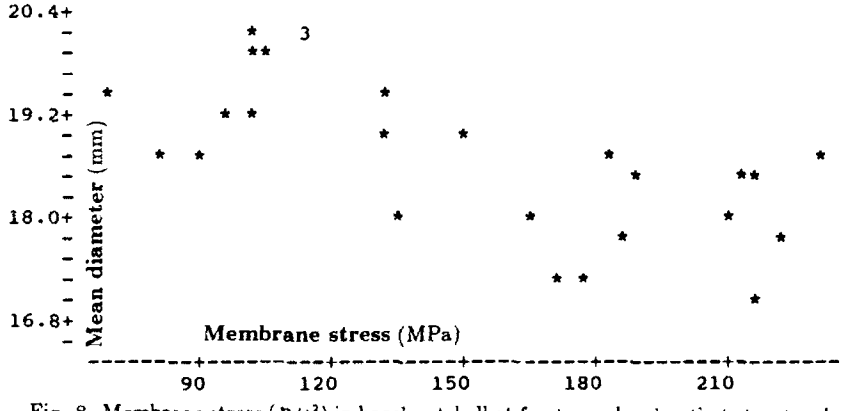

Fig. 8. Membrane stress (P/t^2) in hazel nutshell at fracture, showing that structural strength increases as the size of the nut decreases.

in their samples (which would tend to increase their values rather than reduce them), it is difficult to see why there should be this discrepancy. It may be that there are some Poisson ratio effects since the tests reported here are essentially in two-dimensional strain, whereas Jennings and Macmillan used a C-ring test which is a variant of a beam test. However, the fracture mechanics theory for a sphere compressed over small areas at the poles does not exist, so it is not yet possible to see whether theory can throw light on this. The improved performance figures for macadamia bring the mechanical properties of its shell much closer to those of wood.

The experiments with samples of coconut shell were performed differently, since the original project brief (for 2nd year students) was to see whether coconut shells would make effective crash helmets for children playing on skate boards! Samples cut from the coconut shell were tested in impact using a weight swinging on a pendulum and at low loading rates in three-point bending. Whole nuts were tested in compression. Although not shown on the table, coconut is much more anisotropic in stiffness due to the predominantly circumferential (= equatorial) orientation of the sclerid fibres making the shell.

These tests have not differentiated the properties of the inner and outer layers of the shell: the outer layer, which in the intact nut is more likely to be resisting compression, would be expected to be more brittle since the fracture passes between the cells (figures 2 and 3) and through the cells in the inner layer (figure 6). This is shown to be so in the shell of *Mezzettia leptopoda* [4] where the work of fracture of the outer layer (measured in a notched beam test) is only about 250 J/m^2 and of the inner layer is of the order of 2 kJ/m^2. In this nut the outer layer is like those of walnut, hazel nut and macadamia in that the fracture goes between the cells. The inner layer is more like that of the macadamia [3], being fibrous rather than cellular in appearance [4].

5 Conclusions

The prediction of fracture mechanics (that there should be size effects relating energy input and fracture energy) has been confirmed, although only in a general way since the theory has not been developed specifically for compressed spheres. This seems to be true both within and between species, since the walnut, although larger, stiffer and tougher than the hazel nut, is only just as strong. The walnut shell has opted for improving the 'quality' of the shell material rather than using more of it (i.e. it does not have a thicker, less well-designed, shell) in order to achieve good mechanical properties. The inference must be that design is cheaper than material in energy terms, a deduction previously made in the design of hedgehog spines [5]. However, this does not take into account the biological or evolutionary reason for particular properties, since these different nuts come from different places and are likely to meet different environmental stresses, both mechanical and physiological. It is therefore dangerous to make any generalisations based on comparisons between so few species of nut. As this project develops, more nuts from related species in different habitats, and more nuts from different species in the same habitats, will be investigated and compared. Also, the nuts tested here were all dry. This is not their natural state, at least when fresh. Although Jennings and Macmillan showed water not to have a particularly large effect on macadamia nut shells, it is generally an important factor and is bound to affect different designs of shell in different ways.

In conclusion, nut shells represent an elegant subject for the study of mechanical design in nature since their shape and size are fairly uniform and easy to describe, they have interesting material properties and textures and the results can be related both to engineering and to biology.

6 Acknowledgements

I thank Dr AA Khan for taking the electron micrographs and Dr W Adams for providing the correct provenance of the title of this paper.

7 References

[1] R.J. Roark and W.C. Young, Formulas for stress and strain. 5th edn. McGraw-Hill Int. London (1975).

[2] J.F.V. Vincent, Adv. Bot. Res. **17**, 235 (1990).

[3] J.S. Jennings and N.H. Macmillan, J. Mater. Sci. **21**, 1517 (1984).

[4] P.W. Lucas, T.K. Lowrey, B.P. Pereiras, V. Sarafis and W. Kuhn, Funct. Ecol. **5**, 545 (1991).

[5] J.F.V. Vincent and P. Owers, J. Zool. Lond. **210**, 55 (1986).

Structure and Composition of Rhinoceros Horn

Ann Chidester Van Orden* and Joseph C. Daniel, Jr.,**
* Analytical Services and Materials, 107 Research Dr., Hampton, VA 23666
** Old Dominion University, Dept. of Biology, Norfolk, VA.

ABSTRACT

Rhinoceros horn has been used medicinally and as a talisman in many cultures and animals are slaughtered to obtain the horn. With the dwindling populations of rhinos, and the limited number and breeding success of captive rhinos, there is a critical need to learn as much as is possible about their horns to find an adequate substitute. Examination of rhino horn was made using optical microscopy, scanning electron microscopy (SEM), energy dispersive x-ray spectroscopy (EDS), and x-ray diffraction (XRD). The structure of the horn is unusual and consists of two separate phases, one of hair-like filaments, built around a central core in circumferential layers and the other surrounding and filling in the spaces between the filaments as a matrix. Together, these two structures make up a biological composite, structurally similar to metal, ceramic or polymer based composites. The structural morphology, the dimensions of the structures, and the chemistry of the horn are discussed. Comparisons are made between horn, hoof, and hair of rhinos and hoof and hair from horses, their nearest living relatives.

INTRODUCTION

The horn of the rhinoceros, an anatomical specialization which has evolved to its present functional form over sixty million years, has, in modern times, become the focus for rapid destruction of these animals by poachers who seek it for monetary gain. The severity of the problem is emphasized in the recently released Rhino Global Captive Action Plan, [1] which notes that of twelve subspecies of rhinoceros, composing the five surviving species, seven are considered to be *critical*, four *endangered*, and one *vulnerable*, according to the new Mace-Lande [2] method of classifying the probability of extinction. We concluded that the production of a synthetic horn facsimile, to dominate the market, could reduce, or possibly eliminate poaching pressure on these animals, and/or the mimicry of the chemistry and structure of the horn as a model for new materials could generate a greater demand for conserving rhinos. Both of these concepts require a detailed understanding of the composition and structure of rhino horn and the developmental events that produce it. This paper reports initial studies directed toward that goal.

Reference to the literature reveals some disagreement about the composition of rhinoceros horn. Ryder [3] noted that various early investigators described its basic structure as that of matted hair, coarse fibers, filaments, canals or tubules. Using light microscopy, with histological staining and swelling techniques, Ryder attempted to resolve the issue with studies of horn from the white rhinoceros (*Ceratotherium simum*). He concluded that the horn was built of closely-packed filaments composed of concentric laminae around a solid medulla and with interfilamentous material in the interstices. The same general structure was confirmed in the other four species of rhino by Earland et al. [4]. In 1963, Lynch et al. [5] reported scanning electron microscopy (SEM) studies of white rhino horn. Their results were "broadly consistent with previous studies", and emphasized the presence of flat scale-like cells which compose the layers of laminae and identified another cellular unit "associated with the outer regime of the filaments or the interfilamentous material or both'. In spite of these confirming studies, some recent publications persist in describing rhino horn as consisting of "an aggregation of hollow keratin fibers, similar to hair, but lacking the outer cuticle" [6]. In this paper a variety of techniques, including light and electron microscopy, are employed to assure a clear understanding of the composition of this unique material.

Mat. Res. Soc. Symp. Proc. Vol. 292. © 1993 Materials Research Society

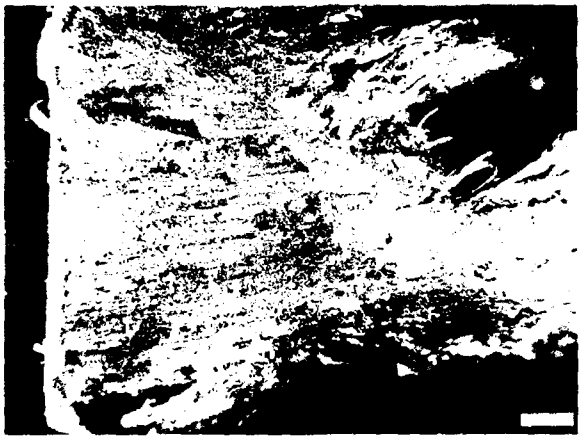

Figure 1: The top surface of rhinoceros horn which the rhino has polished to smoothness by rubbing it against harder surfaces. At this magnification (bar represents 1mm) light and dark striations can be seen on the surface along with rougher areas within the striations.

EXPERIMENTAL PROCEDURES AND RESULTS

The primary sample used in these studies was a two inch piece of horn which was broken from the tip of the horn of a captive male white rhino. It was provided for this study by the Virginia Zoological Park, for which we are appreciative. In the following discussion, this specimen was examined by several different techniques. Each technique is discussed separately with experimental results included.

Light Microscopy

Light microscopy was used to examine the surface and cross-section of the rhino horn. Visually the surface was smooth and rounded in perspective. There was a definite sheen to the top surface of the horn, which is where the animal rubs it against tree trunks, metal fence posts, and the ground. Because the horn has limited wear resistance when rubbed against harder surfaces, continuous wear will polish the surface and this is the natural state of the horn.

When examined under magnification, the surface shows parallel striations of light and darker areas and rougher areas within the striations. These features are noticeable in Figure 1 which shows the smooth surface of a section of the horn.

Figure 2 shows the point at which this section of horn was broken from the main horn. Clearly defined are hair-like filaments which project from the broken interface. The ends of these filaments come to a definite point and their diameters lessen significantly just prior to the formation of the point. Between the filaments is a separate region designated as the matrix phase. It has a fibrous texture, as well. Thinner fibers can be seen in the matrix material, as is demonstrated in Figure 2.

A piece of the rhino horn was cut perpendicularly to the direction of the hair-like structures. It was vacuum encapsulated into epoxy resin and polished using metallographic polishing methods. These methods involve grinding with sand paper starting at 320 grit, followed by 400, 600, and 1200 grit sand papers. It was then polished with 3 micron diamond slurry and final polished with 0.3 micron alumina until a scratch-free surface was produced for photomicroscopy. This type of preparation follows standard metallographic techniques for metal, polymer and composite

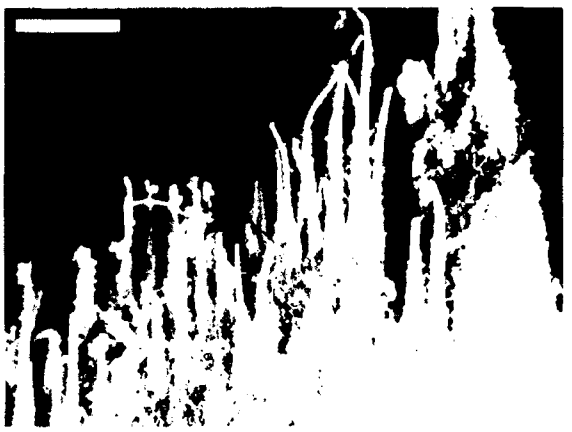

Figure 2: The broken end of the piece of rhinoceros horn with hair like filaments projecting from the interface. Bar represents 1mm. Note that these filaments come to a point with the diameter lessening prior to the point. The fibrous texture of the matrix phase is apparent here as well.

materials, but appears to be the first time that rhino horn has been prepared and examined in this way. Figure 3 shows the result of this process. The structure of the rhino horn can clearly be seen in this cross-sectional view.

In cross-section, the filaments are seen to be built around a central core in circumferential layers and the matrix phase surrounds the hair-like structures, filling in the spaces between them. In the light micrograph, Figure 3, variations in depth can be seen from the highest point at the edge of the filaments, to the matrix phase, the lowest. This suggests differences in hardness of the phases and regions within the phases. The matrix appears to be the softest, since it polishes most easily; while the filaments are harder and polish more slowly. Some of the hair-like filaments have elongated center cores, and some appear to have developed from two separate cores. Examples of both of these features can be seen in Figure 3.

Higher magnification of one of the hair-like structures is shown in Figure 4. Smaller features which were less visible at lower magnification can be seen in this figure. The circumferential layering of the filaments, at this magnification, looks like growth rings. Some cracks can be seen within the hair-like filaments which seem to correspond to growth rings. The cracks do not extend into the matrix. There are also small dark spots at the interfaces of the feature which look like growth rings. Within the matrix phase, the filamental nature of the matrix is evident. At even higher magnification, examination of the cracks within the hair-like phase shows that there are small filaments which bridge the cracks. Some of the cracks appear to initiate at the darker regions noted in Figure 4.

Scanning Electron Microscopy (SEM) of Rhino Horn

The rhinoceros horn was examined both in cross-section and the bulk material, as received. Upon examination in the SEM, of the bulk material, most notable were the ends of the hair-like structures which extended out beyond the edges of the fracture (see Figure 2). Previous authors [5] who have examined rhinoceros horn using SEM have noted the two phases, describing them as "filaments" and "flat scale-like cells". These designate the hair-like phase and the matrix phase, specifically.

The smooth top surface was found to have a directional orientation parallel to that of the

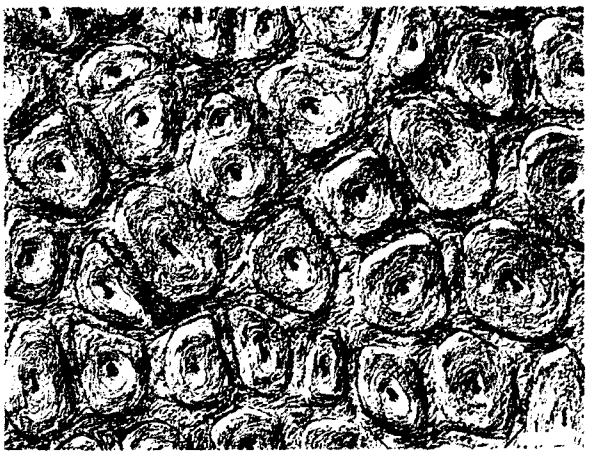

Figure 3: A cross-sectional view of the rhino horn prepared by standard metallographic techniques. Bar represents 0.2mm. In this view both the hair-like filaments and the matrix phase are apparent. The filaments are composed of circumferential layers built around a central core. The matrix phase fills in the spaces between the filaments. Differences in hardness between phases is emphasized by the polishing technique and can be seen as variations in height.

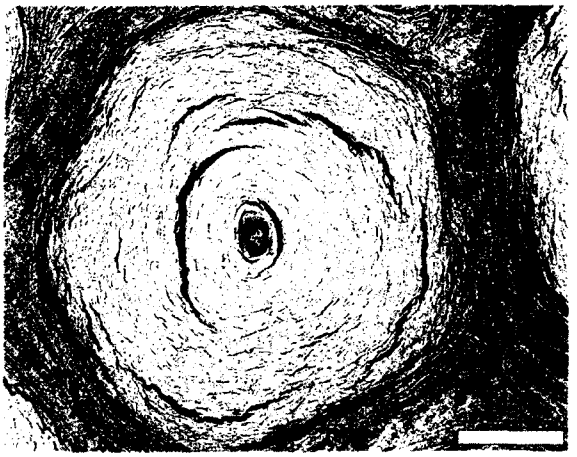

Figure 4: At this magnification (bar represents 0.1mm) the filaments appear to have a structure like growth rings. Cracks can be seen at the interfaces of the circumferential layers. The cracks are confined to the filaments and do not extend into the matrix. Small dark spots can be seen at the interfaces of the circumferential layers.

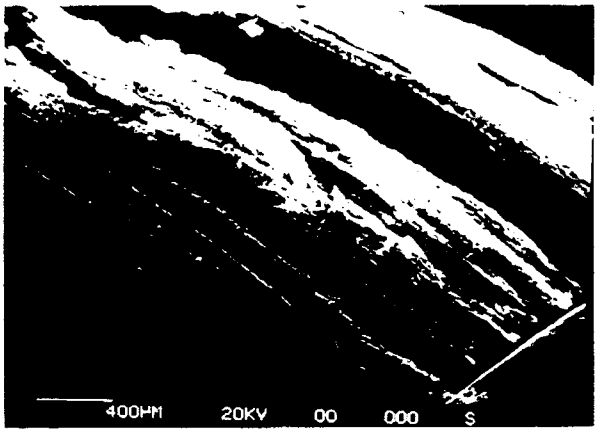

Figure 5: The top surface of the rhinoceros horn as is seen in the SEM, at 20KeV, a tilt angle of 35 degrees with a working distance of 15mm. Magnification is marked on the photo. Individual filaments cannot be noted, although there is a directional orientation to the surface which is parallel to the filament direction.

filaments, but no individual filament could be observed on the top surface. Figure 5 is a view of the surface of one portion of the horn.

Cross-section of the horn, Figure 6, showed structure similar to that demonstrated by light microscopy in Figure 3. Regions which showed black in the light micrograph are distinct and white in the SEM image and are interpreted as cracks or gaps in the horn. These cracks follow the circumference of the central core and appear to be related to the structure of the "growth rings" within the filaments. The interface between the filaments and the matrix is evident as an almost continuous white line following the contours of the edges of the filaments. In the matrix phase, the white regions are less pronounced and smaller than in the filaments. Some directionality can be noted in the white regions in the matrix, as they follow the outer contours of the filaments. The differences in contrast (white to dark) are due to charging within the SEM. Charging occurs when a less conductive area, like a gap, is next to a conductive area. The edges of holes often show charging effects in SEM photographs.

In general, the SEM photographs provided useful comparisons with those taken using light microscopy. The SEM also allowed some of the features in the interior of the cross-section to be imaged directly and emphasized some of the structural aspects of the cross-section to be demonstrated. The SEM provided the imaging capabilities while the energy dispersive x-ray spectroscopy (EDS) system allowed composition to be examined.

Energy Dispersive X-ray Spectroscopy

EDS was performed on the samples which were prepared for the SEM. Both the surface of the horn and polished cross-sections were examined. For analysis of the exterior surfaces, a layer of gold palladium metal was sputtered onto the surface to enhance the conductivity of the surface and eliminate "charging" of the sample, which is caused when a surface charge builds up (due to the electron bombardment) and then discharges suddenly. This adversely affects the elemental analysis, since the specimen may actually move when the discharge occurs. Since neither gold nor palladium were present in the horn itself, the coating did not affect the compositional analysis.

The results of the EDS analysis of the surface of the horn showed that the horn was composed

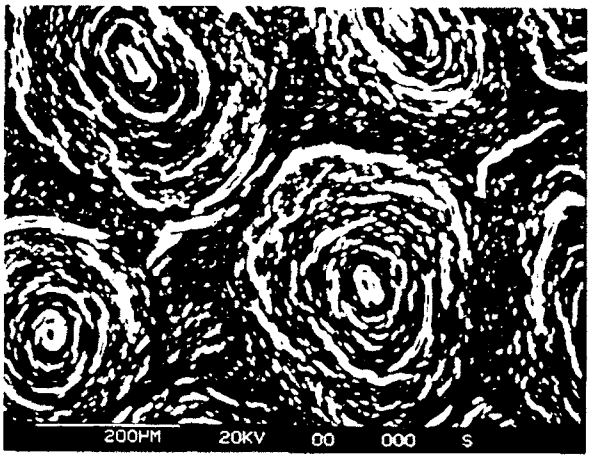

Figure 6: Scanning electron micrograph of the polished cross-section of rhino horn taken at 20KeV at a tilt angle of 35 degrees with a working distance of 15mm. Magnification is marked on the photo. The filaments are apparent with their outer edges defined by an almost continuous white line at a distance from the central core extending around the circumference of the filaments. The matrix can be seen between the filaments. Small cracks or separations are also apparent as smaller white regions within the filaments.

of carbon, oxygen, nitrogen and sulfur. Significant amounts of silicon (Si), calcium (Ca), and phosphorous (P) were also found, most of which can be attributed to the soil in the enclosure where the rhino is kept. This was demonstrated by examining the chemical content of the soil and by comparing the surface composition with the composition in the interior of the horn. The Si, Ca and P were found in higher amounts on the surface of the horn than in the interior. Also present in surprisingly high concentration on the surface was iron (Fe), although some Fe was also found in the cross-section. The question of the existence of the Fe was resolved when the rhino keeper informed us that the animal from which the horn sample was obtained regularly rubs his horn against the iron fence posts in his enclosure.

In cross-section, both phases of the horn were examined. Figure 7 is the EDS spectrum of the hair-like filament and Figure 8 is the spectrum for the matrix. The filaments were found to be significantly higher in S than the matrix phase, although both contain S. Further study is required to draw any specific conclusions that might relate the composition to the structure.

X-ray Diffraction Analysis

Samples of the horn were powdered and examined using x-ray diffraction (XRD). An x-ray tube which provided copper x-rays was used for this analysis. The sample of powdered horn was mounted in a low background holder made of bakelite. A broad scan was done from 0 to 180 degrees in 2Θ. The broad scan provided information on the peaks of interest for this sample. Following this initial run, a region from 20 degrees to 90 degrees was rescanned slowly (over about 8 hours) to concentrate the x-ray counts from the small sample size.

The x-ray data were examined using a computerized peak search program with a database which included organic products. Peaks from the analysis most closely matched those for keratin, but were not an exact match. The inexactness of the match might be due to several factors. For instance, some contamination of the horn material with soil may have occurred, but, it is more

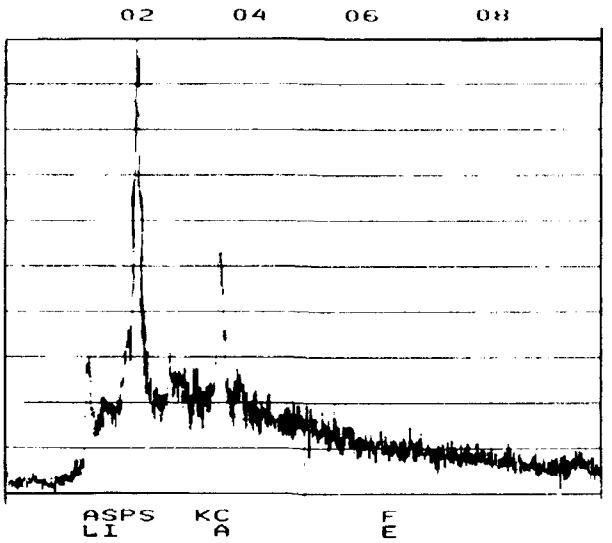

Figure 7: Energy dispersive x-ray spectrum for the filament portion of the rhino horn taken using the spot analysis capability with a spot size of a few microns, at 20KeV with a beryllium window detector. Compare this spectrum with the following spectrum.

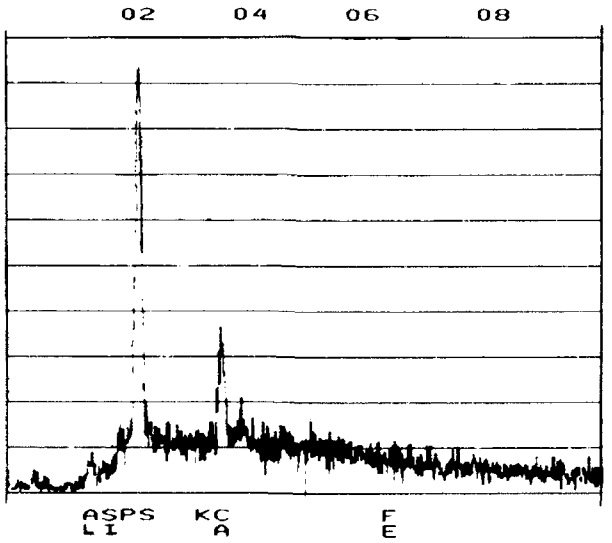

Figure 8: Energy dispersive x-ray spectrum for the matrix phase of the rhino horn. Taken at the same spot size as that used for the filament analysis, this spectrum shows that less sulfur is present in the matrix than in the filaments.

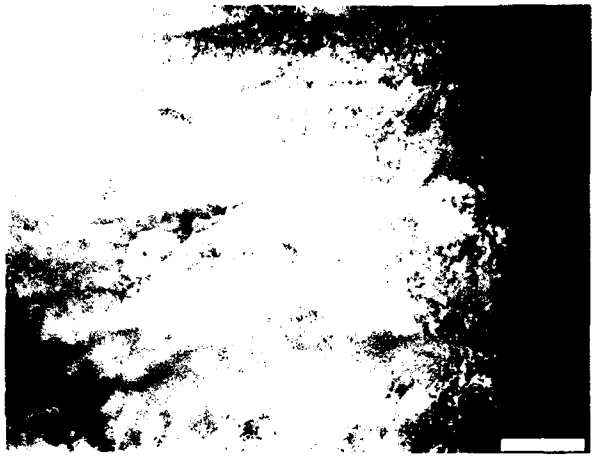

Figure 9: Light micrograph of rhinoceros hoof. Bar represents 1mm. The structure appears different from that of the rhino horn. Note the apparent lack of filaments within the hoof structure, which is closer to hooves of horses than to the rhino horn.

likely that the keratin from the horn is different from that included in the peak search program.

Several investigators [7, 8] have reported differences in keratin based biological materials from different species. Keratin from rhino horns may also be of a different type [9].

Comparisons can be made between the elemental composition found by EDS and the composition determined by XRD. In the XRD analysis, the structure was found to be composed of keratin. In the EDS analysis, sulfur was found to be present in both the filament phase and the matrix. Keratin contains disulfide bonding, which would clearly account for the sulfur content. The elements found by EDS are those from which keratin is formed. The two techniques yield complementary results on the composition of the horn.

Comparisons with Other Materials

Work from early in the twentieth century on rhino horn supported the concept that it is composed of matted hair [10, 11]. Restatements of this premise have continued and are the base for the information which permeates the literature. More recent work [3, 5] has not thoroughly disputed this claim. It is likely that the misconception is due to visual examinations such as that in Figure 2, in which the hair-like filaments are most striking. In examining the cross-sections, such as that of Figure 3, the structure becomes more clear. The presence of the two phases are instantly apparent. Comparisons were made of the hair-like filaments with tail and ear hairs from the rhino. The structure of the hair was found to be more like hair from other species, such as horses, as shown in the literature [12], than like that of the horn itself.

Hoof samples from the rhino were also examined. Figure 9 shows a light micrograph of the sample of hoof. The structure of the hoof is seen to be different from the horn, more like hooves of other animals. Horse hooves and the keratin from which they are made have an extensive literature associated with their study [7, 8]. Differences between rhino hoof and horn, even though both are composed of keratins, are striking.

Figure 10: Light micrograph of a polymer matrix composite material composed of graphite fibers encapsulated within an epoxy matrix. Bar repreesents 0.1mm. Note the striking resemblance to the structure of the rhino horn, composed of fibers within a matrix phase. The graphite fibers in the polymer composite provide tensile strengthening while the epoxy matrix provides ductility. The arrow marks a crack within the matrix. Note that it runs between the graphite fibers; no fibers are broken.

Comparisons to Manmade Composites

Figure 10 shows a light micrograph of a polymer matrix composite with graphite fibers within the polymer matrix. It bears a striking resemblance to the structure of the rhino horn. The graphite fibers are, of course, much smaller in diameter than the filaments in the rhino horn, but the overall nature is quite similar. Graphite reinforced polymer matrix composites are usually not monodirectional such as the rhino horn, but consist of layers of oriented fibers alternating directions by 60 or 90 degrees. This provides the composite material with structural strength in at least two directions. It also provides some torsional stability to the composite. The rhino horn appears to suffer from neither lack of torsional strength nor from debonding along the interface between the filaments (except possibly in old horn or near the base of horns, where the matrix is no longer present). Manmade composite structures will often form cracks parallel to the interface of the fiber with the matrix. This is a very well known problem for composite materials and techniques such as applying coatings or electrostatic charges to the fibers are done to try and optimize the interfaces which are formed.

Figure 11 shows another view of the cross-section of the rhino horn. At the arrow, a crack had formed. The crack has filled in with new material, suggesting that the horn may be a living, growing structure which can repair itself. This is borne out by the fact that, when a rhinoceros's horn is removed or broken, a substantial portion grows back [13]. Contrast this ability to repair itself shown by the rhino horn, with the manmade composite shown in Figure 10, where a crack is marked with an arrow. Obviously, no material has filled in this crack, and no self-repairing mechanism can be demonstrated.

Manmade composites are known to be very weak in compression [14]. The natural composite structure of the rhino horn, by comparison provides a significant amount of compressive strength, as is demonstrated by the use of it by rhinos in battles with other rhinos. Seldom does the horn break under these conditions. The rhino horn appears to provide a good combination of compressive and torsional strength, which is *not* always *present in manmade* composites.

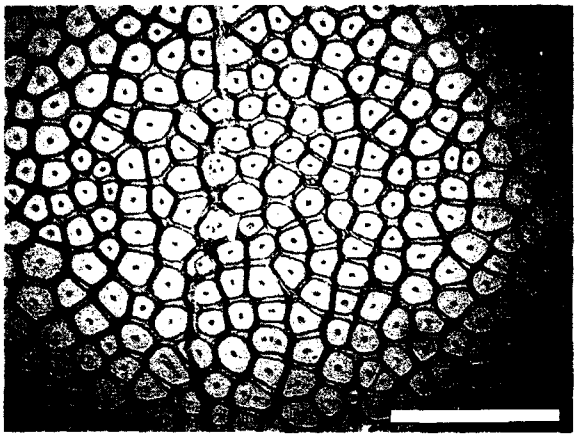

Figure 11: This light micrograph of rhinoceros horn, shown in cross-section, shows the site of a previous crack which has been repaired. Bar represents 1mm. The arrow denotes the crack which has filled in with new material, demonstrating the self-repairing mechanism of the rhino horn

Structure and Composition

The rhino horn has evolved to its present form and evolution has optimized it for the uses made of it by the animal. The structure of the horn, as a composite material, provides some of the same advantages that manmade composites do. The fibers provide greater tensile strength than does the matrix, while the matrix provides greater ductility than the fibers. There is a need to demonstrate that this is the same for the rhino horn. It appears to be the case from the uses made of the horn. The rhino cows use their horns to protect calves from attack. Male rhinos use it in territorial disputes and to drive off interlopers, and all rhinos use their horns for digging in the ground. Other uses that the rhino may make of the horn have been speculated upon. Berger and others are seeking to examine these suggestions in dehorning studies which are being undertaken in rhino populations in Africa [15].

There are a number of lessons which may be possible to learn from studying the rhino horn. Materials science could benefit from information about the interfaces between phases in the horns which are clearly not as weak as they are in manmade composite materials. By studying the mechanical properties of the rhino horn, it may become apparent how the properties of each phase have been optimized for the uses. Since rhino horn has excellent compressive strength, it may be possible to improve the compressive strength of composite materials based on information derived from the study of these horns.

Mimicking the composition and structure of rhino horn may lead to the development of a synthetic material which would serve as a substitute for rhino horn. As was mentioned in the introduction, previous attempts to substitute other types of horn or bone for rhino horn have not been successful with the cultures that use it pharmaceutically. However, no substitute has been tried which is chemically the same as rhino horn. Recently, several authors have suggested that an attempt be made to produce and distribute a synthetic rhino horn [6, 16]. If such a substitute could be made, produced inexpensively, and be accepted, it would provide the possibility for eliminating some of the demand for horn culturally and thereby eliminating some of the poaching pressures on the animal populations. This could impact significantly on their survival and possibly remove them from the threshold of extinction. Detailed information about the chemistry and structure of rhinoceros horn could also be useful in forensic inspection where it may be necessary to confirm the material origin of questionable artifacts.

SUMMARY

Initial experimental analysis was made of rhinoceros horn. Light microscopy of the cross-section of the horn showed it to be composite in structure with two phases present. This work appears to be the first to prepare rhinoceros horn in a manner similar to metal or composite samples. Preparation of the sample in this way allows much detailed information to be available using both light and electron microscopy. One of the two phases present in the composite material of the horn is hair-like in structure and probably accounts for the misconception that rhino horn is composed of matted hair. The hair-like filaments are surrounded by a continuous or matrix phase which is space filling and has some structure within it. The filaments have a central core and circumferential markings similar to growth rings. Cracks in the filaments follow the growth rings, but do not extend into the matrix phase.

Surfaces and cross-sections of the rhino horn were examined using SEM and EDS. The SEM revealed the internal structure of both phases in even greater detail. EDS analysis showed that there were significant differences in the composition of the two phases, specifically in sulfur content. Existence of a surprizing, substantial iron peak in the spectra was concluded to be due to contamination from the soil and the animal rubbing the horn on the iron posts of its enclosure.

X-ray diffraction analysis showed that the overall composition of the horn is, indeed, keratin, but a different type of keratin from that used for the standard in the x-ray diffraction database. A comparison of the x-ray diffraction data with the EDS data presents evidence that the sulfur content is consistent with the disulfide bonds found in all structures formed from keratin.

With the chemical and molecular composition of the rhino horn identified, the possibility of producing a synthetic horn material was discussed. A low cost, chemically equivalent substitute, used instead of natural horn for medicinal purposes, might help alleviate the pressure on the rhino population due to poaching. We are investigating this possibility.

The structure of the rhino horn offers some unique prospects for study and may provide insight into the special combination of strength and ductility along with the unique properties of self repair and biodegradability which are exhibited by rhino horn. Further work to examine the specifics of the mechanical properties of rhino horn is planned.

ACKNOWLEDGEMENTS

We gratefully acknowledge the following:

Virginia Zoological Park for provision of samples; Robert Edahl, Jr., Metallographer, NASA Langley Research Center, for metallographic preparation of samples and photographic assistance; Diane Baum St. Clair Fund for financial support.

REFERENCES

1. *Rhino Global Captive Action Plan*, N.Y., 1992, IUNC and SSC Captive Breeding Specialist Groups Workshop.
2. G. Mace and R. Lande, Conservation Biology **5**, 148 (1991).
3. M. Ryder, Nature **193**, 1199 (1962).
4. C. Earland, P. Blakely, and J. Stell, Nature. **196**, 1287 (1962).
5. L. Lynch, V. Robinson, and C. Anderson, Aust. J. Biol. Sci. **26**, 395 (1973).
6. M. Penny, *Rhinos: Endangered Species*, page 116, Facts on File, N.Y, N.Y., 1992.
7. K.-D. Budras, R. Hullinger, and W. Sack, Am. J. Vet. Res. **50**, 1150 (1989).
8. J. Bertram and J. Gosline, J. Exp. Biol. **130**, 121 (1987).

9. M. Samata and J. Matsuda, Jpn. J. Vet Sci. **50**, 333 (1988).

10. F. Beddard, *Cambridge Natural History Vol. 10*, Macmillian, London, 1902.

11. H. Anthony, Bull. N.Y. Zoo. Soc. **31**, 170 (1928).

12. R. Marshall, D. Orwin, and J. Gillespie, Elect. Mic. Reviews **4**, 47 (1991).

13. E. Martin and C. Martin, *Run, Rhino, Run*, Chatto and Windus, London, 1982.

14. E. Baer, A. Hiltner, and R. Morgan, Physics Today **45** (October), 60 (1992).

15. J. Burger, Buzzworm-Environmental Journal **2**, 20 (1990).

16. E. Martin and L. Vigne, Swara **10**, 25 (1987).

PART II

Cellular Synthesis

GENETIC CODING IN BIOMINERALIZATION OF MICROLAMINATE COMPOSITES

DANIEL E. MORSE*, MARIOS A. CARIOLOU*, GALEN D. STUCKY**, CHARLOTTE M. ZAREMBA** AND PAUL K. HANSMA***
*Marine Biotechnology Center, University of California, Santa Barbara, CA 93106 USA.
**Department of Chemistry, University of California, Santa Barbara, CA 93106 USA.
***Department of Physics, University of California, Santa Barbara, CA 93106 USA.

ABSTRACT

Biomineralization is precisely controlled by complex templating relationships ultimately encoded in the genes. In the formation of the molluscan shell, polyanionic pleated sheet proteins serve as templates for the nucleation and epitaxial growth of calcium carbonate crystalline domains to yield microlaminate composites of exceptional strength and crystal ordering. The strength and fracture-resistance of these composites far exceed those of the minerals themselves, as a result of both the capacity for flexible deformation of the organic matrix layers and the retardation of crack propagation at each mineral-organic interface. The basic principles controlling low temperature biosynthesis of these materials thus are of both fundamental and applied importance. The abalone shell consists of microlaminates with a remarkable regularity of lamina thickness (ca. 0.5 micron), the formation of which defies present understanding. We have found that shells of abalone larvae formed prior to metamorphosis contain only aragonite, whereas the adult shell made after metamorphosis contains both aragonite and calcite. This transition is accompanied by a switch in genetic expression of the template proteins, suggesting that the premetamorphic protein may serve as a template for aragonite nucleation and growth, while template proteins synthesized after metamorphosis may direct crystallization of calcite. These analyses are based on improvements we recently reported for the detection and purification of proteins from the demineralized shell matrix. Genetic cloning experiments now in progress are aimed at discovering additional protein sequences responsible for the programmed control of crystal phase termination, since it is the termination and reinitiation of mineralization that is responsible for the regularity of highly ordered microlaminates produced in nature.

INTRODUCTION: GENETIC CONTROL OF BIOMINERALIZATION

When the genetic code was first cracked in the 1960s, the thinking at that time was that there was only one genetic code. We now realize that in fact all biological structures and functions are encoded in the genes in a complex set of nested codes or correspondences. The relationship between the linear sequence of nucleotides in the genes and the linear sequences of amino acids in the proteins they specify is only one - albeit the most fundamental - of these coding relationships. Molecular biology is now starting to attack the higher-order coding relationships that reliably specify genetically encoded higher-order molecular and cellular structures, shapes and functions. One of the most intriguing of these, and one with great potential for the development of practical applications in the field of materials science, governs the genetic control of biomineralization, in which a complex templating mechanism directs the synthesis of materials such as bone and shell.

The molluscan shell is a microlaminate composite of exceptional strength and regularity (Figure 1). It consists of calcium carbonate crystalline domains, organized on 2-dimensional anionic protein templates. Typically, the organizing organic polymers contribute less than 1% by weight of the composite material [e.g., 1]. Yet the strength and fracture resistance of these composites far exceed those of the crystals themselves. The unique mechanical properties of the biosynthetic microlaminates are due to both the capacity for flexible deformation of the organic matrix layers, and the retardation of crack propagation at each mineral-organic interface. Because of these unique properties, the basic principles controlling the structural organization and biosynthesis of these composites, at the low temperatures characteristic of biological systems, are of both fundamental and applied interest. Thus far, most of the definitive studies have been conducted *in vitro*, using a biomimetic or "reverse engineering" approach [2-6]. Few attempts have yet been made to analyze directly the dynamic biological processes that control the synthesis and ordered assembly of the organizing biopolymers and subsequent mineralization, although

significant progress recently has been achieved in electron micrographic analyses of the layers once they have been deposited, with the observed spatial ordering suggesting the temporal order of secretion [7,8]

Figure 1. Scanning electron micrographs of fractured abalone shell. Transverse (left) and oblique (right) views.

These materials pose a particular challenge to molecular geneticists because their synthesis and structures are clearly under direct genetic control. This genetic control is evident at the macroscopic level; the shells of each species of mollusc are morphologically distinct, and different from the shells of all other species. At the nanoscale level, too, the crystal structures of the shell may differ from one species to another.

In shell formation, calcium carbonate crystal nucleation and subsequent epitaxial growth occur on an organizing sheet of templating protein (Figure 2). These reactions occur in a membrane-enclosed space, from a solution that is ionically enriched by enzymatic pumping. The biopolymer layer containing the template also is hierarchically assembled (Figure 3). The anionic crystal-directing protein template is secreted onto an organizing basal layer that is thought from electron microscopic and histochemical studies to consist of a chitin-like polysaccharide and a silk-like protein [cf. 7,8].

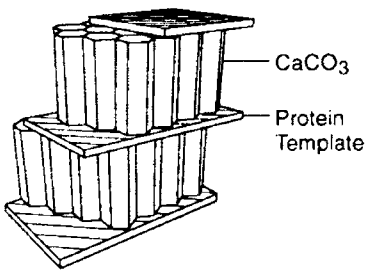

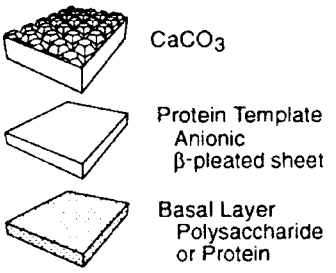

Figure 2 (left). Template-directed biomineralization. Schematic view of calcium carbonate crystal layers formed by nucleation and subsequent epitaxial growth on anionic protein sheets.

Figure 3 (right). Schematic showing hierarchical synthesis of mineral layer on templating protein, which is first secreted on an organizing basal layer of biopolymers.

METAMORPHIC TRANSITION IN ABALONE SHELL PRODUCTION

A clue to the genetic control of crystal structure in biomineralization came from our studies of the metamorphosis of abalone (*Haliotis rufescens*) larvae. We routinely produce several million of these small, planktonic larvae in the laboratory each week [9-11]. These larvae are ca. 200 microns in diameter, and possess a rudimentary larval shell that forms during the first week of larval development. In our previous research, we identified the chemical signal that induces these larvae to metamorphose and begin synthesis of the adult shell [9,10]. This chemical signal is normally found on the surfaces of certain crustose red algae. Chemosensory recognition of the algal signal molecule triggers the swimming larvae to settle from the plankton, attach to the algal surface, and synchronously begin metamorphosis and new shell synthesis. We can duplicate this process conveniently using the purified chemical inducer (Figure 4). As seen in Figure 4, rapid growth of the new shell characteristic of the adult begins quickly after the induction of metamorphosis, while larvae that receive no inducer remain arrested at the larval shell stage.

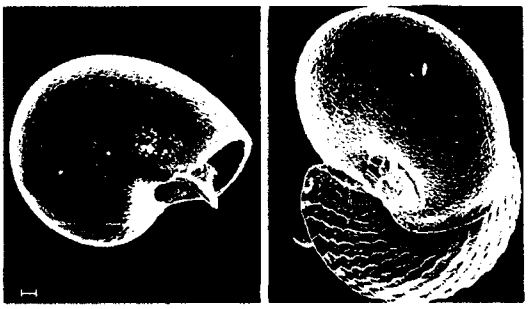

Figure 4. Scanning electron micrographs of an uninduced abalone larva (left; 200 micron diam.), and a sibling that received the chemical inducer of metamorphosis 40 hr before the photograph was taken (right). The two individuals are the same age, and were cultured in parallel. Scale = 10 microns. From [10].

Using x-ray diffraction to analyze the calcium carbonate crystal structures in the larval shell and in the adult shell, we found that the larval shell contains calcium carbonate exclusively in the form of aragonite, while the adult shell contains both calcite and aragonite. This transition to calcite production, we discovered, is linked to a switch in the templating proteins, suggesting a genetic coding relationship in which certain protein sequences may direct aragonite formation, while others direct calcite formation.

METAMORPHIC SWITCH IN TEMPLATING PROTEINS

We first observed this transition in the templating proteins by extracting the bulk proteins from shells at different stages of development and growth, using a chelating agent to demineralize the composite [11]. Extractions performed as a function of time - as the adult shell grew following metamorphosis - revealed a progressive increase in the mole fraction of aspartic acid as the principal anionic amino acid in the shell protein, while the proportion of glutamic acid declined (Figure 5). These are properties of the bulk proteins; numerous problems were encountered when we first tried to purify these proteins, however.

Conventional methods of protein detection proved useless with the shell proteins when we attempted to separate them by polyacrylamide gel electrophoresis. The shell proteins could not be visualized when the electrophoresis gels were stained with Coomassie blue, the most widely used reagent for protein detection (Figure 6, top panel). A more sensitive method employing staining with silver also proved useless, as the patterns were obscured by the staining of many non-protein artifacts. In marked contrast, we found that certain cationic carbocyanin dyes provide excellent detection of shell proteins that were resolved by gel electrophoresis (Figure 6, lower panel). These dyes previously have been used for the detection of nucleic acids, which of course are polyanionic polymers. As we expected, these dyes also react well with the polyanionic shell proteins [11].

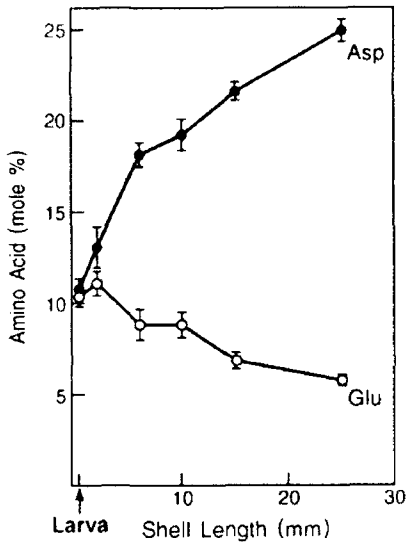

Figure 5. Change in the mole fraction of candidate nucleating amino acids in the bulk shell proteins extracted as a function of shell growth following the induction of metamorphosis. From [1].

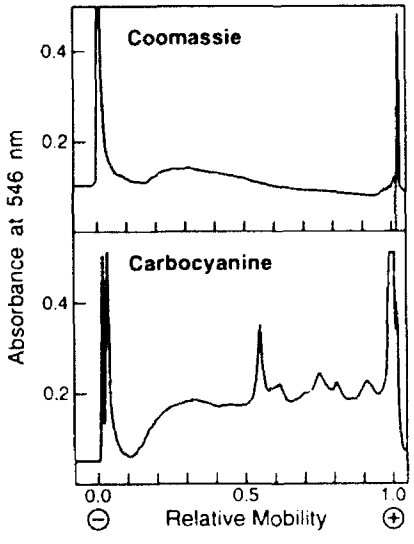

Figure 6. Improved detection of shell proteins using cationic carbocyanin dye. Proteins extracted from the abalone shell were resolved by polyacrylamide gel electrophoresis under non-denaturing conditions, stained *in situ* with either the conventionally used Coomassie blue stain (top panel) or the cationic carbocyanin dye (lower panel), and, after removal of the unbound dye, scanned spectrophotometrically. (The sharp peaks of absorbance at the extreme ends of both traces mark the optical discontinuities at the ends of the gels.) From [1].

Using this improved method of detection, we were able to confirm our hypothesis that new shell proteins are induced following metamorphosis, and that differences in these protein templates may determine the differences in the crystal structure of the deposited calcium carbonate. At metamorphosis, expression of the genes coding for these new proteins is turned on [1]. The proteins extracted from the larval and adult shells migrate differently during electrophoresis, and the proteins extracted from the adult shell show greater complexity than those from the larval shell (Figure 7). The colors of the carbocyanin-stained proteins also differ: proteins from the adult shell stain blue, while the principal protein resolved from the larval shell stains pink, reflecting the differences in their principal anionic chromophores [1].

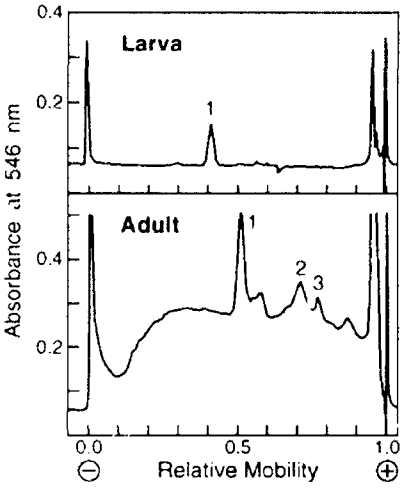

Figure 7. Developmental switch of template proteins confirmed. Proteins were extracted from the larval shells made prior to metamorphosis, and from adult shells. The proteins were extracted and analyzed electrophoretically in parallel, with carbocyanin detection, as in Figure 6. From [1].

Adapting the carbocyanin staining as a spectrophotometric assay, we were able to further purify the major soluble proteins extracted from the larval and adult shells by gel filtration column chromatography. For this purpose, it proved necessary to employ bicarbonate buffers both to remove residual traces of the tightly bound calcium counterions and to prevent aggregation of the proteins [1]. Characterization of the proteins solubilized and purified under these conditions revealed amino acid compositions consistent with extensive domains of alternating anionic and neutral (principally glycine and alanine) residues. In the larval shell protein made prior to metamorphosis, the predominant anionic residue is glutamate; in the most abundant protein solubilized from the adult shell, the predominant anionic residue is aspartate. Preliminary analyses with enzymatic digestion have thus far not detected significant levels of either phosphorylation or glycosylation of the major proteins extracted from the larval and adult shells of *Haliotis* [1], although the presence of these groups on other still-insoluble proteins has not yet been investigated. Figure 8 illustrates hypothetical "canonical" or idealized sequence domains that can be postulated for the larval and adult proteins, although it must be noted that considerable heterogeneity and specific departures from these idealized sequence domains are indicated by the available data [1]. The difference between the two principal anionic amino acids found in the larval and adult shell proteins is only the presence of one additional methylene group in the carboxyl side chain of the glutamate, making this side chain slightly longer and more flexible than that of aspartate. It is possible, then, that this simple difference in side chain structure, and the specific positions of the aspartate and glutamate residues in the template sheets, may directly control the crystalline structures of the calcium carbonate nucleated and grown on the larval and adult template proteins, thereby determining the transition from aragonite to calcite production. We are working now to test this hypothesis *in vitro*.

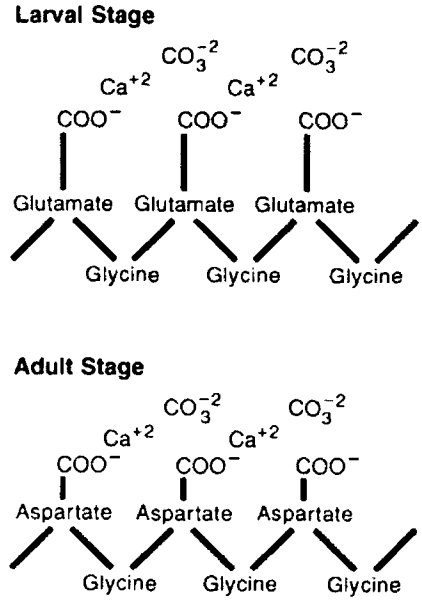

Figure 8. Idealized sequence domains postulated for functional segments of the major proteins thus far characterized from the larval and adult shells. These canonical domains, while consistent with the available data [1], are hypothetical only.

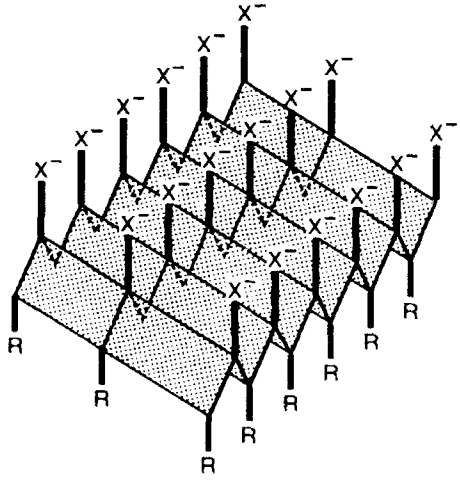

Figure 9. Bifacial templating protein. Three protein chains (or segments of the same chain) with alternating anionic and neutral amino acid sequences are shown in a β-pleated sheet conformation, held together with lateral hydrogen bonds between the protein chains. The anionic side chains (X^-) capable of nucleating calcium carbonate crystallization all project perpendicularly from one face of the template sheet, while the neutral side chains (R) of the anchoring amino acids all project perpendicularly from the opposite face of the sheet.

It is generally believed that the calcification templating proteins contain bifacial β-pleated sheet domains (illustrated schematically in Figure 9), in which multiple protein chains (or loops of a single chain) self-assemble to yield a planar aggregate held together by lateral hydrogen bonding. In such a conformation, the alternation of anionic and neutral amino acids would ensure that all of the crystal-nucleating anionic side chains project perpendicularly from one face of this sheet, while the neutral side chains, that can serve to anchor the sheet, project perpendicularly from the other face (Figure 9).

BIOMIMETIC APPROACH CAN BOTH TEST AND EXTEND RESULTS FROM BIOLOGY

In order to test our hypothesis that differences in the anionic amino acids of templating proteins can determine the crystal structure of calcium carbonate, we must first synthesize the corresponding proteins, and then anchor these to a suitable surface to allow them to self-assemble into the β-pleated sheets appropriately configured for templating. We're now exploring several strategies to accomplish this. One involves replacing some or all of the glycine anchoring amino acids in the synthetic canonical sequence with phenylalanine, which has a projecting benzyl side chain (Figure 10). This would allow us to anchor the template on hydrophobic supports. We will explore the possibility that interaction of these synthetic anchoring benzyl groups with the hydrophobic surface of a cadmium arachidate Langmuir-Blodgett film, for example, may provide the correct orientation for subsequent nucleation and growth of calcium carbonate on the anionic surface of the protein template (Figure 11). By extension of work we reported previously with such films [12-15], we will systematically manipulate the stereochemistry of the coordinating hydrophobic groups in the L-B film to optimize template sheet formation and subsequent crystal growth. Also in extension of our earlier studies [16], we plan to monitor the templating surfaces and calcium carbonate crystallization, in real time, by atomic force microscopy (AFM). Ultimately, by extending these studies to include the effects of other modifications in the structure and chemistry of the anionic templating groups, including the incorporation of functional substituents such as phosphate, we hope to learn how to control the nucleation and growth of other inorganic materials such as aluminum phosphates, silicates and titania.

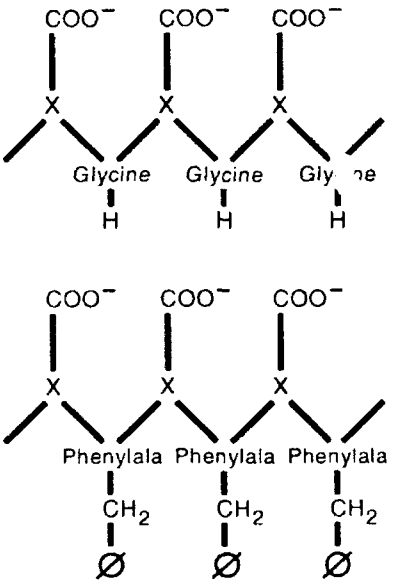

Figure 10. Modification of synthetic canonical template sequence to permit anchoring on hydrophobic surfaces. Substitution of phenylalanine residues for glycine as the anchoring amino acid yields a protein with projecting benzyl side chains, suitable for anchoring the template onto hydrophobic supports.

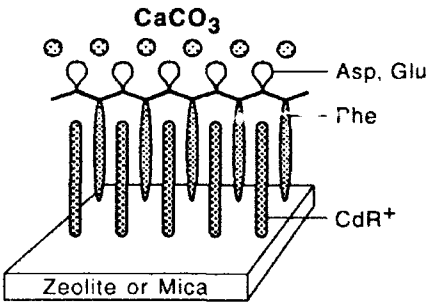

Figure 11. Schematic representation showing hierarchical assembly of a synthetic calcium carbonate-templating protein on a Langmuir-Blodgett film. The benzyl side chains of the anchoring amino acids are shown interdigitating with the projecting hydrophobic chains of a cadmium arachidate L-B film. Alternation of the anchoring and anionic amino acid side chains of the β-pleated sheet protein establishes a bifacial template, permitting nucleation and epitaxial growth of calcium carbonate crystals on the anionic face of the template sheet. Crystal growth on this array can be analyzed in real-time at the atomic level of resolution using AFM.

TERMINATION, AND ITS POSSIBLE ROLE IN THE MYSTERY OF REGULARITY

In addition to the coding relationships that control crystal formation, another puzzle is the process responsible for the incredible regularity of microlaminar thickness in the molluscan shell. Figure 1 shows just a few of the thousands of microlaminae - each approximately 0.5 micron thick - found in the abalone shell. This regularity is unprecedented in the formation of most other biological structures; the mechanism responsible remains a mystery. To help us dissect and understand this process, we now are using genetic cloning to identify specific proteins that may have gone undetected thus far, yet may play a dynamic role in the termination of crystal growth. These studies will test the hypothesis that it is the programmed termination and reinitiation of crystallization that is responsible for the highly ordered microlaminates produced in shell mineralization.

FUTURE GOALS

Our goal in the studies described above is to analyze the templating and terminating reactions at the nanoscale level, to help us understand the genetic coding inherent in the synthesis of ordered microlaminate composites in nature, and to be able to apply this understanding to the design and synthesis of new materials.

ACKNOWLEDGMENTS

Our current work is supported by a Materials Research Laboratory Grant (#NSF DMR91-23048) and a research grant (# MCB-9202775) from the National Science Foundation. We gratefully acknowledge the expertise of Dottie McLaren, Peter Allen and David Folks in preparation of the illustrations, and thank Dr. Fred Lange for the electron micrographs in Figure 1.

REFERENCES

1. M.A. Cariolou and D.E. Morse, J. Comp. Physiol. B **157**, 717 (1988).
2. S. Weiner and W. Traub, Phil. Trans. R. Soc. Lond. B, **304**, 425 (1984).
3. S. Mann, J. Inorg. Biochem. **28**, 363 (1986).
4. S. Mann, J. Webb and R.J.P. Williams, eds. Biomineralization: Chemical and Biochemical Perspectives (VCH Publishers, New York, 1989).
5. S. Weiner and L. Addadi, Trends Biochem. Sci. **16**, 252 (1991).
6. L. Addai and S. Weiner, Angew. Chem. Int. Ed. Engl. **31**, 153 (1992).
7. H. Nakahara, in Biomineralization and Biological Metal Accumulation, edited by P. Westbrock and E. de Jong (W. Reidel Publishers, Amsterdam, 1983), p. 225.
8. M. Sarikaya, K.E. Gunnison, M. Yasrebi and I.A. Aksay in Materials Synthesis Using Biological Processes, edited by P.C. Rieke, P.D. Calvert, and M. Alper (Mater. Res. Soc. Proc. **174**, Pittsburgh, PA, 1990) pp. 109-116.
9. D.E. Morse, N. Hooker, H. Duncan, and L. Jensen, Science **204**, 407 (1979).
10. D.E. Morse, H. Duncan, N. Hooker, A. Baloun and G. Young, Federation Proc. **39**, 3237 (1980).
11. Morse, D.E., in Abalone of the World, edited by S.A. Shepherd, M.J. Tegner and S.A. Guzman del Próo (Blackwell Publishers, Oxford, 1992), p. 107.
12. P.K. Hansma, V.B. Elings, O. Marti and C.E. Bracker, Science **242**, 209 (1988).
13. H.G. Hansma, A.L. Weisenhorn, A.B. Edmundson, H.E. Graub and P.K. Hansma, Clin. Chem. **37**, 1497 (1991).
14. H.G.Hansma, H.E. Gaub, J.A.N. Zasadzinski, M. Longo, S.A.C. Gould and P.K. Hansma, Langmuir **7** 1051 (1991).
15. J. A. N. Zazadzinski, C. A. Helm, M. L. Longo, A. L. Weisenhorn, S. A. C. Gould, and P. K. Hansma, Biophys. J. **59** 755 (1991).
16. G. Friedbacher, P. K. Hansma, E. Ramli, and G.D. Stucky, Science **253**, 1261 (1991).

IS THE TYROSINE RICH EGGSHELL PROTEIN OF *SCHISTOSOMA MANSONI* AN ELECTRON TRANSPORT CHAIN?

John S. Cordingley, John A. Thomson, and C. Russell Middaugh
Dept. of Molecular Biology, University of Wyoming, Box 3944 University Station, Laramie, WY 82071, U.S.A.

ABSTRACT

The schistosome eggshell is composed of two kinds of cross-linked proteins. One is glycine rich and the other is extremely tyrosine rich and highly repetitive. The highly conserved sequence of the tyrosine residues in the tyrosine rich protein suggests that it may play a role as an electron transport chain during eggshell cross-linking. Studies using model synthetic peptides suggest that the tyrosine rich protein may adopt a left-handed structure, possibly a left-handed alpha-helix.

INTRODUCTION

Schistosome eggshells are made of proteins that are cross-linked at the time of eggshell formation to produce a highly protease resistant microcapsule [1,2]. The cross-links are probably produced by a form of quinone tanning in which the phenolic side chains of the tyrosine residues are oxidized to quinones which then react with nucleophilic side chains of other amino acid residues resulting in cross-links between the eggshell proteins. The exact chemistry of these reactions has not been elucidated, however over 90% of the tyrosine side chains in the eggshell precursor proteins are lost in the final cross-linked eggshell and cannot be recovered by acid hydrolysis [1,3] strongly implicating the tyrosine residues in the cross-linking reactions. Eggshell formation can be inhibited by copper chelators which has been taken as evidence that a copper dependent phenol oxidase is involved in the process [4,5]. Whilst this is eminently plausible the supporting evidence is indirect and is open to a number of alternative interpretations. In this paper it is suggested that no phenol-oxidase enzyme homologous to the currently cloned and sequenced phenol oxidase genes is present in this system. The available evidence suggests the possibility that the highly repetitive tyrosine rich eggshell protein, referred to as F4, plays an active and possibly exclusive role in the oxidation and cross-linking reactions leading to the mature eggshell.

RESULTS AND DISCUSSION

The schistosome eggshell comprises two proteins with distinct sequences. The genes for two proteins implicated in eggshell formation have been cloned and sequenced from several laboratory strains of *S. mansoni* [6-8]. These genes are transcribed only in female worms and the transcripts are localized exclusively in the vitelline cells which synthesize the eggshell precursors. The first genes identified belong to a gene family that encodes a family of 14,000 dalton polypeptides (p14) that are very glycine rich (45 mole %) and from estimates of the abundance of their mRNAs [6,9] they are probably the major component of the eggshell. Apart from the inevitable "repetitive" nature of any protein which is 45% glycine the amino acid sequence is not composed of any discernible consensus repeats. This polypeptide will be referred to as the glycine rich protein (GRP).

The second eggshell protein gene was first identified in my laboratory several years ago and encodes a very different protein [2,8]. This protein which we refer to as "F4" (or

"p48" after its apparent molecular weight on SDS gels of 48,000 daltons) is very tyrosine rich and for most of its length is composed of a five amino acid repeat. This repeat has the consensus sequence Gly-Tyr-Asp-Lys-Tyr (GYDKY in single letter code).

Figure 1. The amino acid sequence of F4 in single letter code.

```
1
MNLLVFSILITCLLNSVYSGYNGYTNGISAITSRPGGGESHENSVDVYNKYYDSKKYSYG
61
TEYTSDDSSKYTYGKNYDKYSYDKYSYDKYGHEKGDEKYAYGKNYEKGYDKYAYDKYGYG
121
KYGYDKYGYDKYGYDKYGYDKYGYDKYGYGKYSYDKYGYDKYGYEKYGYDKYGYEKGYDK
181
YGSDKYGYEKGYDKYGSDKYGDEKGYDKYGSDKYGYEKGYDKYGSDKYGYEKGYDKYGSD
241
KYGDEKVYDKYGYDKYGSDKYGYEKGYDKYGYDKYGYEKYGYDKYGYEKYGYDKYGYDKY
301
GYDKYGYEKYGYDKYGNEKYGYDKYGDDKHGHGKDYEKYGYTKEYSKNYKDYYKKYDKYD
361
YGSRYEKYSYRKDHDKHDHDEHDHHDDHHDHRHHHHEHDHHHHHEHDHKNGKGYU
```

Figure 1 shows the amino acid sequence of one of the sequenced F4 proteins and Figure 2 shows the amino acid compositions of GRP, F4 and mature eggshell and shows that the eggshell has very little recoverable tyrosine after the cross-linking reactions are completed. The repeats stretch from residue 76 to residue 325.

Figure 2. The amino acid compositions of the glycine and tyrosine rich eggshell proteins, GRP (p14) and F4 (p48) and mature eggshell. Compositions are from published sources [2,3,9].

	F4	GRP	Egg			F4	GRP	Egg
Ala	0.72	2.8	4		Leu	1.2	2.3	1.8
Arg	1	0	2		Lys	17.2	5.7	9.44
Asn	2.7	5.1	***		Met	0.24	0.6	1
Asp	13.8	5.7	15.4		Phe	0.24	2.3	1.92
Cys	0.24	5.7	2.2		Pro	0.24	1.1	3.37
Gln	0	0.6	***		Ser	5.8	6.2	6.63
Glu	5.8	0.6	4.7		Thr	1.7	5.1	3.1
Gly	15	43	36.7		Trp	0	0	0
His	6	1.7	5.2		Tyr	26.1	10.2	0.78
Ile	1	.6	1.2		Val	1.2	1.1	0.59

The proteins F4 and GRP are synthesized and sequestered into secretory vesicles in the vitelline cells. These secretory vesicles contain an acid stabilized emulsion of eggshell proteins [1]. The cross-linking reactions are triggered when these vesicles exocytose their contents at

the time of eggshell formation. These events have been discussed in detail elsewhere [1]. All of the components of the eggshell are present in the secretory vesicles and all that is necessary to initiate cross-linking is to raise the pH of the vesicles. The cross-linking reactions are then triggered within the secretory vesicles and the resulting cross-linked protein droplets have the same amino acid composition as mature eggshell [1]. Allowing for some loss of amino acids during the cross-linking reactions, the amino acid composition of the eggshell can be accounted for by the two sequenced proteins. Since all of the necessary reagents are apparently present within the vesicles the simplest explanation of these observations is that the two sequenced proteins are the only proteins present in the secretory vesicles and they are sufficient to create the cross-linked eggshell.

It has been assumed that a "phenol oxidase" activity is necessary to cause the cross-linking reactions to occur. Indeed my laboratory long held this as our working hypothesis and this was reflected in the published interpretations we placed on our results [1]. However, negative evidence regarding the putative phenol oxidase has continued to accumulate over the last several years in my laboratory and we have been forced through several stages [2] to the conclusion stated above, i.e., that the two identified proteins may be the only proteins present in the secretory vesicles and must therefore be responsible for eggshell formation including the cross-linking reactions.

Negative evidence regarding the involvement of a schistosome phenol oxidase involved in eggshell formation. The putative existence of a copper dependent phenol oxidase has led a number of investigators to try to identify a gene homologous to (currently) cloned phenol oxidase genes. We have used the mouse phenol oxidase gene cloned and sequenced by Shibahara et al. [10] to try to identify a cross-hybridizing gene in the schistosome genome using low stringency hybridization. All of our attempts have been unsuccessful. Negative experiments of this kind are always inconclusive and unsatisfactory, however all of the reports we have received from colleagues doing similar experiments have also proved to be uniformly negative. All these negative results simply demonstrate that there are no schistosome genes sufficiently similar to the available phenol oxidase sequences to hybridize significantly and it in no way demonstrates that there are no "phenol oxidase" enzymes involved in eggshell cross-linking. However the continued absence of a female specific "phenol oxidase" enzyme either as a protein or as a gene remains surprising and rather unexpected.

Evidence from the sequence of F4, the tyrosine rich protein. The published DNA sequences of the tyrosine rich eggshell protein genes and the proteins they encode have been reported elsewhere and they show some very unusual features [2,8,9]. Figure 3 shows the codon usage for the F4 ORF reported by Chen et al. and the amino acid composition of the F4 protein. Additional sequences of repeats have been reported by my group elsewhere [2,8]. Inspection of the sequence of F4 reveals some unique features. There are 108 tyrosine residues in the F4 protein ORF. This is a very large number for a single protein, larger than any other single protein known to the author. In contrast to the large number (108) of tyrosine residues in the F4 protein is the very small number (1) of phenylalanine residues and the complete absence of tryptophan. The single phenylalanine is in the putative signal peptide and is probably cleaved off the precursor protein during synthesis and transmembrane secretion. Thus there are no phenylalanine or tryptophan residues in the mature F4 protein.

When one considers tyrosine residues in the majority of other proteins this situation becomes more striking. The only substitutions for tyrosine that occur at levels in excess of chance are phenylalanine and tryptophan, the two residues that never occur as replacements for tyrosine in F4. If there were only a few tyrosine residues in F4 this could be ascribed to

chance. Howeve: there are 108 tyrosine residues in F4 and not a single phenylalanine or tryptophan residue. This is very unlikely if the tyrosine residues have conventional roles, i.e., like those in the proteins used to compile the matrix of accepted mutations. This matrix has been compiled using available pairs of homologous proteins and is of course limited by the proteins sequenced at the time of compilation. In these proteins the replacement of tyrosines with phenylalanine or tryptophan strongly implies that these tyrosine residues have essentially hydrophobic roles. In the case of F4 this is presumably not the case and these hydrophobic residues are absolutely forbidden, presumably by selection.

Figure 3. Codon Usage in the F4 ORF.

TTT Phe	0	TCT Ser	7	TAT Tyr	74	TGT Cys	1
TTC Phe	1	TCC Ser	1	TAC Tyr	34	TGC Cys	0
TTA Leu	3	TCA Ser	0	TAA End	1	TGA End	0
TTG Leu	0	TCG Ser	0	TAG End	0	TGG Trp	0
CTT Leu	0	CCT Pro	1	CAT His	20	CGT Arg	2
CTC Leu	0	CCC Pro	0	CAC His	5	CGC Arg	1
CTA Leu	1	CCA Pro	0	CAA Gln	0	CGA Arg	0
CTG Leu	1	CCG Pro	0	CAG Gln	0	CGG Arg	0
ATT Ile	2	ACT Thr	4	AAT Asn	7	AGT Ser	10
ATC Ile	0	ACC Thr	2	AAC Asn	4	AGC Ser	6
ATA Ile	2	ACA Thr	1	AAA Lys	37	AGA Arg	1
ATG Met	1	ACG Thr	0	AAG Lys	34	AGG Arg	0
GTT Val	3	GCT Ala	2	GAT Asp	19	GGT Gly	34
GTC Val	0	GCC Ala	0	GAC Asp	38	GGC Gly	11
GTA Val	2	GCA Ala	1	GAA Glu	16	GGA Gly	14
GTG Val	0	GCG Ala	0	GAG Glu	8	GGG Gly	3

The F4 amino acid sequence is being maintained by selection. Consideration of the DNA sequence and codon usage deduced from it shows that extensive selective pressure is maintaining the amino acid sequence. For example, the glycine residues that are present in the sequenced repeats show extensive variation in the third base of the codons. The codon usage for glycine in F4 is almost identical to the codon usage observed for all other sequenced schistosome genes. Considering the third base position only (TCAG) the respective percentages of each of the 4 codons in F4 are 55, 17, 23 and 5, whereas in all sequenced

schistosome proteins they a· 54, 18, 23 and 5 [11]. From this I infer that mutations have occurred frequently (and been accepted) in the third base of the glycine codons and therefore the same frequency of mutations must have occurred in bases one and two. The presence of accepted amino acid substitutions for the glycine residues is consistent with this. Asparagine, serine, alanine and valine are found as substitutions for glycine. Serine, alanine and valine are one point mutation from glycine codons whereas asparagine is two mutations away. However, also one point mutation away from glycine are aspartate, glutamate, arginine, cysteine and tryptophan, none of which are present as substitutions for glycine. Valine is present only once. Thus point mutations in glycine codons are approximately three times more likely to produce codons for these unrepresented amino acids than for the ones accepted leading to the conclusion that the accepted amino acids are far from random in their usage and that strong selection is maintaining the observed sequence. Serine codons replacing glycine codons in the GYDKY-repeats are one base change from glycine codons whereas serine codons in place of tyrosine residues are all one base change away from tyrosine codons as would be expected if they are a result of mutations of glycine and tyrosine codons respectively.

93% of the time the third amino acid of the consensus repeat is either Asp (66%) or Glu (27%) with the only other accepted amino acid at this position being glycine. All other one base substitutions in the third codon of the repeats have been selected out. Once again this is very unlikely to be solely the result of chance.

Amino acids at positions 4 and 5 within the consensus repeat are always lysine or tyrosine respectively. The tyrosine at position 5 is not always present, but if it is present it is always tyrosine [2].

The tyrosine codons at positions 2 and 5 within the repeat are conserved in a very unusual fashion. As outlined above there are no phenylalanine or tryptophan substitutions at either of the two positions. However some alternative substitutions have been accepted, namely serine, aspartate, histidine and asparagine. These accepted mutations are all one base change from tyrosine codons. The two other one base changes would result in either phenylalanine or cysteine substitutions. Both phenylalanine and cysteine are present once in the complete F4 sequence, both in the signal peptide where their hydrophobic natures are clearly appropriate.

The lysine residue at position 4 of the repeat is completely conserved, no substitutions being accepted within the repeats [2]. Arginine is the most common accepted substitution for lysine in the majority of proteins. In the F4 protein there are three arginine residues all of which lie outside the repeat region in the histidine rich C-terminal region of F4. Arginine is an accepted replacement for histidine in many proteins and this is consistent with their presence in the C-terminal region of F4.

All these data lead to the inescapable conclusion that the selective pressure maintaining the F4 sequence within the repeats is considerably out of the ordinary. The usual reasons for selecting for or against particular residues are not being followed within the repeats. Most strikingly phenylalanine and tryptophan are forbidden substitutes for tyrosine in F4. In other proteins selective pressure to maintain a particular amino acid residue is usually directly dependent on the relative importance of the residue for the protein's function. The best examples are for residues at the active sites of enzymes where particular residues may be absolutely required for activity. In these cases the residue is normally unique being found only once in the sequence with this particular function. Thus individual residues are sometimes completely conserved. The difficulty with the F4 protein is that all of the lysines are conserved and very strict selection is acting on all the repeats. The simplest explanation for their conservation would be that they are all absolutely necessary for the function of F4. To put it into a biological and evolutionary context, if one tyrosine is replaced by a phenylalanine

then the schistosome carrying this mutation will leave no descendants in succeeding generations. This selection is absolute since there is not a single phenylalanine or tryptophan substitution in 108 tyrosine residues. The same reasoning applies to the lysine residues.

How is it possible that this degree of selection can occur in a repetitive protein? The only example I know where phenylalanine is a forbidden substitution for tyrosine is tyrosine 161 of the D1 polypeptide in Photosystem II [12]. In this case the tyrosine is acting as an electron carrier being reversibly oxidized and reduced. Phenylalanine will not perform the same role. Extending this line of reasoning to F4, if tyrosine is acting as an electron carrier in F4 then all of the tyrosines must be required for the putative redox function. Therefore the F4 protein must be acting as an electron transport chain. Only by the necessity for a chain of tyrosines can the complete selection against Phe and Trp be explained. One residue of Phe or Trp would break the "chain" thus destroying the function of the whole molecule. The only accepted mutations for the tyrosine codons are polar, potentially ionizable residues which might be expected to impede electron transfer less than Phe or Trp or Cys.

Why should F4 be required to transport electrons? Cross-linking of the eggshell is a series of reactions beginning with an oxidation step. If a phenol oxidase were carrying out the reactions a copper atom within the enzyme would be the primary electron acceptor with the electron subsequently being transferred to molecular oxygen. In the alternative scheme that our reasoning is leading towards the primary electron acceptor is still probably copper as suggested by the inhibition of cross-linking by copper chelators. However as pointed out in the introduction the source of the oxidizing equivalents is unclear if there is no phenol oxidase with access to the tyrosine side chains. In our alternative scheme, the F4 protein acts as an electron conductor carrying electrons out of the eggshell to copper atoms waiting elsewhere in the eggshell. One attractive possibility for the location of the copper atoms might be in association with the histidine rich C-terminal domain of F4 but this is pure speculation. Compared to the glycine rich protein with an apparent molecular weight of 14,000 daltons F4 is relatively large with a molecular weight of 48,000 daltons. This would be appropriate for a protein whose function was to act as an extended electron transport chain conducting electrons out of the partially cross-linked eggshell.

Since all of the tyrosines appear to participate in cross-links, logical consequences of this scheme are either, 1) cross-linking must begin at one end of F4 and proceed sequentially along the protein to the other end when all the tyrosines are oxidized or, 2) electron transport is not prevented by cross-link formation. Alternatively electrons flowing along the chain keep all tyrosine residues ahead of them reduced resulting in the same effect as the first case. Finally it is possible that F4 serves as an "electron guide" channelling electrons into a waiting conventional "phenol oxidase" enzyme that is sterically prevented from accessing each and every tyrosine residue.

Alternative explanations for the role of the repeats are possible. For example each repeat might possess enzymatic activity. Since there are multiple repeats the absolute selection against Phe or Trp cannot be accounted for by this scheme. The tyrosine residues are almost all destroyed during the cross-linking reactions and presumably therefore participate as reagents in the reactions. Therefore it is possible that the role of F4 is purely structural serving as a substrate for an enzyme catalyzing the cross-linking reactions. The roles of the glycine rich protein and F4 would therefore be similar, acting as passive substrates for another enzyme. If this were the case then the selective pressures on both proteins might be expected to be similar. However, this does not appear to be the case since there are several

Figure 4: Circular Dichroism spectra for a thirty amino acid F4-peptide (GYDKY)^6. CD spectra were recorded at 20°C with a JASCO J500A spectropolarimeter at a peptide concentration of 0.1 mg/ml employing 1 mm cells. Protein concentrations were determined by Tyrosine absorbance. CD spectra of (A) F4-6 in 20 mM sodium phosphate, pH 6.5. (B) F4-6 in 20 mM sodium phosphate, 4 M $LiClO_4$, pH 6.5 heated to 90°C for 30 minutes prior to analysis, (C) F4-6 in trifluoroethanol. The inset shows (a) the effect of $LiClO_4$ concentration on the CD spectrum of F4-6 at 188 nm and 20°C and (b) the effect of temperature on the 188 nm negative ellipticity minimum.

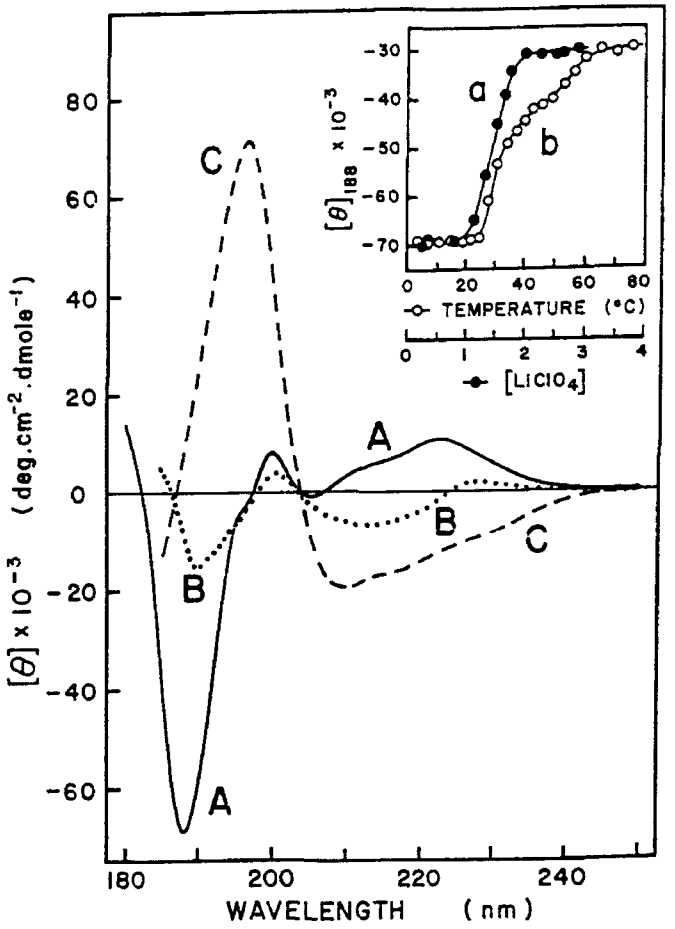

phenylalanine residues within the body of the glycine rich protein although there are far fewer total tyrosine residues than in F4. There are probably other possible roles for F4, but all the explanations we have considered suffer from the same inability to explain the high level and the nature of the sequence conservation of the repeats.

Does the consensus repeat adopt a particular secondary structure? Using a thirty amino acid synthetic peptide $(GYDKY)^6$ referred to as F4-6 we have performed a series of biophysical measurements to determine its potential secondary structure.

Figure 4 shows Circular Dichroism spectra for the F4-6 peptide. In phosphate buffer the CD spectrum of F4-6 shows a marked negative ellipticity at 188nm and positive ellipticity with a peak at 222nm (A in Figure 4). In contrast in trifluoroethanol the spectrum of F4-6 is almost exactly inverted showing a spectrum that is more typical of a conventional right handed alpha helix (C in Figure 4). The majority of these signals are removed by denaturing conditions as shown in trace B and the insert to Figure 4 for the negative ellipticity at 188nm. Our tentative interpretation of these data is that F4-6 is adopting some kind of left-handed structure in phosphate buffer, possibly a left-handed alpha-helix. This conclusion is supported by computer energy minimizations which suggest that the left-handed alpha-helix is an energetically preferred structure. What relevance these observations have for the function of F4 remains to be determined.

At the present time all we can conclude is that the F4 protein has some very significant functional role based on the strong selection that has been maintaining the amino acid sequence over long periods of time. Our suggestion is that the F4 protein acts as an electron transport chain conducting electrons out of the cross-linking eggshell thus helping to overcome problems of steric hindrance preventing access to tyrosine side chains involved in the cross-linking reactions.

ACKNOWLEDGEMENTS. This work was supported in part by grant N00014-90-J-1997 from the Office of Naval Research.

BIBLIOGRAPHY

1. Wells, K.E. and Cordingley, J.S. (1991) Exp. Parasitol., **73**, 295.
2. Wells, K.E. and Cordingley, J.S. (1992) in Case, S.T. (ed.), Structure, Cellular Synthesis and Assembly of Biopolymers, Springer-Verlag, New York, p.97.
3. Byram, J.E. and Senft, A.W. (1979) Am. J. Trop. Med. Hyg., **28**, 539.
4. Seed, J.L. and Bennet, J.L. (1980) Exp. Parasitol., **49**, 430.
5. Seed, J.L., Kilts, C.D. and Bennet, J.L. (1980) Exp. Parasitol., **50**, 33.
6. Bobek, L.A., Rekosh, D.M. and Loverde, P.T. (1988) Molecular and Cellular Biology, **8**, 3008.
7. Kunz, W., Opatz, K., Finken, M. and Symmons, P. (1987) Nucl. Acids Res., **15**, 5894.
8. Johnson, K.S., Taylor, D.W. and Cordingley, J.S. (1987) Mol. Biochem. Parasitol., **22**, 89.
9. Chen, L., Rekosh, D.M. and Loverde, P.T. (1992) Mol. Biochem. Parasitol., **52**, 39.
10. Shibahara, S., Tomita, Y., Sakakura, T., Nager, C., Chaudhuri, B. and Muller, R. (1986) Nucl. Acids Res., **14**, 2413.
11. Meadows, H.M. and Simpson, A.J.G. (1989) Mol. Biochem. Parasitol., **36**, 291.
12. Metz, J.G., Nixon, P.J., Rogner, M., Brudvig, G.W. and Diner, B.A. (1989) Biochemistry, **28**, 6960.

ENGINEERED PROTEINS FOR BIOMATERIALS

PATRICK S. STAYTON, ASHUTOSH CHILKOTI, CYNTHIA J. LONG, DEAN K. PETTIT, PHILIP H. S. TAN, GUOHUA CHEN, AND ALLAN S. HOFFMAN
Center for Bioengineering, WD-12, University of Washington, Seattle, WA 98195

ABSTRACT

A molecular adaptor for interfacing environmentally sensitive, soluble polymers and antibody molecules has been developed. The gene coding for the minimally sized, 55 amino acid IgG binding domain from protein G has been constructed by total gene synthesis. This domain is thermally stable, exhibits a highly reversible folding and unfolding equilibrium, and recognizes IgG and Fab molecules with high affinity. These properties make the protein G domain a potentially useful adaptor for non-covalent immobilization of antibodies to soluble polymers and hydrogels. Engineered single chain Fv antibody fragments have also been constructed and a method for expanding the usefulness of the protein G adaptor to these molecules is proposed. The engineered antibodies also provide a model system for developing general immobilization strategies aimed at maximizing binding affinities and therapeutic responses. The overall goal is to develop optimized engineering designs for functionally optimized antibody-material hybrids.

INTRODUCTION

Rapid advances in the biomedical sciences have resulted in the identification of numerous biomolecules with great therapeutic and diagnostic potential. These developments have created a pressing need for advanced separation materials which are capable of isolating bioactive molecules from complex biological mixtures and sources. Similarly, the development of sophisticated diagnostic materials will be required to take full advantage of the many biomolecule-based markers which have been identified for disease diagnosis and prevention. Both separation and diagnostic materials are usually dependent at some level on an affinity interaction. Because proteins display unmatched molecular recognition capabilities, there is great interest in using these biomolecules for separation and diagnostic purposes. Protein engineering techniques offer the possibility of tailoring protein structural and functional properties for specific applications, in ways not limited to naturally occuring proteins. For example, it would be desirable to have available proteins containing both tailored target recognition domains and tailored domains for interacting with the non-biological supports required of separation and diagnostic materials. Environmentally sensitive soluble polymers represent a fundamentally important target for these protein engineering efforts due to their advanced material properties. The work described here is directed toward combining tailored protein components with intelligent polymer materials to generate advanced separations, diagnostic, therapeutic, and drug delivery technologies.

EXPERIMENTAL

Protein G Gene Design and Construction.

The 55 amino acid IgG binding domain of Protein G, for which high resolution x-ray crystal and NMR solution structures are available [1,2], was reverse translated using the GCG software package. The final gene design incorporated optimal codon usage for *E. coli* expression and Nde I sticky ends on both the 5' and 3' termini. A total of six oligonucleotides were synthesized, with three oligonucleotides encoding the sense and antisense strands respectively. The oligonucleotides were designed with ca. 15 base pair overlaps between complementary strands. The oligonucleotides were phosphorylated, annealed by heating to 90°C with subsequent slow cooling, and ligated into Nde I cut pUC 19. This construction was

transformed into *E. coli* strain TG-1, and transformants were tested for inserts using a PCR based colony screen. Proper sized inserts were then sequenced using ABI fluorescence methodologies.

Antibody Cloning and Single-Chain Fv Construction.

PCR techniques were utilized to clone the variable heavy and light chain domains from three parent monoclonal antibodies (Novagen, Madison WI). Total RNA was isolated from hybridoma cell cultures and reverse transcribed to cDNA. A degenerate set of 5' and 3' oligonucleotide primers, directed against conserved amino acid sequences in the leader peptide and first constant domains respectively, was then used to selectively amplify the variable domain genes. Correctly sized PCR products were subsequently subcloned and sequenced. The single-chain Fv construction also utilizes PCR techniques to join the variable heavy and light chain domains with a 15 amino acid linker (Figure 1).

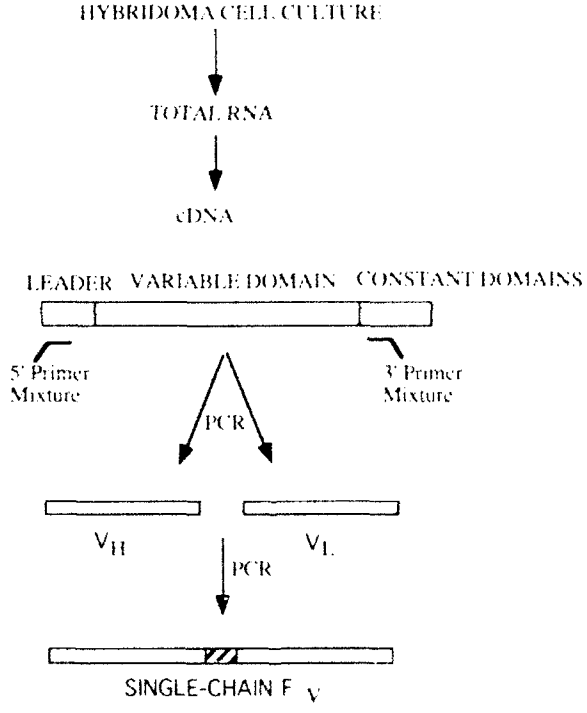

Figure 1. Schematic outline of the genetic construction strategy for the production of single-chain Fv antibody derivatives. The individual variable heavy and light chains are first cloned using degenerate PCR primers directed against conserved leader peptide sequences and the first constant domain sequences. These clones are then spliced together with primers incorporating the 15 amino acid linker which joins the heavy and light chain domains.

THE POLYMER-PROTEIN INTERFACE

A Molecular Adaptor for Soluble Polymer/Antibody Biomaterials

Most biomaterial applications are dependent at some level on surface interactions between a non-biological material and biological molecules. Important examples include [illegible] and separations materials, with required interactions between optical, electrical, and polymer components and the biological sensing and affinity molecules. While biological molecules excel at many recognition-based functions (e.g. sensing and affinity separations), they are seldom found to be simultaneously designed for the materials interface. We have initiated studies aimed at utilizing protein engineering techniques to develop general molecular strategies for controlling the materials-biomolecule interface [3]. One of our first targets is the interface between proteins and water soluble polymers and hydrogels [4,5,6]. These environmentally sensitive polymers show great potential for many separations, diagnostic, and drug delivery applications. The physical state of soluble polymers, such as N-isopropyl acrylamide, can be reversibly cycled between an extended hydrated form and a collapsed precipitated state. The entropy driven phase change can be effected with mild alterations of temperature and pH that fall within an acceptable range for many protein molecules. Proteins can be coupled directly to the polymer backbone via surface lysine residues with conventional cross-linking chemistry. The polymer protein hybrids can be exposed to the target and then separated from solution with a slight change in temperature or pH. The general process is useful for either separations purposes or with immuno-assay diagnostic schemes. In addition to the attractive stimuli-responsiveness of the polymers, these systems greatly reduce the considerable problem of non specific adsorption at solid surfaces associated with conventional chromatography and ELISA techniques.

Antibodies represent a particularly important target biomolecule in the development of these smart polymer hybrid materials. Rather than directly coupling antibodies to the soluble support, however, it is desirable in some cases to have them non covalently bound. For example, we are interested in polymers that could sequentially recognize a variety of antibody molecules with distinct specificities. There is also the practical problem of antibody stability over the course of repeated precipitation cycles. Denaturation of the covalently linked antibodies *effectively inactivates the entire polymer system*. To generate a non-covalent interface between soluble polymers and antibodies, we have utilized a genetically engineered adaptor. The adaptor is a minimally sized, highly stable IgG binding domain from Streptococcal protein G. The gene encoding the 55 amino acid domain was constructed by total gene synthesis and has been expressed at high yields in *E. coli* [7]. This domain exhibits extremely high thermal stability (on the protein scale), and more importantly exhibits a highly reversible, two state folding/unfolding equilibrium [8]. The isolated domain binds both intact IgG and Fab antibodies with high affinity (ca. $10^9 M^{-1}$), and high resolution crystal structures are available for both the isolated protein and the Fab complex [8]. In addition to its desirable physical properties, the native protein G domain does not contain cysteine. This will enable us to genetically engineer a unique thiol side chain at specified points on the protein surface [9]. The current cross-linking chemistry utilizes amino *functionalities on the protein surface. Invariably, however, there are a number of lysine residues* that are generally distributed across the protein surface. It is thus nearly impossible to control the stoichiometry and site of cross-linking at the molecular level. Genetic control of the attachment site will yield molecular control of stoichiometry and cross-linking loci.

A Peptide Adaptor for Engineered Single Chain Fv Antibodies

Protein G associates with Fab antibodies through an interesting recognition motif. The primary protein-protein interface is generated through the formation of inter-protein β-sheet structure. We are attempting to take advantage of this motif to extend the usefulness of the protein G adaptor. The goal is to provide the same non covalent interface for the recognition of genetically engineered single-chain Fv antibodies. Single-chain Fv antibodies are constructed by fusing the variable heavy and light chains with a 15 amino acid flexible peptide linker [10]. These minimally sized antibody fragments retain the specificity and affinity of the parent IgG, but can be produced in *E. coli* and can thus be genetically manipulated. In related work we are attempting to engineer improved antibody components with advanced separation properties (e.g. environmentally regulated and triggered antigen affinity) but these single chain Fv fragments lack the usual constant domains. Since these constant domains (and associated carbohydrate binding

sites) provide the usual cross-linking handles and the recognition sites for protein adaptors such as protein G or protein A, their absence makes it difficult to interface the single-chain Fv with conventional material surfaces. Protein G forms an antiparallel ß-sheet hydrogen-bonding interaction with the last six amino acids of the CH2 Fab domain. When added to the C-terminus of the engineered single-chain Fv antibodies, this peptide sequence should provide a useful adaptor for interfacing with the protein G-soluble polymer hybrid (Figure 2).

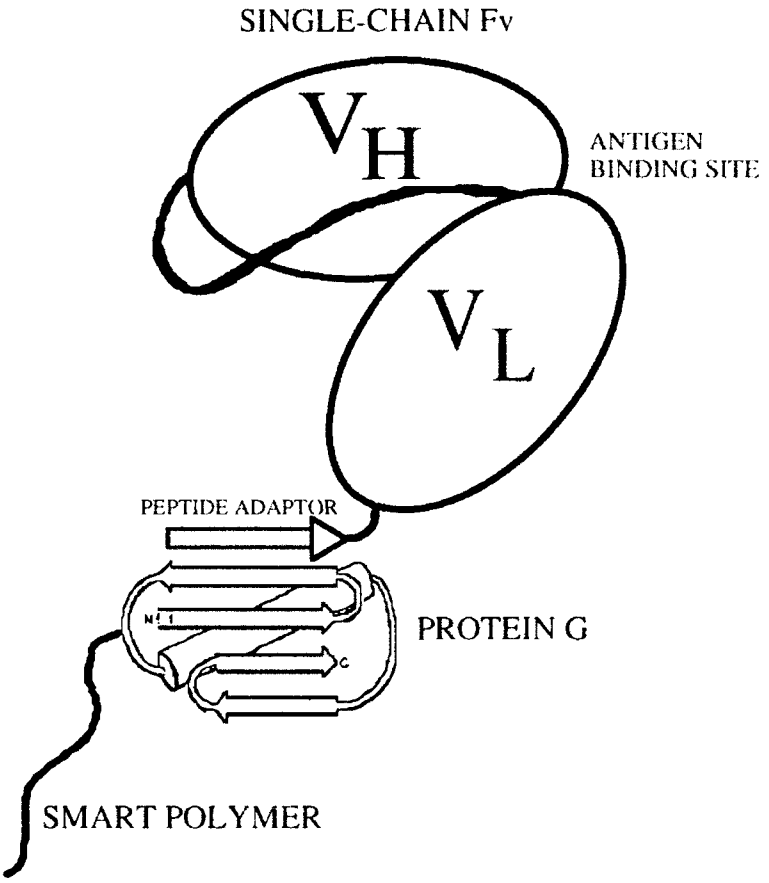

Figure 2. Schematic illustration of the peptide adaptor to be used in conjunction with the protein G-soluble polymer hybrid to generate affinity separation materials for engineered single-chain Fv antibodies.

Engineering Optimized Biomaterial Activity

The control of biomaterial function through the optimization of biomolecule activity remains a fundamental goal. An important example of a specific target is the development of immobilization methods which maximize the binding or enzymatic activity of protein components in biosensors, diagnostic materials, drug delivery materials, and bioreactors. We have developed a model experimental system for addressing the specific goal of maximizing the activity of materials which utilize immobilized antibodies. Genetic engineering techniques will be used to test several immobilization strategies that encompass both covalent and non-covalent interactions between a single-chain Fv and various material surfaces. The principal goal is to identify a set of generally applicable mutations on the highly conserved antibody framework to generate a "universal" design for optimized immobilization (Figure 3).

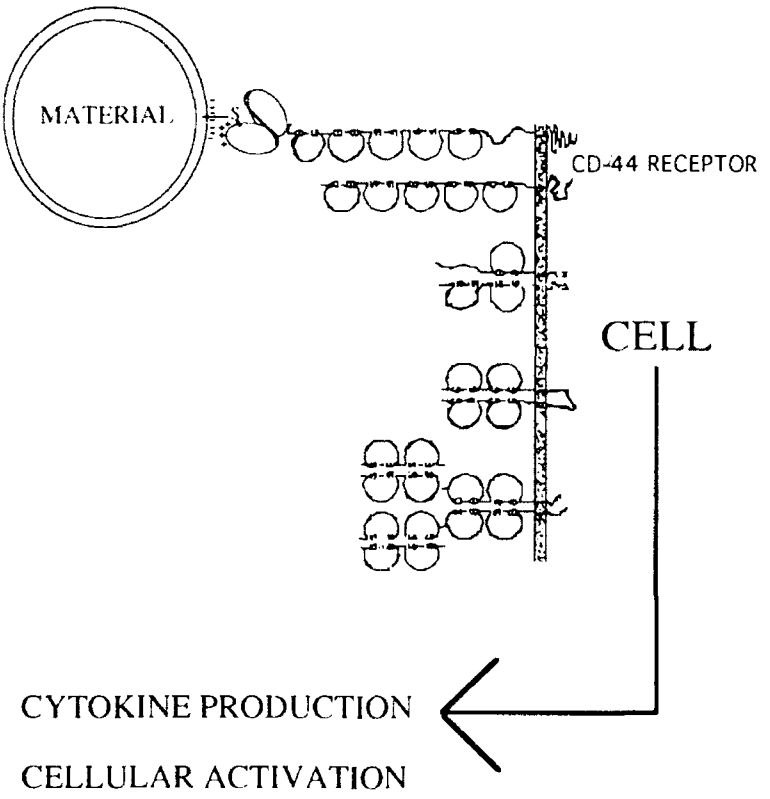

Figure 3. Schematic illustration of bio-activity assay to assess immobilization strategies. The cell response can be quantitated and studied as a function of attachment site and surface engineering.

This system should have direct import to biosensor antibody immobilization, antibody targeted drug delivery materials, antibody-based diagnostic materials, and therapeutic antibody delivery.

The central single-chain Fv, termed S5, can function directly as a therapeutic agent. The S5 parent monoclonal antibody, when administered intravenously at 0.2 mg/kg/day prior to total body irradiation, has been shown to enhance marrow graft acceptance in a canine model [11]. S5 is directed against CD44 [12], a glycoprotein receptor that is widely distributed in the body and responsible for a variety of functional activities related to cellular adhesion and activation. S5 stimulates biological responses through CD44, and its activity has been well-characterized both *in vitro* and *in vivo*. This antibody system provides three key capabilities for evaluating the effectiveness of immobilization strategies: (1) an assay is available for quantitating effective binding affinities (2) *in vitro* cell assays are available for quantitating the effective ability of the immobilized antibodies to stimulate specific biological responses (3) an *in vivo* system is available for testing whether improved *in vitro* designs have any relationship whatsoever to *in vivo* function. Immobilization strategies to be tested include the design of complementary material and antibody surfaces (via electrostatic and hydrophobic mechanisms), where the initial antibody interaction site is narrowed by the selection of a genetically engineered covalent attachment site (e.g. the introduction of a surface thiol). Figure 3 illustrates the general features of the system using a single-chain Fv-targeted liposome as an example of an antibody-material hybrid.

ACKNOWLEDGEMENTS

This work was supported in part by a Whitaker Foundation Development Award to the UW, the UW Royalty Research Foundation, and by NSF Grant BCS 9101716 to A.S.H.

REFERENCES

1. A. Achari, S. P. Hale, A. J. Howard, G. M. Clore, A. M. Gronenborn, K. D. Hardman, and M. Whitlow, *Biochemistry* **31**, 10449 (1992).

2. A. M. Gronenborn, D. R. Filipula, N. Z. Essig, A. Achari, M. Whitlow, P. Wingfield, and G. M. Clore, *Science* **253**, 657 (1991).

3. P. S. Stayton, J. Olinger, P. W. Bohn, and S. G. Sligar, *J. Am. Chem. Soc.* **114**, 9298 (1992).

4. A. S. Hoffman, *MRS Bulletin* **16** (9), 42 (1991).

5. D. DeRossi, K. Kajiwara, Y. Osada, and A. Yamauchi, *Polymer Gels*, (Plenum Press, New York, 1991).

6. J. P. Chen, H. J. Yang, and A. S. Hoffman, *Biomaterials* **11**, 625 (1990).

7. P. Alexander, S. Fahnestock, T. Lee, J. Orban, and P. Bryan, *Biochemistry* **31**, 3597 (1992).

8. J. P. Derrick, and D. B. Wigley, *Nature* **359**, 752 (1992).

9. P. S. Stayton, and S. G. Sligar, *Biochemistry* **29**, 7381 (1990).

10. R. E. Bird, K. D. Hardman, J. W. Jacobson, S. Johnson, B. M. Kaufman, S-M. Lee, T. Lee, S. H. Pope, G. S. Riordan, and M. Whitlow, *Science* **242**, 423 (1988).

11. F. Schuening, R. Storb, S. Goehle, J. Meyer, T. C. Graham, H. J. Deeg, F. R. Appelbaum, G. E. Sale, L. Graf, and T. P. Loughran, *Transplantation* **44**, 607 (1987).

12. B. M. Sandmaier, R. Storb, F. R. Appelbaum, and W. M. Gallatin, *Blood* **76**, 630 (1990).

SELF-ASSEMBLING NANOSTRUCTURES: RECOGNITION AND ORDERED ASSEMBLY IN PROTEIN-BASED MATERIALS

Kevin P. McGrath and David L. Kaplan
Biotechnology Division, U.S. Army Natick RD&E Center
Natick, MA 01760-5020

ABSTRACT

A new approach to materials design is presented, utilizing specific recognition and assembly at the molecular level. The approach described exploits the control over polymer chain microstructure afforded by biosynthesis to produce protein-based materials with precisely defined physical properties. Incorporated into these materials are recognition elements that stringently control the placement and organization of each chain within higher order superstructures. The proteins, designated Recognin A2 through Recognin E2, are recombinant polypeptides designed *de novo* from both natural consensus sequences and an appreciation of the physical principles governing biological recognition. These materials are designed to examine the forces involved in specific recognition and complexation. through control of charge identity and placement, a pattern for specific interaction can be introduced. A subset of these materials are programmed to spontaneously assemble into complex, multicomponent structures and represent the first step in a rational approach to nanometer-scale structural design.

INTRODUCTION

Efficient engineering at the molecular scale relies on two things: 1) the ability of individual molecules to recognize specific counterparts in multicomponent systems, and 2) spontaneous organization into well-defined molecular complexes of hundreds or thousands of molecules. In traditional materials science the level of such organization rarely extends down to the molecular level. The ordering of individual molecules is statistical in nature, and often considerable post-assembly processing is required to achieve the desired physical properties. Nanometer scale fabrication techniques must rely on the molecules *to process themselves* into useful assemblies. This can only be accomplished by incorporating into each component the ability to spontaneously recognize where it belongs within a larger framework and to rapidly incorporate into the final, desired product.

The importance of recognition processes in nature cannot be overemphasized. These interactions form the basis for virtually every biological process in living organisms. Nature has developed a large array of specific recognition patterns, based on shape, hydrophobicity, charge placement, and allosteric interactions. Understanding of these recognition patterns has progressed rapidly in the past few years, particularly in the specificity of interaction seen in transcriptional regulatory proteins. Using these sequences as general models, we have examined electrostatic interactions and their role in determining specificity and extent of dimerization in synthetic leucine zipper proteins. The identity and positioning of charges along the two alpha-helices dramatically influences the specificity of dimerization toward otherwise identical sequences.

Mat. Res. Soc. Symp. Proc. Vol. 292. © 1993 Materials Research Society

MATERIALS AND METHODS

T4 DNA ligase, T4 polynucleotide kinase, Calf Intestinal alkaline phosphatase, and the restriction enzymes EcoRI, BamHI, HindIII, BstEII, and XbaI, were obtained from Pharmacia LKB (Piscataway, NJ). The restriction enzymes NheI, XhoI, and SpeI were obtained from New England Biolabs (Beverly, MA). The plasmid pUC18 and *E. coli* strain NM522 were obtained from Pharmacia. The plasmid pQE-9 and the *E. coli* strain SG13009pREP4 were obtained from Qiagen (Chatsworth, CA). All general procedures for isolation, manipulation, and routine analysis of DNA, along with methods of *E. coli* transformation, were performed as described in Sambrook, Frisch, and Maniatis [1]. DNA sequencing was accomplished using the T7 Sequencing Kit from Pharmacia.

Preparation of Synthetic DNA

Oligonucleotides were synthesized on a Milligen/Biosearch Cyclone Plus DNA Synthesizer using the phosphoramidite chemistry of McBride and Caruthers [2]. Crude oligonucleotides were purified using preparative gel electrophoresis, enzymatically phosphorylated using T4 polynucleotide kinase, and annealed to form heteroduplex DNA.

Cloning and Amplification of Synthetic DNA

Synthetic DNA fragments were inserted into dephosphorylated pUC18 digested with EcoRI and HindIII. The ligation mixture was used to transform *E. coli* strain NM522, and color selection on plates containing isopropyl thiogalactoside (IPTG) and 5-bromo-4-chloro-3-indolyl-galactopyranoside (X-Gal) used to identify recombinants. Plasmids containing inserts were sequenced to identify the encoded protein sequences. Desired genetic sequences were isolated and purified from 50 mL cultures, and the fragments liberated by digestion with the appropriate enzymes.

Construction of pUC-BstEII

Synthetic DNA encoding a 57 base pair linker fragment (Figure 1) was inserted into dephosphorylated pUC18 digested with XbaI using T4 DNA ligase, and the resulting mixture used to transform *E. coli* strain NM522. Recombinants were identified by color screening, and the insert verified by double-stranded plasmid sequencing. The plasmid was purified from 100 mL of liquid culture and digested with BstEII. The linearized vector was then dephosphorylated using Calf intestinal alkaline phosphatase, and gel purified from 1% agarose.

Construction of the Recognition Elements

The 126 base pair DNAs encoding the various recognition elements (Figure 2) were constructed *in situ* by combining and ligating the desired fragments in the presence of linearized pUC-BstEII. The ligation mix was used to transform *E. coli* strain NM522. Recombinant plasmids were identified by digestion with BamHI,

and the constructed recognition elements verified by double-stranded plasmid sequencing.

Construction of Prokaryotic Expression Systems

Properly constructed recognition elements were excised from the recombinant pUC-BstEII by digestion with BamHI and gel purified from 1% agarose. Purified recognition elements were inserted into the BamHI site of pQE-9 (Qiagen, Inc., Chatsworth, CA). The ligation mixes were used to transform *E. coli* NM522. Plasmids containing the recognition elements in the correct orientation were identified by restriction digestion, and were used to transform *E. coli* SG13009 pREP4 (Qiagen, Inc., Chatsworth, CA).

Protein Expression

All protein expressions were performed in TB media (32 g Bacto-Tryptone, 20 g Yeast Extract, 5 g NaCl per liter). Media were supplemented with 400 mg/L ampicillin and 50 mg/L kanamycin. Fifty milliliters of saturated culture were used to inoculate 1 L of freshly sterilized media, and the cultures allowed to grow at 37 °C for 3 h with vigorous aeration. IPTG was added to a final concentration of 2 mM, and protein production induced for 2 h at 37 °C with vigorous aeration. Cells were isolated by centrifugation and lysed in 50 mL of 6 M guanidinium-HCl, 100 mM sodium phosphate, pH 8.0. After 1 h incubation at ambient conditions, the solution was centrifuged at 12,000 rpm for 30 minutes. The clarified supernatant was collected and stored at -20 °C until purified. Proteins were purified by Ni-NTA column chromatography using the method recommended by the manufacturer. Yields of purified protein ranged from 70-140 mg/L.

Protein Characterization

Purity of the recombinant proteins was assayed by amino acid composition, N-terminal sequencing, capillary electrophoresis, and matrix-assisted laser desorption mass spectrometry. In all cases purities exceeded 95%. Turbidity studies were performed on a Beckman DU-70 UV/Vis spectrophotometer operating at 400 nm. Kinetic analyses were performed on a Biacore Biospecific Interaction Analysis System (Pharmacia Biosensor, Sweden) in 20 mM sodium phosphate, 100 mM sodium chloride, pH 7.0.

```
   XbaI     BamHI                 NheI                 BstEII
5'-CTAGA  GGA TCC  ATG  GCT  AGC  GGT  GAC  CTG
      T   CCT AGG  TAC  CGA  TCG  CCA  CTG  GAC
          Gly Ser  Met  Ala  Ser  Gly  Asp  Leu

                        SpeI           BamHI   XbaI
AAT  AAC  ACT  AGT  CGG ATC C  T-3'
TTA  TTG  TGA  TCA  CCC TAG G  AGATC-5'
Asn  Asn  Thr  Ser  Gly  Ile
```

Figure 1. Sequence of the synthetic linker. Important restriction sites are underlined.

```
                BstEII
5'-  CGT  GAC  CTG  [G/A]AA  AAC  [G/A]AA
     Gly  Asp  Leu  Glu/Lys  Asn  Glu/Lys

GTG  GCC  CAG  CTC  [G/A]AA  AGG  [G/A]AA
Val  Ala  Gln  Leu  Glu/Lys  Arg  Glu/Lys

               BglII
GTT  AGA  TCT  CTG  [G/A]AA  GAT  [G/A]AA
Val  Arg  Ser  Leu  Glu/Lys  Asp  Glu/Lys

GCG  GCT  GAA  CTG  [G/A]AA  CAA  [G/A]AA
Ala  Ala  Glu  Leu  Glu/Lys  Gln  Glu/Lys

               XhoI
GTC  TCG  AGA  CTG  [G/A]AA  AAT  [G/A]AA
Val  Ser  Arg  Leu  Glu/Lys  Asn  Glu/Lys

ATC  GAA  GAC  CTG  [G/A]AA  GCC  [G/A]AA
Ile  Glu  Asp  Leu  Glu/Lys  Ala  Glu/Lys

                BstEII
AAT  CGT  GAC  CTG  -3'
Ile  Gly  Asp  Leu
```

Figure 2. Sequences of the DNA monomers. Amino acids are indicated below the appropriate codons. Important restriction sites are underlined.

RESULTS AND DISCUSSION

The ability to incorporate specificity into assembly processes allows for a high level of control over molecular architecture, and in theory permits the precise tailoring of the macroscopic properties of the material (mechanical, thermal, absorptive). Until recently, no clear approach for such self-assembly was envisioned. We present here the first demonstration of a "programmed molecular assembly" using recognition motifs incorporated into synthetic polypeptides. These motifs stringently enforce specific interaction and assembly in complex multicomponent systems.

Various transcription factors, including C/EBP, GCN4 and members of the Fos, Jun, and Myc families form highly specific dimeric complexes involving hydrophobic interactions between leucine residues in laterally aligned coiled-coil structures. These protein regions have been named "leucine zippers" because the leucines interdigitate much like the teeth of a zipper. The sequences of such regions contain regularly spaced hydrophobic residues within a generic heptad repeat $(\mathbf{a\text{-}b\text{-}c\text{-}d\text{-}e\text{-}f\text{-}g})_n$. Within this repeat, hydrophobic residues are usually found at the **a** and **d** positions, while polar and charged residues occupy the **e** and **g** positions. The alpha-helices wrap around each other with a slight superhelical twist having a period of ca. 140 Å. An isolated coiled coil is about 10 Å thick.

The dimerization process is driven by sequestering the hydrophobic residues

into the interior of the coiled coil, with carefully positioned charged residues imparting a specificity in the choice of coiled-coil partners. Site-directed mutagenesis of both the hydrophobic and charged residues demonstrated that while the driving force for dimerization is hydrophobic in nature, the dominant factor in *preferential* heterodimer formation was electrostatic interactions, occurring between sidechains at the **e** and **g** positions in the coiled coil [3].

The degree of specificity in the Fos-Jun interaction has been quantitated using short synthetic peptides identical in sequence to the leucine zipper portions. O'Shea *et al.* [4] showed by HPLC that the preference to form Fos-Jun heterodimers is at least 100-fold greater than the preference to form either homodimer. They also confirmed results reported earlier [5] that within the coiled coil the two alpha-helices align in parallel, contrary to the antiparallel arrangement originally reported [6]. This has been further confirmed by X-ray diffraction data from crystals of the homodimer of GCN4, which indicate both the parallel in-register alignment of chains and the presence of ionic interactions between residues at the **e** and **g** positions [7].

Protein Sequence Design

The degree of organization in coiled coils, at the secondary, tertiary, and quarternary levels, makes them ideal candidates for primary components in self-assembling systems. Unique to these materials is the precise spatial control, over hundreds of angstroms, of functional group placement. The high degree of specificity exhibited in Fos-Jun dimerization can be incorporated into novel synthetic proteins, producing materials capable of spontaneous self-organization into complex supramolecular assemblies.

Toward this end, we have designed and synthesized a library of genetic elements encoding the following protein sequences:

(IGDL[E/K]N[E/K]VAQL[E/K]R[E/K]VRSL[E/K]D[E/K]
AAEL[E/K]Q[E/K]VSRL[E/K]N[E/K]IEDL[E/K]A[E/K])$_n$ 1

Protein sequences were designed with the following considerations in mind: 1) the formation of coiled-coil alpha-helices, 2) the incorporation of specific recognition patterns through precise placement of charged groups, and 3) control of solubility in the dimeric state. This sequence positions leucine residues every seven residues (underlined for visual clarity) at the **d** position. The identity and position of the leucines and charged groups are in agreement with natural leucine zipper proteins, but a number of natural proteins that contain repeated leucine heptads do not form coiled coils. An algorithm recently developed by Lupas, Van Dyke, and Stock to identify coiled coils from primary sequence data was used to refine protein sequences with respect to their propensity for coiled coil formation [8].

The protein sequences represented in **1** were reverse translated to the corresponding DNA sequences (shown in Figure 2). Codons were chosen to maximize expression level in *E. coli* and to introduce useful restriction sites for subsequent genetic manipulation. The length and composition of the amino acid repeat was chosen not only to create sophisticated recognition motifs, but also to minimize the repetitive nature of the corresponding gene. The DNA sequences use a "mixed site" approach at the first base of the codons for amino

acids at the **e** and **g** positions. An [A/G] mixed site synthesis is used to generate either AAA (Lys) or GAA (Glu) codons at these positions. Thus in a single step a library of DNA sequences encoding all 4096 (2^{12}) possible recognition sequences can be generated.

The DNA monomers were constructed via three sets of smaller oligonucleotides to simplify the isolation of recognition sequences (e.g., if the full length monomer were constructed prior to sequencing, an unmanageably large number of sequencing reactions would be needed before complementary recognition sequences were identified). Fragmentation of the monomer into three sections, each having only 16 possible permutations, significantly reduces the effort required to identify sequences. From a limited number of sequenced segments, a large number of monomer recognition sequences can be rapidly constructed. After construction of the various monomer genes, the DNA was re-sequenced to insure that no alterations had occurred from re-transformation.

Design of Charge Patterns for Recognition

We set two guidelines for charge sequence design; that the pattern of glutamates and lysines discourage homodimerization (as this would complicate any assembly scheme), and that the charge pattern controlling the dimerization insure that the orientation of the two helices is parallel and in-register. Using the crystallographic data of Kim and coworkers [7] as guidelines for how electrostatic interactions are formed in such structures, we designed the following materials, designated Recognins A2 through E2:

Recognin A2	EEEE	EEEK	KEKE	EEEE	EEEK	KEKE
Recognin B2	KKKK	KKKE	EEKK	KKKK	KKKE	EEKK
Recognin C2	KKEE	KKKE	EEKK	KKEE	KKKE	EEKK
Recognin D2	EEEE	KKKE	EEKK	EEEE	KKKE	EEKK
Recognin E2	EEEE	EEKE	EEKK	EEEE	EEKE	EEKK

For simplicity, only the charge pattern of the **e** and **g** residues is indicated. All other residues in these proteins are shown in **1**. Electrostatic bonding occurs between the **e** residue of the *i*th heptad and the **g** residue of the *i*th-1 heptad. The rationale for these sequences is that A2 is viewed as a target sequence, with B2 reflecting a perfect electrostatic fit. Recognins C2, D2, and E2 are progressively poorer fits to the A2 charge pattern. These materials can be used to test a number of assumptions about the strength and stability conferred on these structures by electrostatic interaction, and their role in controlling the specificity of interaction.

Turbidometric Analysis

We investigated the interaction between A2 and B2 using turbidity measurements at 400 nm. The proteins are believed to exist as weak homodimers in solution; upon mixing the more stable heterodimer is formed. When these proteins are mixed at equal concentrations, a rapid increase in turbidity is seen. We attribute this to specific heterodimer formation, which subsequently associates into higher order structures that precipitate from solution. Gel analysis of the precipitate indicates that it is a 1:1 complex of A2 and B2. No similar increase in the turbidity of the homodimer solutions is observed prior to mixing.

Surface Plasmon Resonance Analysis of Recognin Interactions

We looked very closely at the interaction of A2 with both B2 and C2, with both components free in solution and when one species was immobilized onto a thin gold film. The latter was done to measure the rates of association and dissociation between the complexes. We used surface plasmon resonance to detect minute changes in refractive index that accompany a specific binding event in the immediate vicinity of the metal surface. This technique is extremely sensitive, and can detect specific interactions at the picogram level. As shown in Figure 3, there is a measurable difference in both the rates and magnitude of interaction between A2-B2 and A2-C2. After an initial increase in refractive index due to solvent exchange, it is seen that the rate of association for the A2-B2 complex is more rapid and that the equilibrium response is achieved sooner. There does not seem to be a great difference in the rates of dissociation (seen in the later portions of the sensorgram). A kinetic analysis of these rate constants run at several different concentrations of A2 reveals that for the A2-B2 interaction, $k_{ass} = 4.11 \times 10^3$, $k_{diss} = 1.31 \times 10^{-3}$, and $K_a = 3.14 \times 10^6$. For the A2-C2 interaction, $k_{ass} = 3.46 \times 10^3$, $k_{diss} = 2.39 \times 10^{-3}$, and $K_a = 1.45 \times 10^6$. The interaction of these molecules when both components are free in solution, along with the analysis of A2's interaction with other Recognins, is presented elsewhere [9].

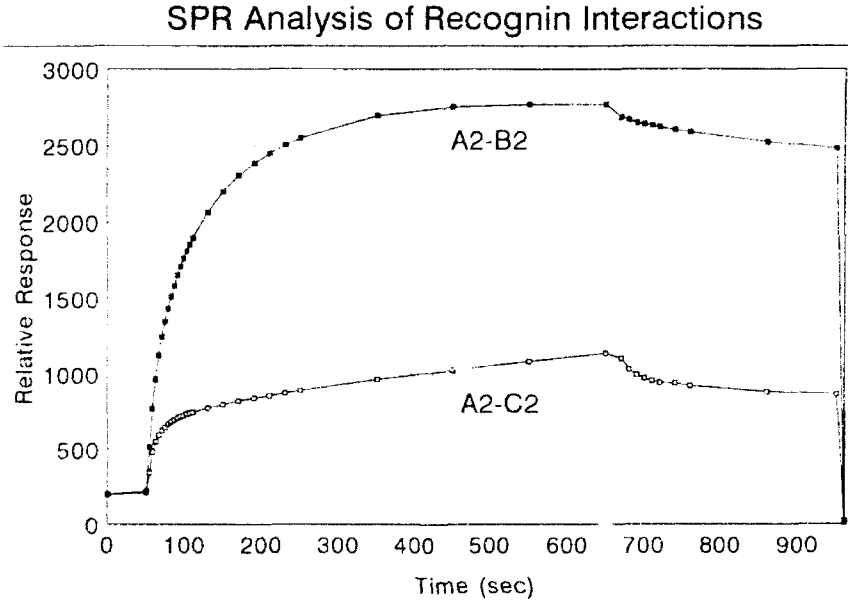

Figure 3. Surface plasmon resonance measurements of the interactions between A2-B2 and A2-C2 at 25 μg/mL concentration of A2.

a)

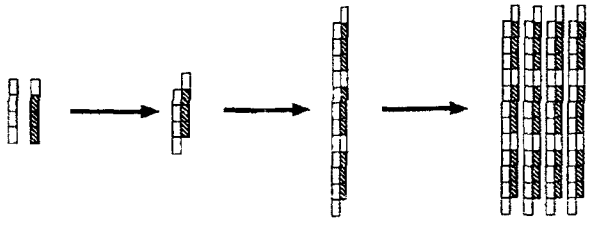

b)

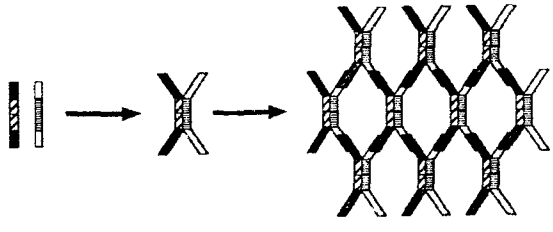

Figure 4. Applications to new materials design. a) Generation of highly oriented fibers through control of molecular assembly. b) Production of 3-D networks with precisely defined pore sizes using the same strategy.

Applications to Materials Science

We have used *de novo* design to produce a series of coiled-coil proteins capable of rapid and selective complex formation in solution. We view these materials as "building blocks" for the design of more complex self-assembling materials. Examples of such materials are postulated in Figures 4a and 4b. In the first case, that of self-assembling fibers, the genes for Recognins A2 and B2 are modified by incorporating additional recognition elements at the N- or C-terminus. These new elements, designed to react with each other and not A2 or B2, impose a new driving force for ordered supramolecular assembly, and align all of the dimers in a "head-to-tail" orientation within a growing fibril. Such fibers should have excellent mechanical properties, along with unique piezo- and pyroelectric activity.

The second example, that of ordered network formation, is a logical extension of ordered fiber assembly. Here the fiber-forming genes are further modified to introduce a third set of recognition sites that will control growth and organization in three dimensions. Such materials will have highly uniform and controlled pore sizes that could be exploited in optics, thermal insulation, selectively permeable membranes, controlled release, or medical reconstruction. Such materials are currently under development.

REFERENCES

1) Sambrook, J., Frisch, E.F., and Maniatis, T., *Molecular Cloning, A Laboratory Manual*, 2nd Ed.; Cold Spring Harbor, 1989.
2) McBride, L.J., and Caruthers, M.H., *Tetrahedron Letters*, **24**, 245, 1983.
3) Scherman, M., Hunter, J.B., Hennig, G., and Müller, R., *Nuc. Acid Res.*, **19(4)**, 739 (1991).
4) O'Shea, E.K., Rutkowski, R., Stafford, W.F., and Kim, P.S., *Science*, **245**, 646 (1989).
5) O'Shea, E.K., Rutkowski, R., and Kim, P.S., *Science*, **243**, 538 (1989).
6) Landschulz, W.H., Johnson, P.F., and McKnight, S.L., *Science*, **240**, 1759 (1988).
7) O'Shea, E.K., Klemm, J.D., Kim, P.S., and Alber, T., *Science*, **254**, 539 (1991).
8) Lupas, A., Van Dyke, M., and Stock, J., *Science*, **252**, 1162 (1991).
9) McGrath, K.P., DiGirolamo, C.M., and Kaplan, D.L., manuscript in preparation.

OVER-EXPRESSION OF A CORE REPEAT FROM AN INSECT SILK PROTEIN THAT FORMS INTRAMOLECULAR DISULFIDE BONDS

STANLEY V. SMITH AND STEVEN T. CASE
Department of Biochemistry, The University of Mississippi Medical Center, 2500 North State Street, Jackson, MS 39216-4505.

ABSTRACT

A gene encoding one complete [C+SR] core repeat from spIa, a 1000-kDa silk protein from Chironomus tentans, was synthesized and its recombinant protein expressed to high levels in bacterial cells. We observed that reducing agents significantly alter the electrophoretic mobility of this protein. A variety of data indicate that the purified recombinant protein is folded and its structure stabilized by two intramolecular disulfide bonds.

INTRODUCTION

Aquatic larvae of the midge, Chironomus tentans, spin insoluble silk fibers composed of about a dozen proteins [1]. Prior to spinning, these proteins exist as soluble supermolecular complexes in the lumen of the salivary gland [2]. Studies of protein complex disassembly and reassembly in vitro indicate that the giant (1000-kDa) spI proteins form the fibrous backbone of the silk [2]. Molecular biological data reveal that spIs consist of 130 to 150 tandem copies of a core repeat which can be divided into two domains; the constant (C) domain, which contains four conserved cysteines, and the subrepeat (SR) domain, which contains multiple copies of the motif, basic residue-proline-acidic residue [1]. Circular dichroism and Fourier transform infrared spectroscopic studies of synthetic peptides suggest that the C domain is mainly α-helical and the SR domain forms a poly(glycine)-type II helix [3]. Both domains contain ß-turns.

Studies using synthetic peptides are restricted by practical size limitations. In order to obtain monomeric and multimeric [C+SR] proteins with a defined number of repeats, we turned to genetic engineering [4]. Here we report the successful expression in bacteria of a monomeric recombinant Constant-And-Subrepeat (rCAS) protein and the unexpected finding that purified rCAS is folded and stabilized by disulfide bonds.

GENE SYNTHESIS AND EXPRESSION

Codon usage in Escherichia coli and C. tentans differs significantly. Therefore, to optimize expression in a bacterial cell, a gene was designed such that the amino acid sequence of the insect protein was encoded by codons preferred by E. coli. The gene was synthesized in three steps (Fig 1): assembly, priming and amplification.

Mat. Res. Soc. Symp. Proc. Vol. 292. 1993 Materials Research Society

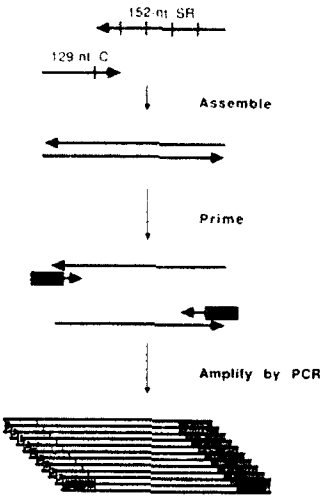

Fig. 1. Steps in the synthesis of the C+SR gene encoding rCAS.

Assembly

Two oligonucleotides were synthesized. The C oligonucleotide is 129 nucleotides long and overlaps the first SR. The SR oligonucleotide is 152 nucleotides long, contains four SRs and is complementary to part of the C oligonucleotide. Upon annealing, the oligonucleotides yielded template-primer complexes suitable for DNA polymerase to complete the synthesis of the two strands.

Priming

The assembled gene was denatured and mixed with an excess of two different oligonucleotides which, besides providing primers for the polymerase chain reaction (below), provided sequences necessary for subsequent manipulations of the gene. These primers contain restriction enzyme cleavage sites necessary for inserting the gene into an expression vector as well as providing sites that will enable head-to-tail ligation of tandem [C+SR] repeats.

Amplification

The primed synthetic gene was amplified using the polymerase chain reaction [5] with a thermostable DNA polymerase. After 25 cycles, microgram quantities of a 298-bp fragment were obtained.

Insertion and Expression

After purification by gel electrophoresis, the amplified gene was cleaved with restriction enzymes and inserted downstream from the bacteriophage T7 gene 10 promotor on the plasmid, pET3a [6] (Fig. 2). By fusing the start codon of the T7 gene 10 promotor with a methionine codon in the C domain, we were able to produce rCAS devoid of extraneous amino acids. The bacterial host, BL21(DE3), was transformed with the recombinant pET3a::C+SR construct and cells were tested for inducible synthesis of rCAS. rCAS synthesis requires the synthesis of T7 RNA polymerase which, in turn, depends upon the ability of isopropyl-ß-thiogalactopyranoside (IPTG) to bind a repressor protein that otherwise binds the lac operator preventing synthesis of T7 RNA polymerase (Fig. 3).

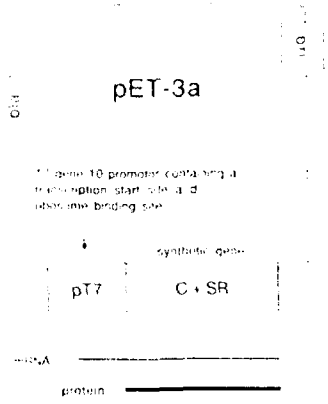

Fig. 2. The recombinant expression plasmid, pET3a::C+SR

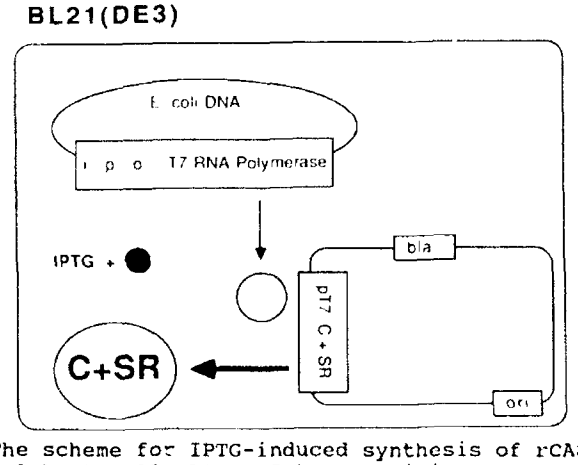

Fig. 3. The scheme for IPTG-induced synthesis of rCAS in the bacterial host cell, BL21(DE3), containing pET3a::C+SR.

The successful application of this scheme is illustrated in Fig. 4. While IPTG induction leads to an apparent decrease in the amount of protein synthesized per cell, induced and non-induced BL21(DE3) cells containing pET3a display a similar spectrum of proteins. In contrast, IPTG-induced cells containing pET3a::C+SR produce a single, prominent protein, rCAS.

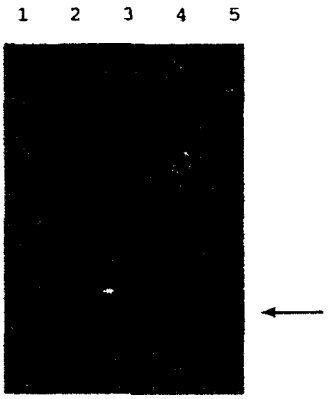

Fig. 4. Electrophoretic comparison of proteins in whole-cell lysates of IPTG-induced (lanes 3 and 5) and uninduced (lanes 2 and 4) bacterial cells containing pET3a (lanes 2 and 3) or pET3a::C+SR (lanes 4 and 5). Lane 1 contains molecular weight standards. The arrow indicates the position of inducible rCAS.

PRESENCE OF DISULFIDE BONDS

During the characterization and purification of rCAS, we discovered that its electrophoretic mobility on sodium dodecyl sulfate-polyacrylamide gels was altered if the protein was first treated with reducing agents such as ß-mercaptoethanol or dithiothreitol. This implied that at least some of the four cysteine residues in the C region may be involved in formation of one or more disulfide bonds. Quantitative Ellman assays [7] indicated that native rCAS contained less than 1 mole of sulfhydryl per mole of protein. However, upon treatment with reducing agents, we measured about 3 moles of sulfhydryl per mole of rCAS.

To better quantitate cysteine sulfhydryls, laser desorption mass spectrometry was performed on rCAS that was denatured and alkylated with iodoacetamide with and without reduction. The mass of reduced rCAS was 227 daltons greater than native rCAS, a value consistent with the reduction-dependent addition of four carboxyamidomethyl groups.

Direct evidence for cystine (two cysteines joined by a disulfide bond) was obtained by amino acid analysis of denatured, alkylated rCAS with and without reduction. In the absence of reduction, rCAS contained a cystine peak with no evidence of any carboxymethyl-cysteine. Treatment with reducing agents abolished the cystine peak and yielded four carboxymethyl-cysteines per mole of rCAS.

From these data we conclude that purified rCAS contains two disulfide bonds which, upon denaturation and reduction, can be converted to four cysteine residues.

FOLDING OF CORE REPEATS IN spIa

rCAS apparently contains the information required to fold, bringing pairs of cysteines within the minimum distance required for disulfide bond formation. We are currently trying to map the paired cysteines that form these disulfide bonds to determine whether or not they are homogeneous. Such information will be useful for locating the ß-turns that were predicted from our spectroscopic data obtained using synthetic peptides [3].

It has been proposed that conserved cysteine residues in the C domains participate in forming intermolecular disulfide bonds that covalently cross-link spI complexes and decrease their solubility [8]. The presence of intramolecular disulfide bonds in rCAS suggests another possible role for these cysteines. Perhaps the maintenance of spI solubility within the cell and initial prevention of the formation of insoluble spI complexes is accomplished by folding and formation of intramolecular disulfide bonds similar to those found in rCAS. The expression of recombinant proteins with multiple tandem copies of rCAS will enable us to test this hypothesis.

PERSPECTIVE

Our results raise two items of interest for this symposium. First, in terms of understanding the cellular processing of a biological material (C. tentans silk), in vivo formation of spI intramolecular disulfide bonds would require an oxidizing environment. Oxidized glutathione in the endoplasmic reticulum may already provide the necessary redox state during protein synthesis and secretion [9]. As of yet, there is no candidate for an agent in the processing pathway that would promote shuffling of disulfide bonds from intraprotein to protein-protein interactions. Secondly, rCAS derivatives may provide useful biomolecular materials, serving as vehicles for protein "sites" that could be buried or exposed in response to the redox state of the solvent.

ACKNOWLEDGEMENTS

This research was supported by grant DAAL03-91-G-0239 from the U.S. Army Research Office. We thank Rosemary T. Hoffman for reading this manuscript.

REFERENCES

1. S.T. Case and L. Wieslander, in Results and Problems in Cell Differentiation, edited by S.T. Case (Springer-Verlag, Berlin Heidelberg, 1992) p. 187.

2. S.E. Wellman and S.T. Case, J. Biol. Chem. **264**, 10878 (1989).

3. S.E. Wellman, S.J. Hamodrakas, E.I. Kamitsos and S.T. Case, Biochim. Biophys. Acta **1121**, 279 (1992).

4. D.A. Tirrell, M.J. Fournier, and T.L. Mason, Mater. Res. Bull. **16** (7), 23 (1991).

5. K.B. Mullis and F.A. Faloona, Methods Enzymol. **155**, 335 (1987).

6. F.W. Studier, A.H. Rosenberg, J.D. Dunn and J.W. *Dubendorff*, *Methods Enzymol.* **185**, 60 (1990).

7. G.L. Ellman, Arch. Biochem. Biophys. **82**, 70 (1959).

8. S.J. Hamodrakas and F.C. Kafatos, J. Mol. Evol. **20**, 296 (1984).

9. C. Hwang, A.J. Sinskey, and H.F. Lodish, Science **257**, 1496 (1992).

CLONING AND EXPRESSION OF A SYNTHETIC *MUSSEL ADHESIVE PROTEIN IN ESCHERICHIA COLI*

ANTHONY J. SALERNO AND INA GOLDBERG
Allied-Signal Inc., 101 Columbia Road, Morristown, NJ 07962.

ABSTRACT

Repetitious gene cassettes that encode the consensus decapeptide repeat of *Mytilus edulis* bioadhesive protein were cloned and expressed in *Escherichia coli*. The bioadhesive precursor (BP, M_r=25,000) was expressed from one 600-bp gene comprised of a 30-bp unit repeat. The repetitious gene appeared stable in a T7-based host/vector system.

Using the T7 expression system for induction, BP was produced at levels approaching 60% of total cell protein. BP was found both in intracellular inclusions and in the soluble fraction. Interestingly, methionine was processed from the N-terminus of the purified protein to give an authentic consensus precursor protein.

INTRODUCTION

The marine mussel *Mytilus edulis* anchors itself to the environment by means of a byssus, which is composed of threads that extend from the ventral base of its foot and end in an attachment plaque at the substrate surface [1]. Several proteins are found in the plaque including collagen, catechol oxidase and a bioadhesive polyphenolic protein [2]. Most of the bioadhesive protein is comprised of about 75 repeats of the decapeptide sequence Ala-Lys-Pro-Ser-Tyr-Hyp-Hyp-Thr-Dopa-Lys [3]. To obtain the adhesive and cohesive properties of bioadhesive protein, enzymatic processing of tyrosine to dihydroxyphenylalanine (dopa) and orthoquinone is essential [4]. Its impressive properties as a water-compatible adhesive have stimulated interest into its use in dental and medical applications, a coating for cell attachment to tissue culture surfaces and industrial applications such as coatings and underwater adhesives. One requirement for these applications is an economical, large-scale supply of bioadhesive proteins. A recent report aiming towards this goal was the isolation of a partial cDNA clone encoding *M. edulis* bioadhesive protein and its expression in yeast to give a BP lacking the post-translational hydroxylations [5].

In this work, we describe a different approach based on the construction and expression at high yields in *E. coli* of synthetic genes encoding BP that is based on the consensus decapeptide repeat of the native protein.

MATERIALS AND METHODS

Bacterial Strains and Plasmids

E. coli strain AG1 was used for the construction of pET derivatives. The *Δ(srlR-recA)306::Tn10* allele was transferred into BL21[DE3](pLysS) by P1 transduction to give AS002.

General Methods

DNA manipulation, transformation of *E. coli*, colony hybridization, sequencing and protein determination were all done using standard procedures

[6]. Stability of polydecapeptide glue analog gene (*gag*) cassettes was assessed by restricting the purified plasmid (10 μg) with *Sty*I and electrophoresis on 5% polyacrylamide gels to size the population of gag cassettes. Coupled *in vitro* transcription-translation reactions were done using a commercial kit (Amersham) according to the manufacturer's directions.

Construction of *gag*

The method of constructing the 30-bp repeat unit *gag* cassette was disclosed previously [7]. Briefly, internal oligos:

5'-CCAACCTACAAAGCTAACCCGTCTTATCCG3'-
3'-TTTCGATTCGGCACAATAGGCGGTTGGATG-5';

and external oligos:

5'-CCAACCTACAAAGCCAAGGCTTCTTATCCG-3'
3'-TTTCGGTTCCGAAGAATAGGCGGTTGGATG-5';
*Sty*I

were heated and allowed to anneal to form short duplex DNA. The double-stranded sequences were then combined in a 20 to 1 molar ratio and allowed to anneal by further cooling to form long duplex DNA. The DNA mixture was ligated, restricted with *Sty*I, and fractionated by size-exclusion chromatography. Fractions containing oligomers >210 bp were pooled for cloning.

The 600-bp *gag* comprised of 30-bp repeat units was moved as an *Nde*I+*Bam*HI DNA fragment into pET3a.

The 125-bp diversified *gag* cassette was constructed by mutually primed extension of oligonucleotides

5'-GAGTTGACCTACGTAATGCAGCCAAGGCCAGCTATCCCCCAACGTATAAGGCTAAACCGAGTTACCCTCCCAC
ATACAAAGCAAAACCATC-3' and
5'-GTTTGATGACCTCAACGTACCTTGGCCTTGTAAGTCGGTGGGTATGAGGGCTTCGCTTTATAGGTAGGCGGAT
ACGATGGTTTTGCTTTG-3'

using T7 DNA polymerase. Tandem 125-bp *gag* cassettes were prepared by digestion with *Sty*I, recovering the vector and *gag* cassette, and ligating the *gag* cassettes to form multimers.

Expression and Detection of BP

Induction of strains containing T7-based expression systems was as described previously [8]. Culture samples were pelleted by centrifugation and resuspended in 0.1 volume of solution A [50 mM TRIS HCL, 2% β-mercaptoethanol, 0.5% cetyl trimethyl ammonium bromide (CTAB)]. Samples were freeze/thawed and sonicated prior to analysis. For fractionation of AS002(pAG9) cells to detect the presence of inclusion bodies, a culture was pelleted after 2 h of induction and resuspended in 0.1 volumes of solution B (40 mM TRIS, pH 8.0, 50 mM sodium chloride, 1 mM EDTA, 1% β-mercaptoethanol). Samples were then freeze/thawed and insoluble material pelleted. After suspending the pellet in an equal volume of buffer, the equivalent of 0.1 OD_{600} units of the original culture was used for gel analysis.

Samples were analyzed for BP content on a gel adapted for basic proteins [9]. The protocol was modified to include CTAB in the buffer at a concentration of 0.05%. Riboflavin was used for gel polymerization. Samples were loaded after adding an equal volume of sample buffer (2X: 5 M urea, 0.8 M acetic acid, 2% β-mercaptoethanol, 1% CTAB, 50 mM Tris-HCl, 0.5 mg/ml methyl green) and heating to 50°C for 4 min. Gels were stained with fast green to detect proteins and BP was quantitated by scanning densitometry.

Purification of BP

One liter shake-flask cultures of AS002(pAG9) were harvested and resuspended in 0.1 volume of solution A followed by freeze/thawing and sonication to give a homogeneous suspension. Alternatively, in some experiments the pellet was suspended in solution B and then subjected to three freeze-thaw cycles followed by three cycles of sonication. Both procedures give good yields. CTAB was added to 0.5% (for lysates of solution B only) followed by urea to 2.5 M and acetic acid to 0.8 M. The solution was incubated for 0.5 h with occasional mixing to extract BP and then centrifuged. To the supernatant was added an equal volume of 0.8 M acetic acid. BP was purified over a 2.5x7 cm cellex-P column. Fractions were concentrated and dialyzed against 0.3 M ammonium acetate, pH 4.3. For structural studies, BP was further purified by size-exclusion chromatography. BP was quantitated spectrophotometrically by tyrosine content at 276 nm and using a molar absorbtivity of 1400 M^{-1} cm^{-1}.

Physical Analyses of BP

The N-terminal amino acid sequence of BP was determined by sequential Edman degradation using an automated protein sequencer (470; Applied Biosystems, Foster City, CA). Amino acid composition was performed by the post-column o-phthaldialdehyde method [10] except for phenthiocarbamoyl derivatization of proline, which was normalized with respect to alanine.

RESULTS AND DISCUSSION

Design and Cloning of *gag*

The decapeptide consensus repeat from the *M. edulis* bioadhesive protein was used as a basis for design of repetitious genes enabling the production of a polydecapeptide analog precursor protein [3]. Two gene cassettes with repeat unit lengths of 30- and 120-bp were designed in order to compare production levels and gene stability. The 30-bp repeat was comprised of codons optimized for *E. coli* expression. The 120-bp repeat represents the maximum length of unique sequence DNA that can be designed without the introduction of nested repeat sites. It was necessary to incorporate a number of non-optimal codons to achieve this level of sequence diversity. Two T7 expression vectors carrying 600 bp gene cassettes, pAG9 (30-bp repeat) and pAG16 (120-bp repeat), were chosen for detailed expression and gene stability studies.

Expression of BP

Production of BP was examined using the T7 expression system. Initial gel analysis of *in vitro* coupled transcription-translation reactions containing pAG9 showed a unique protein band compared to the vector control that was consistent with the predicted size. *In vivo* strain AS002(pAG9) synthesized BP at the highest rates and was selected for further analysis (Fig. 1A, lane 1). Fig. 1B shows the time course of accumulation of BP. Strain AS002(pAG9) accumulates BP to levels of up to 60% of total cell protein. Levels of up to 5% of total cell protein have been reported for expression of a partial cDNA clone of *M. edulis* BP protein in yeast [5].

Interestingly, BP accumulation in strain AS002(pAG16) was similar to that observed for AS002(pAG9). This result indicates that the less-than-optimal codon usage in the diversified *gag* (pAG16) did not lead to any decrease in the yield of BP. Since the promoter and Shine-and-Delgarno sequence are identical on both plasmids, the level of gene expression must be predominantly controlled by these two regulatory regions.

A

B

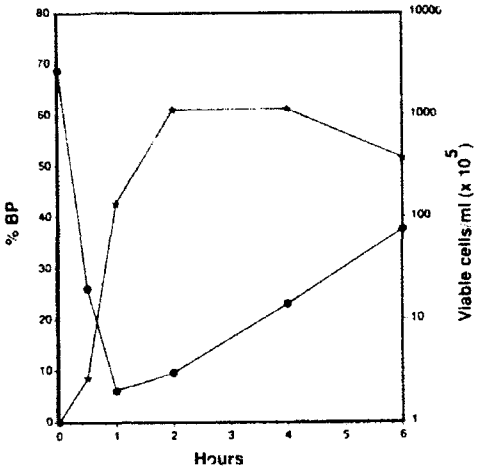

Fig. 1. Expression of BP. A Accumulation of BP in strain AS002(pAG9) (lane 1), 2 h following induction. Lane 2 is purified BP. B Time course of accumulation of BP in strain AS002(pAG9).

Purification of BP

To develop an appropriate purification procedure for BP, induced cultures of AS002(pAG9) were harvested, lysed, separated into soluble and insoluble fractions and analyzed for the distribution of BP. The majority of BP was present in the insoluble fraction, which indicates that BP forms intracellular inclusions (Fig. 2A, lanes 3 and 4). However, about 33% of BP was present in the supernatant (Fig. 2A, lanes 5 and 6).

Since a significant proportion of BP is soluble in the crude lysate prepared from the culture, a purification strategy based on selective extraction of BP was developed. BP is solubilized in a solution containing 2.5 M urea, 0.8 M acetic acid and 0.5 CTAB. Separation of the insoluble material results in supernatant that is up to 90% pure with respect to total protein (Fig. 2B, lane 3). BP can be further purified by cation-exchange chromatography to give 93-95% purity (Fig. 2B, lane 4). Full-length BP was released from the cellex-P column when the gradient composition reached 2.4 M urea, 0.6 M potassium acetate, pH 5.0. For physical characterization, BP was further purified by size-exclusion chromatography to yield full-length protein of greater than 99% purity (Fig. 2B, lane 5).

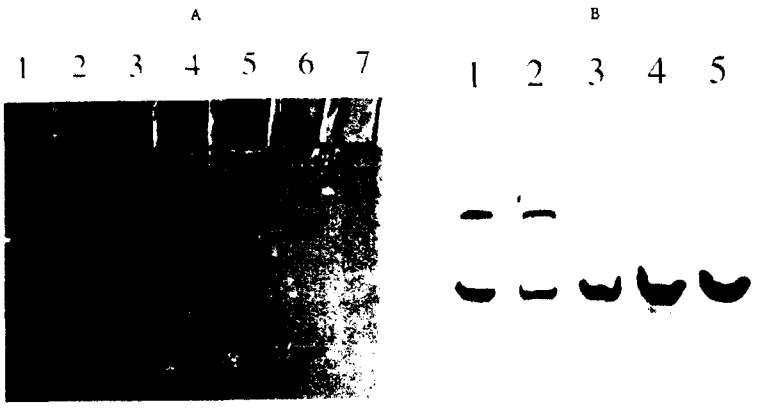

Fig. 2. A Cellular disposition of BP. Separation of crude lysate (lanes 1 and 2) prepared from AS002(pAG9) into insoluble (lanes 3 and 4) and soluble (lanes 5 and 6) fractions. Lane 7 is the crude lysate of AS002(pET-3a) cells. B Purification of BP. Lane 1, crude lysate; lane 2, insoluble material following BP extraction; lane 3, extracted BP; lane 4, after chromatography on cellex-P; lane 5, after P-60 gel chromatography.

Characterization of BP

Purified BP was shown to be authentic by amino acid composition and sequencing analyses. The experimentally obtained amino acid composition agrees well with the predicted composition based on the polydecapeptide gene cassette. Interestingly, no methionine was detected which suggested the N-terminal Met was removed. Sequencing of BP provided further evidence for Met processing. The N-terminal sequence was determined for 24 residues into the protein. The sequences agreed perfectly starting with the Ala following the Met residue. The initial sequencing yield based on amino acid analysis was greater than 80%. Therefore, we suggest that methionine aminopeptidase removes the methionine from BP to generate a protein lacking any amino acids not normally found in the consensus decapeptide. The aggregation of nascent BP into inclusions does not seem to interfere with this process.

Genetic Stability of *gag* Cassettes

It is well established that repetitious DNA is subject to considerable length polymorphism [11]. The tandem DNA of repetitious genes cloned in *E. coli* is also subject to analogous fluidity that is manifested as deletion of repeat units [12]. The *gag* cassettes described here are no exception. BP was used as a model to investigate whether this problem could be alleviated by diversifying codon usage and thus increasing the unit repeat size. The rationale for this approach is the empirical observation that unique DNA undergoes deletion events relatively infrequently compared to repetitious DNA.

Surprisingly, no detectable deletions were observed for the AS002(pET3a) host-vector pairs. Thus, the $gag600._{55}$ and $gag600._{122}$ repeat unit cassettes showed similar low levels of deletion. The T7 host/vector system appears to be a promising candidate for scale-up experiments. Since $gag600._{32}$ did not show higher deletion levels, codon diversification is of little value in stabilizing *gag*.

CONCLUSIONS

The T7 expression system is extraordinarily efficient at producing repetitive proteins. In *E. coli*, we demonstrated that a bioadhesive precursor expressed from a highly repetitive gene can accumulate at levels of up to 60% of total cell protein. Similar yields were achieved when BP was expressed from a diversified cassette using less-than-optimal codons. The level of gene expression must therefore be predominantly controlled by the promoter and/or Shine-and-Delgarno sequence.

BP was shown to be present in the insoluble cell fraction as well as in the supernatant. Purified BP was shown to be authentic based on amino acid analysis and protein sequencing. Interestingly, the N-terminal Met was removed from the purified protein.

The repetitive cassette containing a 30-bp repeat was shown to be highly stable in a pET-derived vector system. The T7 expression system therefore appears to be a good choice for the maintenance and over-expression of highly repetitive genes.

ACKNOWLEDGEMENTS

The authors would like to thank P. Allenza, M. Berenbaum, J. Williams and D. Masilamani for their interest and support of this project. D. Piasčik and M. Kuroiwa are acknowledged for technical assistance and Henry Lackland for performing the amino acid analysis and protein sequencing. We are grateful to Marylou Grumka for typing the manuscript. This work was funded in part by contract #N00014-89-C-0293 from the Office of Naval Research.

REFERENCES

1. J. H. Waite, Biol. Rev. **58**, 209 (1983).
2. J. H. Waite, Comp. Biochem. Physiol. **97B**, 19 (1990).
3. J. H. Waite, J. Biol. Chem. **258**, 2911 (1983).
4. J. H. Waite, CHEMTECH 17, 692 (1987).
5. D. R. Filpula, S. M. Lee, R. P. Link, S. L. Strausberg, and R. L. Strausberg, Biotechnol. Prog. **6**, 171 (1990).
6. F. M. Ausubel, R. Brent, R. E. Kingston, D. D. Moore, J. J. Seidman, J. A. Smith, and K. Struhl, Current Protocols in Molecular Biology (Greene Publishing Associates, New York, 1987).
7. Jon I. Williams, A. J. Salerno, I. Goldberg, and W. T. McAllister, U. S. Patent No. 5089406 (11 February 1992).
8. F. W. Studier, A. H. Rosenberg, J. J. Dunn, and J. W. Dubendorff, Meth. Enzymol. **185**, 60 (1990).
9. S. Panyim and R. Chalkey, Arch. Biochem. Biophys. **130**, 337 (1969).
10. N. M. Meltzer, G. I. Tous, S. Gruber, and S. Stein, Anal. Biochem. **160**, 356 (1987).
11. P. G. Debenham, TIBTECH, **10**, 96 (1992).
12. I. Goldberg and A. J. Salerno in Materials Synthesis Utilizing Biological Processes, edited by P. C. Rieke, P. D. Calvert, and M. Alper (Mater. Res. Soc. Proc. **174**, Pittsburgh, PA, 1990) pp. 229-236.

PART III

Non-Cellular Synthesis

BIOMIMETIC PROCESS FOR PREPARING MAGNETITE FIBERS

CARL W. LAWTON AND CHRISTOPHER S. SHIELDS
Department of Chemical and Nuclear Engineering, University of Massachusetts Lowell, Lowell, MA 01854

ABSTRACT

Two different biomimetic strategies were utilized in the formation of magnetite fibers. The first strategy utilized natural (*Sphaerotilus natans* sheaths) or synthetic (hollow fibers) matrices for magnetite formation. The second strategy made use of an iron-hydroxide intermediate that was subsequently chemically converted to magnetite within the biomimetic matrix. The formation of magnetite was determined by both visual and x-ray diffraction analysis. This process has advantages over conventional routes because of the expense and handling problems associated with the production of ceramic whiskers and fibers. The magnetite formed by this process may prove to have unique properties due to its unusual fiber structure.

INTRODUCTION

There is a great deal of interest in microwave absorbing materials. Advanced composites that combine the properties of different materials are needed for this application. A composite that incorporates a low resistivity ferrite within a high dielectric, high capacitance material is effective at microwave absorption. The resistivity of magnetite is very low, 4×10^{-3} ohm-cm, compared to other ferrites. [1] This feature is detrimental for most magnetic applications but is an advantage for this application. Utilizing fibers within the dielectric matrix instead of particulate material should significantly improve the performance of a microwave absorption device. The improvement in properties is achieved because the probability of an incoming wave contacting a fiber is much greater than contacting a particle. The more random the configuration and the larger the fiber's aspect ratio, the greater the probability becomes. Therefore, a random configuration of high aspect ratio magnetite fibers dispersed in a suitable dielectric material should produce devices that can be utilized in many microwave applications. Because of the expense of current processing routes and the inherent problems associated with handling whiskers a synthetic route that mimics the biological production of magnetite would prove to be extremely useful.

A biomimetic process mimics the biological pathways used by organisms in their production of materials. Biomineralization holds the potential for developing advanced material properties in ceramics by controlling crystal structure and the orientation of crystal growth. Oriented crystal growth is important because many electrical and optical properties are highly anisotropic. We have tried to utilize biomimetic synthesis techniques to produce magnetite fibers within a polymeric matrix. We have utilized three different types of matrices each utilizing ferrous hydroxide as a precursor to magnetite.

Microwave Absorption

The microwave region of the electromagnetic spectrum spans the frequency range between 300 MHz and 300 GHz (wavelengths 1 m to 1mm). Electromagnetic waves consist of electric

and magnetic field components. [2] The interaction of these waves with different materials produces varied results. These interactions can be utilized in designing advanced materials with specialized properties for a variety of microwave applications. Microwave heating within a material is the result of an interaction between the electromagnetic force fields and the molecular and electronic structure of the material. The microwave power absorbed which leads to heating is described by:

$$P_{abs} = \int v\, \sigma\, |E|^2\, dv$$

where E is the electric field, v is the voltage and σ is the ionic conductance and dipole orientation losses at commercial power source frequencies.

Eddy current losses, P_e, increase in ferrites as the AC frequency of exposure increases. This relationship is given by:

$$P_e = (\text{constant})\ B_m^2\ f^2\ d^2\ /\ \rho$$

where:
(constant) = geometry dependent factor
B_m = maximum induction (gauss)
f = frequency (Hz)
d = smallest dimension transverse to flux
ρ = resistivity [1]

Microwaves adhere to boundary conditions. Boundary conditions are typically interfaces within a ceramic material. Electric fields parallel to the material interface are continuous (figure 1) and a partial reflection of the wave modifies the power flow at the interface. The absorbed power is proportional to the dielectric loss factor of the material multiplied by the square of the electric field magnitude. When the electric field is perpendicular to the material interface, (figure 2) the amount of absorbed power is dependent upon the difference in dielectric constant of the two media. It is important to recognize the sensitivity of the electromagnetic radiation to the polarization of the incoming wave. [1]

At microwave frequencies, polarization in ferroelectric materials typically results from ionic and electronic contributions. Space charge and dipolar polarizibility will not have an effect. To maintain a high capacitance at these frequencies a material with a high dielectric constant is needed. High dielectric constant materials exhibit resistivities on the order of 10^{12}-10^{15} ohm-cm. [3] By combining a low resistivity, microwave absorbing ferrite, such as magnetite, in a high dielectric constant material with a high capacitance, a composite that absorbs microwave energy can be produced.

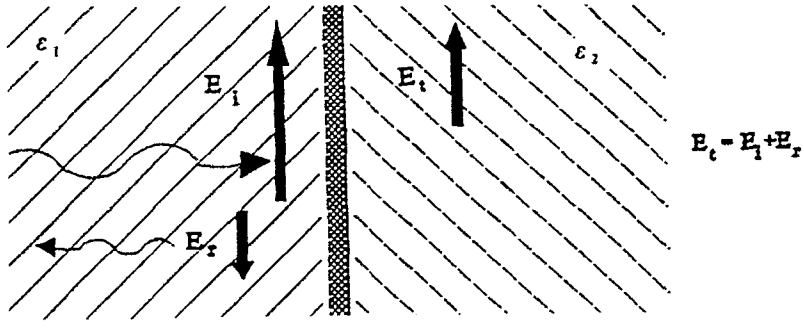

Figure 1 Electric fields parallel to the material interface.

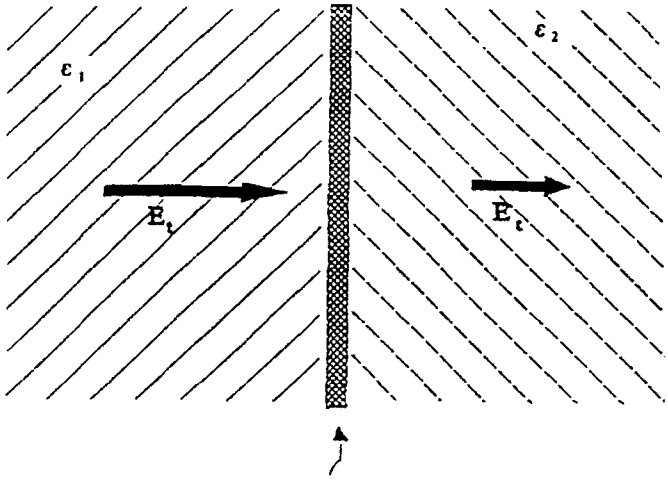

Figure 2 Electric fields perpendicular to the material interface.

Biomineralization

Experimental and theoretical work during the last decade has demonstrated that general principles apply to most biomineralization systems. Crystal growth can be controlled by utilizing polymer matrices or vesicle compartmentallization.

Biological Magnetite Formation

Magnetite can be formed biologically by two different mechanisms: (1) single magnetic domain crystals by *Aquaspirillum magnetotacticum* and (2) heterogeneous particles by iron reducing bacteria.

> (1) *A. magnetotacticum* - A ferric oxy-hydroxide precursor is accumulated intracellularly in membrane vesicles in an amorphous state. [4] Ferrous ions produced by the bacterium react to form crystalline magnetite.
>
> (2) Iron-reducing bacteria - These bacteria reduce ferric ions from iron hydroxides in the environment. The reduced iron (ferrous iron) is exported to the outside of the cell where it reacts with the ferric oxy-hydroxides to form magnetite. [5]

MATERIALS and METHODS

Magnetite fibers were produced using two different biomimetic strategies. The first strategy makes use of natural (*Sphaerotilus natans* sheaths) or synthetic (hollow fibers) matrices for fiber formation. The second strategy makes use of an iron-hydroxide intermediate that is chemically converted to magnetite within the biomimetic matrix. The use of these two strategies allow for versatile processing of a wide range of magnetite/fiber composites.

Strategy #1

***Sphaerotilus natans* sheath formation**

Sphaerotilus natans is one of several species of bacteria that form an extracellular sheath that the bacteria grow in. The sheath is composed of protein polysaccarides and lipids that resemble a pipe in geometry. The dimensions are approximately 1 μm in diameter by 50 μm in length. Wall thickness is on the order of 0.1 μm.

Sphaerotilus natans ATCC 15291 was grown in a standing culture on complex media (g/l: peptone 5, yeast extract 1, glycerol 10, pH 7.0) and was allowed to form a surface film. The *S. natans* film (sheath complex) was washed twice with 0.9% NaCl and subsequently used for magnetite formation.

Synthetic hollow fiber infiltration

This method involves the infiltration of synthetic hollow fibers and subsequent chemical conversion to magnetite. Two different microtubular fibers were used as our polymeric matrices. The fiber in figures 3 and 4 is a porous, ultrafiltration fiber used in biological separation and has an inside diameter of approximately 100 μm. The fibers in figures 5 and 6 are non-porous carpet fibers with an inside diameter of approximately 10 μm.

Figure 3 Optical micrograph of the porous wall structure of an ultrafiltration fiber.

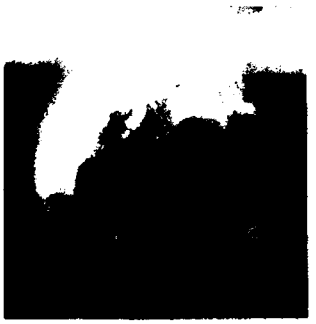

Figure 4 Optical micrograph revealing the cross section of an ultrafiltration fiber.

Figure 5 Optical micrograph of a non-porous carpet fiber.

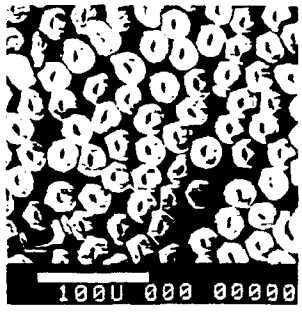

Figure 6 Scanning electron micrograph revealing the cross section of carpet fibers.

The infiltration of the porous, ultrafiltration fibers in figures 3 and 4 was accomplished by pumping the desired solution through the inside channels of the fibers. The non-porous, carpet fibers in figures 5 and 6 were infiltrated by capillary action. This was achieved by inserting a fiber bundle into the desired solution. In the case where the infiltrating solution wets the fiber channels, it will be drawn up by capillary action. The equation for capillarity is :

$$2 \Pi r \gamma \cos \Theta = \Pi r^2 h \rho g$$

where:
- r = radius of capillary
- γ = surface tension
- Θ = contact angle
- h = height of solution in capillary
- ρ = solution density
- g = acceleration due to gravity

Strategy #2

Magnetite Formation

A modification of Krones [6] chemical procedure for magnetite formation was used on all polymeric matrices. Magnetite can be chemically synthesized by reacting an aqueous solution of ferrous sulfate with sodium hydroxide or ammonium hydroxide producing ferrous hydroxide. The ferrous hydroxide that is formed is a whitish-grey fine precipitate. Ferrous hydroxide can be oxidized to magnetite with sodium nitrate at 70-90 °C. The magnetite produced is a black powder. Sodium nitrate is used because its oxidizing potential is insufficient to form haemetite from ferrous hydroxide. The procedure for magnetite formation is as follows:

$$FeSO_4 + 2NaOH \rightarrow Fe(OH)_2 + Na_2SO_4$$

$$3Fe(OH)_2 + \tfrac{1}{2}O_2 \xrightarrow{NaNO_3} Fe_3O_4 + 3H_2O$$

Sphaerotilus natans

Ferrous sulfate (0.01 - 1.0%) was dissolved in distilled water deoxygenated with bubbling argon at room temperature. *S. natans* sheaths were added to the ferrous sulfate solutions and incubated at room temperature for 1 hour. Ferrous hydroxide was then formed by the addition of ammonium hydroxide. Sodium nitrate (0.1 - 1.0%) was then added, the reaction mixture sealed, and incubated at 70 °C for 2 hours to induce magnetite formation.

Synthetic hollow fibers

Ferrous sulfate was dissolved in distilled water deoxygenated with bubbling argon at room temperature. The fibers were infiltrated with the ferrous sulfate solution by the methods described above. Ferrous hydroxide was formed by placing the fiber bundle in a solution of ammonium hydroxide. The fibers were removed and placed in a solution of sodium nitrate, the reaction mixture sealed, and incubated at 70 °C for 2 hours to induce magnetite formation.

RESULTS and DISCUSSION

S. natans Iron/Sheath Composite

Utilization of *S. natans* sheath complex for magnetite formation yielded composites that were macroscopically dark brown. Microscopic examination reveals that the color formation is due to uniform coating of the sheaths and not due to particulate formation. Untreated sheaths are white. The untreated sheath complex (figure 7a) resembles the treated sheath complex (figure 7b) in respect to uniformity of diameter and composition. Work, currently in progress, is directed at the generation of sufficient material necessary for x-ray diffraction and crystal morphology data that will be published in a complete characterization study.

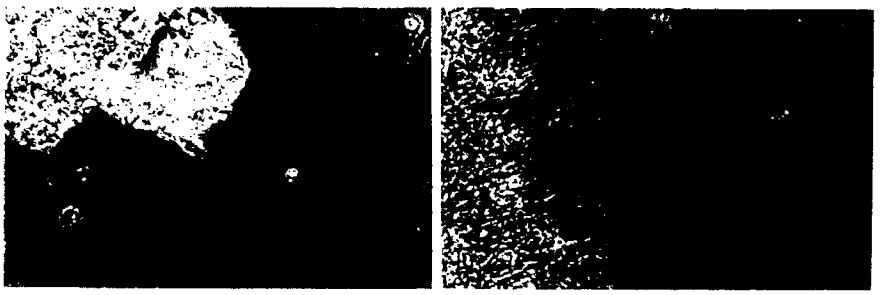

(a) (b)

Figure 7 Optical micrograph of untreated sheath complex (a) and treated sheath complex (b).

Synthetic Iron Fiber Composites

The utilization of synthetic fibers for magnetite formation yielded composites that were macroscopically dark brown. Untreated fibers were white. Microscopic examination of the synthetic fibers reveals that the color formation is due to a uniform coating of the sheaths and not to particulate formation. Close examination of the cross section of the larger diameter fibers shows that the concentration of magnetite or dark color is highest on the inside wall but is present throughout the fiber wall. Figure 8 is an x ray diffraction analysis pattern of the larger synthetic fibers compared with magnetite powder produced by the same method without a fiber matrix. The two patterns have identical peaks. The x ray patterns clearly show peaks for Fe_3O_4, Na_2SO_4 and NH_4NO_3. Washing removes the Na_2SO_4 and NH_4NO_3 leaving peaks of magnetite *and* FeOOH (figure 9). The ferric oxy hydroxide formed from unreacted ferrous hydroxide.

Work, currently in progress is directed at optimizing the conversion of FeOOH to Fe_3O_4 and producing larger quantities of the smaller magnetite fiber composite material for x ray diffraction analysis. The results will be published with the *S. natans* iron sheath composite characterization data.

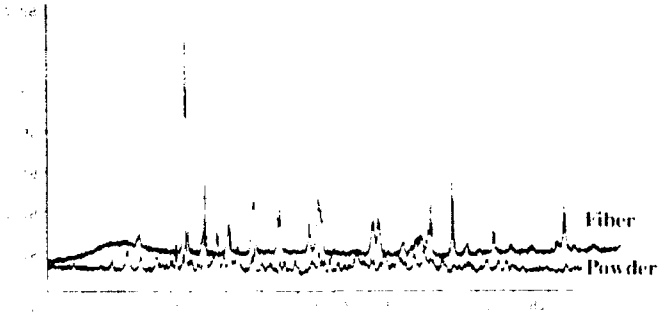

Figure 8 X-ray diffraction patterns of magnetite formed within the ultrafiltration fiber (Top pattern) and magnetite powder formed without a fiber matrix. (Bottom pattern) Patterns were produced by a Vax 3100 computer driven Phillips APD 1700 x-ray diffraction system using Cu radiation and graphite monochromation.

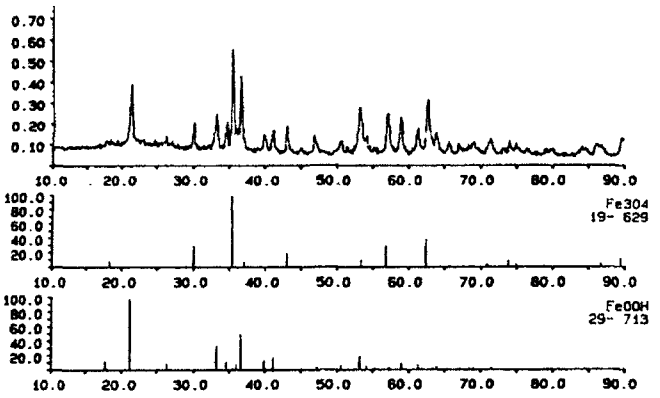

Figure 9 X-ray diffraction pattern of washed sample revealing magnetite and ferric oxy-hydroxide peaks. Patterns were produced by a Vax 3100 computer driven Phillips APD 1700 x-ray diffraction system using Cu radiation and graphite monochromation.

CONCLUSIONS

Our preliminary study of the formation of magnetite fibers successfully produced three different size composite materials by utilizing two different biomimetic strategies. The first strategy utilized natural (*Sphaerotilus natans* sheaths) or synthetic (hollow fibers) matrices for magnetite formation. The second strategy made use of an iron-hydroxide intermediate that was subsequently converted to magnetite within a biomimetic matrix. Microscopic examination of the fibers revealed a dark brown uniform coating with no macroscopic particulate formation. The magnetite structure formed on the porous ultrafiltration fibers was confirmed by x-ray diffraction analysis. Future work will confirm the visual analysis of the two smaller fiber composite materials and optimize the conversion of FeOOH to magnetite.

REFERENCES

1. Goldman, Alex, Modern Ferrite Technology, Van Nostrand Reinhold, New York, NY (1990).

2. Bruce, R.W., New Frontiers in the use of Microwave Energy: Power and Meteorology, MRS Symp. Proc., 124:3 (1988).

3. Kingery, W.D., et al., Introduction to Ceramics, 2nd Edition, John Wiley & Sons, New York, NY (1976).

4. Mann, S., et al., Biomineralization: New Routes to Crystal Engineering, MRS Symp. Proc., 174:25 (1990).

5. Atkinson, R.J. et al., Inorg Chem., 30:2371 (1968).

6. Bate, G., Magnetic Oxides, edited by D.J. Craik (John Wiley & Sons, New York, NY (1965).

ANGULAR-RESOLVED ESCA STUDIES OF CADMIUM ARACHIDATE MONOLAYERS ON Si (100): INELASTIC MEAN-FREE PATH AND DEPTH PROFILE ANALYSIS

SHELLI R. LETELLIER[1], VIOLA VOGEL[1], BUDDY D. RATNER[1,2] AND DEBORAH LEACH-SCAMPAVIA[2]
University of Washington, Center for Bioengineering[1] and Department of Chemical Engineering[2], Seattle, WA, 98195

ABSTRACT

Angular-resolved ESCA was used to study single cadmium arachidate monolayers transferred to Si (100) wafers by the Langmuir-Blodgett technique. We find the monolayers to be of high integrity with respect to those defects which enhance the escape probability of substrate photoelectrons through the overlayer. The inelastic mean-free pathlengths of Si (2p) and C (1s) electrons were calculated to be 49±6 Å and 45±6 Å for the kinetic energies of 1388 eV and 1202 eV, respectively. The overall ordering of the hydrocarbon chains is less than for alkane thiols assembled on noble metals. We find that the precision of the Tyler algorithm to deconvolute angular-resolved ESCA data into depth profiles is accurate within 10% for predicting the thickness of the hydrocarbon overlayer but less precise for intermediate layers.

INTRODUCTION

Whereas diverse surface analytical techniques, including x-ray diffraction, low energy electron diffraction (LEED), and near-edge x-ray adsorption fine structure technique (NEXAFS), probe the orientation and packing of surface adsorbates, additional information regarding the integrity of the surface film is often crucial especially for technical applications. Angular-resolved electron spectroscopy for chemical analysis (ESCA) has proven to be powerful in yielding such information. The attenuation of the characteristic photoelectrons exhibits a significant dependency on the take-off angle and thereby provides quantitative depth information on the outer surface region as well as information on its integrity.

Angular-resolved ESCA data will be presented on single cadmium arachidate (CdC20) monolayers transferred to the native oxide surface of Si(100) wafers with the following goals: (a) to establish how the inelastic mean-free pathlength and integrity of this LB-film compares to thiol self-assemblies on noble metals [1], and (b) to determine the accuracy of the Tyler algorithm [2], which deconvolutes angular-dependent ESCA data into depth profiles, by applying it to molecular-scale organic overlayers. This is currently one of the few algorithms that does not require a priori information regarding the depth composition; however, it is necessarily based on simplifying assumptions.

THEORY

The normalized intensity of the photoelectron flux from a given orbital, i, of an element, j, is approximated as [1]

$$I_{ij}(\theta) = \frac{A}{\lambda_{ij}} \int_0^{\infty} n_j(x) \exp(-x / \lambda_{ij} \cos\theta)\, dx \qquad (1)$$

where I_{ij} is the normalized signal intensity which is the absolute signal intensity corrected for differences in photoelectron cross-section, transmission function and sampling depth; $n_j(x)$ is the concentration depth profile; λ_{ij} is the inelastic mean-free pathlength; x is the depth from the

surface; θ is the take-off angle defined between the surface normal and the photoelectron trajectory; and A includes instrumental calibration factors. This is the fundamental equation that has been used for our data analysis as well as by Tyler for deriving the algorithm. The underlying assumptions are [3] that (a) the photoelectron attenuation follows a single exponential decay which implies that elastic scattering [4,5] is negligible, and hence the attenuation length equals the inelastic mean-free pathlength (IMFP: the average distance travelled by an electron between successive inelastic collisions), (b) the IMFP is a function of kinetic energy and independent of the take-off angle, (c) the IMFP for a given element is constant within the sampled depth, (d) the effects of surface roughness are negligible, and (e) X-ray diffraction is negligible.

EXPERIMENTAL

LB-film Preparation: Monolayers were prepared by spreading a solution of arachidic acid, $CH_3(CH_2)_{18}COOH$, (2 mM, Larodan Fine Chemicals, 99+%) dissolved in chloroform (Aldrich, 99.9% HPLC grade) on an aqueous subphase of ultrapure water (Barnstead, 18 MΩ-cm, organic content <10 ppb, pH 5.6) containing cadmium chloride (5 mM, Aldrich, 99.99+%). The monolayers were prepared in a small, vibrationally dampened Langmuir trough interfaced with a Mac IIci computer and Labview II software for completely automated feedback control. Surface pressure was measured as a function of surface area using a standard Wilhelmy plate. A single monolayer was transferred by compressing the cadmium arachidate film between two movable barriers to a surface pressure of 20 mN/m. The hydrophilic silicon wafer with its native oxide layer (100, Prime Grade from Silicon Quest) was withdrawn through the monolayer-covered air/water interface at a constant rate of 10 mm/min. Transfer ratios, calculated as the ratio of the change in surface area of the monolayer to the surface area of the substrate, were approximately one. The wafers were previously cleaned by soaking in Nochromix cleaning solution, rinsing with ultrapure water, soaking in sodium hydroxide (~0.05 N), and rinsing repeatedly with ultrapure water.

ESCA Analysis. Monolayer films were analyzed in a Surface Science Instruments Spectrometer (Model SSX-100) with a monochromatized AlK_α x-ray source (1486.6 eV), and a spot diameter of 1000 μm. Photoelectrons were collected using a pass energy of 150 eV and a 12° collection aperture. Absolute and normalized signal intensities, as well as relative compositions, were calculated from standard SSX-100 software.

Cadmium arachidate monolayers were analyzed based on the peak areas from the C(1s), O(1s), Si(2p) and Cd(3d) core level electrons obtained at five take-off angles relative to the surface normal: 80°, 68°, 55°, 39°, and 10°. The number of scans for each element was varied at each angle to obtain an adequate signal to noise ratio; thus, more detection time was spent at larger take-off angles. Total analysis time for one sample was approximately 3 hours. The transmission function of the instrument was assumed to be constant over the time period of analysis. Initial and final survey spectra showed only small differences in the atomic percentages; we therefore conclude that any x-ray induced damage to the monolayers is negligible.

RESULTS

Angular-resolved ESCA data are presented in Fig. 1 for five samples of a cadmium arachidate (CdC20) monolayer transferred to Si(100). The atomic percentage is given at five take-off angles for the elements Si (2p), C(1s), O(1s) and Cd(3d), with the kinetic energies of 1388 eV, 1202 eV, 955 eV, and 1082 eV, respectively. At the near-normal take-off angle of 10° the signal shows contributions from both the silicon substrate and the carbon overlayer. At

the glancing take-off angle of 80° the signal is dominated by carbon from the organic overlayer.

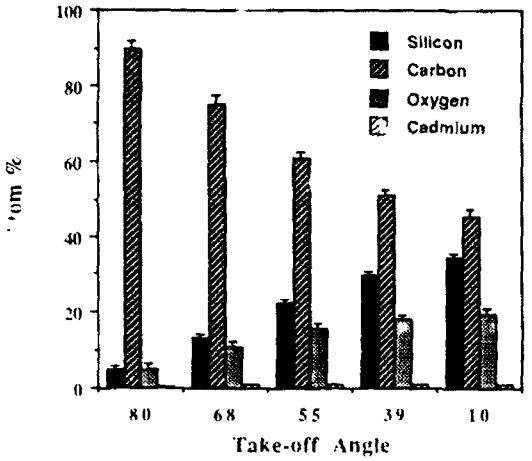

Figure 1. *Relative* elemental composition of CdC20 LB-monolayers on native oxide silicon (100) substrates as a function of the take-off angle. Error bars represent the variance from six spectra taken from five different samples.

The error bars represent the variance in elemental composition between six spectra taken from five samples. Four of the samples were prepared on the same day from different monolayers but were analyzed on consecutive days. Two spectra were taken from one sample at two separate locations on the sample with one week's time between analyses. No spectra were discarded due to low quality. The small variance between spectra is an indication of the *stability and high degree of integrity of the films and the reproducibility between samples* prepared and analyzed on different days.

DATA ANALYSIS AND DISCUSSION

Inelastic Mean-Free Pathlength

Two conceptually different approaches have been taken in the past to assess the inelastic mean free pathlength, λ, through organic overlayers: varying the overlayer thickness while maintaining a fixed take-off angle, and vice versa. Variation of the take-off angle is advantageous since the determination of the λ values does not depend on the use of reference samples.

The inelastic mean free pathlength for carbon (C(1s), 1202 eV) is obtained by integrating Eq. (1) over the thickness, d_{HC}, of the hydrocarbon layer of the CdC20-monolayer

$$I(C^{1s}) = A \cdot n \cdot \cos^{-1}\{1 - \exp(-d / \lambda_{C^{1s}} \cos\vartheta)\} \qquad (2)$$

The tilt angle of the hydrocarbon chains for cadmium arachidate on Si(111) is close to the surface normal [6,7] which gives a thickness of the hydrocarbon moiety of $d_{HC} = 25$ Å. A fit to Eq. (2) using the carbon intensities at each of the five take-off angles gives an average value of $\lambda_{C^{1s}} = 45 \pm 6$ Å.

The inelastic mean-free pathlength of Si(2p) electrons (1388 eV) from the substrate may be obtained by integrating Eq. (1) from d to ∞.

$$I_{Si}(\theta) = A\ n\ \cos\theta\ \exp(-d / \lambda_{Si} \cos\theta) \qquad (3)$$

where d is the thickness of the LB-film. This assumes that the Si density of the substrate is constant over the sampled thickness. Equation (3) is easily rearranged into the linear format of $\ln(I_{Si}(\theta)/\cos\theta) - \ln(A\ n) = (-d / \lambda_{Si})*(1/\cos\theta)$ such that a plot of $\ln(I_{Si}(\theta)/\cos\theta)$ vs. $(1/\cos\theta)$ yields λ_{Si} from the slope. Figure 2 displays the experimental results for the six individual LB-monolayer samples (lower six data sets). As reference for a homogeneous overlayer system we have included the signal intensity of elemental Si (99 eV) through an uncovered native oxide film (upper data set). Each data set has been fit by a linear least squares analysis of the first four take-off angles. A deviation at the glancing take-off angle of 80° is observed for both the LB-monolayer and the native oxide film; however, this is not unexpected since the impact of surface roughness is strongly enhanced at shallow take-off angles. The fact that all four of the other take-off angles can be fit well with a straight line suggests that λ_{Si} through the LB-monolayer is independent of θ (except at glancing angle) which is indicative of monolayers with high integrity. With regard to the existence of monolayer defects, ESCA is only sensitive to those which will enhance the escape probability of photoelectrons from the substrate through the overlayer. An average λ_{Si} value has been calculated from the data using a literature value for the layer thickness of cadmium aracnidate of $d_{CdC20} = 26.8$ Å [8].

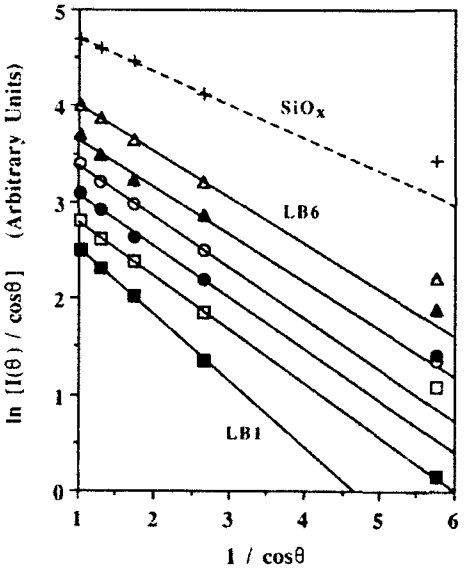

Figure 2. Analysis of the silicon inelastic mean-free pathlength. Straight lines represent least squares fits through all take-off angles except glancing angle. Data are offset vertically to avoid overlap. Six LB-monolayer samples are presented (solid lines) along with an uncovered native silicon oxide layer (dashed line). Samples five and six were analyzed from the same monolayer at two different spots with one week's time between analyses.

Table 1 summarizes our experimental λ-values in comparison to values calculated from empirical expressions: (a) The IMFP is shown to increase with the kinetic energy, E, of the electrons according to $\lambda = B\ E^{1/2}$, where the proportionality factor B can either be calculated on the basis of the material density, B_D, or can be approximated by the empirical values B_E = 0.087, 0.096, and 0.054, for organics, inorganics and gold, respectively [9]. Note that the assumption made in Eq. (1) of constant λ_{Si} throughout the sampling depth is approximately valid for organics on Si but not for organics on gold. (b) A second expression was derived by Laibinis, et al. [1], $\lambda_{SA} = 9.0 + 0.022 \cdot E$, as a best fit to their experimental data of self-assembled alkane thiol monolayers on Ag, Au, and Cu. Our experimental λ-values derived for C(1s) and Si(2p) electrons from a CdC20-monolayer on SiO are larger than those of Laibinis, et al. for thiol self-assemblies, λ_{SA}, as well as those derived for amorphous organics, λ_E [9].

However, our results agree, within experimental error, to the λ-values calculated on the basis of the monolayer density, λ_D.

Table 1. Inelastic Mean-Free Pathlengths

element	E (eV)	d (Å)	λ_{exp} (Å)	calculated λ_E (Å)[a]	calculated λ_{SA} (Å)[b]	calculated λ_D (Å)[c]
Si (2p)	1388	26.8	49±6	32	40	42
C (1s)	1202	25	45±6	30	35	39

(a) $\lambda_E = B_E \cdot E^{1/2}$ where $B_E = 0.087$ for organics, λ_E (nm), Seah and Dench [9].
(b) $\lambda_{SA} = 9.0 + 0.022 \cdot E$, λ_{SA} (Å), Laibinis et al. [1].
(c) $\lambda_D = 0.11 \cdot E^{1/2}$, λ_D (mg/m^3), Seah and Dench [9]. To convert to Å, divide λ_D by the material density in g/cm^3. For calculations of the monolayer density we have used a headgroup packing of 19.8 Å^2/molecule, a chain extension of 24 Å and assumed that the electron density in the headgroup region is the same as for the tails.

We therefore conclude that the packing density of CdC20-monolayers on SiO is less than that obtained for alkane thiol monolayers on noble metals. If we make the assumption that the equation $\lambda_D = B_D E^{1/2}$ holds true, the average packing density of alkane thiols on noble metals would be 5-10% higher than the LB-packing density. The data analysis of the Si(2p) electrons has demonstrated that the reduced density cannot be due to monolayer imperfections; this implies that the hydrocarbon chains have to be on average less densely packed in the case of CdC20-monolayers on SiO. Further conclusions about the microstructure of the film cannot be drawn from this experiment. Our interpretation is supported by NEXAFS studies which also indicate that chain ordering for CdC20-monolayers on SiO is less than for alkane thiols on gold [7]. Our experimental values are also in agreement with those obtained from ESCA studies of related LB-systems: barium stearate LB-monolayers on Ge and Cu [10] and multilayers of cadmium stearate on gold [11].

Depth Profile Analysis

For the surface analysis of substrates with an unknown chemical composition, algorithms have been derived to deconvolute angular-resolved ESCA data into depth profiles. The intent here is to use a well defined overlayer model system to test the quality and resolution of an algorithm that does not require any initial information about the relative depth composition, as proposed by Tyler [2]. The Tyler algorithm is derived from Eq. (1) and hence based on the same set of assumptions.

The composition depth profile generated by the Tyler algorithm by deconvoluting the normalized photoelectron intensities at each of the five take-off angles for the elements Si (1388 eV), C (1202 eV), O (955 eV) and Cd (1082 eV) from a CdC20-monolayer on silicon oxide (Sample 6) is displayed in Fig. 3. The algorithm requires the input of inelastic mean-free pathlength values. For the profile displayed they have been calculated from the expression derived by Seah and Dench [9] on the basis of the monolayer density, $\lambda_D = 0.11 \cdot E^{1/2}$: 42 Å (1388 eV), 39 Å (1202 eV), 37 Å (1082 eV), and 35 Å (955 eV).

The depth profile generated for CdC20 on silicon oxide by the Tyler algorithm predicts (a) a carbon overlayer of approximately 23 Å, (b) an interfacial region containing Cd and O, and (c) a silicon substrate underlayer. Cadmium is associated with the carboxyl head groups. Oxygen contributions arise from the head group region and the oxidized silicon surface. The profile compares within 10% accuracy to the expected thickness of 25 Å for the hydrocarbon

moiety. The sensitivity of the predicted carbon overlayer thickness to properly chosen λ values is as follows: by decreasing the λ values by 20% the algorithm would predict a 5 Å thinner overlayer. The good agreement between the thickness of the actual model system and the algorithm-based predictions indicate that the assumptions made to derive Eq. (1) are reasonable for describing CdC20-monolayers on silicon.

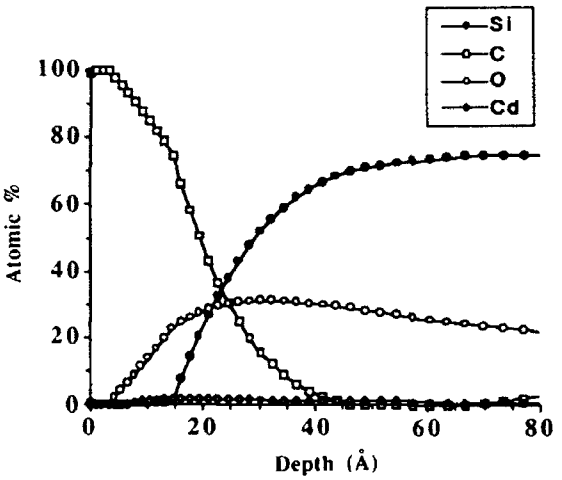

Figure 3. Elemental depth profile of the top 80 Å of a CdC20 LB-monolayer (Sample 6) on a native oxide Si (100) substrate as generated by the Tyler algorithm based on the following λ-values: 42 Å (1388 eV), 39 Å (1202 eV), 37 Å (1082 eV), and 35 Å (955 eV).

Finally, it should be noted that the potential of the algorithm for predicting compositions at intermediate depths is less accurate. Applying the algorithm to angular-resolved ESCA data from our uncovered native silicon substrate results in an oxide layer of approximately 18 Å. In the presence of the monolayer the algorithm predicts a thickness of the underlying oxide layer of more than 80 Å. We conclude that the accuracy of the algorithm in reconstructing intermediate depth profiles is less since the intermediate layers do not lie within the sampling depth of all the take-off angles. Further discussion is given elsewhere [12].

CONCLUSIONS

We have shown that monolayers of CdC20 on silicon oxide form films of high integrity, as probed by angular-resolved ESCA analysis. The average packing density of the hydrocarbon chains, however, is less than for alkane thiols self-assembled on noble metals [1]. We further find that the depth profile of the hydrocarbon overlayer is predicted by the Tyler algorithm within an error of 10%. However, the algorithm is less accurate for predicting intermediate layer compositions.

ACKNOWLEDGEMENTS

This material is based upon work supported under a National Science Foundation Graduate Research Fellowship (SRL). We would like to thank the Whitaker Foundation for financial support, the National ESCA and Surface Analysis Center for Biomedical Problems at the University of Washington where the ESCA analysis was conducted, and Dr. David G. Castner for insightful discussions.

REFERENCES

1. P. E. Laibinis, C. D. Bain and G. M. Whitesides, J. Phys. Chem., 95, 7017 (1991).
2. B. J. Tyler, D. G. Castner and B. D. Ratner, Surf. Interface Anal., 14, 443 (1989).
3. C. S. Fadley, F. J. Baird, W. Siekhaus, T. Novakov and S. Å. L. Bergström, J. Electron Spectrosc. Relat. Phenom., 4, 93 (1974).
4. W. S. M. Werner and H. Störi, Surf. Interface Anal., 19, 83 (1992).
5. S. Tougaard and P. Sigmund, Phys. Rev. B, 25, 4452 (1982).
6. D. A. Outka, J. Stöhr, J. P. Rabe and J. D. Swalen, J. Chem. Phys., 88, 4076 (1988).
7. G. Hähner, M. Kinzler, C. Thümmler, C. Wöll and M. Grunze, J. Vac. Sci. Technol. A, 10(4), 2758 (1992).
8. J. D. Swalen, K. E. Rieckhoff and M. Tacke, Opt. Commun., 24, 146 (1978).
9. M. P. Seah and W. A. Dench, Surf. Interface Anal., 1, 2 (1979).
10. S. M. Hall, J. D. Andrade, S. M. Ma and R. N. King, J. Electron Spectrosc. Relat. Phenom., 17, 181 (1979).
11. D. T. Clark, Y. C. T. Fok and G. G. Roberts, J. Electron Spectrosc. Relat. Phenom., 22, 173 (1981).
12. S. R. Letellier, V. Vogel and B. D. Ratner, in preparation.

NANOENGINEERING WITH DNA

NADRIAN C. SEEMAN
Department of Chemistry, New York University, New York, NY 10003 USA

ABSTRACT

DNA is a tractable medium for controlling the structure of matter on the nanometer scale. We have explored ligating together stable branched DNA molecules to form geometrical objects. By this means, we have assembled a 3-connected molecule whose helix axes have the connectivity of a cube. The construct is a hexacatenane, each of whose cyclic strands corresponds to a face of the object. Each of its twelve edges contains a unique recognition site for cleavage by a restriction enzyme; these sites are used to demonstrate the assembly of the object. The plectonemic structure of DNA also permits the directed synthesis of molecular knots. Recently, we have constructed trefoil knots from B-DNA and an amphichiral figure-8 knot whose helical domains contain both B-DNA and Z-DNA.

We have developed a solid-support methodology for the synthesis of geometrical objects. This approach provides greater control over products and topological purity, and lends itself better to automation. Branched molecules containing 3-6 double helical arms can be formed from equimolar mixtures of their component strands, thereby enabling the construction of 3-6 connected networks. The goals of this work include the construction of periodic multiply-connected networks of DNA. The aims of these DNA constructions include using them as scaffolding to build periodic macromolecular arrays for diffraction purposes, as well as directing the assembly of molecular electronic devices. There are well-characterized molecular transformations of DNA that make nano-scale machines feasible to build in this molecular context. These materials are likely to be useful for understanding crystallization processes and structure-function relationships.

INTRODUCTION

The ability to control the structure of matter on the nanometer scale is likely to lead to new structural materials and devices. This scale is an order of magnitude larger than the chemical scale, where individual atoms are bonded together to create molecules with distinct chemical properties. In the nanometer range, 3-dimensional relationships and connections may be established, but new chemical properties are not a consequence expected of new objects. The nanometer scale is used by the living cell to construct its components, which often cohere by non-bonded interactions. Biological systems are replete with tubules, filaments and force-producing structures built from protein subunits [e.g., 1-3]. Protein engineering on the levels of tertiary [e.g., 4-6] and quaternary [7] structure is a growing and vital field, but the control of protein structure is not yet in hand. Nevertheless, there is another biopolymer whose intramolecular and intermolecular associations can be used for structural engineering: DNA.

The structural engineering of DNA seems an unlikely and possibly trivial topic. After all, we have known for 40 years that DNA is an antiparallel double helical molecule; schoolchildren are taught the reproductive complementarity rule that adenine (A) always pairs with thymine (T) and that guanine (G) always pairs with cytosine (C). The genetic information for protein synthesis is known to be encrypted linearly in the sequence of nucleotides along the DNA molecule. Although there is obvious merit in engineering the functioning of proteins for various ends, DNA acts in the cell primarily as a repository of genetic information. What is to be gained from building particular nucleic acid structures?

The surprising answer to this question is that DNA is a molecule that is unusually well suited to be engineered in three dimensions, and that it may also serve as a convenient scaffolding material to juxtapose and orient other molecules with well-defined functional characteristics. Indeed, DNA may turn out to be the most practical chemical for constructing objects on the nanometer scale. This response raises another question: How can a linear

Mat. Res. Soc. Symp. Proc. Vol. 292. © 1993 Materials Research Society

polymer like DNA be used to construct 'objects' of interest and utility? The answer is that DNA is not always linear: Sometimes it is branched. The most prominent biological example of branched DNA involves the Holliday [8] recombination intermediate. Naturally-occurring branched structures are unstable, because the branch is energetically less favored than linear DNA. Furthermore, Holliday structures contain twofold sequence symmetry that enables them to undergo a structural isomerization called branch migration [e.g., 9]; a branched molecule that repeatedly branch migrates will eventually separate, without cleavage, to become two linear duplex molecules. Synthetic branched DNA molecules need not have this property. It is possible to design sequences lacking in twofold symmetry [10,11]; these molecules are unable to branch migrate, and are stable under convenient solution conditions [12].

MINIMIZING SYMMETRY IN DNA SEQUENCE DESIGN

Branched DNA molecules are often called 'junctions'. Figure 1 illustrates a branched junction molecule. This molecule is an analog of a Holliday junction, with an asymmetric sequence. It contains 4 single strands (indicated by Arabic numbers) arranged into 4 double helical 'arms' (indicated by Roman numerals). Note that the 5' and 3' portions of each strand form parts of two different arms.

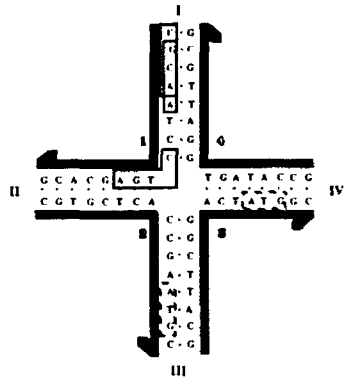

Figure 1. *A Stable DNA Branched Junction.* The junction shown is composed of four strands of DNA, labeled with Arabic numerals. The 3' end of each strand is indicated by the half-arrows. Each strand is paired with two other strands to form a double helical arm; the arms are numbered with Roman numerals. The hydrogen bonded base paring that forms the double helices is indicated by the dots between the bases. The sequence of this junction has been optimized to minimize symmetry and non-Watson-Crick base pairing. There is no homologous twofold sequence symmetry flanking the central branch point, thereby stabilizing the branch point. At the upper part of arm I, two of the 52 unique tetrameric elements in this complex are boxed; these are CGCA and GCAA. At the corner of strand 1, the sequence CTGA is boxed. This is one of twelve sequences in the complex (3 on each strand) that span a junction. The complements to each of these 12 sequences are absent. Whereas tetrameric elements have been used to assign the sequence of this molecule, there is redundancy in the molecule amongst trimers, such as the ATG sequences shown in dashed boxes.

Nucleic acid engineering involving duplex components has been based on directing the tendency of DNA molecules to maximize base pairing. If one wishes to make a molecule containing branched helix axes, the target molecule will contain features that do not correspond to the lowest energy form of DNA. For example, the formation of a four-arm branched junction from two linear duplex molecules is disfavored by 1.1 kcal/mol at 18 °C [13]. Nevertheless, one can ensure the formation of the 'excited state' molecule, if one precludes the possibility of more favorable arrangements. Control in this system derives from minimizing DNA sequence symmetry, which involves more than eliminating twofold symmetry across the junction [11].

The minimization of sequence symmetry is illustrated for the junction shown in Figure 1. Each strand of the junction contains 16 nucleotides, which have been broken up into 13 overlapping tetramers, indicated by the solid boxes. If we insist that each of the 52 tetramers in the entire molecule be unique, base pairing competitive with the designed

molecule can come only from redundant trimers (e.g., the ATG sequences indicated by the dashed boxes). As a further constraint, we insist that the molecule contain no tetramer complementary to a bend; for example, there is no TCAG complementary to the boxed CTGA. The use of tetramers allows a 'vocabulary' of 240 elements [(4^4 = 256) - 16 self-complementary sequences]. To design larger structures, one must divide the strands into longer elements of length **n**, and competition from redundant (**n**-1)-mers can assume greater importance. When they are mixed together, the strands in Figure 1 self-assemble to form the illustrated branched structure [12].

DIRECTING MOLECULAR ASSOCIATIONS BY STICKY ENDS

Linear DNA is a construction medium familiar to those involved in biotechnological endeavors. The sticky-ended ligation of DNA fragments [14], shown in Figure 2, is the

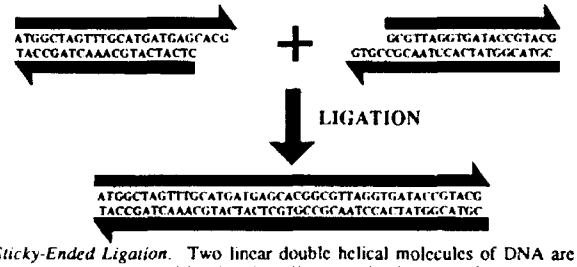

Figure 2. *Sticky-Ended Ligation.* Two linear double helical molecules of DNA are shown. The antiparallel backbones are indicated by the black lines terminating in half-arrows. The half-arrows indicate the 5'-->3' directions of the backbones. The right end of the left molecule and the left end of the right molecule have single-stranded extensions that are complementary to each other. Under the proper conditions, these bind to each other, and ligate to covalency with the proper enzymes and cofactors.

fundamental reaction of biotechnology; it enables genetic engineers to assemble genetic units with particular functional characteristics. From the structural viewpoint, linear duplex DNA can function as a building block for lines, circles, or knots [e.g., 15], but it does not provide vertices: Branched molecules are needed to furnish vertices. The attachment of particular sticky ends to a branched nucleic acid structure converts it, in principle, into a highly specific nanoscale valence cluster with addressable ends [10,16,17]. By treating them as molecular lego, branched DNA molecules become building blocks that can be assembled into multiply-connected stick-figures and networks. The edges of these figures consist of double helical DNA, and the vertices correspond to the branch points. Thus, it seems possible to design and build complex structures from branched DNA molecules. The basic principles of self-association are shown in Figure 3; here we illustrate the assembly of a 4-arm junction into a

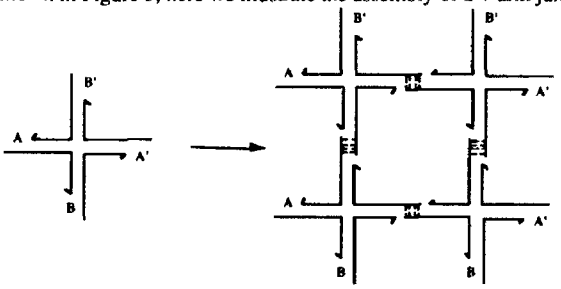

Figure 3. *Formation of a Two-Dimensional Lattice from a Junction with Sticky Ends.* A is a sticky end and A' is its complement. The same relationship exists between B and B'. Four of the monomeric junctions on the left are complexed in parallel orientation to yield the structure on the right. Note that A and B are different from each other, as indicated by the pairing in the complex. DNA ligase can close the gaps left in the complex. Note that the complex has maintained open valences, so that it can be extended by the addition of more monomers.

quadrilateral, which has the potential to form a 2-D lattice. The single-stranded region A is designed to pair with A' and B with B'.

When this type of assembly scheme is attempted, one discovers that individual junctions are not completely rigid [19,20]. We can expect that the double helical edges of each object are torsionally and flexurally stiff, because the persistence length of DNA varies from 450 Å to 1000 Å, depending on conditions [21]. However, the 'valence angles' between the double helical edges of each object are flexible. If a given junction is oligomerized to yield oligolaterals with two turns between branch points, it readily forms a series of cyclic products: trimers, tetramers, pentamers and so on. Thus, oligomerization of individual junctions is not a useful technique to generate a particular cyclic polygon. However, the specificity of sticky-ended ligation can be used to direct the assembly of particular junctions into target structures. Thus, the control of connectivity is robust, but the control of 3-D structure is more elusive. The assembly of a particular quadrilateral, directed by a set of junctions with individually addressable sticky ends [22], is shown in Figure 4.

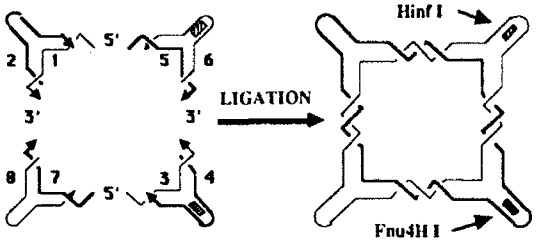

Figure 4. *The Scheme of Synthesis of a DNA Quadrilateral.* The individual reactant junctions are shown on the left of the figure and the product is shown on the right. For clarity, the double helicity of the DNA has been represented merely as parallel lines in the vicinity of the branch sites, and is confined to regions distal to the branch sites; nevertheless, all the twisting expected on the main cycle is shown on both sides of the figure. Likewise, one should not think that there is unpaired DNA between the parallel lines--each edge represents only 16 nucleotides on each strand. On the left, thick strands and thin strands are associated in pairs to form 3-arm junctions, in which one 'exocyclic' arm is closed in a hairpin loop. Arrowheads represent the 3' ends of individual strands. Strand numbering is indicated on the left by the numbers from 1 to 8. The 5' and 3' symbols indicate the sense of the single-stranded overhangs. The overhangs are all on the short strands. The filled regions in the exocyclic stems formed by strands 4 and 6 represent restriction sites, indicated on the two different strands.

Each of the four 3-arm junctions connected together in this construction consists of two strands, because two of the three strands making up the junction have been joined by a hairpin loop. The sticky ends on each junction are unique, so this assembly represents directed synthesis, rather than oligomerization. Two pairs of sticky ends are 5' overlaps, and two pairs are 3' overlaps. Each edge consists of sixteen nucleotide pairs, or 1.5 turns of double helical DNA. Thus, the four junctions are ligated to form two separate strands that are designed to be hextuply linked. Each final strand contains a recognition site for a restriction endonuclease on an exocyclic arm (indicated as filled regions in strands 4 and 6), so that it can be cleaved for analytical purposes. It is our convention to show the twisting condensed to the middle of each edge for clarity; the viewer should not be confused by the different domains on each edge--the twisting extends all the way to the vertices.

A key concept here is *connectedness* [18], which is the number of edges of a closed object or a lattice that meet at a vertex; the number of arms of the junction at a given vertex limits the maximum connectedness of that vertex. Thus, 3-connected objects and lattices can be built with 3-arm junctions, and 4-connected structures can be built with 4-arm junctions. Junctions with 3-6 arms have been constructed and characterized [12,19,23].

The catenated nature of the two strands in Figure 4 introduces an important point about the double helical structure of DNA. Even though one often can think usefully about helix axis connectivity, without taking the helical twist into account, the braiding of the strands about the helix axis is a valuable and critical structural property of any DNA molecule. For example, the two strands in the quadrilateral can be separated from nicked failure products by electrophoresis under denaturing conditions, because the catenane holds together, but nicked molecules separate into separate strands [22]. Ultimately, the twist cannot be ignored in structural design: Changing the separation between branch points from 20 to 16 nucleotide pairs can change the distribution of oligomerization products [20]. The

twisting of DNA strands about each other implies that individual objects will be complex catenanes, and materials constructed from this medium will have polycatenated substructures, much like chain mail. In addition, the plectonemic structure of DNA enables one to design and construct molecular knots, which are described below.

THE CONSTRUCTION OF A DNA POLYHEDRON

We have seen above that it is possible to construct DNA stick figures, where the edges are double helical DNA molecules. We are certainly not limited to 2-dimensional objects when we build molecules from branched DNA. Whereas the connections between vertices are helical, not parallel, branched DNA structures are inherently 3-dimensional: The

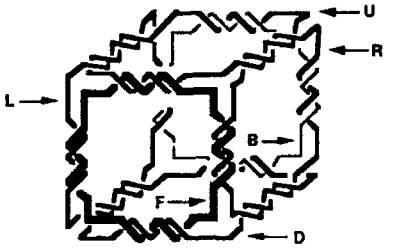

Figure 5. *A DNA Molecule Whose Helix Axes Have the Connectivity of a Cube.* The molecule shown consists of six cyclic strands that have been catenated together in this particular arrangement. They are labeled by the first letters of their positional designations, Up, Down, Front, Back, Left and Right (like a Rubik Cube).

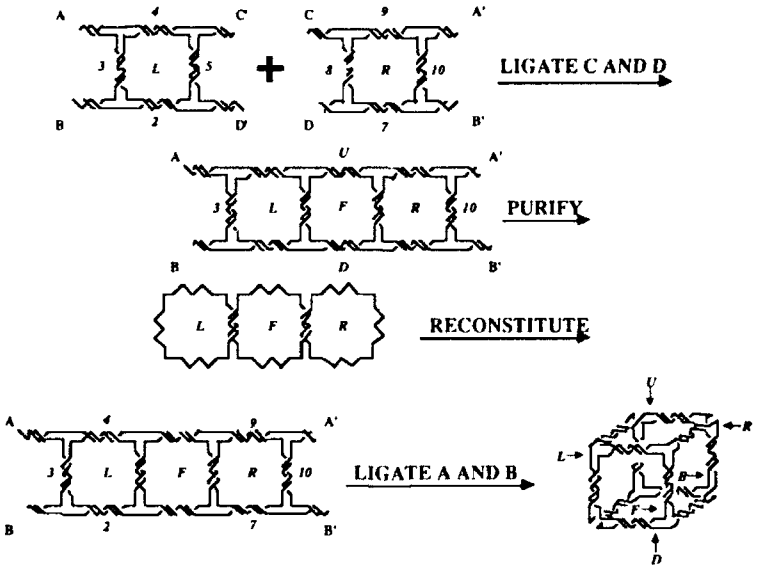

Figure 6. *The Synthesis of a DNA Cube.* The molecule is built from 10 chemically synthesized strands, two 80-mers and eight strands containing about 40 nucleotides. These are hybridized to form two quadrilaterals in the first step. Two ends (C and D) are ligated to form a belt-like molecule that must be denatured and reconstituted in order to purify it from side-products. The belt-like molecule is then cyclized to form the cube-like molecule.

relative mean orientations of arms that branch from the vertices flanking an edge are a function of the length of the edge, just like two wing nuts on a screw [16,17]. We have exploited the flexibility of branched junctions to construct from 3-arm junctions a molecule whose helix axes have the connectivity of a cube [24]. A schematic of the 3-dimensional, 3-connected [18,25] object is shown in Figure 5, and its synthesis is shown in Figure 6.

The object in Figure 5 is shown as a cube, although there has been no characterization of the angles between the edges. It contains 12 edges formed from double helical DNA. Since each edge contains 20 nucleotide pairs of DNA, we expect that their lengths will be about 68 Å. Each of the edges contains a unique site for recognition and cleavage by a restriction endonuclease, thereby enabling us to establish the validity of the synthesis. From model building [26], the axis-to-axis distance across a square face appears to be about 100 Å, with a volume (in a cubic configuration) of approximately 1760 nm^3, when the cube is folded so that major grooves form the outsides of the corners; it is markedly smaller than when the corners are formed from minor grooves. The direction of folding is currently unknown. Another way to regard the object is as a complex catenane of 6 single-stranded cycles, each doubly linked to its four nearest neighbors.

A SYNTHETIC METHODOLOGY USING A SOLID-SUPPORT

Control in the synthetic scheme of Figure 6 derives solely from the ability to phosphorylate sticky ends in a selective fashion. This level of control limits a synthetic scheme involving all strands to two effective steps: Hybridization of phosphorylated and unphosphorylated strands preceding the first ligation, followed by phosphorylation of the remaining strands and a second ligation step. This is an insufficient amount of control for complex objects, so we have developed a new methodology that is more effective [27].

This methodology is based on the use of a solid support, which lends itself to automation by permitting convenient removal of reagents and catalysts from the growing product. Each ligation cycle creates an intermediate object that is covalently closed and topologically bonded together. This feature permits exonuclease digestion of incompletely ligated edges, thereby purifying the growing object during synthesis. A single edge of an object can be built at a time. Control derives from the restriction endonuclease digestion of hairpin loops forming each side of the new edge. Sequences are chosen to destroy

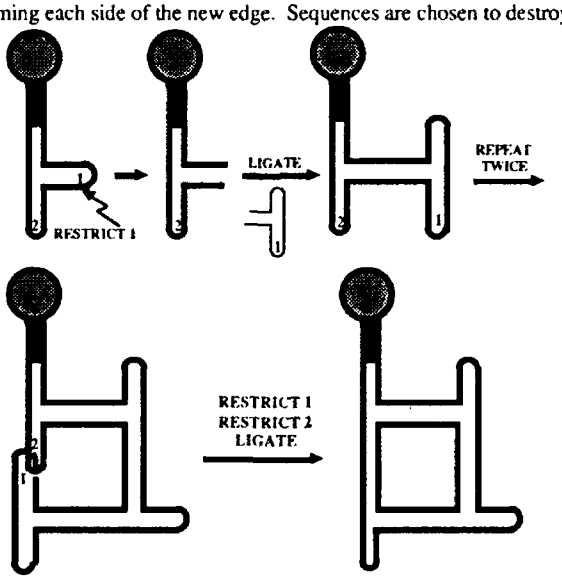

Figure 7. *Protocol for the Synthesis of a Quadrilateral.* Beginning with the support (shaded) bonded to a junction, alternate cycles of restriction and ligation are performed, always at the position indicated as '1'. The target product (triangle, quadrilateral, pentalateral,...) is determined by the point at which one chooses to restrict at site 2, exposing a sticky end complementary to that exposed by restriction at site 1.

restriction sites when the edge forms. Figure 7 illustrates the synthesis of a quadrilateral from 3-arm junctions, four times as efficient as that in Figure 4 [27]. In principle, the object added to the growing construct can be a polygon, a polyhedron or an array of polyhedra.

THE ENGINEERING OF SINGLE-STRANDED DNA KNOTS

The closed, branched DNA molecules discussed above are all catenanes of single-stranded DNA molecules. An intimate relationship exists between catenanes and knots [15]: Removal of a node by switching strands, yet maintaining strand polarity (sometimes called forming a zero node) converts a catenane to a knot, and a knot to a catenane (Figure 8). This relationship is important here, because the possibility of cloning these DNA structures appears today to be most readily achievable by getting single-stranded DNA molecules to fold up into complex knots, whose restriction will lead to the desired stick figures [28]. It is not possible to clone branched structures directly, because a single round of replication will

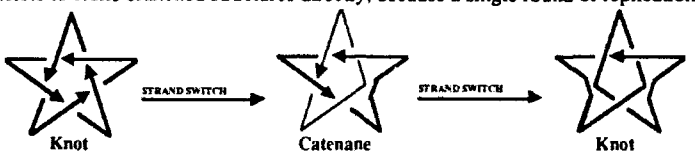

Figure 8. *Interconversions of Knots and Catenanes by Switching Strands at a Node.* The structure shown on the left is a 5_1 knot. The strand direction is indicated by the arrowheads appearing along the strand. When the two strands entering the lower node on the right exchange outgoing partners, the node disappears, and a 'zero node' [15] is introduced. This converts the knot to a catenane, shown in the middle; the two linked cycles are drawn so as to retain their shapes, but they are drawn with pens of different thicknesses. The lower left node of the catenane undergoes a strand switch, and the structure is converted to a trefoil knot, illustrated on the right. The trefoil knot is one strand, so it is drawn with one pen.

reduce a branch to linear duplexes. Nevertheless, it is possible, in principle, to make an entire structure from a single strand, as illustrated for a dodecahedron in Figure 9. The key

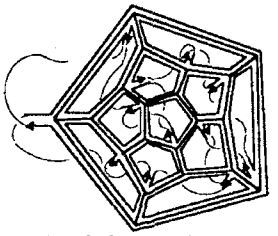

Figure 9. *A Single-Stranded Representation of a Pentagonal Dodecahedron.* A pentagonal dodecahedron is illustrated with twelve exocyclic arms, in a representation known as a Schlegel diagram. This is a 2-D representation of a 3-D object in which the central polygon is closest to the reader, the polygons removed from the center are distorted and further behind in the page, and the outer polygon is at the rear of the figure. The Schlegel diagram of the dodecahedron is shown in the thickest lines. Flanking these are lines that represent the double helical DNA corresponding to each edge of the dodecahedron. Each of the twelve pentagons contains an exocyclic double helical arm, with one strand terminating in an arrowhead, indicating the 5'-->3' polarity of the strand. In addition, each of the individual faces has been connected to a neighboring face via the exocyclic arms and connecting very thin strands, so that the entire representation is a single long strand. The structure shown would need to be cleaved in order to fold. Each exocyclic double helical segment would contain a restriction site, to sever it from connecting DNA upon formation of the structure. No topological representation is made here: connecting DNA lies behind the polygonal DNA for clarity.

to this strategy is to add an extra external arm for every strand; for molecules whose edges all contain an integral number of helical turns, this corresponds to an extra arm per face. The external arms are then connected together to form the complex knotted structure shown. The sequence of such a single-stranded molecule could be cloned. Whereas one needs external arms on a polyhedral structure to form a lattice, the target structure is likely to contain such restrictable external arms. Nevertheless, an optimal-connection protocol and a folding

algorithm within the constraints of symmetry minimization must be developed so that the knot can be directed to thread itself properly.

The nodes formed by ordinary right-handed B-DNA correspond to negative topological nodes, if one establishes polarity in the usual 5'-->3' direction. However, there is a left-handed form of DNA, Z-DNA [29], that is formed readily by certain sequences, given the appropriate solution conditions [30]. The relationship between nodes and DNA structures is illustrated in Figure 10.

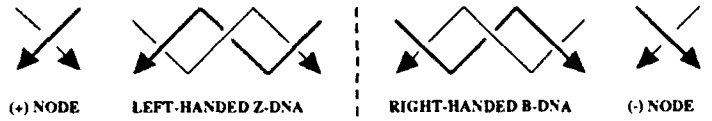

Figure 10. *Nodes and DNA Handedness.* The mirrored sides of this diagram show positive and negative topological nodes and their relationship to DNA structure. The nodes and their indicated signs are shown on the outsides, the DNA on the insides, and a dotted vertical line separates the two halves. It is useful to think of the arrows as indicating the 5'-->3' directions of the DNA backbone. Left of the negative node is a representation of about one and a half turns of a right-handed B-DNA molecule. Note that the nodes are all negative. To the right of the positive node is a left-handed DNA molecule, termed Z-DNA. Note that the nodes are all positive. The Z-DNA molecule has been drawn so as to appear to be a left-handed version of B-DNA. This has been done to clarify the relationship between the handedness of a double helix and the signs of the nodes generated; *this drawing is not intended to represent accurately the structural nature of the Z-DNA helix, in which the minor groove is less exposed than in the B-DNA helix, the major groove is non-existent, and the backbone has a zig-zag character* [29].

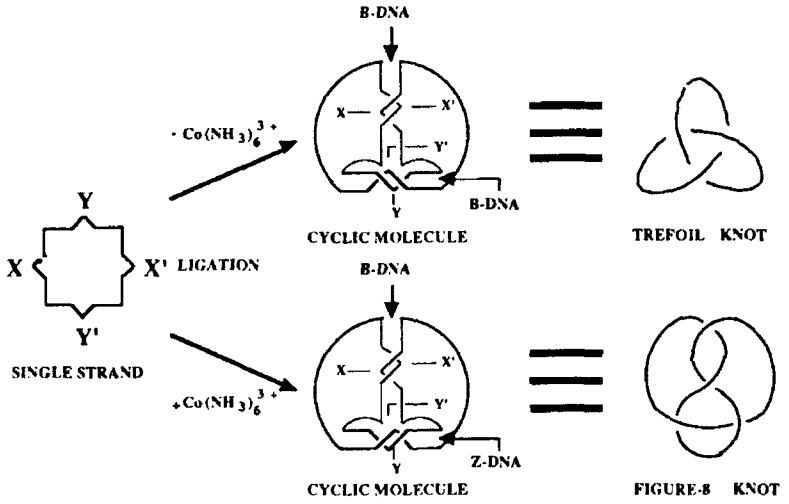

Figure 11. *Synthetic Scheme for the Single-Stranded DNA Knots.* The starting material is a 104-mer illustrated on the far left--X (A.C.T.G.G.A.C.C.T.C.T), Y (dCpdGp)$_6$; X' and Y' refer to sequences that are expected to pair to them by Watson-Crick hydrogen bonding. Each side of the square figure shown corresponds to a quarter of the molecule. The projections represent the regions that will pair according to the letter codes; they are flanked by the oligo-dT linkers. The arrowhead within the X projection represents the 3' end of the strand. There are two routes to the central portion of the figure, the bottom route, including Z-promoting $Co(NH_3)_6^{3+}$, and the top route, without it. The central section of the figure illustrates the interlinking of the strands. The oligo-dT linkers are represented here by the curved portions of the strand. The upper far-right drawing illustrates the denatured trefoil structure in an idealized fashion. Note that the handedness of the trefoil shown here is the correct one for right-handed double helical DNA. The lower far-right drawing represents the figure-8 knot similarly. Reversing the sense of all the nodes of this knot results in no change in handedness.

We have explored the possibilities for threading knots experimentally. A DNA molecule can be synthesized containing the sequence **X-T-Y-T-X'-T-Y'-T**, where **X** and **Y** correspond to one helical turn, **X'** and **Y'** are their Watson-Crick complements, respectively, and **T** is dT_n linker. When cyclized, this molecule yields a trefoil (3_1) knot [31,32]. In addition, it is possible to incorporate a sequence capable of forming Z-DNA in one of the two domains. Thus, if the **Y-Y'** domain contains the proto-Z sequence $(dCpdGp)_6$, ligation in a Z-promoting solution [30] {10 mM $Co(NH_3)_6^{3+}$} will produce an amphichiral figure-8 (4_1) knot, containing two positive nodes and two negative nodes.

The synthetic scheme for the synthesis of these two knots is summarized in Figure 11 [32]: Each pairing region is separated by a dT_{14} or dT_{15} spacer. The 5' and 3' ends of the synthetic molecule fall between the eighth and ninth nucleotide of the **X** segment, producing a nick that can be sealed by T4 DNA ligase. Ligation in B-promoting conditions produces a trefoil knot (Figure 11, top); ligation in Z-promoting conditions generates a figure-8 knot (Figure 11, bottom). Products of these reactions are characterized on polyacrylamide gels under denaturing conditions, which are sensitive to topology, regardless of molecular conformation [31]. The circle of the same sequence can be prepared as a control; a linear complement, whose presence is incompatible with knot formation, is hybridized to the DNA flanking the nick during the ligation reaction.

There is a general relationship between the nodes of DNA molecules and the nodes of single-stranded DNA knots: A half-turn of duplex DNA can be used to generate a node in a knot [33]. Figure 12 illustrates this point with a trefoil knot. The three nodes of the knot shown are formed by perpendicular lines, whose polarity is indicated by arrowheads. The nodes act as the diagonals of a square, which they divide into four regions, two between antiparallel arrows and two between parallel arrows. The transition from topology to nucleic acid chemistry can be made by drawing parallel base pairs between strands in the antiparallel regions. The axes of the helices are drawn perpendicular to the base pairs, and the twofold axes are perpendicular to the helix axes. The individual nodes can be usefully condensed into larger DNA structures to avoid undesired braiding [33]. For example, the trefoil and figure-8 knots synthesized above have their nodes condensed into linear structures, and the trefoil in Figure 12 could be condensed into a 3-arm branched DNA junction. Excess braiding can be avoided in catenanes [24], and possibly in knots, by using 'topological protecting groups' [33]. These are unclosable single-stranded DNA molecules that pair with parts of the strand whose role is not to form nodes. Protection prevents these segments from forming unwanted braids, and then it is removed by denaturing the final molecule.

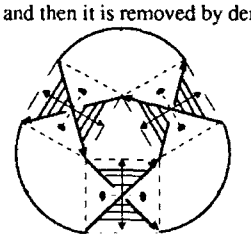

Figure 12. *The Relationship Between Nodes and Antiparallel B-DNA Illustrated on a Trefoil Knot.* A trefoil knot is drawn with negative nodes. The path is indicated by the arrows and the very thick curved lines connecting them. The nodes are formed by individual arrows drawn at right angles to each other. Each pair of arrows forming a node defines a quadrilateral (a square in this figure), which is drawn in dotted lines. Double-arrowheaded helix axes are shown perpendicular to these lines. The twofold axis that relates the two strands is perpendicular to the helix axis; its ends are indicated by lens-shaped figures. The twofold axis intersects the helix axis and lies halfway between the upper and lower strands. The amount of DNA shown base paired at each node corresponds to about half a double helical turn.

STRUCTURAL TARGETS FOR DNA ENGINEERING

Suggestions for the utility of DNA structural engineering are currently in the realm of speculation. A key use envisioned for DNA arrays [10] is to function as macromolecular zeolites, serving as hosts for globular macromolecular species, as an aid in crystallographic structure determination. The rate-determining step in macromolecular crystallography is the preparation of adequate crystals. The ability to assemble periodic arrays of cages that contain ordered guests would contribute to a solution of that problem. Intracage orientation

could be done through binding by site-specific fusion molecules. A cartoon of such an array is illustrated in Figure 13, using 5-connected and 6-connected networks. The assembly of periodic lattices is likely to be a difficult goal to achieve: Control over the synthesis of an individual object can be derived from minimization of sticky-end symmetry, but it is not possible to exploit symmetry minimization to build an entire crystalline array [16], since the lattice inherently contains translational symmetry. The solution that seems most likely to work is to use an automated version of the solid-support methodology to build a hierarchy of structures, culminating in a group of unit cells. These could be aligned by masking the same sticky end with different restrictable hairpins, as done previously [27]: Special sticky ends could be deprotected by the first enzyme, and ligated, and then the rest could be deprotected by the second enzyme prior to their ligation.

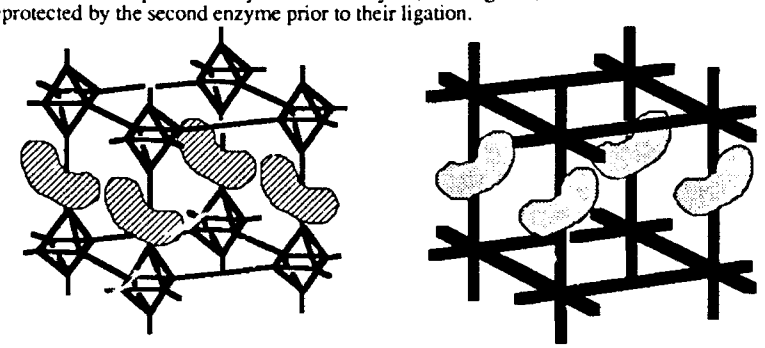

Figure 13. *5-Connected and 6-Connected Networks Acting as Hosts for Macromolecular Guests.* The simplest conceptual network, the 6-connected cubic lattice, is shown on the right side of this drawing. Macromolecular guests, represented as shaded kidney-shaped objects, have been added to four unit cells. Note that if the guests are all aligned in the parallel fashion shown, the entire material will be a crystal, and it will be possible to determine the structure of the guests by crystallography.

Due to its special role as the genetic material of all living organisms, including humans, there has been a lot of effort devoted to the synthesis [34] and modification of DNA for diagnostic and therapeutic purposes. For this reason, a great deal of chemistry is known, and indeed is commercially available, by which it is possible to derivatize synthetic DNA molecules with special functional groups, both on the bases and on the backbone (reviewed in [35]). In addition, there are natural mechanisms by which drugs and particular proteins recognize and bind to specific sites on DNA. These methods could be used to attach molecular electronic components to DNA molecules [36]. The self-assembly of the DNA molecules could in turn direct the assembly of these other components (Figure 14). The specific proposal that has been forwarded is that a crystalline array of such an assembly could act as a memory device. The DNA in this proposed biochip is limited to a structural role. The components suggested include conducting polymers, such as *trans*-polyacetylene or polyphenothiazine (PTL), a PTL-ruthenium switch, and a redox bit [36].

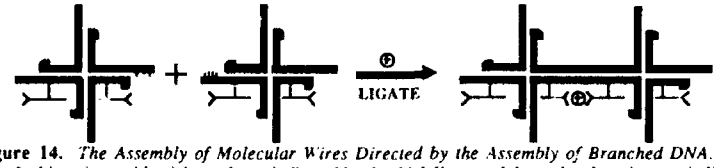

Figure 14. *The Assembly of Molecular Wires Directed by the Assembly of Branched DNA.* The branched junctions with sticky ends are indicated by the thick lines, and the molecular wires are indicated by the horizontal thin lines tethered to them. A metal (circle with + sign) is indicated as being added to them to form a molecular wire synapse [36].

The properties of multiply-connected DNA objects also make them excellent potential scaffolds for the attachment of proteins. The marked stiffness of DNA [21] suggests that large substituents are unlikely to perturb its structure extensively. However, linear DNA molecules present a limited set of sites for the juxtaposition and orientation of tethered

proteins. For example, two proteins tethered in the same manner five nucleotides apart will be on the opposite sides of the DNA double helix. Branched structures present attachment sites with a wider choice of intermolecular distances on the same surface. Among the utilities envisioned for tethering molecules to DNA objects are the production of new catalysts [22] and the solubilization and delivery of otherwise-insoluble proteins and drugs. The scaffolded threading of polymeric species has also been suggested [33].

What about mechanical action? There are several ways, in principle, in which controlled motion can be achieved in isolated DNA structures, or in parts of a periodic array that are not involved in the stabilization of the lattice. There are at least two dramatic isomerizations of DNA that ought to be useful to achieve motion. One is the B-Z transition, in which a segment of DNA changes from its normal right-handed structure (B-DNA), to a left-handed structure (Z-DNA). This largely-torsional transition (about -64°/residue) occurs most readily in $(CG)_n$ sequences; it can be controlled by solution conditions [30]. Another isomerization is branch migration, which is influenced by the torsional state of DNA [37]. The details of branch migration remain unclear, but one can estimate that two residues will each move about 3.4 Å and rotate about 35° for each step taken. These isomerizations are illustrated in Figure 15.

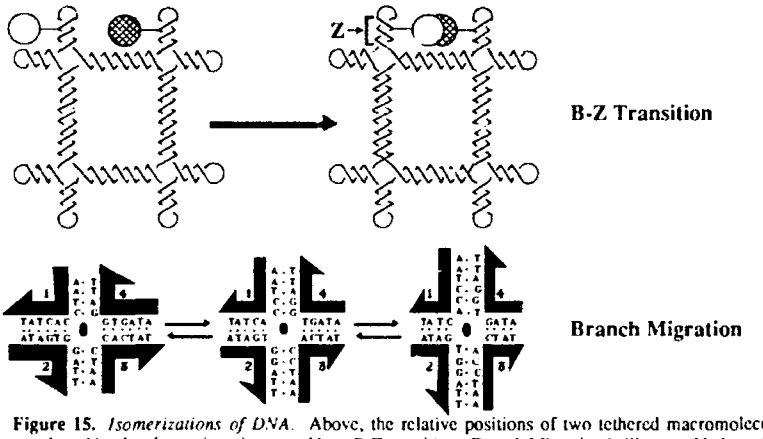

Figure 15. *Isomerizations of DNA.* Above, the relative positions of two tethered macromolecules are altered by the change in twist caused by a B-Z transition. Branch Migration is illustrated below. The position of a branch is relocated by the isomerization reaction.

CONCLUDING REMARKS

DNA turns out to be a surprisingly tractable medium for engineering both structure and topology on the nanometer scale. It is important to realize that DNA stick figures are topologically DNA catenanes, intimately related to knots [33]. Indeed, at this point, the major features of stick figures that are experimentally available are their topologies. The cube-like molecule, for example, has been characterized only by its connectivity; it can be broken down to its more tractable substructure catenanes. Further techniques are necessary to characterize such molecules structurally. Similarly, the theory of producing DNA knots described above is well ahead of experimental confirmation. Whereas it is possible to differentiate knots with different numbers of nodes by their gel mobilities, it is unlikely that such techniques can differentiate isomers of higher knots containing the same number of nodes. It is to be hoped that new techniques, such as scanning tunneling microscopy [e.g., 38], will facilitate the structural characterization of these new and exciting molecules.

ACKNOWLEDGMENTS

This research has been supported by grants N00014-89-J-3078 from the Office of Naval Research and GM-29554 from the NIH. The support of Biomolecular Imaging on the NYU campus by the W. M. Keck Foundation is gratefully acknowledged. The experimental

contributions of Junghuei Chen, John E. Mueller, Shou Ming Du, Yuwen Zhang, Yinli Wang, Tsu-Ju Fu, Siwei Zhang and Hui Wang have been invaluable to this research.

REFERENCES

1. Kabsch, W., and Vandekerckhove, J., Ann. Rev. Biophys.Biomol. Struc. **21**, 49-76 (1992).
2. Erickson, H.P., and O'Brien, E.T., Ann. Rev. Biophys.Biomol.Struc. **21**, 145-166 (1992).
3. Blair, D.F., Nanotechnology **2**, 123-133 (1991).
4. Bowie, J.U., Luthy, R., and Eisenberg, D., Science **253**, 164-170 (1991).
5. Yue, K. and Dill, K.A., Proc. Natl. Acad. Sci. (USA) **89**, 4163-4167 (1992).
6. Urry, D.W., Gowda, D.C., Peng, S.Q., Parker, T.M. and Harris, R.D., J. Am. Chem. Soc. **114**, 8716-8717 (1992).
7. Stoddard, B.L. and Koshland, D.E., Jr., Nature (London) **358**, 774-776 (1992).
8. Holliday, R., Genet. Res. **5**, 282-304 (1964).
9. Thompson, B.J., Camien, M.N., and Warner, R.C., Proc. Natl. Acad. Sci. (USA) **73**, 2299-2303 (1976).
10. Seeman, N.C., J. Theor. Biol. **99**, 237-247 (1982).
11. Seeman, N.C., J. Biomol. Str. & Dyns. **8**, 573-581 (1990).
12. Kallenbach,N.R., Ma,R.I. and Seeman, N.C.,Nature (London) **305**, 829-831 (1983).
13. M. Lu, Q. Guo, L.A. Marky, N.C Seeman and N.R. Kallenbach, J. Mol. Biol. **223**, 781-789 (1992).
14. Cohen, S.N., Chang, A.C.Y., Boyer, H.W. and Helling, R.B., Proc. Natl. Acad. Sci. (USA) **70**, 3240-3244 (1973).
15. White, J.H., Millett, K.C. and Cozzarelli, N.R., J Mol. Biol.**197**,585-603(1987).
16. Seeman, N.C., J. Biomol. Str. & Dyns. **3**, 11-34 (1985).
17. Seeman, N.C., J. Mol. Graphics **3**, 34-39 (1985).
18. Wells, A.F., Three-dimensional Nets and Polyhedra (John Wiley & Sons, New York, 1977).
19. Ma, R.-I., Kallenbach, N.R., Sheardy, R.D., Petrillo, M.L. and Seeman, N.C., Nucl. Acids Res. **14**, 9745-9753 (1986).
20. Petrillo, M.L., Newton, C.J., Cunningham, R.P., R.-I. Ma, Kallenbach, N.R.and Seeman, N.C., Biopolymers **27**, 1337-1352 (1988).
21. Hagerman, P.J., Ann. Rev. Biophys. & Biophys. Chem .**17**, 265-286 (1988).
22. Chen, J.-H., Kallenbach, N.R. and Seeman, N.C., J. Am. Chem. Soc. **111**, 6402-6407 (1989).
23. Wang, Y., Mueller, J.E., Kemper, B. and Seeman, N.C. Biochem. **30**, 5667-5674, (1991).
24. Chen, J. and Seeman, N.C., Nature **350**, 631-633 (1991).
25. Williams, R., The Geometrical Foundation of Natural Structure (Dover, New York, 1979).
26. Seeman, N.C., J. Biomol. Str. & Dyns. **5**, 977-1004 (1988).
27. Zhang, Y. and Seeman, N.C., J. Am. Chem.Soc. **114**, 2656-2663 (1992).
28. Seeman, N.C., DNA and Cell Biology **10**, 475-486 (1991).
29. Wang, A.H.-J., Quigley, G.J., Kolpak, F.J., Crawford, J.L., van Boom, J.H., van der Marel, G. and Rich, A., Nature **282**, 680-686 (1979).
30. Behe, M. and Felsenfeld, G., Proc. Natl. Acad. Sci. (USA) **78**, 1619-1623 (1981).
31. Mueller,J.E.,Du, S.M. and Seeman,N.C.,J. Am.Chem.Soc.**113**,6306-6308 (1991).
32. Du, S.M. and Seeman, N.C., J. Am. Chem.Soc. **114**, 9652-9655 (1992).
33. Seeman, N.C., Molecular Engineering **2**, in press (1992).
34. Caruthers, M.H., *in* Chemical and Enzymatic Synthesis of Gene Fragments, ed. by H.G. Gassen and A. Lang, (Verlag Chemie, Weinheim, 1982) pp. 71-79.
35. Chrisey, L.A. (1990), Synthecell Synthesis **2(1)**, 4-65.
36. Robinson, B.H. and Seeman, N.C., Prot. Eng. **1**, 295-300 (1987).
37. Gellert, M., Mizuuchi, K., O'Dea, M.H., Ohmori, H. and Tomizawa, J., Cold Spring Harbor Symp. Quant. Biol. **43**, 35-40 (1978).
38. Allison, D.P., Bottomley, L.A., Thundat, T., Brown, G.M., Woychik, R.P., Schrick, J.J., Jacobson, K.B. and Warmack, R.J., Proc. Natl. Acad Sci. (USA) **89**, 10129-10133 (1992).

COMPARISON OF SINGLE AND DOUBLE STRANDED DNA BINDING TO POLYPYRROLE.

Rajiv Pande, Jeong - Ok Lim, Kenneth A. Marx, Sukant K. Tripathy and David L. Kaplan*,
Center for Advanced Materials and Department of Chemistry, University of Massachusetts Lowell, Lowell, MA 01854,
*Biotechnology Division, U.S. Army Natick Research, Development & Engineering Center, Natick, MA 01760.

ABSTRACT

The polycation conducting polymer, oxidized polypyrrole (PPy), possesses the ability to form complexes with DNA. Our previously proposed diffusion limited binding model for double helical DNA was also found to be applicable to single stranded DNA in this study. Single stranded DNA was found to bind PPy at a nearly identical level to that of double helical DNA. An investigation of electropolymerized PPy film morphology using SEM revealed two distinctly differing surface morphologies for the Platinum (Pt) electrode face (smooth) and polymeric growth face (rough). The DNA uptake levels were found to be consistently different on either surface, being higher on the rough surface. DNA penetrated into the disk interior with increasing time periods of exposure while a similar phenomenon but to a lesser extent was observed for single stranded DNA.

INTRODUCTION

The oxidized form of polypyrrole (PPy) is electrically conducting with conductivity in the range of 10^{-3} - 10^{2} S cm^{-1} [1,2]. Conduction in PPy is due to the mobility of positive charged defect structures in the highly conjugated polymer backbone [3,4]. The cations form donor - acceptor complexes with electrolyte ions during the synthesis of the conducting polymer. Past studies performed by our group have shown that polyanionic DNA binds PPy, presumably by replacing the dopant counterions upon binding. We have demonstrated that the uptake kinetics of double helical DNA follows a classical diffusion limited adsorption model with no significant activation energy to binding [5 -7].

Observation of the surface of electropolymerized PPy disks using scanning

Mat. Res. Soc. Symp. Proc. Vol. 292 1993 Materials Research Society

electron microscopy (SEM) has revealed two distinct morphologies, a rough surface (polymer growth face) characterized by the presence of grooves, channels and craters, and a smooth surface (electrode face) devoid of these structures. Since DNA binding routes could involve diffusion or capillary uptake into internal channels as well as surface adsorption in the PPy disk we undertook the following studies. A comparative study of the binding properties of single and double stranded DNA to polypyrrole was undertaken by counting decay events from both sides of PPy disks to determine time dependent DNA penetration into the disk interior. The DNA binding and matrix penetration phenomena may find uses for PPy as a new material in biotechnology applications. The optoelectronic properties of conducting polymers may find uses in signal transduction in biosensors where nucleic acids form the molecular recognition system utilizing molecular hybridization.

EXPERIMENTAL METHODS

The electrochemical polymerizations were performed as previously described [7]. After 4 hours of reaction time a film of 100 - 130 μm thickness was deposited on the Pt electrode. The free standing film was peeled off with a razor blade and tweezers, followed by soaking in acetonitrile for 24 hours and drying at 25° C for 12 hours. The film was cut into circular disks 0.60 cm in diameter and stored in the dark.

Native pBR 322 DNA (New England Biolabs) was linearized by restriction cleavage with EcoRI (New England Biolabs). The linearized DNA was then ^{35}S radiolabeled using a 3' end labeling kit NEK 009Z (New England Nuclear) achieving a specific activity of 5 X 10 ^{4} cpm/pmol. The radiolabeled DNA was dissolved in 500 μl of TE buffer (1 mM EDTA and 10 mM Tris, pH 8) and was stored at - 20° C. Samples containing 160 nanograms of ^{35}S DNA in a 200 μl droplet in 1X TE buffer were placed on a polypropylene tray. The tray was placed in a petri dish which contained a reservoir of 1X TE buffer to minimize sample droplet evaporation. The disk shaped PPy substrate was then placed upon the DNA solution droplets for varying lengths of time at 37° C. Following exposure to the DNA droplet, the substrate was treated to three 10 minute washes in 1X TE buffer. For single stranded DNA binding 160 nanograms of DNA were aliquoted out of the stock solution. This was heated in a water bath at 95° C for 10 minutes and immersed into ice cold 1X TE buffer to a final volume of 200 μl.

Radioactivity on disks was detected by both scintillation counting of total radioactivity and using a high voltage proportional counter for counting from rough and smooth disk faces. Samples were counted over 200 minute periods. A substrate disk, treated identically without being exposed to the radiolabeled DNA was used as a control. All the raw sample counts were corrected for

background (control value) radiation levels. Scanning electron microscopy was performed as previously described [6].

RESULTS AND DISCUSSION

The low resolution scanning electron microscope (SEM) images in figure 1 reveal differences in the texture of the rough (R) and smooth (S) surfaces and cross-sectional views of the electropolymerized PPy film used in DNA binding experiments.

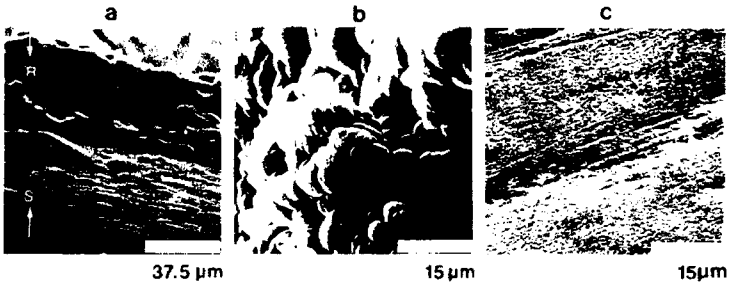

Fig.1. SEM images of PPy (a) Cross-sectional end view, (b) surface morphology of the rough surface, (c) surface morphology of the smooth surface.

The conductivity measurements of the two sides being identical, the only difference observed relevant to DNA binding is the difference in the surface morphology. The rough side of the film (polymer growth face) shows a regular array of craters and bumps whereas the smooth side (Pt electrode face) is devoid of any such structures. In fact preliminary studies (data not shown) have shown that DNA binding is higher on the rough surface than on the smooth surface which would agree with our SEM observations of the apparent lower surface area of the smooth side relative to the rough side.

Rough face binding kinetics experiments of single and double stranded DNA shown in figure 2 are in agreement with the previously suggested diffusion limited binding model which is expressed in equation 1.

$$n = 2C(Dt/\pi)^{1/2} \qquad (1)$$

where n is the number of molecules binding per unit area, C is the bulk solution DNA concentration, D is the diffusion coefficient and t is the time.

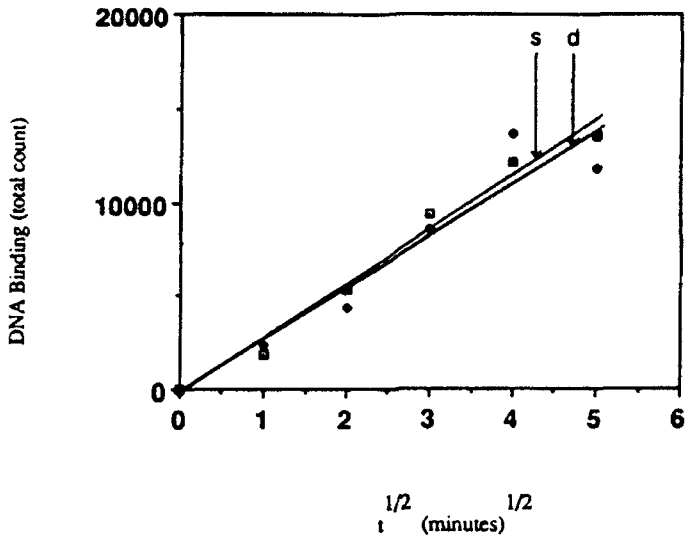

Fig. 2. DNA binding kinetics onto the rough surface of PPy: (■) single stranded DNA (s); (●) double stranded DNA (d). Best fit linear regressions to these data are shown.

It can be seen that for the initial stages of binding, a $t^{1/2}$ dependence is observed. Our studies seem to suggest that single stranded DNA binding to PPy takes place similarly to that of the double stranded DNA. We measured the R / S radioactivity ratio (the ratio of radioactivity detected on the rough surface to that detected on the smooth surface) for rough side uptake of both the single and double stranded DNA as shown in figure 3. There was a progressive decrease in the R / S ratio for both DNAs indicating that at longer exposure times each DNA was penetrating the disk and moving toward the smooth side. The higher level of R / S for the single stranded DNA might be explained by its decreased mobility once bound to PPy. The exposed bases of single stranded DNA may have the capability to bind PPy by hydrogen bonding or even through base stacking interactions with the PPy backbone ring system. These bonding opportunities are absent in double stranded DNA and may be responsible for its higher internal mobility and consequently lower R / S ratio. The quantitative levels of R / S ratios agree with a simple experiment indicating that the half attenuation thickness for PPy measuring S^{35} disintegration was about 40 microns. For 120 micron disks the ratio should be about 8:1.

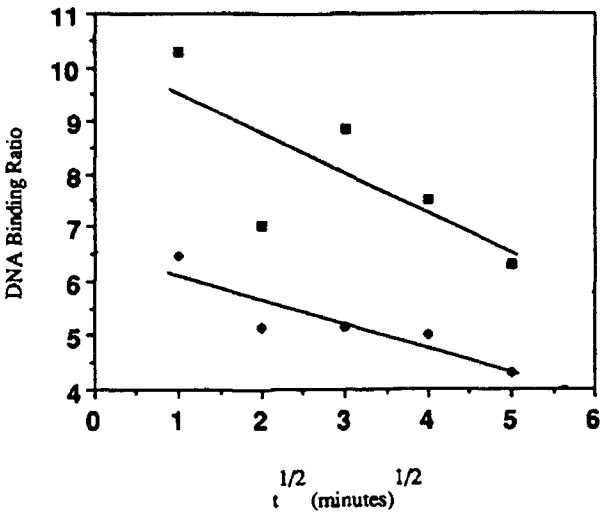

Fig. 3. Ratio of R / S surface radioactivity following rough surface DNA uptake on PPy : (■) single stranded ; (●) double stranded DNA uptake. Best fit linear regression to these data are shown.

These binding results suggested we probe the surface of the PPy films at very high resolution using TEM techniques. We have undertaken such studies and preliminary TEM images of the rough surface (data not shown) shows the presence of an abundance of grooves or channels [9]. The dimensions of these channels support our observations that the DNA could easily penetrate into these channels and move towards the interior. The smooth surface is almost devoid of such channels and has the appearance of very regular and dense chain packing. We have not yet determined whether DNA penetrates this surface. These observations are thus in agreement with our DNA binding experiments.

CONCLUSIONS

We have demonstrated that the diffusion limited binding model proposed for double stranded DNA applies to single stranded DNA as well. The penetration of DNA from the rough surface into the interior of the disk has been observed. This phenomenon is in agreement with SEM and high resolution TEM images showing channels and grooves on the rough surface. The DNA binding and matrix penetration phenomena may find uses for PPy as a new material in biotechnology applications.

ACKNOWLEDGEMENTS

Support from URI grant DAAL 03-91-G-0064 from the Army Research Office is gratefully acknowledged.

REFERENCES

(1) J. Roncali, A. Yassar and F. Garnier, Synthetic Metals, 28 C 275 (1989).
(2) S. Hotta, Synthetic Metals, 22, 103 (1987); 26, (1988).
(3) A. F. Diaz and J. C. Lacroix, New J. Chem, 12, 171 (1988).
(4) B. D. Malhotra, N. Kumar and S. Chandra, Prog. Poly. Sci., 12 179 (1988).
(5) D. S. Minehan, K. A. Marx and S. K. Tripathy, Macromolecules in Press.
(6) J. O. Lim, D.S. Minehan, M. Kamath, K. A. Marx and S. K. Tripathy MRS Proceedings 255 (1992).
(7) D. S. Minehan, K. A. Marx and S. K. Tripathy, Proc. Amer. Chem. Soc. Div. Polymeric Materials: Science & Eng. 64, 341-342
(8) J. S. Vrentas and J. L. Duda, "Diffusion", in Encyclopedia of Polymer Science and Engineering, Vol. 5, eds. H.F. Mark et al. (John Wiley Inc, New York 1986), pp 462-507.
(9) K. A. Marx, G. C. Ruben, Rajiv Pande, J. O. Lim, S. K. Tripathy and D. L. Kaplan, manuscript in preparation.

BIOTINYLATED POLYTHIOPHENE COPOLYMER - A NOVEL ELECTROACTIVE BIOMATERIAL UTILIZING THE BIOTIN-STREPTAVIDIN INTERACTION

Jeong-Ok Lim, Manjunath Kamath, Kenneth A. Marx, and Sukant K. Tripathy, Center for Advanced Materials, Department of Chemistry, University of Massachusetts Lowell, Lowell, Massachusetts 01854,
David L. Kaplan, Lynne A. Samuelson, Biotechnology Division, U.S. Army Natick Research, Development & Engineering Center, Natick, Massachusetts 01760

ABSTRACT

A novel hierarchical biomaterial capable of incorporating any biotinylated biomolecule has been created. Our strategy is to biotinylate one-dimensional electroactive polymers and use a bridging streptavidin protein on Langmuir-Blodgett (LB) organized films. The following copolymeric system which enables functionalization of other molecules and formation of good monolayers was employed. Biotinylated poly(3-methanolthiophene-co-3-undecylthiophene) (B-PMUT) demonstrated a significantly better isotherm implying superior molecular packing compared to poly(3-methanolthiophene-co-3-undecylthiophene) (PMUT) on the LB air-water surface. The isotherm showed significant area expansion when streptavidin was injected below the B-PMUT monolayer in 0.1mM NaH_2PO_4/0.1M NaCl buffer (pH 6.8) subphase. We then incorporated biotinylated phycoerythrin (B-PE) into this novel biomaterial by binding the unoccupied biotin binding sites on the bound streptavidin (4 sites total). The pressure-area isotherm of the protein injected monolayer showed area expansion. A characteristic fluorescent emission peak at 576nm was detected from the monolayer transferred onto a solid substrate. These observations demonstrated the function of B-PMUT in hierarchical monolayer assembly of molecules incorporating the biotin / streptavidin interaction.

INTRODUCTION

Polythiophene is one of the most important heteroaromatic electrically conducting polymers. It possesses good thermal and environmental stability and its ease in processibility makes it attractive for possible applications in electronics, sensors and nonlinear optics [1-4]. Although the aromatic rings are responsible for rigidity and strong intra- and interchain interactions, solubility can be obtained by substituting alkyl chains (longer than 4 carbons) on the polymer backbone [5].

Incorporation of biological molecules, which possess inherent intelligent properties, into well-defined, oriented assemblies is extremely important for potential bioelectronic, biomedical and biotechnological applications. Here, the polymeric material primarily serves to immobilize biological molecules but could potentially function in a signal transduction role as well. The Langmuir-Blodgett technique is advantageous for the fabrication of a hierarchical structure due to its ability to organize molecules into an ordered monolayer and subsequently to manipulate monomers into multilayer films toward a desired architecture. Recently, this technique has been used to prepare spatially oriented organized protein molecular assemblies [6].

Our approach has involved the highly specific recognition of biotin by streptavidin. The binding affinity of biotin to the tetrameric protein streptavidin is strong (10^{15} M) and once formed the complex is essentially irreversible [7]. It was demonstrated earlier that one can use the LB cassette approach to create ordered monolayers using biotinylated lipid which first binds to streptavidin [8,9]. This streptavidin can subsequently bind biotinylated phycoerythrin, a fluorescent protein. The advantages of using polymer material over lipid include the monolayer film stability and strength.

Here, we have chosen the copolymer system of 3-undecylthiophene and 3-methanolthiophene, with modification of the hydroxyl group of methanol by biotin in order to extend the cassette approach. Our goal is to combine the conductivity

Mat. Res. Soc. Symp. Proc. Vol. 292. 1993 Materials Research Society

properties of the copolymer with the inherent flexibility of the biotin / streptavidin binding system. In the present study, we present the method of synthesis of the novel biotinylated copolymer and demonstrate the self-assembly of the cassette system using the fluorescent properties of biotinylated phycoerythrin.

EXPERIMENTAL

Polymer Synthesis

Synthesis of poly(3-undecylthiophene-co-3-methanolthiophene) (PMUT)

Synthetic grade anhydrous ferric chloride (Aldrich), 0.09 mol. was dried under vacuum at 100^{o}C prior to reaction. Then nitrogen was introduced along with 100 ml of dry chloroform (Aldrich). 0.02 mol of 3-undecylthiophene (TCI America) and 0.01 mol of 3-methanolthiophene (Aldrich) in 10 ml of chloroform was added dropwise under vigorous stirring. The reaction mixture was allowed to stir for two days till the reaction was complete. The reactant solution was precipitated into 500 ml methanol (Aldrich). The product was then cleansed with methanol in a Soxhlet extractor for two days.

Synthesis of biotinylated poly(3-undecylthiophene-co-3-methanolthiophene) (B-PMUT)

A solution of 0.01 mol biotin (Biomeda), 0.011 mol N,N-dicyclo-hexylcarbodiimide (Aldrich), 0.011 mol poly (3-undecylthiophene-co-3-methanolthiophene) and 0.001 mol 4-pyrrolidinopyridine (Aldrich) in 50 ml dichloromethane (Aldrich) was stirred at room temperature until esterification was complete. The N,N-dicycloundecyl urea was filtered and the filtrate was washed with water (3x50 ml), 5% acetic acid solution (3x50 ml) and again with water (3x50 ml), dried ($MgSO_4$) and solvent was evaporated in rotary evaporator under reduced pressure to give the biotinylated copolymer.

LB monolayer formation

All monolayer studies were carried out on a Lauda MGW Filmwaag trough with a surface area of approximately 930cm^2. In the case of pressure-area isotherms of BMUT and B-PMUT, 0.5 mM chloroform solution was spread onto the purified MilliQ water subphase. For the measurement of pressure-area isotherms following streptavidin injection under the B-PMUT monolayer, the subphase was composed of an aqueous solution of 0.1mM NaH_2PO_4 and 0.1M NaCl, at pH 6.8. Streptavidin (0.1mg in 5ml of the buffered subphase) was injected under the spread film and left to incubate for two hours at 30^{o}C, and subsequently biotinylated phycoerythrin was introduced under the polymer and streptavidin layer. The streptavidin and biotinylated phycoerythrin were purchased from Biomeda Co. and used as received. Compression was then carried out at a speed of 2 mm^2/min until collapse of the film was observed. For transfer studies, the polymer was spread, followed by streptavidin introduction and incubation in the expanded state for two hours, subsequently followed by B-PE introduction and incubation for two hours and then compressed to an annealing surface pressure of approximately 15 mN/m for deposition. Monolayer films were then transferred onto glass solid supports for fluorescence spectroscopy.

RESULTS AND DISCUSSION

Materials Synthesis and Characterization

The synthesis of biotinylated copolymer involves two steps, the synthesis of copolymer of 3-undecylthiophene and 3-methanolthiophene and attachment of biotin in the second step as shown in Figure 1.

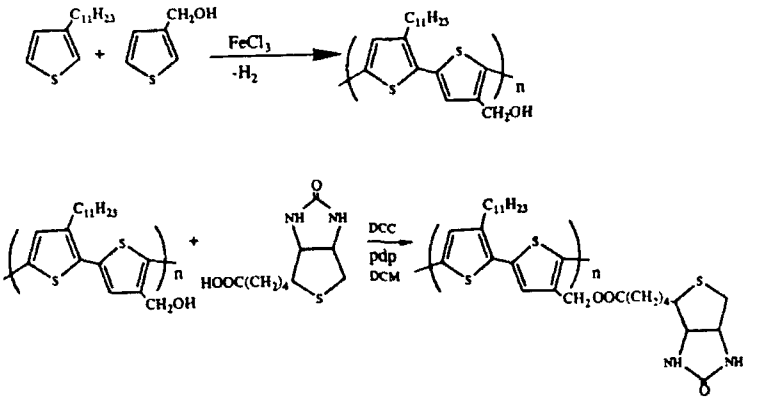

Figure 1. The synthesis schematic of PMUT and B-PMUT.

Infrared measurements of PMUT and B-PMUT were carried out on KBr discs and are shown in Figure 2. Both PMUT and B-PMUT showed a principal absorption peak at 780 cm^{-1} due to the C-H out-of-plane vibration of the 2,5-disubstituted thiophene and a distinct peak around 810 cm^{-1} due to the C-H out-of-plane vibration of the 2,3,5-trisubstituted thiophene [10]. B-PMUT exhibited new characteristic peaks at 1678cm^{-1} due to ester linkage and a sharp peak at 3400 cm^{-1} from N-H stretching. Meanwhile, the broad O-H absorption peak at 3400cm^{-1} shown in PMUT disappeared in B-PMUT.

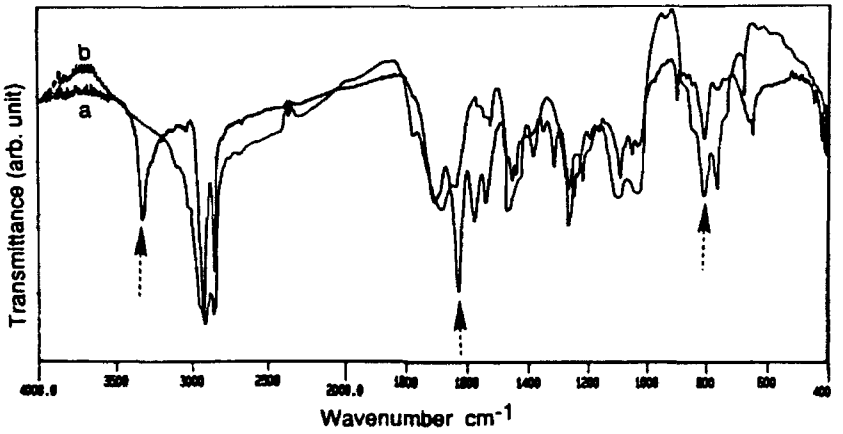

Figure 2. FT-IR spectra of (a). PMUT (b). B-PMUT.

Visible spectra were measured in chloroform and are shown in Figure 3. Both the copolymers showed a broad λ_{max} around 400-450 nm with absorption increasing from 600 nm indicating the presence of an extended π-conjugation along the polymer backbone. B-PMUT showed a blue shift due to the interruption of π-conjugation by the introduction of biotin.

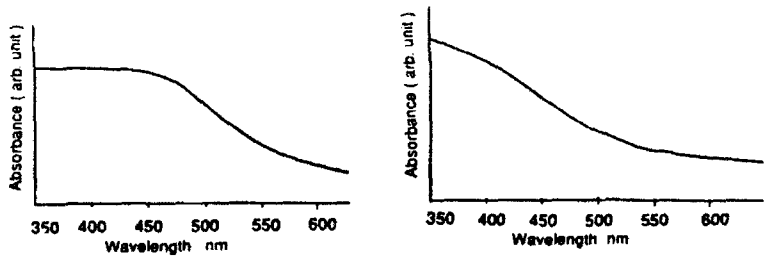

Figure 3. Visible spectra of (a). PMUT (b). B-PMUT.

In order to evaluate the effectiveness of biotinylation of PMUT in the functions of LB formation and subsequent bindings with streptavidin and B-PE, a series of pressure-area isotherm measurements were performed. The isotherms of the PMUT, B-PMUT, streptavidin injected B-PMUT monolayers and B-PE injected streptavidin/ B-PMUT monolayers are given in Figures 4 and 5.

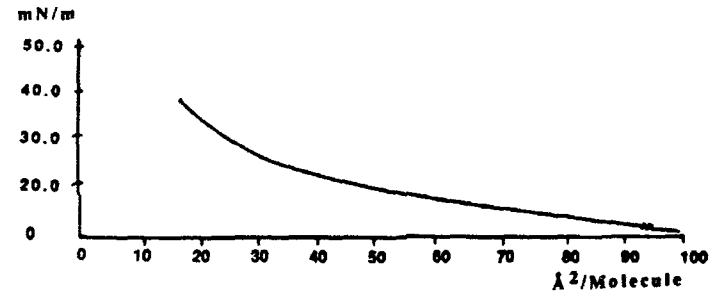

Figure 4. The pressure-area isotherm of PMUT on MilliQ water at 30°C.

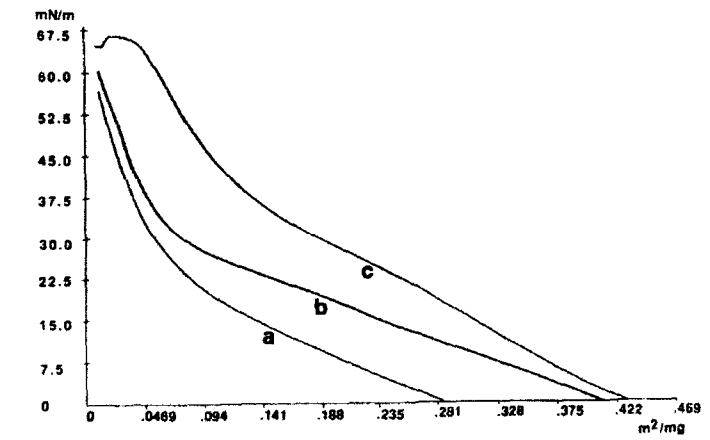

Figure 5. The pressure-area isotherms of (a). B-PMUT (b). B-PMUT / Streptavidin (c). B-PMUT / Streptavidin / B-PE.

Biotinylated copolymer (B-PMUT) demonstrated a significantly better isotherm than copolymer (PMUT) implying superior packing compared to the copolymer on the air-water interface. This significant improvement in the formation of a B-PMUT monolayer suggests that the biotinylation enhanced the LB film formation by contributing hydrophilicity to the copolymer molecule.

Another advantage of the B-PMUT includes increased stability of the monolayer during transfer and efficient deposition onto solid supports. It was found that a constant surface pressure of 15 mN/m was maintained over a period of 15 minutes with a transfer ratio of approximately 65%. B-PMUT was observed to possess fairly strong mechanical properties as shown by the formation of an elastic fiber-like string when the collapsed monolayer film was drawn up using a teflon-coated tip.

The isotherm shown in Figure 5 showed area expansions when streptavidin and B-PE were injected below the B-PMUT monolayer indicating the occurrence of effective binding between the biotin and streptavidin and subsequently biotinylated PE with streptavidin. This change supports the original goal of the biotinylation of this polymer, which was to employ the biotin-streptavidin complexation for subsequent immobilization of any biotinylated macromolecular assembly into LB films.

The monolayer films were transferred to hydrophobic solid glass supports using the horizontal dipping technique at an annealing pressure of 15 mN/m. The presence of the phycoerythrin is probed by its intense and characteristic fluorescence. Measurements were carried out by exciting the samples with 496 nm light from an Argon ion laser and scanning from 510 to 670 nm [8]. The fluorescence spectra of B-PMUT with streptavidin, and B-PMUT and streptavidin with B-PE, are shown in Figure 6. As shown, only the B-PMUT/streptavidin/B-PE monolayer gives a strong emission at 576 nm which corresponds to the fluorescence spectrum of the native phycoerythrin [9]. These results along with other controls provide convincing evidence that the protein has adsorbed to the B-PMUT / streptavidin monolayer via the bridging biotin / streptavidin interaction.

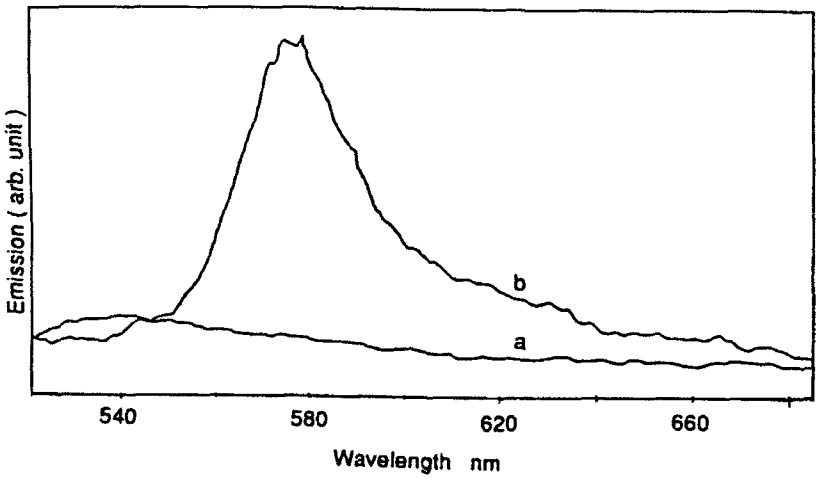

Figure 6. Fluorescence spectra of (a). B-PMUT / Streptavidin
(b). B-PMUT / Streptavidin / B-PE.

CONCLUSION

We have shown that biotinylation of thiophene copolymer enabled formation of superior LB films at the air-water interface by contributing a flexible spacer group and enhancing the hydrophilicity of the copolymeric molecule. In addition, through the biotin / streptavidin complexation, hierarchical structure fabrication containing protein was demonstrated. These results suggest that this novel copolymer is a promising material for potential device applications in which any biotinylated macromolecule may be attached to the polymer monolayer via the bridging biotin / streptavidin interaction system.

ACKNOWLEDGEMENTS

We would like to acknowledge the support from DOD-URI grant DAAL 03-91-G-0064, and Harry Gao for his technical assistance with laser fluorescence spectroscopy.

REFERENCES

1. H.S. Nalwa, Die Angewandte Makromolekulare Chemie, 188, 105 (1991).
2. R.L. Elsenbaumer, K.Y. Jen, G.G. Miller and L.W. Shacklette, Synthetic Metals, 18, 277 (1987).
3. H. Naarmann, Adv. Matel., 2, 345 (1990).
4. S.R. Marder, J .N. Perry, F.L. Klavetter and R.H. Grubbs, Chem.Mater., 1, 171 (1989).
5. S.Hotta, Synthetic Metals, 22, 103 (1987) ; 26, 267 (1988).
6. H. Hass and H. Molhald, Thin Solid Films, 180, 101 (1990).
7. R.K. Gimlick and R.W. Giese, J. Biol. Chem., 263, 210 (1980).
8. L. A. Samuelson, P. Miller, D. Galotti, K. A. Marx, J. Kumar, and S. K. Tripathy, Langmuir, 8, 604 (1992).
9. R. Blankenburg, P. Mellur, P. Ringsdorf and C. Salesse, Biochem., 28, 8214 (1989).
10. T. Yamamoto, K. Sanechika, and A. Yamamoto, Bull. Chem. Soc. Jpn., 56, 1497 (1983).

THE ENZYMATIC MEDIATED POLYMERIZATION OF PHENOL AND ANILINE DERIVATIVES ON A LANGMUIR TROUGH

Ferdinando F. Bruno*, Joseph A. Akkara+, Lynne A. Samuelson+, David L. Kaplan+, Kenneth A. Marx*, and Sukant K. Tripathy*[1]

*Center for Advanced Materials, Department of Chemistry, University of Massachusetts-Lowell, Lowell, Massachusetts 01854.

+Biotechnology Division, U.S. Army Natick Research, Development & Engineering Center, Natick, Massachusetts, 01760-5020.

ABSTRACT

Enzymatic polymerization of a number of monomers in an ordered lattice on a Langmuir trough (L-T) was investigated. The assembly and polymerization of two mixed monomeric systems consisting of 4-tetradecyloxyphenol (C14PP) with phenol, and 4-hexadecylaniline (C16PA) with aniline, in various ratios were carried out. Polymerization was obtained with C14PF and phenol (in the ratio 1:10), and C16PA and aniline (in the ratio 1:2) on buffered MilliQ water (pH 7.5) using the enzyme horseradish peroxidase (HRP) at 20°C. Polymerized monolayers were then transferred to appropriate substrates for UV-Vis, third order non linear optical (NLO) properties, and thickness measurements. Thermogravimetric analysis (TGA) was performed on the final polymers. Results suggest that the lattice controlled polymerization results in highly ordered conjugated polymers with improved functional, electronic, NLO and processability properties, which form a basis for intelligent materials design and applications.

INTRODUCTION

Phenolic resins are one of the most studied polymeric materials because of the increased product demand ranging from commodity construction materials to high technology applications in electronics and aerospace. The starting materials for the production of these resins are phenols, or derivatized phenols, and aldehydes in the presence of a basic or acidic catalyst. However, since formaldehyde is a toxic chemical and potentially carcinogenic agent, production of the resins is strongly questioned from a safety standpoint.

A possible safe alternative is the use of biological enzymes for

[1]To whom reprint requests should be addressed

Mat. Res. Soc. Symp. Proc. Vol. 292. 1993 Materials Research Society

the coupling of phenols in the presence of hydrogen peroxide. The high specificity and catalytic rate of the enzyme minimizes the undesirable byproducts and simultaneously leads to the development of an environmentally friendly chemical process. This synthetic procedure in bulk solution was studied by Dordick et al. [1] and more recently by Akkara et al. [2]. They found that in dioxane/water systems, HRP catalyzes the polymerization of derivatized phenol and aniline compounds. The polymers exhibited good thermal stability and also interesting non linear optical (NLO) properties.

One major limitation of these polymer products is the difficulty found in the processing due to the presence of extensive crosslinking in the structure. To overcome this problem we employed enzymatic synthesis on a L-T. This approach significantly decreases the possibility of crosslinking, thereby improving the processability, while maintaining or even improving the electrical and third order NLO properties. This methodology was found to be applicable to various related compounds [3]. Here we report data on polymers formed by C14PP and phenol (1:10 ratio) and by C16PA and aniline (1:2 ratio). In particular, we characterized the two systems by pressure-area isotherms, TGA, and UV-Vis spectroscopy. Furthermore, for the C14PP/phenol we measured optical/electrical properties and thickness by means of ellipsometry and Atomic Force Microscopy (AFM).

EXPERIMENTAL

A Lauda film balance equipped with a constant temperature bath (Langmuir Filmwaage, Model D, Lauda-Brinkman, Westbury, NY) was used. The surfactant C14PP was chemically synthesized by O-alkylation of hydroquinone with 1-bromotetradecane. C16PA was purchased from Aldrich Chemical Co. (Milwauke, WI) and used as received. Monomers at 1-2 mg/ml concentration were solubilized in chloroform and spread at the air-water interface. The monolayers were prepared at the air-water interface according to a published procedure [3]. The subphase contained two liters of 0.85 mM HEPES buffer, pH 7.5, with 12-25 mg of enzyme per liter. Powdered horseradish peroxidase (HRP) (EC 1.11.1.7), was preadded to the L-T subphase (Type II, 150-200 units/mg, Sigma Chemical Co., St. Louis MO). Once the monomer at the air-water interface was spread onto the aqueous subphase containing HRP and compressed to 15 mN/m, hydrogen peroxide was injected into the subphase to commence the polymerization reaction.

Spectral characterization of monolayers on quartz slides was performed with a Perkin-Elmer Lambda 9 UV-Vis-Near IR spectrophotometer (Norwalk, CT). TGA measurements of the monomers and surface skimmed polymers were performed under nitrogen with a 10 C/min rate of temperature increase. A TGA 2950 from TA

Instrument Inc (New Castle, DE) was used.

Five monolayers of C14PP/Phenol polymer deposited on fused silica (refractive index n=1.457) were measured for thickness by ellipsometry using a Thin Film Ellipsometer (43603-200E, Rudolph Research, Flanders, NJ) at λ=0.6328 μm. One monolayer of C14PP/Phenol was deposited on a silica wafer for AFM using a Digital Instrument Inc NANOSCOPE AFM (Santa Barbara CA).

For electrical measurements, an "Interdigitated Microsensor Electrodes" (IME) was used. The IME was composed of fifty gold fingers, each 15 μm wide, 4985 μm long, and with a space of 15 μm between each finger. This sensor was covered with bulk C14PP/phenol or C16PA/aniline polymer and then placed in a sealed chamber which was alternately flushed with nitrogen and evacuated three times, followed by resistance measurements of the undoped polymer. Nitrogen was gradually introduced along with dopant (iodine) into the chamber and electrical resistance was monitored. The measurement process was halted when saturation in conductivity resulted.

Third order non linear optical susceptibility ($\chi^{(3)}$) was determined in solution by degenerate four wave mixing with a frequency doubled Nd:YAG laser with 17 ps pulses at 532 nm. The average energy per pulse was 25mJ. The vertically polarized output was split into three beams, which are temporally and spatially overlapped in the sample contained in a 1 or 2 mm cuvette. The intensity of the phase conjugate beam proportional to the square of $\chi^{(3)}$ was measured.

RESULTS AND DISCUSSION

Pressure-area isotherms with unreacted monomers C14PP and C16PA, and mixtures of these monomers with phenol and aniline are shown in Fig. 1. An area of approximately 22 $Å^2$ to 25 $Å^2$ per molecule was observed for the pure monomer systems. This increased area per molecule in comparison to the area per molecule of an alkyl chain (20 $Å^2$/molecule [4]) may be attributed to the presence of the phenyl group. The presence of the phenyl group imposes a disk-shaped benzene ring of maximum dimensions of 7.4 Å across by 3.4 Å thick and of minimum dimension of 6.4 Å across by 3.4 Å thick (the thickness of the π-cloud) on the alkyl chain. The calculated area of the phenyl group from molecular modeling ranges from 21.8 to 25.2 $Å^2$. It is interesting to note that the introduction of the phenoxy group into the interior of the monolayer does not perturb the stability of the close packed monolayer shown by the C16PA isotherm which reaches a relatively high collapsed pressure of about 70 mN/m.

The expansion in area with added enzyme and underivatized phenol or aniline was encouraging because this indicates that these

components were permeating the monolayer. For reaction, underivatized phenol or aniline was added to the trough in ratios ranging from 1:1 to 500:1 (underivatized/derivatized). The reaction rate, upon injection of H_2O_2, was observed to increase as the ratio increased. UV-Vis spectroscopy characterizations (Fig.2) of the C16PA/aniline polymer multilayers exhibited a broad absorption in the visible spectrum, indicative of formation of a conjugated polymeric backbone structure. This absorption feature was absent in controls containing only the monomer mixtures. Controls run in the absence of either hydrogen peroxide or HRP also gave no evidence of polymer formation. Collapsed polymerized films, skimmed from the subphase surface, were dark in appearance, and highly stretchable. Similar results were found for the C14PP/phenol system [5].

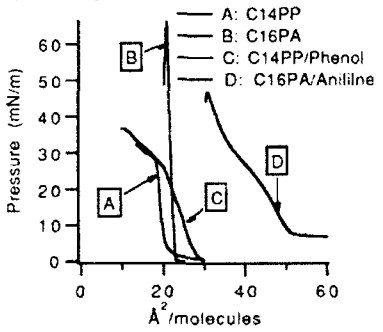

Figure 1. Isotherms of diferent monomers on MilliQ water (A,B), and in presence of HRP (C,D) at 20°C.

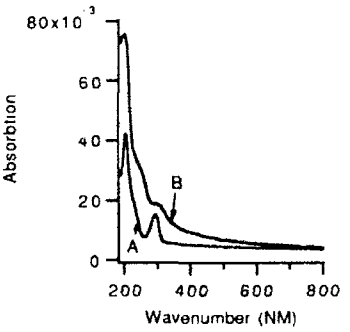

Figure 2. UV-Vis spectra of ten layers of C16PA/Aniline: (A) ten layers of the monomer, (B) ten layers of the polymer.

Thermal properties of the polymers were determined by TGA and are presented in Figure 3. The TGA analysis indicated that a significant amount of material remains after heating the polymer to 900°C. TGA of the C14PP/phenol polymer indicated about a 15% final residue value with two major temperature ranges of degradation; one between 250-400°C and the other between 400-470°C. Thermal analysis carried out for the C16PA/aniline polymer showed a 50% final residue value and similarly the presence of two different temperature ranges during the degradation process. The chemical and physical properties of this residual material have not been studied.

Optical ellipsometry is a way to measure the monomolecular thickness and quality of the films formed. By ellipsometry, we obtained a film thickness of 27.8±1 Å for the C14PP/phenol polymer. Our results are in reasonable agreement with the data (25Å) obtained by modelling calculations. We employed a value of n_f= 1.50 for the real refractive index of the film in the calculation of film

thickness. The use of this refractive index has precedent from previous investigations of monolayers [6], where values of 1.45-1.50 have been employed. The high end of this range was used, since the phenoxy and the phenyl group would be expected to increase the refractive index of the film, as can be seen by a comparison of the bulk refractive indices of tetradecane (n_D=1.4290), anisole (n_D=1.5160) and phenol (n_D=1.5509). Thickness results were confirmed by AFM measurements where the micrograph showed a regular flat surface of 30 Å or lower thickness.

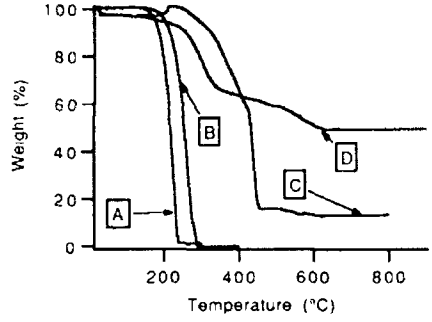

Figure 3. TGA of monomers (A) C14PP, (B) C16PA, and of polymers (C) C14PP/phenol (1:10), (D) C16PA/aniline (1:2).

Conductivity values of iodine doped polymerized multilayers of the C16PA/aniline (1:2) ranged from $3*10^{-3}$ to $1*10^{-5}$ S/cm. One such polymer sample was relatively stable and maintained a conductivity of $2.00*10^{-4}$ S/cm over a 3 day period after doping. The C14PP/phenol polymer showed similar behaviour [7] with a higher initial conductivity. There was also significant enhancement of the third order optical nonlinearities to values of $1*10^{-9}$ esu upon polymerization of the C14PP/phenol system. Such a result would be expected upon formation of a conjugated backbone structure.

A schematic of two possible arrangements of the polymerization products is given in figure 4.

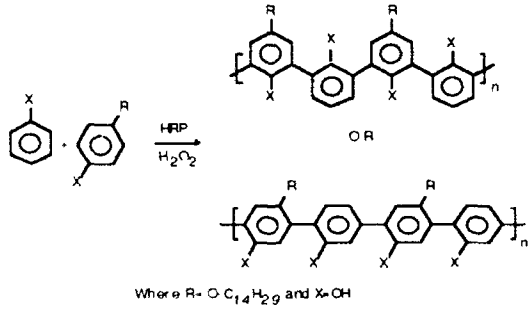

Figure 4. Schematic of two proposed polymer structures.

CONCLUSION

The biocatalytic approach to 2-D polymeric synthesis we have described is a free radical polymerization process [8]. A wide range of monomers will react under these conditions to provide a diversity of potential polymeric products for systematic studies of the effect of monomer substituents on mechanical, thermal, electronic and linear/non linear optical properties [3]. The process described here represents a general technique for the assembly and polymerization of conductive and optically active polymers in 2-D networks. Processing limitations observed with intractable polymers synthesized in bulk are surmounted with this technique and thin films are formed as the reaction progresses.

ACKNOWLEDGMENTS

The authors would like to acknowledge support from grant DAAL03-91-G-0064 from the Army Research Office. FFB would like to thank the Natick Army RD&E Center for a student grant.

REFERENCES

1) J. Dordick, M. A. Marletta and A. M. Klibanov, Biotechnol. Bioeng. 30, 31 (1987).

2) J.A. Akkara, K.J. Senecal and D. L. Kaplan, J. Polym. Sci. Part A: Polym. Chem. 29, 1561 (1991).

3) J. A. Akkara, F. F. Bruno, L. A. Samuelson, B. Mandal, D. L. Kaplan, K. A. Marx and S. Tripathy, U. S. Patent 5143828, (1992).

4) G. L. Gaines, in Insoluble Monolayers at Liquid-Gas Interfaces, Interscience Publishers edited by I. Prigogine, New York (1966).

5) F. F. Bruno, J. A. Akkara, L. A. Samuelson, B. Mandal, D. L. Kaplan, K. A. Marx and S. Tripathy. Polymer Preprints - ACS Div. Poly. Chem. 32 (1), 232 (1991).

6) D. L. Allara, R. G. Nuzzo, Langmuir 1, 45 (1985).

7) F. F. Bruno, J. A. Akkara, L. A. Samuelson, D. L. Kaplan, K. A. Marx and S. Tripathy, Proceedings of The First Intern. Confer. on Intel. Materials, Technomic Press, edited by T. Takagi, 78 (1992).

8) K. Ryu, D. R. Stafford and J. S. Dordick, ACS Symposium Series 389, 141 (1989).

SPECIFIC INTERACTION OF INFLUENZA VIRUS WITH ORGANIZED ASSEMBLIES OF POLYDIACETYLENES

DEBORAH H. CHARYCH, WAYNE SPEVAK, JON O. NAGY, AND MARK D. BEDNARSKI
The Center for Advanced Materials, Lawrence Berkeley Laboratory, Berkeley, California 94720

ABSTRACT

Supramolecular organizates of liposomes and Langmuir-Blodgett (LB) films are described which are capable of specifically binding to pathogens such as influenza virus. The specific interaction is between the hemagglutinin protein of the virus and an α-C-glycoside of sialic acid expressed on the surface of the liposome or LB film. Sialic acid-containing liposomes were found to inhibit influenza virus infectivity in cell culture, and may provide a basis for new materials which act as therapeutic agents. Sialic acid-containing LB films also specifically bind to the influenza virus. In this case, the conjugated polymer backbone acts as a built-in reporter of the binding event, measurable by a chromatic change in the visible absorption spectrum. These films may provide a basis for new materials which act as direct detectors of binding.

INTRODUCTION

This paper describes functionalized polydiacetylene liposomes and LB films which are tailored to bind pathogens, in this case, the influenza virus. Lipid monomers containing a diacetylenic unit are readily polymerized by ultraviolet (UV) irradiation, forming a polymer backbone of alternating ene-yne groups.[1,2,3]

The surface lectin of the influenza virus, hemagglutinin (HA), is known to bind to terminal α-glycosides of N-acetyl neuraminic acid (sialic acid), found in cell surface glycoproteins and glycolipids.[4,5] This binding event is the first step of the influenza infectious cycle.[6] We have synthesized a polymerizable lipid which contains a C-glycoside of sialic acid as the head group. This lipid was incorporated into mixed LB monolayers and mixed liposomes. The design of this molecule imparts several important features to the supramolecular assembly: the C-glycoside is stable to viral enzymatic hydrolysis relative to the naturally occuring α-O glycoside, polymerization of the layers renders the entire organizate stable under a variety of conditions of temperature and solvent, and finally, polymerization imparts the structures with the desirable optical properties of a conjugated polymer.

Mat. Res. Soc. Symp. Proc. Vol. 292. 1993 Materials Research Society

Polymerized liposomes containing the sialic acid lipid are found to inhibit influenza virus infectivity and hemagglutination of erythrocytes. Polymerized LB flims containing the same α-C glycoside also specifically bind the influenza to a surface. The visible absorption of the conjugated polydiacetylene provides a "built-in" detector of the binding event.

EXPERIMENTAL

Liposomes were prepared by combining chloroform solutions of the monomers **3** and **4** (Figure 1A) to give the desired percentage of sialoside-lipid **3** to be expressed at the liposome surface. The chloroform was removed by rotary evaporation and deionized water was added to give approximately the desired concentration of total lipid (0.5 mM to 1 mM). This mixture was probe sonicated (Fisher sonic dismembrator model 300, 50% maximum output) for 15 minutes while maintaining a sample temperature between 70°C and 80°C. This produced a clear solution which was filtered through a 0.8 mm nylon filter to remove any undispersed lipid.[7] Polymerization was accomplished at room temperature under an argon atmosphere by irradiation at 254 nm.

Langmuir-Blodgett films were prepared by spreading a chloroform solution of the appropriate percentage of sialic acid lipid and matrix lipid onto the water surface contained in a standard Langmuir-Blodgett trough (KSV Instruments, Connecticut). Subsequent compression to the solid-analogous phase and irradition at 254 nm polymerizes the diacetylene units yielding an alternating ene-yne polymer backbone. The film is irradiated under a constant lateral surface pressure. The polymerized film is lifted onto glass slides coated with a monolayer of an octadecyl silane (octadecyltriethoxysilane, Huls America) by the horizontal touch method.

Hemagglutination inhibition (HAI) and Plaque reduction (PRA) were determined using a standard assay.[8] X31 influenza virus was prepared by infection in MDCK cells.[9]

RESULTS AND DISCUSSION

Inhibition of Influenza Infectivity by Polymerized Liposomes

Recently, dramatic enhancements in the inhibition of viral adhesion to erythrocytes have been achieved using synthetic polymeric polyvalent sialosides.[10,11,12] The greater potency of these synthetic polyvalent sialosides is postulated to arise from the additivity of binding energies[13] as is the case with naturally occurring polyvalent *glycoproteins. On the other hand, the binding of* monovalent sialosides such as compound **1** is relatively weak (KD ≈ 2 mM).[14] Our approach is to produce polyvalent sialosides by incorporating sialic acid lipids into a

Figure 1

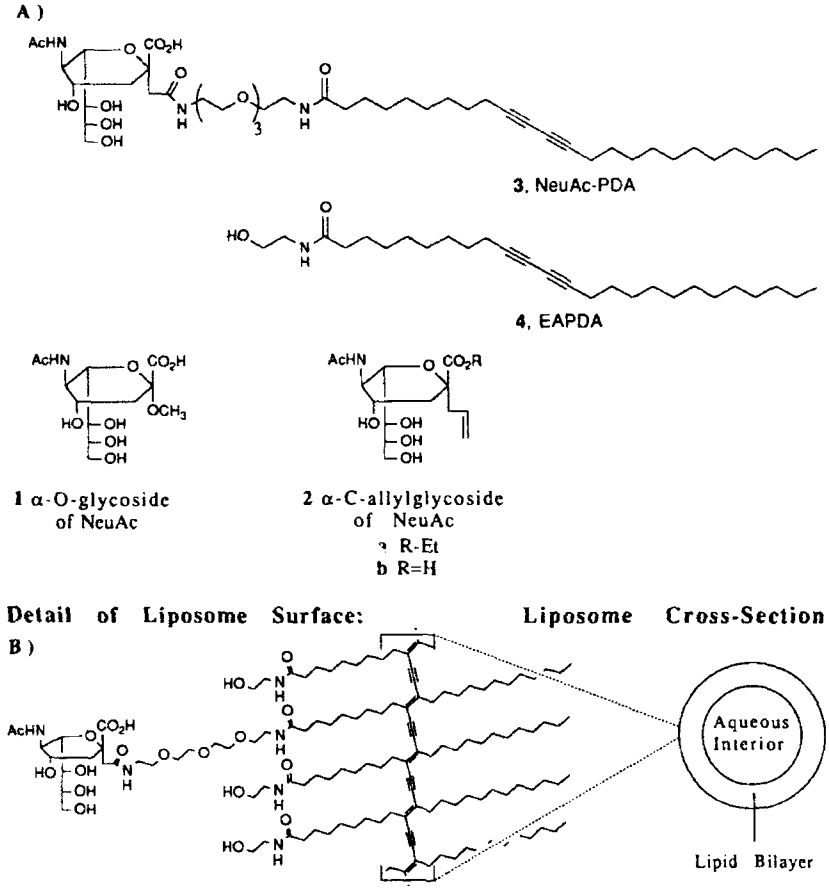

polymerized liposome. The liposome structure is anticipated to more closely resemble the natural cell surface by localization of pendant sialic acid head groups into a lipid bilayer matrix.

The liposomes are composed of sialoside lipid **3**, Figure 1A, which was synthesized from **2a**,[15] and mixed with a matrix lipid **4**,[16] Figure 1A. The percentage of sialoside presented at the liposome surface (0%, 1%, 5%, 10%, 30% and 60%) represents the mole percentage of lipid monomer **3** used in the liposome preparation. A representation of the liposome surface and the polymerized backbone is shown in Figure 1B. Transmission electron microscopy of the liposome solution reveals ellipsoid structures averaging on the order of 100 nm in length and 30 nm in width.

The data presented in Table 1 clearly indicate that the specific interaction of the influenza virus with the sialic acid lipids in the polymerized liposomes both inhibits hemagglutination and significantly reduces infectivity *in vitro*. For comparison, to achieve 50% inhibition of viral binding, the α-O-methyl glycoside of sialic acid (compound **1**) required a concentration of 2 mM and compound **2B** required a concentration of 10 mM. In sharp contrast, liposome preparations **III** and **IV** (5% and 10% of sialoside **3**) required as little as 5.7×10^{-7} M and 3.3×10^{-7} M concentrations of the sialoside to achieve complete inhibition of agglutination. This represents an increase in potency of more than 30,000 times over the corresponding monovalent sialic acid derivatives and is one of the most potent synthetic inhibitors of hemagglutination reported to date. In addition, liposome preparations

Table 1. Hemagglutination inhibition (HAI) and plaque reduction assays of liposome preparations **I-VI.**

Entry	Inhibitor	HAI[a] [3], M	Plaque Reduction [3], mM	Plaque Reduction[b]
1	Liposome **I** (0%,3)	0 (-)	0.000	0%
2	Liposome **II** (1%,3)	4.0×10^{-6} (-)	0.003	96%
3	Liposome **III** (5%,3)	5.7×10^{-7} (+)	0.016	97%
4	Liposome **IV** (10%,3)	3.3×10^{-7} (+)	0.030	46%
5	Liposome **V** (30%,3)	8.0×10^{-5} (-)	3.750	0%
6	Liposome **VI** (60%,3)	1.5×10^{-4} (-)	7.500	0%

[a]A (+) indicates complete inhibition while a (-) indicates no inhibition was observed at the given concentrations of **3**.

[b]The values represent the percent reduction in the number of plaques per well due to viral lysis of infected cells.

II and **III** (1% and 5% sialoside) inhibit plaque formation (infectivity) in cell culture by over 95% at concentrations in the micromolar range. The decrease in activity at higher loading of sialic acid is postulated to arise from steric effects which prevent effective binding to hemagglutinin. Liposomes which contain no sialoside (liposome **I**) do not specifically bind the influenza virus as demonstrated by the lack of inhibition of hemagglutination and cell infectivity.

Detection of Influenza Virus by Langmuir-Blodgett Films of Functionalized Polydiacetylenes

Supported LB films of polydiacetylene lipids[17,18] enable a well-defined surface to be constructed with full control of lipid surface density, surface pressure and composition. These films are readily amenable to microscopic, spectroscopic, and surface analysis. Figure 2 schematically represents the construction of a polydiacetylene LB film. The polymerized film is lifted using the horizontal touch method resulting in a "headgroup-out" orientation of the lipid. LB films for viral

binding typically contain 2-5% of the sialic acid lipid **3** in the matrix lipid. The supported films exhibit two absorption maxima, a 'blue form', (λ max = 625 nm) and a 'red' form (λ max = 530 nm).[19] The ratio of the two peaks is sensitive to temperature (thermochromism)[20,21] and, as will be shown, to binding of the influenza virus to the surface at room temperature.

Figure 2

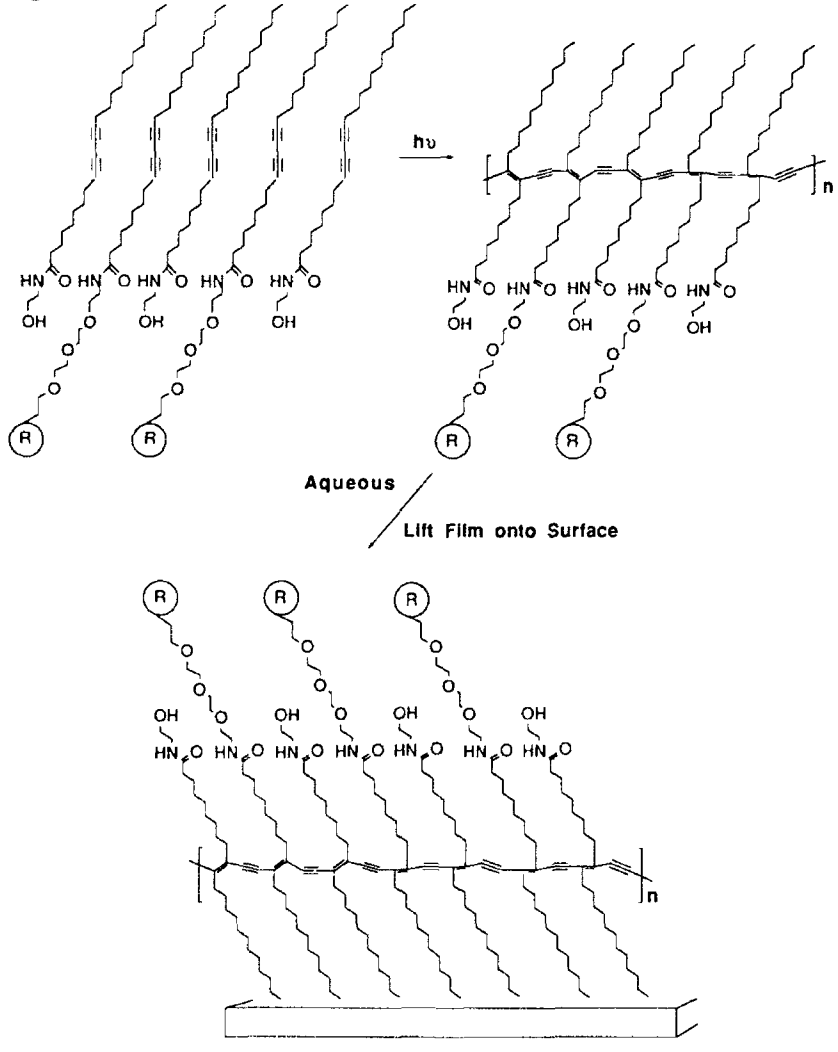

Angle-resolved X-ray photoelectron spectrosocopy of the N(1s) and C(1s) = O signal from the supported LB films indicates that the functional headgroups are expressed at the surface. These signals show the expected increase in intensity with decreasing take-off angle (angle between sample plane and detector). Ellipsometric analysis yields a film thickness of ca. 45-50 Å, in agreement with the expected thickness based on molecular models.

The absorption spectra of freshly prepared polymerized LB films typically exhibit a blue/red ratio (I_{625}/I_{530}) of 0.97 ± 0.005 (Figure 3A). However, upon incubation of a film containing sialic acid with the influenza virus, the intensity of the blue form decreases with a corresponding increase in the intensity of the red form where I_{625}/I_{530} is now 0.74 ± 0.004, or a 24% change in the ratio (Figure 3B). Films which contain no sialic acid show a change in ratio of less than 1% and films containing sialic acid but incubated with a buffer blank show a change in ratio of less than 5% (Figure 4 A,B,C). The chromatic change in film may be a result of disorder induced by the binding of the viral particle to the film.[22] Preliminary transmission electron microscopy independently verified specific binding of the virus to films containing sialic acid in the head group region. The films were incubated with the influenza virus and then subjected to a detergent wash followed by a series of rinses just prior to viewing in the electron microscope. As shown in Figure 5, films containing 5% of the sialic acid lipid bind to the virus. In contrast, films containing no sialic acid show an absence of virus particles following the rinsing procedure.

Figure 3. Visible absorption spectra of polymerized LB film containing 5% sialic acid lipid. **A**: film prior to incubation with influenza virus. **B**: film following incubation with influenza virus.

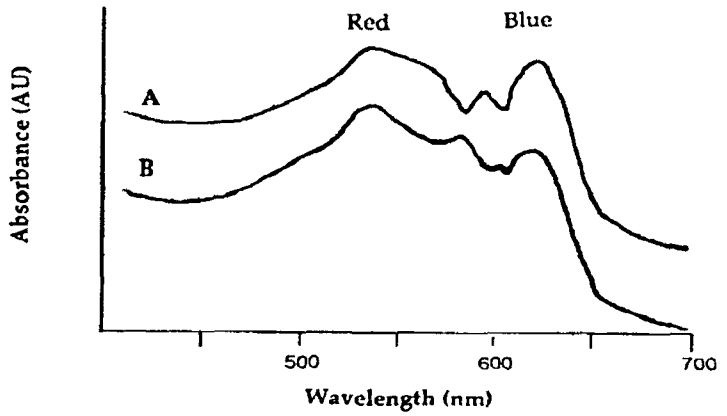

Thus, LB films of polydiacetylenes containing sialic acid were found to act as direct detectors of viral binding, where changes in the visible absorption of the film's polymer backbone were monitored. This system has the advantage of incorporating both the molecular recognition element and the optical 'reporter' unit within the same supramolecular organizate. This is in contrast to classical biosensor devices which generally require a fabricated device coupled to the molecular recognition element to transduce the binding event into a measurable signal.[23] We are currently working on improving the system's response by varying the nature of the conjugation.

CONCLUSION

New materials were described which provide a well-defined surface for specific interaction with the influenza virus. These materials show promise as new therapeutic and diagnostic agents based on multivalent carbohydrate structures. We have shown that polymerized liposomes incorporating sialic acid lipids are potent inhibitors of influenza virus *in vitro* infectivity and hemagglutination. These liposomes should also serve as important models for understanding pathogen-cell interactions.

Functionalized LB films of polydiacetylenes containing the sialoside-lipid also specifically bind influenza virus. These surfaces contain a 'built-in' optical detector which directly reports the binding event using visible absorption spectroscopy. Further development of these films may lead to an important new class of biosensors.

Figure 4. Relative response of LB films to influenza virus (see text) with appropriate controls. **A**: Film contains 5% sialic acid lipid, and incubated with influenza virus in PBS buffer. **B**: Film contains 0% sialic acid lipid, and incubated with influenza virus in PBS buffer. **C**: Film contains 5% sialic acid lipid, but incubated with PBS buffer only.

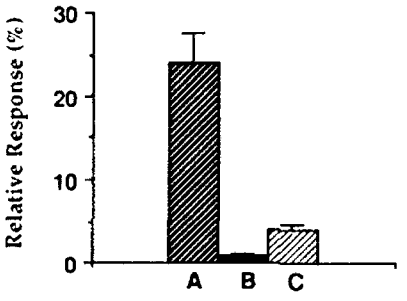

Figure 5. Transmission electron micrograph of influenza virus bound to film containing 5% sialic acid lipid. Films containing no sialic acid lipid show an absence of virus particles.

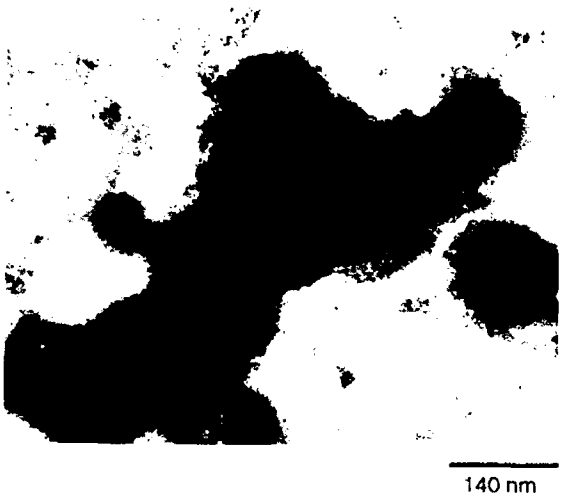

ACKNOWLEDGMENTS

This research was supported by the Director, Office of Energy Research, Office of Basic Energy Sciences, Division of Materials Sciences, by the Division of Energy Biosciences of the U.S. Department of Energy (DE-AC03-76SF00098 MB) and the National Institute of Health (Award #R29 GM43037-02). Mark Bednarski thanks the American Cancer Society for a Junior Faculty Award and Eli Lilly for a Young Investigator Grant. Wayne Spevak thanks the NIH for a predoctoral training grant.

REFERENCES

1. O. Albrecht, D.S. Johnston, C. Villaverde, and D. Chapman, Biochim. Biophys. Acta *687*, 165 (1982).
2. H. Bader and H. Ringsdorf, J. Poly. Sci., Polymer Chemistry Edition *20*, 1623 (1982).
3. H. Bader, R. Van Wagenen, J.D. Andrade, and H. Ringsdorf, J. Colloid and Interface Science *101*, 246 (1984).
4. J.C. Paulson, in *The Receptors*, edited by M. Conn, (Academic Press, New York, 1985), v. 2, pp. 131-219.
5. D.C. Wiley and J.J. Skehel, Annu. Rev. Biochem. *56*, 365 (1987).
6. K.S. Matlin, H. Reggio, A. Helenius, and K. Simons, J. Cell Biology *91*, 601 (1981).

7. R.R. New, in *Liposomes, A Practical Approach*, edited by R.R. New, (Oxford University Press, Oxford, 1990) pp. 33-104.
8. G.N. Rogers, T.J. Pritchett, J.L. Lane, and J.C. Paulson, Virology *131*, 394 (1983).
9. T. Barrett and S.C. Inglis in *Virology, A Practical Approach*, edited by B.W.J. Mahy, (Oxford University Press, Oxford, '985) pp. 123.
10. A. Spaltenstein and G.M. Whitesides, J. Am. Chem. Soc. *113*, 686 (1991).
11. M.N. Matrosovich, L.V. Mochalova, V.P. Marinina, N.E. Byramova, and N.V. Bovin, FEBS Lett. *272*, 209 (1990).
12. J.O. Nagy, P. Wang, J.H. Gilbert, M. Schaefer, T.G. Hill, M.R. Callstrom, and M.D. Bednarski, J. Med. Chem. (1992, in press).
13. W.P. Jencks, Proc. Natl. Acad. Sci., USA *78*, 4046 (1981).
14. N.K. Sauter, M.D. Bednarski, B.A. Wurzburg, J.E. Hanson, G.M. Whitesides, and D.C. Wiley, Biochemistry, *28*, 8388 (1989).
15. J.O. Nagy and M.D. Bednarski, Tetrahedron Lett. *32*, 3953 (1991).
16. W. Spevak, J.O. Nagy, D.H. Charych, M.E. Schaefer, J.H. Gilbert, and M.D. Bednarski, J. Am. Chem. Soc. (1992, in press).
17. B. Tieke, H.J. Graf, G. Wegner, B. Naegele, H. Ringsdorf, A. Banerjie, D. Day, and J.B. Lando, Colloid and Polymer Sci. *255*, 521 (1977).
18. D. Day and H. Ringsdorf, J. Polymer Sci. Polymer Letters Edition *16*, 205 (1978).
19. E. Lopez, D.F. O'Brien, and T.H. Whitesides, J. Am. Chem. Soc. *104*, 305 (1982).
20. B. Chu and R. Xu, Acc. Chem. Res. *24*, 384 (1991).
21. M. Wenzel and G.H. Atkinson, J. Am. Chem. Soc. *111*, 6123 (1989).
22. N. Mino, H. Tamura, and K. Ogawa, Langmuir *7*, 2336 (1991).
23. J.N. Row, Pharmaceutical Research *9*, 835 (1992).

α-HELICAL POLYPEPTIDE MATERIALS[1]

E. P. ENRIQUEZ, M. Y. JIN, R. C. JARNAGIN, and E. T. SAMULSKI
Dept. of Chemistry, University of North Carolina, Chapel Hill, NC 27599-3290

ABSTRACT

Poly(γ-benzyl-L-glutamate) (PBLG) may be derivatized on its periphery by covalently attaching $\chi^{(2)}$-active NLO chromophores at the termini of its sidechains and thereby give a new class of SHG materials.[1] The inherent liquid crystalline properties of concentrated solutions of α-helical PBLG may be exploited to establish unique supramolecular structures prior to E-field poling. When PBLG is derivatized at its N-terminus with lipoic acid, it will self-assemble on gold to give a thin film.[2] Angle-dependent XPS, ellipsometry, contact angle measurements, and grazing angle IR reflection-absorption spectroscopy give quantitative information about the orientation of the polypeptide α-helices relative to the substrate surface. Consequently, polypeptides, in particular, Merrifield-synthesized or recombinant DNA-expressed synthetic polypeptides, present a novel fabrication route to thin films wherein molecular-engineered functionalities (chemical, electrical, or optically active species) may be encoded into the macromolecule's primary structure and subsequently expressed spatially via the spontaneous self-organization of these rod-like polymers.

INTRODUCTION

The α-helical secondary structural motif in proteins has captured the interest of the scientific community since its conception in 1951 by Pauling and co-workers[3] and continues to be widely investigated to this date. Poly(γ-benzyl-L-glutamate) [PBLG], for instance, is one of the most extensively studied among synthetic polypeptides primarily because of its robust α-helical conformation—a rigid, rod-like macromolecule in a variety of solutions and in the solid state.[4] Oriented fibers of PBLG gave the first X-ray crystallographic proof[5] of the protein α-helix having internal hydrogen bonding between amide groups separated by 4 residues within the helical chain. PBLG forms the 18/5 helix, that is, there are 18 residues in between exact repeats of the secondary structure, corresponding to about 5 turns of the helix (3.6 residues per turn); this translates to 2.7 nm exact repeat distance, a helical pitch of 0.54 nm, and a 0.15 nm axial translation per residue.[4-6] The continued fascination with this secondary structure is evident by the recent attempts to obtain a molecular image of the helical structure of PBLG using the scanning tunneling microscope.[7-8]

These well-defined attributes of the α-helix and its packing in condensed phases have motivated us in our present work. There are attractive possibilities—by controlling the primary structure of the polypeptide either by Merrifield-type synthesis[9] or recombinant DNA technology,[10] a spatial organization of various chemical, electrical or optical functionalities is possible.[11] Herein, we report two types of "derivatives" of PBLG wherein each type retains

the rod-like character of the helical backbone: type I, the poly(glutamate) sidechains have been replaced by NLO (nonlinear optics) chromophores,[1] and type II, the N-terminus of the polypeptide was labelled with a disulfide-containing moiety which allows the helices to spontaneously adsorb (self-assemble) from solution onto gold surfaces.[2] Thus, NLO-active polypeptides in (oriented) macroscopic films and self-assembled monolayers are possible wherein the α-helical secondary structure persists.

POLYPEPTIDE DERIVATIVES

PBLG belongs to that class of synthetic homopolypeptides—the poly(glutamates)—which, under certain conditions, exhibit lyotropic (i.e., in solution)[6] or thermotropic (in the melt)[12] liquid crystalline phases depending on the character of the sidechain. Sidechain derivatization via transesterification is normally done starting from poly(L-glutamic acid), poly(γ-methyl-L-glutamate) [PMLG], or PBLG. PBLG was the most exclusively studied of these polypeptides because of its availability and excellent solubility properties. As the parent molecule itself, derivatives of the poly(glutamate)s normally exhibit the characteristic stability of the α-helical conformation of PBLG.

Type I. NLO-Active Sidechains

We have prepared polypeptide materials wherein the sidechain was replaced by second-order NLO chromophores. Figure 1 shows the general scheme of preparation for these materials; the starting homopolyptide in this case was PMLG. The NLO chromophores used, 3-(2-hydroxyethoxy)-4-methoxy-4'-nitrostilbene [3HEOMONS] and 4-(2-hydroxyethoxy)-3-methyl-4'-nitrostilbene [4HEONS], both have an electron donor group at one end of the conjugated structure and an acceptor group at the other end of the molecule. These molecules have large hyperpolarizabilities (β) making them excellent second-order NLO chromophores.[13-14] The type of linkage of the chromophore to the polypeptide backbone, either *ortho* or *para*, could influence the sidechain secondary structure of the polymer; possible structures are schematically shown in Figure 1. The degree of substitution affects the solubility properties of the polymer. The polypeptide which was moderately transesterified with ~53% of 3HEOMONS [P(3HEOMONS)LG] forms a gel phase in N,N-dimethylacetamide (DMAc) at high concentrations (20 weight % polymer) at room temperature, which upon heating to about 45 °C slowly transforms to a lyotropic liquid crystalline phase. The P(4HEONS)LG was less soluble than P(3HEOMONS)LG; apparently, the chromophores which have large dipole moments were able to stack with dipolar associations in between neighboring P(4HEONS)LG helices to form tightly bound side-by-side aggregates of the polymer. Solution-cast films from both polymers show amide vibrational frequencies that are characteristic of the α-helical secondary structure.[1]

It is well known that liquid crystalline solutions can be aligned in a magnetic or electric field[15] or by applying mechanical stress to the solution in one direction.[6] One can then make homogeneously (planar) aligned films from this same solution by drying. For example, a thermomechanically aligned

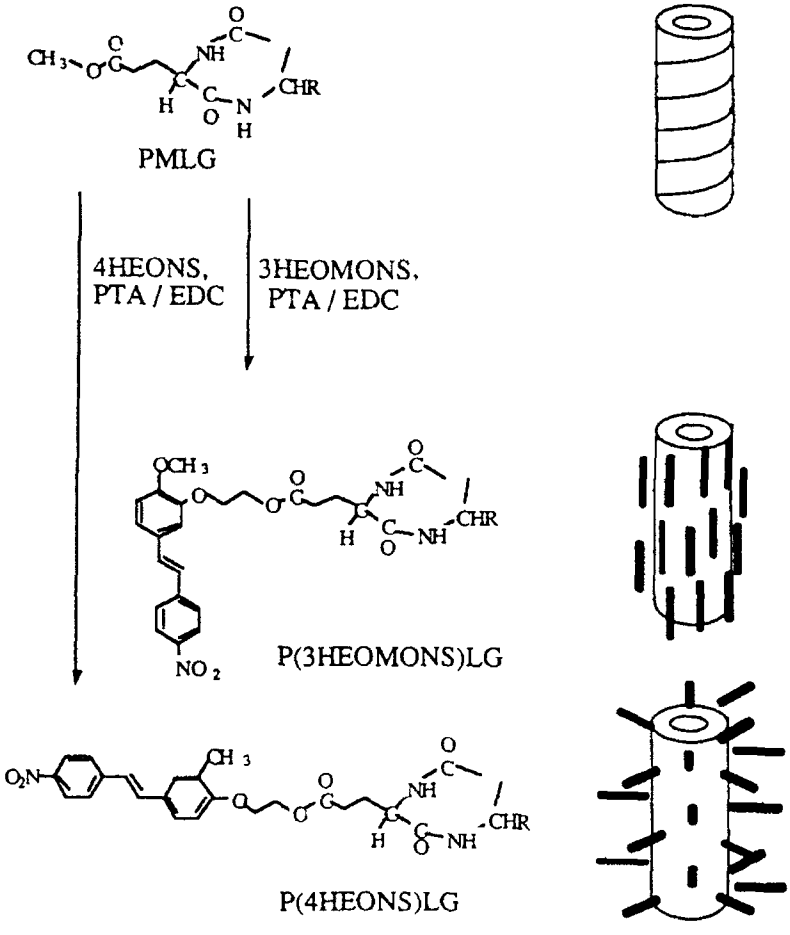

Figure 1. Transesterification of PMLG with second-order NLO-active chromophores (see text); PTA = *p* -toluenesulfonic acid catalyst, EDC = ethylene dichloride solvent. Typical reaction condition: PMLG (15% in EDC, 6 g), 3HEOMONS (5 times excess, 10.2 g), and PTA (3 times excess, 3.6 g) dissolved in 120 mL EDC at 60 °C, 24 h. The figures on the right are schematic diagrams of possible structures for the polypeptides.

P(3HEOMONS)LG film was prepared from a dilute solution in DMAc by slowly (over 24 hours) drying the solution on a glass substrate that had a temperature gradient; the polymer solution dried first on the hot side of the substrate resulting in a film/solution interface that moved slowly to the cool side. This slow movement of the interface caused mechanical stress which produced a partially homogeneous alignment as can be observed between crossed polars in a microscope.[1] The lyotropic phase that formed upon drying yields a suitable matrix for the NLO chromophores wherein the repulsive interaction between the polypeptide rods caused partial alignment of the NLO chromophores that was maintained in the film. Figure 2 shows the linear ultraviolet (UV) dichroism of the chromophore in the aligned P(3HEOMONS)LG film; a higher absorbance was observed from the geometry with the long helix axis parallel to the electric vector of incident polarized light than from the perpendicular geometry. The dichroic ratio ($A_{\parallel}/A_{\perp}$) of this aligned chromophore is 1.5. Since the transition moment of the chromophore is almost parallel to the molecular axis,[16] the UV-dichroism confirms the alignment of the chromophores along the helix alignment direction.

A basic requirement for large second-order NLO activity is a non-centrosymmetric packing of the chromophores in the bulk material; for practical optical applications, one major challenge is the preparation of NLO materials with the required temporal stability of this non-centrosymmetric order.[17] In the film described above, only the molecular axes of the chromophores were aligned (by excluded volume packing considerations). There is apolar symmetry: the probabilities of finding the dipole moment in parallel and antiparallel orientation are the same, that is, the non-centrosymmetric requirement for second-order NLO activity remains unsatisfied. This means that electric poling is needed to induce the chromophores into a non-centrosymmetric order. Figure 3 shows a schematic diagram of a corona poling experiment. A polypeptide on a conducting surface, such as indium tin oxide (ITO)-coated glass is subjected to a poling field: a large potential was applied between the tungsten tip and the ITO surface causing charges to accumulate in the air/film interface and equal, opposite charges in the film/ITO interface; this in turn results in a large electric field in the order of MV/cm through the film. This field interacts with the permanent dipole moments of the chromophores yielding a net polar orientation in a mobile phase at elevated temperature that can be retained below the glass transition temperature (T_g) of the poled film.

The second-order NLO property of the derivatized polypeptide may then be characterized by measuring the second harmonic generation (SHG) which is directly related to the second-order nonlinear susceptibility, $\chi^{(2)}$, of the material.[17] When a very intense light (e. g., laser light) of certain frequency is passed through a second-order NLO material, the frequency of the transmitted (harmonic) light is double that of the incident light; in SHG experiments, the frequency-doubling efficiency of the material is measured. In Figure 4, the change in the SHG intensity was monitored as a function of temperature while poling the film; the incident light was an infrared laser (1064 nm) and the harmonic light is in the visible region (532 nm). The polymer system has 35% covalently linked 3HEOMONS in the backbone and does not absorb light above 500 nm wavelength which is far away from the resonance excitation.[1] The slow initial rise in the SHG intensity below the T_g (= 81 °C) of the polymer indicates some poling effect on the chromophores which implies slight chromophore mobility even in the glassy state of the polymer; the SHG signal gradually increased as the free volume in the

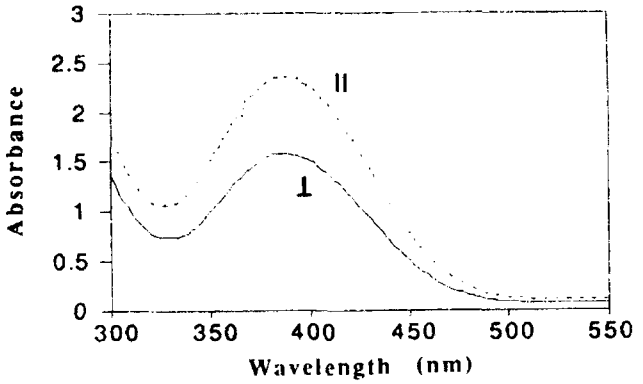

Figure 2. Linear UV dichroism of thermomechanically oriented film of P(3HEOMONS)LG.

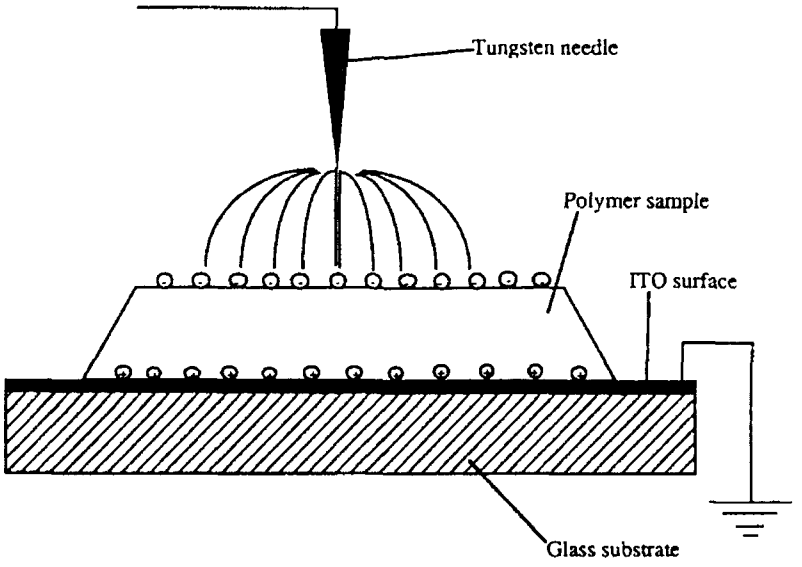

Figure 3. Schematic drawing of a corona poling experiment.

polymer increased with temperature. The SHG signal reached a maximum just above the T_g for this polymer and then decreased again on further heating. The decrease in SHG above the T_g was a concerted effect arising from (a) the increased thermal energy of the chromophores, and (b) the increased conductivity of the polymer due to increased temperature and increased polar alignment of the chromophores, which diminished the charges on the interfaces thus lowering the net poling field. Overall, this suggests an optimum poling condition for the polymer which may vary from polymer to polymer. A hysteresis was observed upon cooling, which was again a complicated function of the factors mentioned above. As the system was further cooled below T_g the chromophores reduce their mobility and re-align due to packing effects in the helix array. [The orientation of the polypeptide rods (~ 500 repeat units) is not affected by the poling field and remained parallel to the substrate surface in these solid films.] At room temperature, there was a net SHG signal indicating that some polar alignment of the chromophores remains fixed in the polymer matrix. This alignment was found to be relatively stable in time compared with the isotropic system of say, poly(methyl methacrylate) doped with the same chromophore. This enhanced stability is attributed to the nature of the excluded volume in the close-packed array of the helices.

If the helices can be aligned homeotropically, that is, perpendicular to the substrate surface, then a larger net SHG signal is expected. To date, homeotropic alignment has not been achieved in solid polypeptide films.

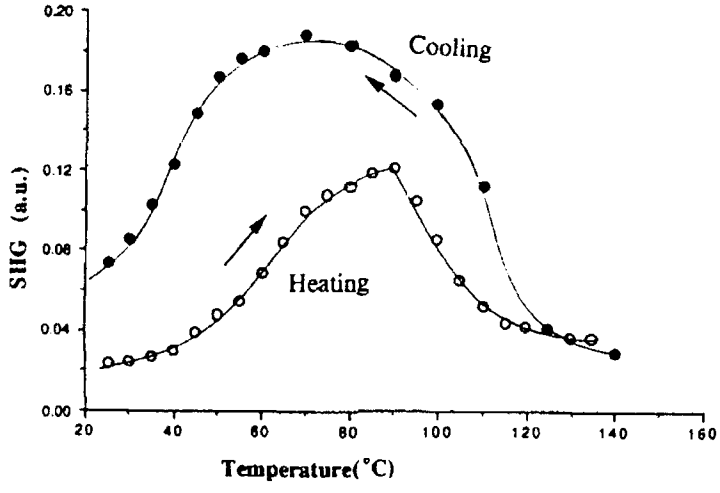

Figure 4. SHG intensity of P(3HEOMONS)LG during heating and cooling while poling; -12.5 KV of corona potential was applied to the tip of the tungsten needle which was 1.5 cm above the sample, The angle of the sample normal with respect to the laser beam was 52°. The lines are plotted only as guide to the reader.

Type II. Chemisorptive End-group

PBLG may also be functionalized at the amino end of the polypeptide by a disulfide-containing moiety (hereon referred to as PBLGSS, Figure 5).[2] This latter technique utilizes the self-assembly[18] procedure for preparing well-ordered monolayers of organosulfur compounds on gold substrates. In the case of long-chain alkanethiolates on gold,[19] the self-assembled monolayer is analogous to an orthogonal two-dimensional crystallization of the molecules at the gold surface owing to the strong affinity of sulfur to the metal and the strong van der Waals interaction between the long (> 10 C atoms) alkyl chains. In the case of PBLGSS, the monolayer that is formed in the self-assembly is unique in that α-helical chains are all tethered to the gold at the N-terminus with the potential for creating

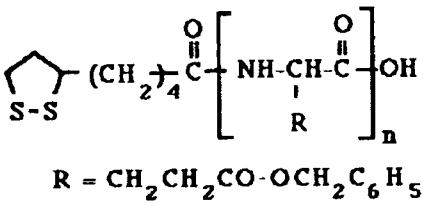

Figure 5. Primary structure of the disulfide-labelled PBLG—PBLGSS.

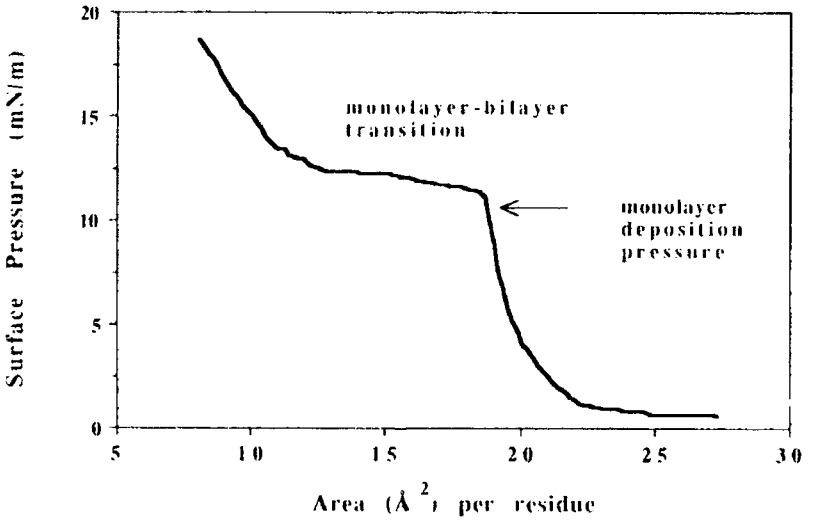

Figure 6. Pressure-area isotherm for PBLG (viscosity average molecular weight = 20,100) at an air/water interface at 25 °C.

an average polar orientation in the monolayer. The disulfide-labelled PBLG—PBLGSS—thus presents a route to preparation of a single monolayer of helices on gold surfaces via the chemisorption interaction of the disulfide to gold. This is in contrast to the unlabelled PBLG samples that may be either physisorbed from solution or prepared by deposition of condensed monolayers at an air/water interface onto the solid substrate [Langmuir-Blodgett (LB) technique[20]] where the interaction will be of a non-specific nature between the peptide units and gold.

Figure 6 shows a typical pressure-surface area isotherm for PBLG (viscosity average molecular weight = 20,100) at the air/water interface. The PBLG rods lie flat at the interface[21-22] and are compressed to a condensed monolayer just before the plateau. Right at the plateau region, the rods start to roll on top of one another; this region of the isotherm is assigned to the monolayer-bilayer transition. Subsequent deposition of this monolayer (or bilayer) onto a solid substrate results in a planar orientation of the rods on the substrate surface.[21-22] The self-assembled PBLGSS, in comparison with this LB-deposited monolayer, shows a different average orientation of the helices as examined by a number of surface analytical techniques.[2] Angle dependent X-ray photoelectron spectroscopy (ADXPS) presents a depth profile of relative atomic composition in the film; it was found that the sulfur was indeed bound closer to the gold surface than the rest of the polypeptide. The thicknesses of the films measured from ellipsometry as well as ADXPS indicate thicker (about 1.5 times) films of PBLGSS than the LB PBLG single monolayer on the gold surface; this is further corroborated by the RA-IR results.[23] The dichroic properties of the amide vibrational frequencies,[24] as measured in the RA-IR spectra, show that the average orientation in the PBLGSS film is non-planar. The amide I band (1656 cm^{-1}) has a dichroic ratio $(A_{\parallel}/A_{\perp}) > 1$; for the amide II band (1550 cm^{-1}) $(A_{\parallel}/A_{\perp}) < 1$. In the grazing angle RA-IR experiment the light is polarized perpendicular to the metal surface, therefore, only those components of the vibrational moments along the same direction are excited.[25] It can be seen in Figure 7 that for the PBLGSS film there was enhanced intensity of the amide I band compared with the amide II band; the opposite trend was observed for the PBLG LB films. Apparently, in the PBLGSS film there is an isotropic orientational distribution of the helices[23] as schematically depicted in Figure 7. These results are promising in that it shows that tethering the helices onto a substrate via a chemisorptive moiety allows them to adopt an "unnatural" orientation, that is, non-planar, and possibly, by appropriate derivatization of the PBLG sidechains a better control of this orientation may be achieved. This, in fact, could be a route to preparing a homeotropically aligned film of α-helices with NLO chromophores at its sidechains (see above).

CONCLUDING REMARKS

Polypeptides that have inherently stable α-helical conformation, e. g., PBLG-type, show promise either as a matrix for NLO chromophores or in the fabrication of interfaces that have well-defined spatial and orientational organization. The amenability of changing the sidechain, backbone, and/or end-group functionality of these polymeric materials presents unusual versatility with regards to the design of novel materials.

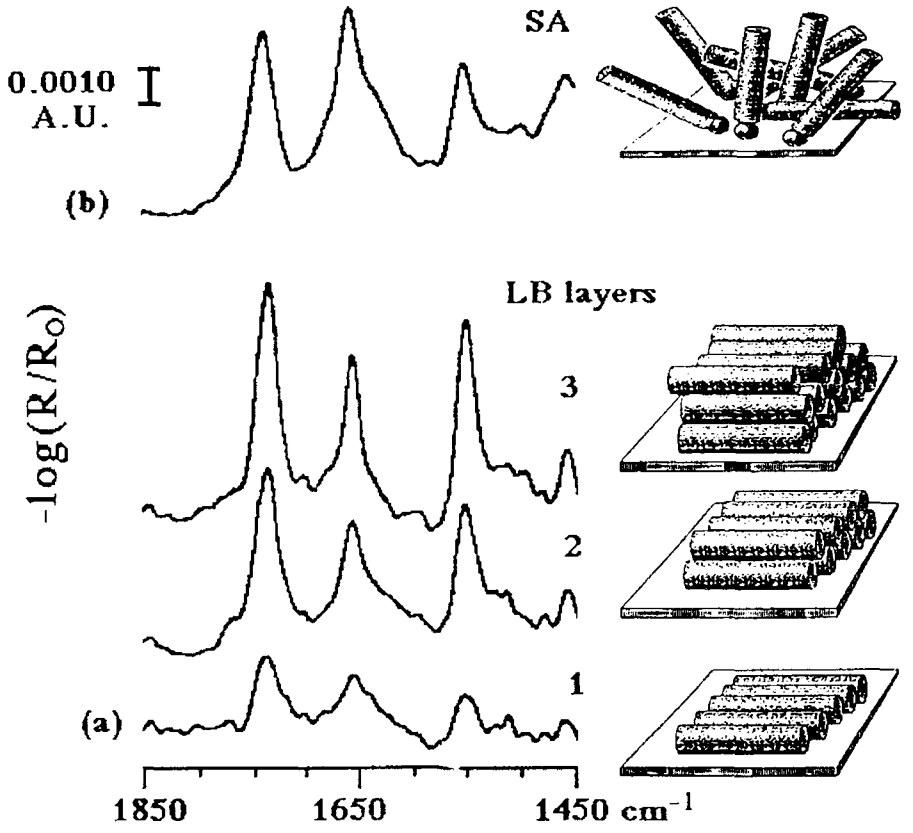

Figure 7. Reflection-absorption IR spectra of (a) PBLG LB films and (b) self-assembled PBLGSS monolayer; the possible packing of the rods in these films are schematically shown.

ACKNOWLEDGEMENTS

We thank M. Pauley for help with the SHG measurements, V. Guarisco for the LB depositions, and N. L. Thompson for the LB trough facility. This work was supported in part by subcontract from the University of Pennsylvania (DARPA/ONR Contract No. N0014-90-J-1559).

REFERENCES

1. Based in part on M. Y. Jin's Ph. D. Thesis, University of North Carolina at Chapel Hill, 1991.

2. E. P. Enriquez, K. H. Gray, V. F. Guarisco, R. W. Linton, K. D. Mar, and E. T. Samulski, J. Vac. Sci. Technol. A **10**, 2775 (1992).

3. L. Pauling, R. B. Corey, and H. R. Branson, Proc. Natl. Acad. Sci., USA **37**, 205 (1951).

4. H. Block, *Poly(γ-Benzyl-L-glutamate) and Other Glutamic Acid Containing Polymers* (Gordon and Breach, New York, 1983); and references cited therein.

5. M. F. Perutz, Nature **167**, 1053 (1951).

6. D. B. Dupré and E. T. Samulski in *Liquid Crystals: The Fourth State of Matter*, edited by F. D. Saeva (Marcel and Dekker, New York, 1979), chap. 5.

7. T. J. McMaster, H. J. Carr, M. J. Miles, P. Cairns, and V. J. Morris, Macromolecules **24**, 1428 (1991); J. Vac. Sci. Technol. A **8**, 648 (1990).

8. J. J. Breen and G. W. Flynn, J. Phys. Chem. **96**, 6825 (1992).

9. B. Merrifield, Science **232**, 341 (1986).

10. See for example, H. S. Creel, M. J. Fournier, T. L. Mason, and D. A. Tirrell, Macromolecules **24**, 1213 (1991).

11. See for example, Y. Inai, M. Sisido, and Y. Imanishi, J. Phys. Chem. **95**, 3847 (1991).

12. J. Watanabe, H. Ono, I. Uematsu, and A. Abe, Macromolecules **18**, 1241 (1985).

13. A. Coda and F. Pandarese, J. Appl. Cryst. **9**, 193 (1976).

14. W. Tam, B. Guerin, J. C. Calabrese, and S. H. Stevenson, Chem. Phys. Lett. **154**, 93 (1989).

15. E. T. Samulski and A. V. Tobolsky, Macromolecules **1**, 555 (1968).

16. J. Michl and E. W. Thulstrup, *Spectroscopy with Polarized Light* (VCH, New York, 1986).

17. P. N. Prasad and D. J. Williams, *Introductio · to Nonlinear Optical Effects in Molecules and Polymers* (John Wiley & Sons, New York, 1991).

18. A. Ulman, *An Introduction to Ultrathin Organic Films: From Langmuir-Blodgett to Self-assembly* (Academic Press, New York, 1991); and references cited therein.

19. C. D. Bain, E. B. Troughton, Y. Tao, J. Evall, G. M. Whitesides, and R. G. Nuzzo, J. Am. Chem. Soc. **111**, 321 (1989); C. D. Bain, H. A. Biebuyck, and G. M. Whitesides, Langmuir **5**, 723 (1989).

20. See for example, N. L. Thompson and A. G. Palmer III, Comments Mol. Cell. Biophys. **5**, 39 (1988).

21. T. Takenaka, K. Harada, and M. Matsumoto, J. Colloid & Interface Sci. **73**, 569 (1980).

22. R. Jones and R. H. Tredgold, J. Phys. D: Appl. Phys. **21**, 449 (1988).

23. E. P. Enriquez and E. T. Samulski, Mat. Res. Soc. Symp. Proc. **255**, 423 (1992).

24. M. Tsuboi, J. Polymer Sci. **59**, 139 (1962).

25. R. G. Greenler, J. Chem. Phys. **44**, 310 (1966).

BIOPOLYMER-THIN FILM INTERACTIONS

K. M. Maloney and D.W. Grainger*, Department of Chemical and Biological Sciences, Oregon Graduate Institute of Science and Technology, 19600 N.W. von Neumann Drive, Beaverton, OR 97006-1999

ABSTRACT

Biopolymer self assembly in heterogeneous lipid monolayers at the air-water interface was investigated. Fluorescence microscopy allowed the visualization of protein recognition and binding to these microstructured membranes. Mimicking protein-induced membrane microstructuring and protein docking was achieved in ternary mixed lipid monolayer systems.

INTRODUCTION

Considerable research activity has been focused on the technological applications of organized organic ultrathin films. Langmuir-Blodgett (LB) films, monomolecular and polymeric thin films at the air-water interface and self-assembled films have been used as non-linear optical devices, waveguides, physical, chemical and biological sensors, and insulators. Potential use of self-assembled and LB films in microlithography, lubrication, molecular electronics, synthesis of advanced materials and molecular devices have also been noted.

LB films and self-assembled monolayers possess several characteristics which lend themselves to device fabrication. In particular, on the atomic scale these ultrathin films are highly organized. Thus, when anisotropic arrangement of molecules is required, thin film assemblies are excellent candidates. Books by Ulman[1] and Roberts[2] offer excellent reviews on the technological applications of these systems.

Incorporation of biopolymers into mono- and multi-layered assemblies leads to functionalized hybrid thin films that can mimic natural processes. Examples include use of photoreaction centers in holographic arrays, membrane channels in sensors, and enzymes in bioreactor assemblies. However, biopolymer-membrane interactions are poorly understood. Furthermore, selectively accessing defined regions of thin films is crucial for optical device development. Only after membrane-macromolecule interactions are fully understood can we expect to employ these systems as technologically useful devices.

We present here our investigations on lipid membrane microstructures and lipid-protein self-assembly. Our previous work has demonstrated assembly of other proteins in thin film arrays.[3-11] In this contribution, we extend our previous work with the membrane-active enzyme phospholipase A_2 (PLA_2) and its self-assembly on heterogeneous membrane interfaces. PLA_2 catalyzes the hydrolysis of the sn-2 acyl ester bond in phospholipids. The result of PLA_2 action on phospholipid monolayers at the air-water interface is the creation of a ternary phase separated interface consisting of phospholipid, lysophospholipid, and fatty acid.

PLA_2 forms two-dimensional domains directly beneath phase separated fatty acid microstructures in these ternary mixed systems. Characterization of the ternary mixed monolayer system has shown that the physical state and charge density of the interface are important for 2-D enzyme domain formation. More importantly, we are able to induce phase separation in ternary mixed monolayers in the absence of enzyme. Mimicking enzyme-induced interfacial phase transformation is one important step in constructing biomimetic devices.

Mat. Res. Soc. Symp. Proc. Vol. 292. © 1993 Materials Research Society

EXPERIMENTAL

Video-Enhanced Epifluorescence Microscopy of Lipid Monolayers and Lipid-Protein Microstructures at Air-Water Interfaces

Recently, fluorescence microscopes have been configured to allow direct visualization of lipid monolayer films at the air-water interface[4-6]; domains of organized amphiphilic molecules formed by a monolayer phase transition from liquid-expanded to solid-condensed physical states are normally observed.[4-7] Analogously, this technique has also proven valuable to study interactions of labeled proteins with monolayers.[8-11] Protein labeled with a fluorescent marker is introduced into the subphase under a lipid monolayer and its interactions with the layer monitored both visually over time and as a function of lipid physical state. A specially designed miniaturized, thermostated Langmuir film balance on the stage of an epifluorescence microscope limits the required quantities of protein to microgram scales.[12]

Phospholipase A_2 - Phospholipid Monolayer Studies

Various phospholipids were spread as pure monolayers and compressed into their phase transition regions, providing a physically heterogeneous monolayer surface comprising fluid lipid coexisting with domains of solid phase organized lipid. Fluorescein-labeled phospholipase A_2 (PLA_2, *Naja naja*, Sigma, 500-2500 U/mg) was introduced under these monolayers and the hydrolytic reaction of the enzyme against the monolayer followed under the microscope.

Cationic Dye Binding Studies

Cationic water-soluble fluorescent dye, 1,1',3,3,3',3'-hexamethylindocarbocyanine iodide (H-379, Molecular Probes, Eugene, OR) was dissolved in buffer (0.4 μM). Ternary mixed monolayer systems of dipalmitoylphosphatidylcholine (DPPC), palmitic acid (PA), and lysopalmitoylphosphatidylcholine (LysoPC, Avanti Polar Lipids, Birmingham, AL) containing 1 mol% lipid-fluorescein dye were spread from chloroform solutions onto buffered subphases at 30°C. Various ratios of DPPC to equimolar concentrations of palmitic acid and LysoPC (e.g., 1:5:5, DPPC:LysoPC:PA) were examined. These monolayers were compressed under the fluorescent microscope until substantial monolayer phase separation was observed (typically 25-30 mN/m surface pressure). H-379 solution was then carefully injected into the subphase underneath the phase-separated monolayer and observed through a rhodamine filter.[13]

RESULTS AND DISCUSSION

PLA_2 Hydrolysis of Phospholipid Monolayers

Figure 1 depicts time dependent L-α-DPPC lipid monolayer hydrolysis by PLA_2. Shown is the enzyme recognition, binding, hydrolysis and ultimately protein domain formation. Figure 1A shows the lipid monolayer as seen through the rhodamine filter, while Figure 1B shows the same image through the fluorescein filter where signal is generated by fluorescently labeled enzyme under the monolayer immediately after injection. Starting from timepoint zero (immediately after PLA_2 injection) the enzyme binds to phospholipids in the monolayer and starts to hydrolyze. PLA_2 hydrolysis as observed through the rhodamine filter proceeds from the initial binding

Rhodamine Filter
(DPPC Monolayer)

Fluorescein Filter
(Phospholipase)

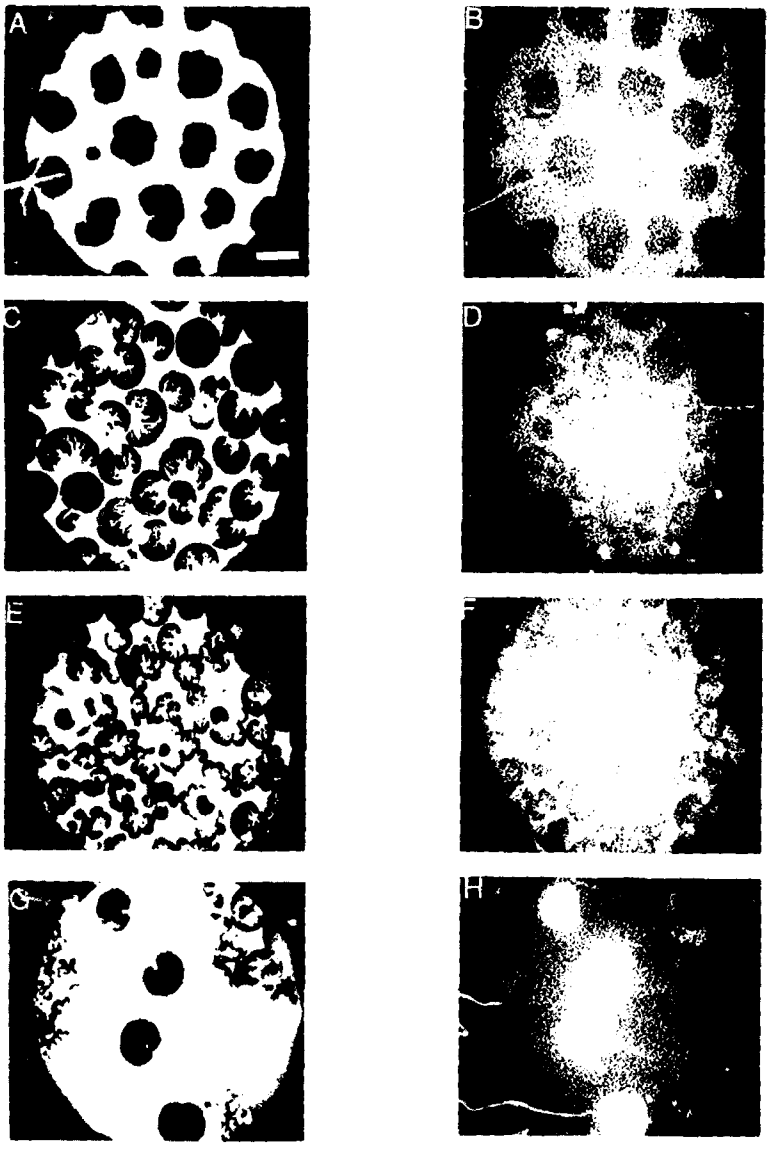

Figure 1 (previous page). Real-time fluorescent observation of L-α-DPPC monolayer solid domain hydrolysis by PLA_2. Surface pressure = 22 mN/m, buffered subphase at 30 °C. **Monolayer filter** (Rhodamine): **A**, Time = 0 (immediately after fluorescein-PLA_2 injection in subphase). **C**, 15, **E**, 25, **G**, 60 min. **PLA_2 filter** (fluorescein): Images in **B**, **D**, **F**, **H**, correspond to times of **A**, **C**, **E**, and **G**, respectively. Scale: white bar in **A** = 25 μm.

sites on the interfacial boundary between solid and liquid phases into the interior of the solid lipid domains (Figures **1C**, **E**). Observation through the fluorescein filter (Figure **1D**) shows that, at certain locations in the partially hydrolyzed monolayer, bright domains of enzyme have formed. These domains of labeled enzyme increase in size as hydrolysis continues with time (Figure **1F**). At later timepoints (60 minutes, Figure **1G**), enzyme hydrolysis has destroyed nearly all solid domains. Moreover, the small enzyme aggregates seen at earlier timepoints (Figure **1D**, **F**) have grown to form large, regular enzyme domains of consistent morphology (bright domains seen with fluorescein filter, Figure **1H**).[9]

A mechanism for the formation of organized, two-dimensional enzyme domains within monolayers of phospholipids is proposed in Figure **2**. Active enzyme under the layer recognizes its substrate, binds to the monolayer and hydrolyzes in an interfacial region between liquid and solid lipid phases. Slight increases in surface pressure after enzyme injection indicate that PLA_2 penetrates into the monolayer during its interfacial recognition of the substrate in the monolayer. After a critical degree of hydrolysis, products of hydrolysis--lysolipids and fatty acids--build up in the localized regions of the monolayer. Phase separation of these products from pure lipid is proposed to occur, leading to areas of increased charge density in the case of fatty acids. Enzyme, with its relatively basic character, may then be prompted to bind and build domains in these areas of localized negative charge (fatty acid), leading to the enzyme domain phenomenon witnessed in DPPC, DMPC, and DPPE monolayers.[9,10] Fatty acid charge density appears to be critical as phase-separated dense-packed solid domains of diacetylenic fatty acid adsorb no PLA_2,[14] while less organized fatty acid domains do adsorb enzyme. Additionally, work has suggested[14] that the phospholipid head group is necessary for PLA_2 domain formation in conjunction with anionic phase separation.

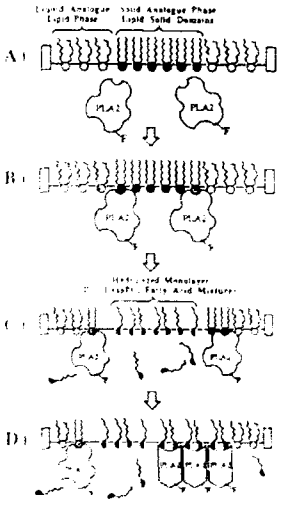

Figure 2. Proposed mechanism for recognition, binding, hydrolysis and PLA_2 domain formation prompted by critical concentrations of hydrolytic products mixed with substrate lipids in phospholipid monolayers. A. Injection of PLA_2 into aqueous lipid monolayer subphase. B. Enzyme recognition and binding to lipid interface. C. Hydrolysis of monolayer by PLA_2 with buildup of hydrolysis products (lysolipid and fatty acid). D. Organization of bound PLA_2 into protein domains at the lipid-water interface prompted by critical concentrations and phase separation of hydrolysis products in the monolayer (from ref. 10).

Cationic Dye Binding to Phase Separated Microstructures in Mixed Monolayers

Figure 3 shows results of the water-soluble cationic fluorescent dye, H-379, binding to phase separated areas in ternary mixed monolayers of DPPC:LysoPC:palmitic acid (0.2:1:1, mol:mol:mol). The grey character of these domains has been attributed to phase separation of fatty acid components within the monolayer.[9,10,14] Different stoichiometric mixtures of DPPC:LysoPC:PA (always maintaining LysoPC:PA = 1:1) demonstrate these grey domains as well.

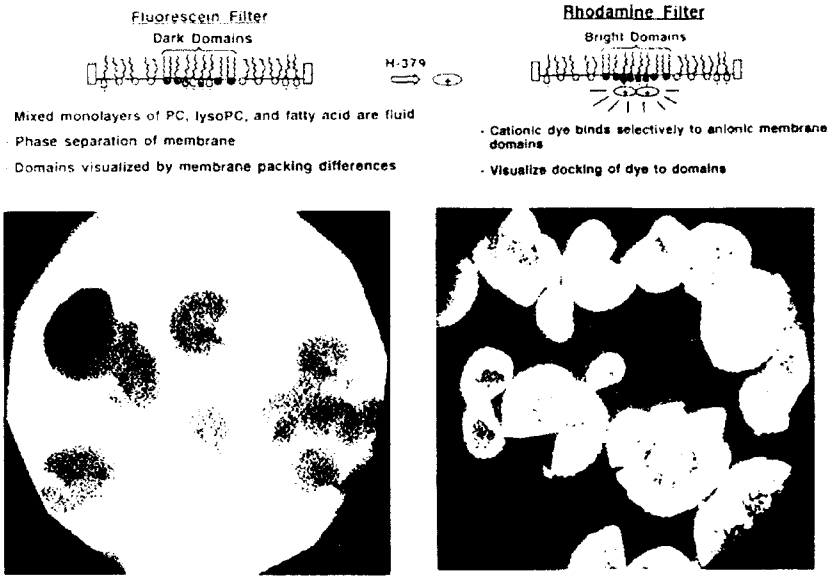

Figure 3. Binding of water-soluble cationic H-379 to phase separated regions in ternary mixed monolayers. Surface pressure = 25 mN/m, buffered subphase at 30°C, DPPC:LysoPC:PA ratio = 1:5:5 (mol:mol:mol). Fluorescein filter: Shown are phase separated fatty acid microstructures. Rhodamine filter: After injection of H-379 in subphase, dye quickly binds to phase separated region shown in rhodamine filter. Same scale as Figure 1.

The use of cationic dye was intended to probe the nature of these phase separated domains. Data from zwitterionic vesicle systems[15] had shown strong adsorption of dye to vesicles after buildup of fatty acid after PLA_2 hydrolysis. Our approach attempts to show a relationship between monolayer fatty acid domains (negative surface charge) analogous to those created by PLA_2 hydrolysis of phospholipid monolayers, and cationic dye via electrostatic binding. As shown in Figure 3, grey phase separated areas seen before cationic dye addition transform to bright fluorescing domains after dye addition, demonstrating a rapid and stable

electrostatic adsorption of H-379 to selected domains at the interface. Dye is not adsorbed if no fatty acid is present in monolayer mixtures. Phase separation is not observed if Ca^{2+} is not present or subphase pH is below 7. These results present strong evidence in line with our hypothesis (Figure **2**) that these phase separated domains are, in fact, enriched in fatty acid.

In conclusion, model biomembranes can provide information on biopolymer-amphiphile and amphiphile-amphiphile interactions. During enzymatic hydrolysis of phospholipid monolayer films, microstructuring in these mixed monolayers leads to the formation of two-dimensional protein aggregates. Enzyme-induced monolayer microstructuring is mimicked with enzyme-free ternary mixed monolayers. Compression of these mixed films also leads to fatty acid phase separation. These domains are selectively accessed through the use of a water-soluble cationic dye, H-379. H-379 adsorption to fatty acid domains supports our hypothesis on PLA_2 interfacial activity in monolayer systems. Most importantly, though, we have demonstrated an organizational hierarchy where protein aggregation is mediated directly by monolayer microstructuring. Understanding and mimicking interfacial molecular recognition events such as those presented here are significant steps in ultrathin film-based biological device fabrication.

REFERENCES

1. A. Ulman, *An Introduction to Ultrathin Organic Films: From Langmuir-Blodgett to Self Assembly* (Harcourt, Brace, Jovanovich, Publishers, Boston, 1991).
2. G. Roberts, *Langmuir-Blodgett Films* (Plenum Press, New York, 1990).
3. M. Ahlers, R. Blankenburg, D. W. Grainger, P. Meller, H. Ringsdorf, and C. Salesse, Thin Solid Films **180**, 93 (1989).
4. P. Meller, Rev. Sci. Instrum. **59**, 2225 (1988).
5. M. Lösche and H. Möhwald, Rev. Sci. Instrum. **55**, 1968 (1984).
6. R. M. Weiss and H. M. McConnell, Nature **310**, 47 (1984).
7. R. M. Weiss, L. K. Tamm, and H. M. McConnell, Proc. Nat. Acad. Sci. USA **81**, 3249 (1984).
8. R. Blankenburg, P. Meller, H. Ringsdorf, and C. Salesse, Biochemistry **28**, 8214 (1989).
9. D. W. Grainger, A. Reichert, H. Ringsdorf, and C. Salesse, FEBS Lett. **252**, 73 (1989).
10. D. W. Grainger, A. Reichert, H. Ringsdorf, and C. Salesse, Biochim. Biophys. Acta **1023**, 365 (1990).
11. M. Ahlers, R. Blankenburg, D. W. Grainger, P. Meller, H. Ringsdorf, and C. Saless, Thin Solid Films **180**, 93 (1990).
12. P. Meller, J. Microsc. **156**, 241 (1989).
13. K. M. Maloney and D. W. Grainger, Chem. Phys. Lipids, in press (1993).
14. A. Riechert, A. Wagenknecht, and H. Ringsdorf, Biochim. Biophys. Acta **1106**, 188 (1992).
15. B. Z. Yu, Z. Kozubek, and M. K. Jain, Biochim. Biophys. Acta **910**, 15 (1989).

FORMATION OF SILK MONOLAYERS

WAYNE S. MULLER, LYNNE A. SAMUELSON, STEPHEN A. FOSSEY, DAVID L. KAPLAN
Biotechnology Division, US Army Natick Research, Development and Engineering Center, Natick, MA 01760.

ABSTRACT

Cast silk membranes exhibit useful properties. However, there is limited control over the molecular architecture in these structures. The Langmuir-Blodgett technique can enhance the control of the membrane structure and allow improved control over membrane properties. We have formed natural silk monolayers using the Langmuir technique. Silk fibroin, regenerated from Bombyx mori cocoons, formed stable monolayers evident from pressure/area isotherms. Multilayers of the silk fibroin monolayers were deposited on a number of substrates and characterized. Transmission Electron Microscopy (TEM) and ellipsometry data provide basic information about the physical characteristics of the monolayer. Preliminary analysis of electron diffraction data of the monolayer indicate polycrystalline structure, consistent with the known structure of silk. Infrared spectrometric analysis of the monolayer using Attenuated Total Reflectance (ATR) gave wavenumbers for Amide I, II, III and V bands which compare with the silk II conformation reported for cast silk membranes.

INTRODUCTION

Over the centuries, silk has been valued as a textile fiber, because of its qualities of strength, elasticity, softness, lustre, absorbency and affinity for dyes. Silk fibroin is used in various forms, such as gels, powders, fibers, or membranes, depending on application. Recently [1-5] silk fibroin has been used as an excellent immobilization matrix for enzymes. As a biomaterial it has many advantages over both natural and synthetic materials used in biosensor systems. These attributes include its biological compatibility, stablity to most solvents including water, good tensile strength and elasticity properties. Silk fibroin has been used as a surgical thread due to its excellent mechanical and physical properties, good thermal stability and microbial resistance [6]. Our interests lie in the membrane properties of silk fibroin.

Fibroin is the primary structural element in silkworm cocoon silk and is embedded in a glue-like sericin protein matrix. Fibroin contains a unique amino acid composition and primary structure. Its major advantage as an enzyme immobilization matrix is that it entraps the enzyme. This entrapment of the enzyme without the usual cross-linking chemicals alleviates a major problem of residual cross-linking chemicals in the matrix which can deactivate the enzyme. The entrapment process is accomplished by physical, chemical or mechanical treatment of the membrane (e.g., change in temperature, pH, solvent, mechanical shear or

Mat. Res. Soc. Symp. Proc. Vol. 292. 1993 Materials Research Society

stretch) which induces a phase transition. Bombyx mori silk fibroin has been used as an immobilization matrix for enzymes such as glucose oxidase [1-4], alkaline phophatase [7], peroxidase [5], and invertase [8].

Silk fibroin has three known conformations, random coil, silk I, and silk II. All three conformations can be prepared by the appropriate preparation conditions and each is interchangeable under certain conditions [9]. The effect of casting temperature and initial fibroin concentration during membrane formation was studied using an aqueous silk fibroin solution [10]. With casting solutions above 50° C, a silk II conformation was obtained irrespective of initial fibroin concentration. However, casting at temperatures below 40° C resulted in a silk I conformation when concentrated fibroin solutions were used, and random coil conformation when dilute solutions were used. Solvent-induced crystallization or conformation has also been reported, with silk II induced in polar hydrophilic solvents such as methanol and silk I induced in hydrophobic solvents [11].

Silk structures studied for phase transitions as immobilization matrices have been in the form of cast membranes. The cast silk membranes have good properties as membrane materials; however, the casting process has limitations. There is limited control over the thickness of the membrane or the density and the orientation of the polymer chains. Since the functionality of these membranes, including permeability, the activity of entrapped enzymes, and mechanical integrity, is dependent in part on conformation, density, and orientation of the polymer chains, new processing techniques to control these properties would be useful. The Langmuir-Blodgett (LB) technique is used in this study in an attempt to enhance the control of the physical processing of silk fibroin protein.

We describe the formation and characterization of natural silk fibroin monolayers using the LB technique. Some basic information on the physical characteristics of the monolayers is obtained from pressure-area isotherms, electron micrographs, and ellipsometry. Analysis of the monolayers with infrared spectroscopy and electron diffraction provides insight into the silk conformation favored at ambient temperature and the expected polycrystalline order of the silk monolayer.

EXPERIMENTAL

B. mori cocoon silk was regenerated as shown in Figure 1. A Pasteur pipet was used to apply the solubilized silk to a Lauda Filmbalance FW2 (Brinkmann Instr. Inc., Westbury, NY). To study pressure/area isotherms, the silk fibroin was added to the surface of a Milli Q water subphase at 24° C with a compression rate of 46 cm^2/min. Transmission Electron Microscopy (TEM) was performed on the monolayers using a Hitachi H 600 (Rockville, MD) with samples collected from the surface of the trough using T 1000 grids. The TEM samples were air dried at room temperature. Fourier Transform Infrared Reflectance (FTIR) Attenuated Total Reflection (ATR) analysis was performed on a Nicolet 20SXB Infrared Spectrometer (Madison, WI) with an accessory holder for ATR (Harrick Scientific Co., Ossining, NY) Silk samples for FTIR analysis were collected on germanium prisms at a pressure of 16.7 mN/m, a dipping speed of 0.2 cm/min and a temperature of 20° C. The silk films were deposited on frosted glass slides under the same conditions used for the FTIR

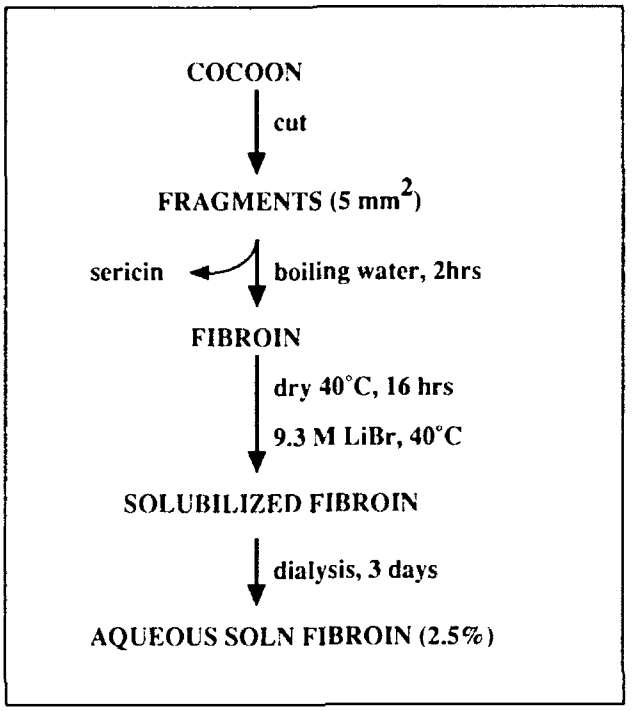

Figure 1. Schematic of the procedure to regenerate (solubilize) B. mori cocoon silk.

samples. These films were analyzed on a Thin Film Ellipsometer Type 43603-200E (Rudolph Research, Flanders, NJ) to determine the thickness of the transferred material. The refractive indices of silk fiber 1.591 and 1.538 were used as a guide in ellipsometric calculations of film thickness.

RESULTS & DISCUSSION

Figure 2 is a pressure/area isotherm of the soluble silk. The consistent repeat slope and stability of the curve indicate film formation. It should be noted that the x-axis of the isotherm is in arbitrary units because the silk fibroin has an estimated molecular weight of 350 KDa to 415 KDa [11] which exceeds the limits of the Lauda software program. A molecular weight of 75.53 was used as the basis of standardizing the calculation for the x-axis, derived from the amino acid composition of fibroin [12,13] and is based on the average weight of each amino acid monomer in the silk fibroin polymer. It has been difficult to obtain an accurate quantitation of the area per molecule due to the complex secondary structure of the silk fibroin protein.

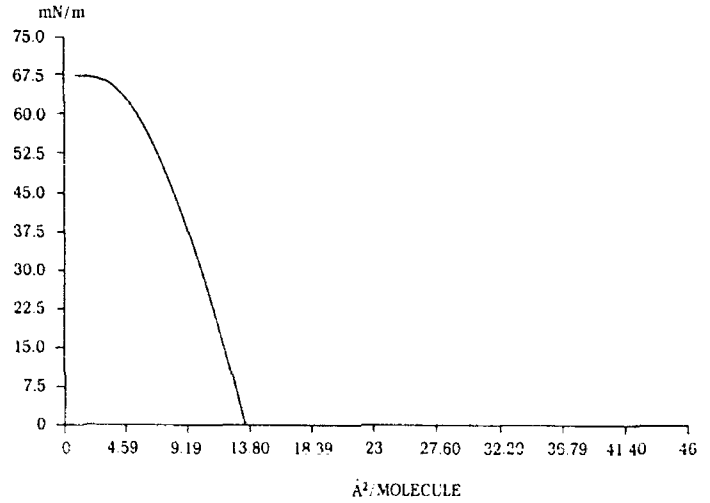

Figure 2. Typical pressure/area isotherm of solubilized silk fibroin at 24° C.

Silk fibroin does not exhibit the typical amphipathic character of LB materials suitable for monolayer formation. Also, silk fibroin exhibits unique solubility characteristics which can make the material difficult to work with in an LB system. Silk fibroin is insoluble in volatile non-polar solvents often used in the application of surfactants to an aqueous subphase. Silk fibroin is also insoluble in dilute acids and alkali, and resistant to most proteolytic enzymes, [11,14], but soluble in 9.3M LiBr aqueous solution. After dialysis, the solubilized silk fibroin remains in solution if undisturbed. After application to the trough, a portion of the polymer enters the aqueous subphase. This event is evident from the protein residue observed when cleaning the trough. This unusual solubility behavior adds to the difficulty in obtaining an accurate determination of the area per polymer chain.

The silk fibroin films demonstrate excellent stability and transfer properties indicative of a well behaved monolayer system. The compression barrier has been stabilized for half hour to hour time periods at various pressures (10, 15, 20, 25, 30, 35 mN/m) with no indication of film collapse. Films remained stable overnight (16 hrs) without a change in area when studied at our usual working pressure for transfer at 16.7 mN/m. In Figure 2, a typical isotherm for silk, there is no sudden drop in surface pressure with compression which would be indicative of a collapsed film. The steady rise in surface pressure of the isotherm may be indicative of the increasing resistance to dense molecular packing. Upon complete collapse of the monolayer, it was possible to remove very long fibers with the tip of a pipet, indicative of the characteristic strength and elasticity properties of silk [15,16].

Table 1 presents the ellipsometry data for silk films. The data provided the relative thickness of a transferred monolayer. Many biomolecular materials exhibit Y or Z type deposition [17]. We believe that Y type deposition is characteristic of the silk fibroin monolayer based on our observations of the change in area and shape of the meniscus at the air/water interface during vertical deposition. The average thickness of a monolayer determined from the data in Table 1 was approximately

Film Characteristic	Number of Layers		
	3	5	7
Multi-Layer Thickness Å	37	65	94
Calculated Monolayer Thickness Å	12.3	13	13.4

Table 1. Ellipsometry data on silk fibroin LB films deposited on frosted glass slides.

11.6 to 11.9 Å. The ellipsometry data indicated that the average thickness increased with the number of layers deposited. Therefore, by extrapolation back to a single monolayer, a value of 11.6 to 11.9 Å was established.

The estimated thickness of the silk monolayer agrees with the published structure of silk. Silk from B. mori consists of antiparallel ß sheets as first described by Marsh et al. [18]. The fibroin consists of both crystalline (short side chain amino acid monomers - glycine, alanine, serine) and amorphous (amino acids with bulkier side chains) domains. There have been two types of crystalline structures proposed for silk, silk I and silk II. For silk II, the insoluble and more stable form of silk, the reported unit cell based on X-ray diffraction data has an interchain distance of 9.4 Å, a fiber axis distance of 6.97 Å, and an intersheet distance of 9.2 Å [18]. The intersheet distance of 9.2 Å is close to the estimated monolayer thickness for the LB silk film based on the ellipsometry data. Fraser and MacRae [19] used X-ray reflections for silk II to calculate crystalline domains of 59 Å x 97 Å x 22 Å. This would mean that five or six of the crystalline chain segments of several fibroin chains are associated in a crystalline domain [20] as compared to the three crystalline chains that form a unit cell of silk II. The smaller crystalline domains in the monolayer, proposed from the ellipsometry data, may be a result of the processing procedure used in regenerating the silk as well as the initial unrestrained spreading of the solubilized silk on the surface of the trough.

Infrared spectroscopy was used to partially characterize the structure of silk in the LB film. Yoshimizu and Asakura [21], in a study on cast films with a thickness of 100-250 µm, employed FTIR (ATR) to determine the conformational transition of the silk membrane surface treated with methanol. The absorption bands observed for membranes treated with methanol had wavenumbers of 1625 (amide I), 1528 (amide II), and 1260 cm^{-1} (amide III), characteristic of a silk II structure. Membranes without methanol treatment showed absorption bands at 1650 (amide I), 1535 (amide II), and 1235 cm^{-1} (amide III), which were assigned the random coil conformation. In addition, Asakura et al. [22] observed that the amide V band had a frequency of 700 cm^{-1} for a silk II compared to a 650 cm^{-1} for the random coil conformation.

Table 2 compares the FTIR wavenumbers for cast membranes (silk I, silk II) with results obtained on silk fibroin LB films. A total of eleven silk layers were deposited on a germanium prism. Absorption bands were observed at 1624 (amide I), 1522 (amide II), 1258 cm^{-1} (amide III), and 700 (amide V). A pronounced shoulder at 1260 cm^{-1} is a critical feature to distinguish silk II from random coil/silk I

Absorption Bands	Cast Membranes		Silk Fibroin LB Films
	Silk I	Silk II	
Amide I	1650	1625	1624
Amide II	1535	1528	1522
Amide III	1235	1260	1258
Amide V	650	700	700

Table 2. Comparison of FTIR wavenumbers(cm^{-1}) reported for cast films [21,22] (silk I,silk II) versus those obtained for silk fibroin LB films.

in cast silk films treated with methanol. In the FTIR spectra for silk fibroin LB film we have identified this shoulder at 1258 cm^{-1}. This confirms that at least part of the silk fibroin in the monolayers has a silk II conformation.

The explanation for the dominance of a silk II structure in these thin films may be in the mechanical forces present during the application of the solubilized fibroin to the surface of the trough, during compression of the surface of the trough, and/or during transfer of the silk fibroin. During application with the Pasteur pipet some shear may induce, in part, a silk II conformation. The silk II conformation, due to its insolubility in the aqueous subphase, would form the thin film. Another possible source of mechanical shear is the stretching of silk fibroin during transfer and

Figure 3. A transmission electron micrograph of the deposited silk fibroin LB film at 24° C.

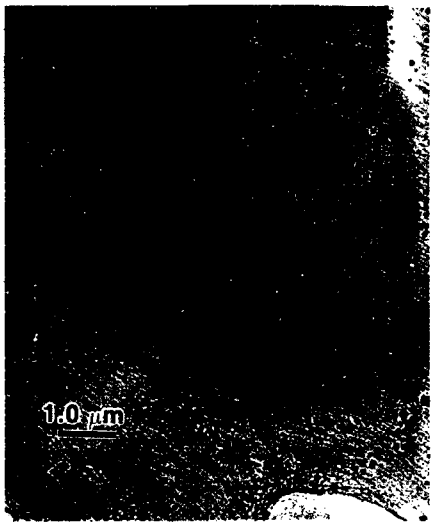

Figure 4. A transmission electron micrograph of the deposited silk fibroin LB film at 45° C.

deposition on solid support. Once a silk fibroin monolayer is formed there may be resistance to transfer and deposition by interchain forces between the polymer chains. The energy needed to break these interchain forces may contribute to the phase transition of the deposited material.

Figure 3 is a TEM of the LB silk fibroin film formed at 24°C. The edge of the TEM grid appears in the micrograph as the black areas at the upper and lower corner, while the dark areas in the field are assumed to be thicker regions of the film. The clear or spherical areas in the micrograph are holes in the film. These holes appear irregularly throughout the film as do the thicker regions, and may arise during film drying on the TEM grid. This conclusion is supported by the absence of these holes in some films. The physical appearance of the film is affected by the drying and processing conditions. Figure 4 is a micrograph of a silk fibroin LB film where the temperature of the subphase was elevated to 45°C. The physical appearance of the film is different from that seen in Figure 3. The film has striations throughout. The small dark cubic shapes in the film are crystals of LiBr not removed during dialysis. Altering the temperature of the subphase imparts significant changes in the physical appearance of the silk fibroin film. Further studies are underway to correlate the physical environment of the subphase and drying conditions of transferred films with the structure of the LB silk film formed.

Figure 5 shows a micrograph of an electron diffraction pattern of an LB silk fibroin film. The electron diffraction pattern is typical of a polycrystalline material which is characteristic of silk. Minoura et al. [23] and Magoshi et al. [10] have published X-ray diffraction data on cast silk thick films which have similar patterns as those observed here for the LB silk fibroin film. Asakura et al. [22] and Minoura et al.

[23], using X-ray diffraction, observed that the preparation and physical treatment of silk films are critical factors in determining whether silk I or silk II structures form. We have yet to confirm, with electron diffraction, whether the silk present in these monolayers is silk I or silk II. Based on the IR data discussed earlier, we expect a silk II conformation to be confirmed for the conditions under which these films were prepared. Under the appropriate conditions, using the Langmuir method, it may be possible to obtain a well oriented silk I film. This would provide a unique opportunity to experimentally characterize the silk I structure since this structure has eluded definitive structural characterization due to its metastable state.

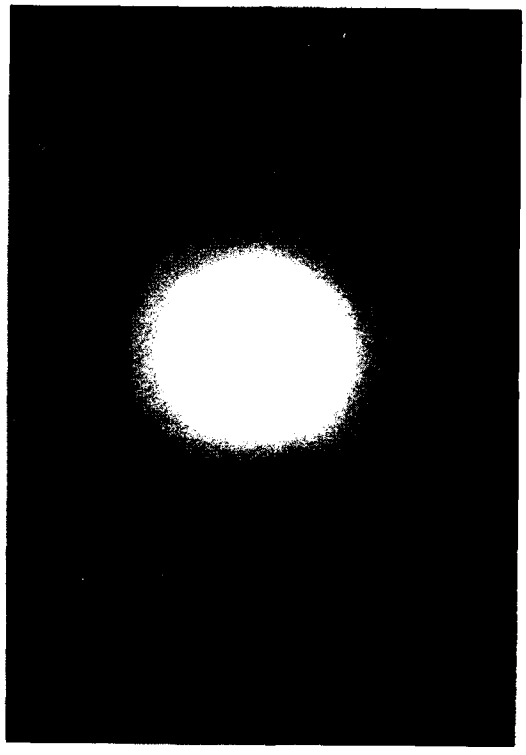

Figure 5. Electron diffraction pattern of silk fibroin LB film.

ACKNOWLEDGMENTS

We thank Marian Goldsmith (University of Rhode Island, Kingston, R.I.) for supplying the silkworm cocoons, Abe King and Sam Cohen (Natick RD&E Center) for the TEM analysis and helpful discussions, Aaron Bluhm (Natick RD&E Center) for the FTIR analysis, and Tony Chen (University of Massachusetts, Lowell, MA) for the ellipsometry analysis.

REFERENCES

1. A. Kuzuhara, T. Asakura, R. Tomoda, T. Matsunaga, J. Biotechnology **5**, 199 (1987).

2. T. Asakura, H. Yoshimizu, A. Kuzuhara, T. J. Matsunaga, J. Seric. Sci. Jpn. **57**, 203 (1988).

3. M. Demura, T. Asakura, Biotechnol. Bioeng. **33**, 598 (1989).

4. M. Demura, T. Asakura, T. Kurso, Biosensors **4**, 361 (1989).

5. M. Demura, T. Asakura, E. Nakamura, H. Tamura, Journal of Biotechnol. **10**, 113 (1989).

6. L. Grasset, D. Cordier, A. Ville, Process Biochem. **14**, 2 (1979).

7. T. Asakura, J. Kanetake, M. Demura, Poly-Plast. Technol. Eng. **28**, 453 (1989).

8. H. Yoshimizu, T. Asakura, Journal of Applied Polymer Science **40**, 127 (1990).

9. J. Magoshi, Y. Magoshi, S. Nakamura, Journal of Applied Polymer Science, Appl. Polym. Symp. **41**, 187 (1985).

10. J. Magoshi, S. Kamiyama, S. Nakamura, Proceedings of the 7th International Wool Textile Research Conference, Tokyo **1**, 337 (1985).

11. D.L. Kaplan, S.J. Lombardi, W.S. Muller, S. Fossey, Biomaterials Novel Materials from Biological Sources, edited by D. Byrom (Stockton Press, New York, 1991), p. 1.

12. F. Lucas, J.T.B. Shaw, S.G. Smith, Adv. Prot. Chem. **13**, 107 (1958).

13. F. Lucas, Nature **210**, 952 (1966).

14. N. Minoura, M. Tsukada, N. Masanobu, Biomaterials **11**, 430 (1990).

15. P.D. Calvert, Encyclopedia Materials Science and Engineering, Biological Macromolecules, (Pergamon Press, Oxford, 1988) p. 334.

16. J.C. Zemlin, Technical Report 69-29-CM (AD684333), US Army Natick Laboratories, Natick MA 1968.

17. R.M. Swart, Langmuir-Blodgett Films, edited by G. Roberts (Plenum Press, New York, 1990) p. 273.

18. R.E. Marsh, R.B. Corey, L. Pauling, Biochim. Biophysics Acta **16**, 1 (1955).

19. R.D.B. Fraser, T.R. MacRae, Conformation of Fibrous Proteins (Academic Press, New York, 1973).

20. D.L. Kaplan, S. Fossey, C. Viney, and W. Muller in Hierarchically Structured Materials, edited by I.A. Aksay, Eric Baer, M. Sarikaya, and D. Tirrell (Mater. Res. Soc. Symp. Proc. **255**, Pittsburgh, PA, 1992) pp. 19-30.

21. H. Yoshimizu, T. Asakura, J. Appl. Poly. Sci. **40**, 1745 (1990).

22. T. Asakura, A. Kuzuhara, R. Tabeta, H. Saito, Macromolecules **18**, 1841 (1985).

23. N. Minoura, T. Masuhiro, N. Masanobu, Polymer **31**, 265 (1990).

PART IV

Structural and Mechanical Properties

PHOTOVOLTAIC EFFECTS AND CHARGE TRANSPORT STUDIES IN PHYCOBILIPROTEINS

N. N. BELADAKERE, T. RAVINDRAN*, B. BIHARI*, S. SENGUPTA, K. A. MARX, J. KUMAR* AND S. K. TRIPATHY.
Center for Advanced Materials, Departments of Chemistry and Physics*, University of Massachusetts Lowell, Lowell, MA 01854, U.S.A.
B. WILEY AND D. L. KAPLAN
Biotechnology Branch, U.S. Army Natick Research, Development and Engineering Center, Natick, MA 01760, U.S.A.

ABSTRACT

Phycobiliproteins form highly efficient light absorbing systems in certain algae. We have investigated the charge-transport phenomena in these proteins by analyzing the dark current-voltage and photocurrent characteristics obtained across Au-phycobiliprotein-Au samples. A photovoltaic effect was observed for Au-phycoerythrin-Au sample. At low intensity levels, the photocurrent closely follows Onsager's law of geminate recombination in three dimensions.

INTRODUCTION

Phycobiliproteins, porphyrins and carotenoids in supramolecular assemblies play a central role in energy and electron transfer processes in natural systems. Stacked porphyrin systems have been proposed as potentially useful materials in the fabrication of photovoltaic devices of exceptionally high performance and efficiency [1-2].

Photodynamic proteins containing small pigment chromophores form the photosynthetic apparatus in plants and algae. Photosynthetic pigments comprise a broad category such as chlorophyll, bilins and carotenoids. The role of chlorophylls and bilins have been well-established in the light-harvesting process [3].

In algae, phycobiliproteins form large, highly organized supramolecular antenna complexes called phycobilisomes. These complexes are responsible for harvesting visible light [4-5]. Studies on these complexes have been on isolation and separation of the individual pigment proteins from their native environments [6], crystallographic structure determination [7], and the absorption and fluorescence properties [8-9] of these molecules and assemblies. The molecular structures of some of the phycobilins are shown in Figure 1. Phycoerythrin (PE), phycocyanin (PC) and allophycocyanin (APC) are the individual biliproteins that self-assemble to form the phycobilisomes. The most remarkable feature of this supramolecular complex lies in the ordered hierarchy of the assembly. The absorption and fluorescence properties of each of these individual biliproteins form the basis for this hierarchy. These assemblies are responsible for maximizing the efficiency of light-harvest and energy transfer between the individual biliproteins down to photosystem II [3-5].

In an earlier study, it was demonstrated that phycoerythrin can be incorporated into conducting polymers creating ordered systems possessing unusual optical and electronic properties [10]. In the present investigation,

Mat. Res. Soc. Symp. Proc. Vol. 292. ©1993 Materials Research Society

we have carried out experiments on pure proteins in order to understand the charge-generation and charge-transport phenomena. These results have been used in delineating the electron transport mechanisms in this important class of proteins.

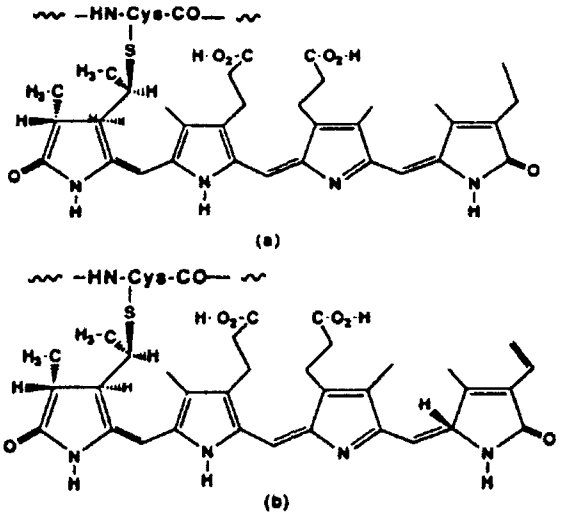

Figure 1 Molecular structure of common phycobilins (a) phycocyanobilin and (b) phycoerythrobilin.

EXPERIMENTAL

Interdigitated gold electrode geometry was used for photoconductivity measurements. These electrodes consisted of digits separated by 15 μm, and of 5000 Å length and 1000 Å thickness. A drop of aqueous protein solution was placed on the electrode. After evaporation of the solvent, thin insulating protein films sandwiched between the Au digits were obtained. The resistance of these films was of the order of several megaohms.

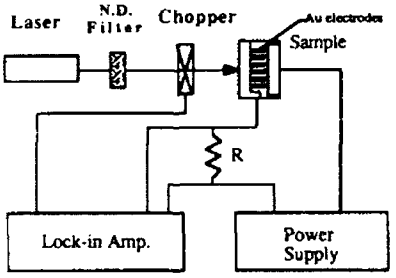

Figure 2 Experimental setup for steady state photoconductivity measurements.

The experimental setup for steady state photoconductivity measurements is shown in Figure 2. Continuous wave (CW) light of wavelength 488nm from an Ar^+ laser was used as the light source. The light beam was chopped at 15 Hz. The signal across a 1 megaOhm resistor, which is in series with the sample, was detected by a lock-in detector. The sample was mounted on a cold finger type cryostat which can be cooled down to 20 K. All the measurements were done in a vacuum better than 10^{-3} torr. The

absorption spectra of the proteins in the thin film form were obtained in the UV-visible range. The dark current-voltage characteristics of the resulting metal-protein-metal configurations were measured in air.

RESULTS AND DISCUSSION

The UV-visible absorption spectra of the proteins PC and PE in thin film form are shown in Figures 3(a) and (b). Both the absorbance and fluorescence spectra of these proteins in their dried thin film form closely resemble their solution spectra (fluorescence spectra not shown here).

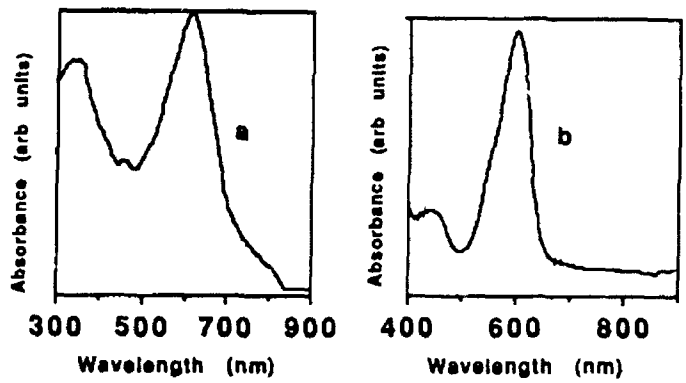

Figure 3 Absorption spectra of (a) phycocyanin and (b) phycoerythrin. thin films.

The dark current-voltage (I-V) characteristics of the Au-protein-Au samples were determined prior to optical measurements. Figures 4(a) and (b) show the I-V characteristics of the proteins PE and PC respectively, as measured in air. From the geometry of the sample, the field across the protein is estimated to be in the range of 10^5 - 10^6 V/m. The non-linear or non-Ohmic nature of the I-V characteristics is apparent from the figure. Such non-linear characteristics could arise either from the bulk material or from the metal/insulator junctions. In the latter case this would suggest to the formation of a barrier across the junction or a possible formation of space-charges near the electrodes. A detailed analysis o' the work functions of the proteins and the metal forming the electrode is essential for further elucidation of these characteristics.

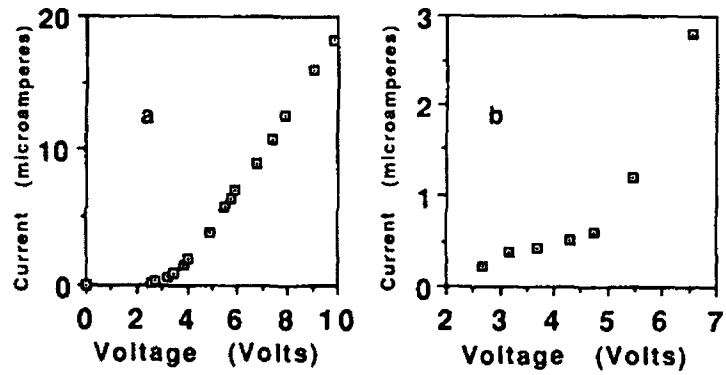

Figure 4 The current-voltage characteristics of (a) Au-PE-Au and (b) Au-PC-Au in air.

Phycoerythrin was chosen for further detailed investigation in the present work. The Au-PE-Au sample was placed in a vacuum chamber. The photocurrent across the sample was measured before and after evacuation. It was observed that photocurrent signals were stronger before evacuation. Steady-state photoconductivity across the Au-PE-Au sample was measured as a function of applied electric field, light intensity and temperature after evacuation. The variation of steady-state photocurrent with intensity at room temperature is shown in Figure 5. The applied voltage across the sample was 70 Volts. It was found that at very low excitation intensities (<1 mW/cm^2) there was negligible photocurrent across the sample. However, at intensities above 1 mW/cm^2, the photocurrent across the sample increases linearly with intensity up to 30mW/cm^2. Saturation of photocurrent is observed at higher intensities.

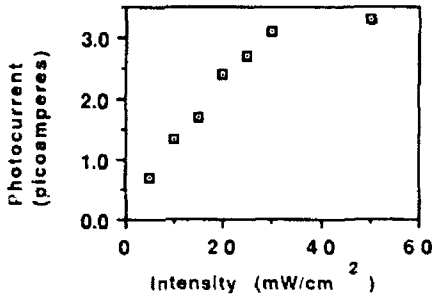

Figure 5 Steady state photocurrent characteristics as a function of intensity at 296 K.

The variation of the photocurrent with the square root of the applied voltage is shown in figure 6 on a semi-log scale. The lower curve corresponds to an excitation intensity of 20 mW/cm^2 and the upper curve to 50 mW/cm^2. The linearity of these characteristics at lower intensity suggests that the photocurrent I follows the relationship

$$I \alpha \exp ((\beta E^{1/2} / kT) - (E_o / kT))$$

where E is the field across the sample, k is the Boltzmann's constant and T is the absolute temperature. The linearity also indicates that the photocurrent generation closely follows Onsager's law of geminate recombination in three dimensions [11]. At higher intensity, a deviation from this law is observed indicating that other conduction mechanisms dominate in this regime.

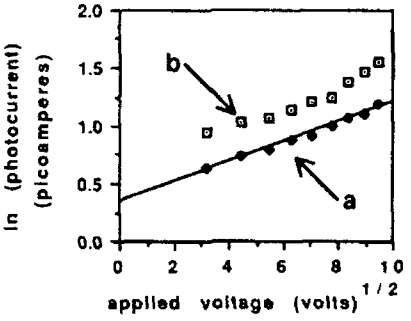

Figure 6 Variation of steady state photocurrent with square root of applied voltage for PE at 296 K (a) 20 mW/cm^2 and (b) 50 mW/cm^2.

The temperature dependence of the photocurrent across the sample was studied at 50 mW/cm^2 light intensity and at an applied voltage of 50 V. Figure 7 shows the functional form of temperature dependence of photocurrent for PE. The photocurrent remains constant at lower temperatures (70 K - 150 K) and increases exponentially at higher temperatures. The activation energy for the process is estimated to be 300 meV.

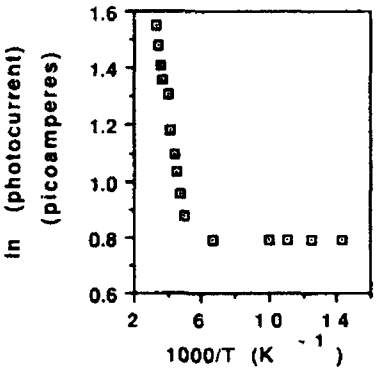

Figure 7 Temperature dependence of photocurrent for PE.

CONCLUSIONS

Au-phycobiliprotein-Au systems were fabricated and their dark I-V characteristics as well as photocurrent characteristics have been investigated. We observed for PE a photovoltage of 0.2 microvolts, 1.9 microvolts and 2.6 microvolts for incident light intensities of 1 mW/cm^2, 20 mW/cm^2 and 50 mW/cm^2 respectively. Non-linear dark I-V characteristics were obtained for both PC and PE. The linear variation of the logarithm of photocurrent with square root of the applied voltage at lower intensities suggests that the photocurrent closely follows Onsager's law of geminate recombination in three dimensions [11]. It is also observed that the photocurrent decreases exponentially with decrease in temperature according to the predictions of Onsager's law. The activation energy obtained from the Arrhenius plot (Figure 7) is estimated to be 300 meV (114.8 x 10^{-17} K. cal).

It should be noted that PE shows photoconducting properties in addition to being a good luminescent material. PE and other phycobiliproteins are strongly fluorescent. Fluorescence implies thermal freeing of trapped carriers which in turn indicates that free charge carriers are formed by the excitation process. The weak dependence of the observed photocurrent magnitude on applied electric field could be attributed to the luminescent properties of PE. Good luminescent materials require rapid recombination while good photoconductors require slow recombination. Simultaneous measurements of luminescence and photoconductivity would give us a deeper knowledge of charge generation, transport and recombination processes [12]. Such investigations will lead to a better understanding of the potential of these proteins in device applications and may lead to a more fundamental appreciation of the biochemistry and photophysics of how they function in the phycobilisome in vivo.

ACKNOWLEDGEMENT

Supported by URI grant DAAL 03-91-G-0064 from the Army Research Office.

REFERENCES

1. P. G. Schouten, J. M. Warman, M. P. de Haas, M. A. Fox and H-L. Pan, Nature, **353**, 736 (1991).

2. T. E. Mallouk, Nature, **353**, 698 (1991).

3. K. S. Rowan, Photosynthetic pigments of algae (Cambridge University Press, Cambridge, 1989).

4. A. N. Glazer, Ann. Rev. Biophys. Biophys. Chem. **14**, 47 (1985).

5. E. Gantt, BioScience, **25**, No. 12, 781 (1975).

6. E. Gantt, C. A. Lipschutz, J. Grabowski and B. K. Zimmerman, Plant. Physiol. **63**, 615 (1979).

7. T. Schirmer, W. Bode, R. Huber, W. Sidler and H. Zuber, Biol. **185**, 257 (1985).

8. A. R. Holzwarth, Photochemistry and Photobiology, **43**, No. 6, 707 (1986).

9. A. R. Holzwarth, The light Reactions, edited by J. Barber (Elsevier Science Publishers B. V. (Biomedical Division), 1987), Chapter 3.

10. K. A. Marx, L. A. Samuelson, M. Kamath, S. Sengupta, D. L. Kaplan, J. Kumar and S. K. Tripathy in "Molecular and Biomolecular Electronics", edited by R. R. Birge (Advances in Chemistry series, American Chemical Society, Washington D.C., 1992) in press.

11. L. Onsager, Phys. Rev. **54**, 554 (1938).

12 R. H. Bube, Photoconductivity of Solids (John Wiley and Sons Inc. New York, 1960).

MECHANICAL PROPERTIES OF BIOPOLYMER CHAINS

RUTH PACHTER, PETER D. HAALAND, ROBERT L. CRANE AND W. WADE ADAMS
Materials Directorate, Wright Laboratory, Wright-Patterson Air Force Base, Ohio 45433

ABSTRACT

Molecular simulations that predict the molecular mechanical response of alpha-helical biopolymers with a reinforcing intra-molecular hydrogen bonding network, *viz.*, a 'spring-like' behavior, are presented in this study. Mechanical properties of extended biopolymer strands based on naturally occurring amino acids, namely poly(L-Ala) and for comparison poly(L-Glu), *versus* synthetic PPTA containing an amide bond, are compared to those assuming alpha-helical structures. Thus, the pivotal role of such motifs in biological systems utilizing superior compressive mechanical properties can be inferred.

INTRODUCTION

It is the purpose of the present study to report an application of a semi-empirical quantum mechanical approach to the study of biopolymers *versus* similar synthetic molecular structures, which offers new insight into the mechanical properties of flexible *coiled coil* arrangements of alpha-helical motifs found in Nature, while also holding promise for the design of new materials. The importance of such biopolymers and their function is profound and cannot be covered in detail, and thus is only referred to by example: alpha-helical structures as found in keratin in hair, myosin and tropomyosin in muscle, epidermin in skin; and fibrin in blood clots, all of which play vital mechanical roles. In the case of the myosin tail, the *coiled coil* superstructure leads to a hierarchy of reinforcing interactions within the alpha-helices, hence culminating in the highly ordered array of a thick filament that provides the means for its mechanical function in muscle contraction [1]. Another significant model is offered by membrane skeletons that consist of spectrin networks which enable erythrocytes to resist strong shearing forces in blood flow. These are comprised of flexible triple-stranded alpha-helical *coiled coils* that provide the underlying mechanical stability and resilience of the erythrocyte membrane [2]. Other similar membrane skeletons in erythrocytes play meaningful roles in altering and stabilizing the shapes of various types of cells [3] and structural elements. Likewise, it is supposed that alpha-helical strands are acting as a rubbery reinforcement matrix to provide elasticity to spider silk [4], validated to some extent by our experimental study of these fibers in compression [5] that indicate no 'kinking' [6] failure. Indeed, the development of new biopolymer fibers is of special interest since spider silk designs were found to be governed by the same principles that apply to synthetic materials [4]. This analysis presents a theoretical verification of the absence of 'kinking' in biopolymer chains of an alpha-helical structure, thus explaining their extraordinary mechanical functions in these examples, and especially in *supercoiling* architectures.

RESULTS AND DISCUSSION

The prediction of mechanical properties of polymers based on calculations employing empirical potential energy functions has been addressed [7,8,9]. However, such an approach is limited because it applies a classical force-field dependent on a particular parametrization scheme, but more important is that not all the possible deformation modes can be taken into account. In our analysis we employ a rigorous method recently developed and applied [10,11]. The polymer calculations we performed apply the semi-empirical Neglect of Differential Overlap approximation at the modified level AM1 (Austin Model 1). Furthermore, within this approach [12] the so-called 'cluster method' that characterizes a polymer by a translation vector

Mat. Res. Soc. Symp. Proc. Vol. 292. ©1993 Materials Research Society

is applied. In this approximation, a segment of a polymer is defined by a number of repeat units, with periodic boundary conditions applied to describe different unit cells [13]. The advantage of this technique is that end effects are eliminated. The equilibrium geometry of the cluster is optimized and the translation vector thereafter incrementally increased or decreased, representing the molecular strain. By optimizing the geometry for different translations, the dependence of the heat of formation on tension and compression is established, thereby defining the force constant.

The elastic modulus E for a polymer is given by:

$$E = \frac{\sigma}{\varepsilon} = \left(F/A_{eq}\right) / \left(\Delta L/L_{eq}\right) = KL_{eq}/A_{eq} \qquad (1)$$

where σ is the stress (force/area), ε is the strain (fractional change in cluster length ΔL), K the force constant ($F/\Delta L$) and L_{eq} the equilibrium length of the polymer as obtained from the calculation. The force constant is derived [14] from the dependence of the change in heat of formation ΔH_{ff} on ΔL:

$$\Delta H_{ff} = a_1(\Delta L)^3 + a_2(\Delta L)^2 + a_3(\Delta L) + a_4 \qquad (2)$$

where $K=2a_2$ at equilibrium at 0 K. The cross sectional area A_{eq} is obtained from X-ray diffraction or the density d (grams/cm^3) by:

$$d = m/V = m/A_{eq}L_{eq} = nM_w/A_{eq}L_{eq} \qquad (3)$$

so that $A_{eq}=M_w/dN_AL_{eq}$; M_w is the molecular weight, n number of moles, V volume, and N_A Avogadro's number. The force constant can be alternatively derived by numerical differentiation, but the values obtained by either method are within the fitting procedure error.

In this study we examine extended biopolymer strands based on naturally occurring amino acids, namely poly(L-Ala) and for comparison poly(L-Glu), *vs.* synthetic PPTA [15] containing an amide bond, to those assuming an alpha-helical structure. The polypeptides are helix 'makers' and are used as model compounds. The biomolecular models were derived to assume either an extended or an alpha-helical configuration for poly(L-Ala), while PPTA has an extended conformation. The cluster length requisite for this calculation is determined by the electron delocalization length within the polymer [16]. Six repeat units for poly(L-Ala) and five repeat units for poly(L-Glu) in the unit cell were simulated, showing that our use of the maximal possible cluster length with such a calculation ensures that there are no non-zero off-diagonal elements in the density matrix. The equilibrium geometry and heat of formation for both one- and two- repeat units of PPTA were also determined, indicating a difference in {ΔH_{ff} /repeat unit} of *ca.* 5 kcal/mol. We compared the geometries calculated by using the amide bond correction to the Hamiltonian [12] to those optimized with a classical force-field [17], confirming that the alpha-helical configuration is conserved within our approach since we use a large number of repeat units [16] within the unit cell.

The calculated response of the extended PPTA, poly(L-Ala) and poly(L-Glu) to the application of strain is outlined in Figures 1*a*-1*b*. Although mechanical properties of PPTA have been previously calculated [18], none were carried out at this level of theory. We have also evaluated the strain-dependence of the vibrational frequencies for this polymer. Specifically, we carried out a study of the vibrational frequencies strain dependence for PPTA, indicating a linear dependence on strain for 1056 cm^{-1} and 3454 cm^{-1}, with slopes of -10.8 cm^{-1} /% strain and 4.1 cm^{-1}/% strain, respectively. The former normal mode represents a torsional vibration between the phenyl groups and the latter a C-H motion at the joints linking the phenyl groups. A negative slope for a strain-induced frequency change in PPTA single fibers was observed experimentally [19], enabling further characterization of the molecular deformation.

It is interesting to point out that a computation of the modulus from the equilibrium structure of poly(L-Ala) by a novel method we recently derived is in good agreement with the calculated result obtained by straining the molecule. Within this approach an applied force $\boldsymbol{F}$

$$\boldsymbol{H}\delta\boldsymbol{R} = \boldsymbol{F} \tag{4}$$

and $H_{ij}=\partial^2 E/\partial R_i \partial R_j$, is left multiplied by the inverse of $\boldsymbol{H}$ to yield the virtual displacements of all atoms

$$\delta\boldsymbol{R} = \boldsymbol{H}^{-1}\boldsymbol{F} \tag{5}$$

The modulus is then calculated by using the cluster's geometry. An application of the method to the extended chain of poly(L-Ala) by using a force of 2 mD along the translation vector, results in a modulus of 179 GPa. We also applied this method to a mechanical properties calculation of C_{60} molecules [20]. Obviously, high tensile strengths are predicted for PPTA and extended biopolymers. More significant is the behavior of these molecular systems in compression, where a molecular buckling phenomenon is observed in PPTA that is especially important to the understanding of the possible mode of failure in these fibers. This calculated result supports in part the supposition of a conformational change in PPTA upon compression [21]. Also, the molecular structure of the extended biopolymers enables more conformational variation since there is an additional rotatable bond, resulting in only a small change in energy in compression. These data suggest new design possibilities for 'molecular engineering' of polymers with enhanced compressional strength.

The ΔH_f vs. ΔL dependence (Figure 1*a*) for PPTA results in a modulus of *ca.* 330 GPa, where d=1.5 g/cm^3, L_{eq}=13.1 Å, M_w=238.25 g/mol, A_{eq}=20.1Å^2, and K=50.6 N/m , which overestimates the experimental range of 120-200 GPa. However, the overestimation can be partially corrected *by biasing the Hessian with* experimental vibrational frequencies [11]. The overall response is similar to that of other rigid-rod polymers [10]. The dashed line is the force curve (10^{-10} N) obtained by taking a numerical derivative of the energy, and is given as an example of the additional data that can be derived, namely that 'kinking' occurs at approximately 2.5% compressive strain. The force curve is the molecular equivalent of a strain-stress curve. For the extended biopolymer chains (Figure 1*b*), a modulus of *ca.* 160 GPa is calculated for poly(L-Ala), where A_{eq}=20 Å^2, L_{eq}=21.7 Å, and K=145 N/m, and for poly(L-Glu) a modulus of *ca.* 230 GPa (A_{eq}=20 Å^2, L_{eq}=14.5 Å, and K=320 N/m) is evaluated.

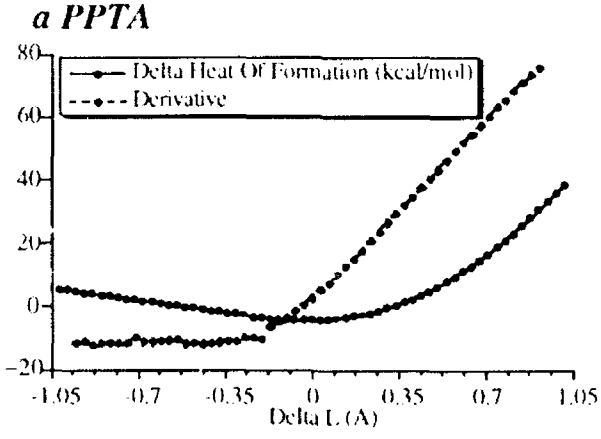

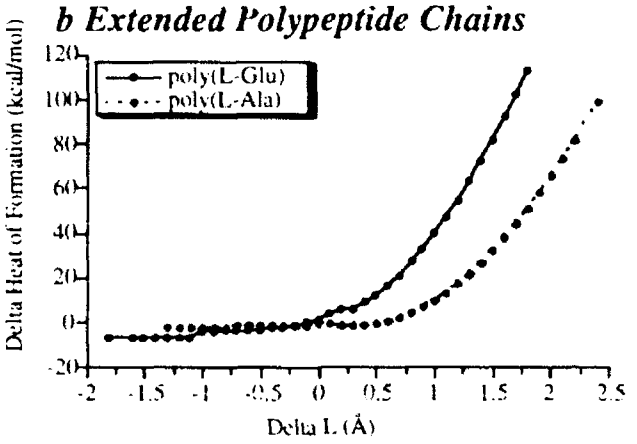

Figure 1: ΔH_{ff} *vs.* ΔL dependence for ***a*** PPTA and ***b*** extended polymer chains

A clearly different response of an alpha-helical chain to the application of strain is shown in Figure 2, revealing a large energy change in compression but no buckling, while small variations are calculated in tension. Specifically, the ΔH_{ff} *vs.* ΔL dependence for the alpha-helical model of poly(L-Ala) results in a modulus of *ca.* 60 GPa, where A_{eq}=20 Å^2, L_{eq}=10.2 Å, and K=107 N/m. The force (10^{-10} N) curve (dashed line) shows that in distinct contrast to PPTA (Figure 1b), there is no evidence for 'kinking'. This observation is supported by the fact that no buckling is found in the alpha-helical biopolymer conformations in compression.

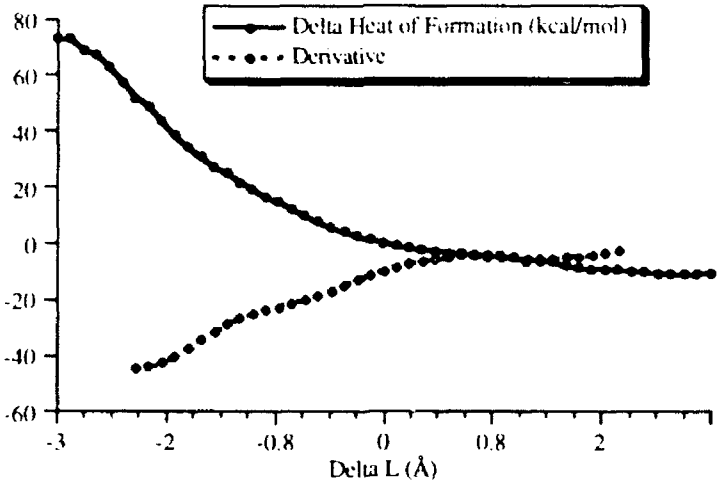

Figure 2: The ΔH_{ff} *vs.* ΔL dependence for the alpha-helical model of poly(L-Ala)

A similar response is predicted for poly(L-Glu), and although overestimated, the predicted modulus for poly(L-Glu) is in qualitative agreement with experiment [22]. Particularly, the ΔH_{ff} *vs.* ΔL dependence for the alpha-helical model of poly(L-Glu) results in a modulus of ca. 60 GPa, where the A_{eq}= 20 Å^2, L_{eq}=5.2 Å, and K=240 N/m. These results reveal a 'spring-like' behavior of alpha-helical biopolymer chains, in contrast to the extended systems. Interestingly, it has been shown experimentally that all synthetic high performance polymers [15,23] fail by buckling [6], whereas spider silk fibers that contain alpha-helical structures on

the surface do not 'kink' [5], which is consistent with our calculations. Indeed, our simulation may explain the molecular elasticity and resistance to 'kinking' of biopolymers that consist of alpha helical strands, hence the apparent prevalence in Nature of *coiled coils*.

In conclusion, this study reveals the potential of molecular simulations to predict the macroscopic mechanical response of alpha helical biopolymers with a reinforcing hydrogen bonding network, viz., a 'spring-like' behavior. This calculation explains the pivotal role of such motifs in biological systems requiring superior compressive mechanical properties [1–5]. Our foreknowledge of the absence of 'kinking' and the understanding of the structure to function relationships in biopolymers is significant in that it may enable the synthesis of structural motifs consistent with molecular frameworks optimized by Nature, e.g., damage resistant composites. Indeed, this investigation is important for the design of materials based on the doubtless efficient molecular architecture found in Nature, especially in recognizing the emerging interest in developing new polymers [24]. For example, the advent of rigid rod polymer fibers [23] led to a series of studies [25] revealing tensile strengths high enough to make them promising candidates for incorporation into aerospace structures, although their application to date is limited due to low axial compressive strength. These results further support the pursuit of new materials that do not have this mechanical drawback and also exhibit enhanced optical properties, as initiated by our examination of polypeptide bound chromophores [26]. Moreover, direct comparisons of our predictive capability with experimental studies of the mechanical properties of biomaterials, as have been recently initiated [27], for example, for DNA strands [27], will further enhance the ability to design new materials.

REFERENCES

[1] H.M. Wyss and J.A. Spudich, Ann. Rev. Cell Biol. **3**, 329 (1987), and references therein.

[2] T.J. Byers and D. Branton, Proc. Nat. Acad. Sci. **82**, 6153 (1985).

[3] V.T. Marchesi, Ann. Rev. Cell Biol. **1**, 531 (1985).

[4] D.L. Kaplan, S.J. Lombardi, W.S. Muller, and S.A. Fossey, "Silks: Chemistry, Properties, and Genetics Biomaterials: Novel Materials from Biological Sources", Macmillan Press (1991); F. Vollrath, *Scientific American*, 70–76, March (1992); F. Vollrath and D.T. Edmonds, Nature, **340**, 305 (1989).

[5] D. Mahoney, D.L. Vezie, R.K. Eby, and W.W. Adams, manuscript in preparation.

[6] F.J. McGarry and J.E. Moalli, Polymer, **32**, 1816 (1991); S.J. LeTeresa, R.S. Porter, and R.J. Farris, J. Mater. Sci., **23** 1886 (1988).

[7] G.C. Rutledge and U.W. Suter, Polymer, **32**, 179 (1991).

[8] R.A. Sorensen, W.B. Liau, and R.H. Boyd, Macromolecules, **21**, 194 (1988).

[9] K. Tashiro, M. Kobayashi, and H. Tadokoro, Macromolecules, **11**, 908 (1978).

[10] S.G. Wierschke, J.R. Shoemaker, R. Pachter, P.D. Haaland, and W.W. Adams, Polymer, **33**, 357 (1992).

[11] J.R. Shoemaker, L.R. Horn, P.D. Haaland, R. Pachter, and W.W. Adams, Polymer, **33**, 3 (1992).

[12] J.J.P. Stewart in MOPAC (Version 5.0), Quantum Chemistry Program Exchange #455.

[13] J.J.P. Stewart, *New Polym. Materials*, **1**, 53–59 (1987).

[14] H.E. Klei and J.J.P. Stewart, Int. J. Quant. Chem., Quant. Chem. Symp., **20**, 529 (1986).

[15] The invention by DuPont of the spinning of liquid crystalline acid solutions of stiff-chain poly(para-phenylene terephthalamide) (PPTA) [KEVLAR™] opened the field of high performance organic fibers (S. Kwolek, U. S. Patent No. 3 600 356 (1971).

[16] P.G. Perkins and J.J.P. Stewart, J. Chem. Soc. Faraday Trans. II, **76**, 520 (1980).

[17] CHARMm (Chemistry at HARvard Macromolecular mechanics) (B.R. Brooks, R.E. Bruccoleri, B.D. Olafson, D.J. States, S. Swaminathan, and M. Karplus, J. Comp. Chem **4**, 187 (1983); coded in Quanta: Release 3.0, Polygen Corporation, 1990.

[18] G.C. Rutledge, U.W. Suter, and C.D. Papaspyrides, Macromolecules, **24**, 1934 (1991).

[19] C. Chang and S.L. Hsu, Macromolecules, **23** 1484 (1990), and R.J. Young, private communication.

[20] P. D. Haaland, R. Pachter, M. Pachter, W.W. Adams, Chemical Phys. Lett., **199**, 379 (1992).

[21] D. Tanner, J.A. Fitzgerald, and B.R. Phillips, Adv. Mater., No. 5, 151 (1989).

[22] G. Wegner, private communication, estimates the modulus as ca. 30 GPa.

[23] *Cis*- and *trans*- isomers of poly(*para*-phenylene benzobisimidazole) rigid rods were first synthesized by R.F. Kovar and F.E. Arnold, J. Poly. Sci., Poly. Chem. Ed., **14**, 2807 (1976), *cis*- and *trans*- poly(*para*-phenylene benzobisoxazole) by T.E. Helminiak, F.E. Arnold, and C.L. Benner, Polymer Preprints, ACS Poly. Div. **16**(2), 659 (1975), and *cis*- and *trans*- poly(*para*-phenylene benzobisthiazole) by J. F. Wolfe, B.H. Loo, and F.E. Arnold, Polymer Preprints, ACS Poly. Div., **19**(2), 1 (1978).

[24] H.R. Allcock, Science, **255**, 1106-1112 (1992).

[25] S. Kumar, International Encyclopedia of Composites, **4**, 51 (1991).

[26] T.M. Cooper, K.A. Obermeier, L.V. Natarajan, and R.L. Crane, Photochem. Photobio., **55**, 1 (1991); R. Pachter, T.M. Cooper, L.V. Natarajan, K.A. Obermeier, R.L. Crane, and W.W. Adams, Biopolymers, **32**, 1129 (1992).

[27] S.B. Smith, L. Finzi, and C. Bustamante, Science, **258**, 1122 (1992).

SYNTHESIS AND CHARACTERIZATION OF PERIODIC POLYPEPTIDES CONTAINING REPEATING —(AlaGly)$_x$GluGly— SEQUENCES

YOSHIKUNI DEGUCHI*, MARK T. KREJCHI*, JANOS BORBELY*, *LAURILLE J. FOURNIER**, THOMAS L. MASON** and DAVID A. TIRRELL*

*Department of Polymer Science and Engineering and **Department of Biochemistry and Molecular Biology, University of Massachusetts, Amherst, Massachusetts 01003

ABSTRACT

We have expressed in *E. coli* a series of periodic polypeptides represented by sequence **1**. Our objective has been an understanding of the role of chemical sequence in determining the chain folding behavior of periodic macromolecules. Molecular organization has been examined by infrared spectroscopy and ^{1}H and ^{13}C NMR methods and a preliminary model of the folded structure has been developed.

$$+(\text{AlaGly})_x\text{GluGly}+_n \qquad \mathbf{1}$$

a: x=3, n=36
b: x=4, n=18
c: x=4, n=28
d: x=5, n=14
e: x=5, n=20
f: x=6, n=10
g: x=6, n=14

INTRODUCTION

We have been studying a series of periodic polypeptides represented by the general formula **2**, wherein the repeating alanylglycine dyads are expected to bias the chain toward an anti-parallel β-sheet conformation [1,2]. Our objective is control of chain folding in the solid state, by incorporating periodic β-sheet breakers into the sequence. Our first attempt used a variant of sequence **2** in which x=3, Z=ProGlu, and n=54 [3]. X-ray diffraction analysis of this protein afforded no evidence of crystalline structure. In this paper we report recent progress in characterization of the similar family of polymers represented by sequence **1**.

$$+(\text{AlaGly})_x\text{ZGly}+_n \qquad \mathbf{2}$$

EXPERIMENTAL SECTION

Synthetic strategy. The overall strategy for the production of the target material is shown in Figure 1. Detailed experimental conditions are described elsewhere [3,4].

Protein expression. Artificial genes encoding proteins containing sequences **1a-g** were constructed and expressed in the pET3-b vector and *E. coli* strain BL21(DE3)pLysS developed by Studier and coworkers [5]. Expression was initially monitored by the incorporation of ^{3}H-glycine into the target protein. A rich medium (YT) was used for sample preparation. β-Isopropylthiogalactoside (IPTG, final concentration 95 mg/L) was added to the culture to induce protein production when OD at 600 nm reached ca. 0.8.

Purification. Cell extracts were prepared by freezing, thawing, sonication and spinning out of cell debris. The extract was adjusted sequentially to pH 5.0, 4.5 and 4.0 with glacial acetic acid. After each pH adjustment, precipitated material was removed by centrifugation. After enzymatic removal of contaminating nucleic acids, the target protein was precipitated by addition of ethanol to 40 v/v%. Crude product was washed with water repeatedly until the absorbance of the supernatant at 260 nm disappeared.

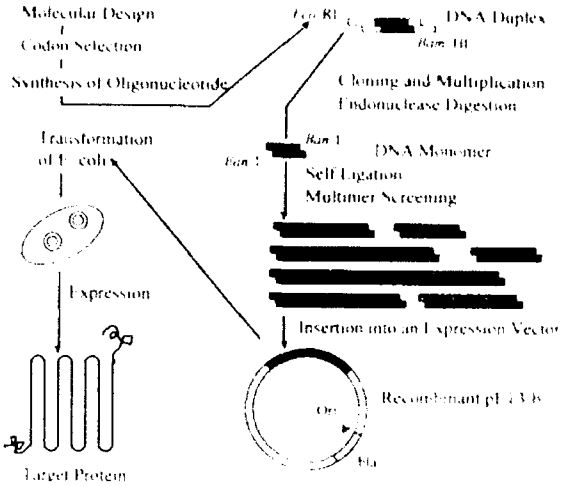

Figure 1. Overall strategy for biosynthesis of polymers of sequence 1.

Cyanogen bromide cleavage. Fusion ends were chemically removed by selective cyanogen bromide cleavage at room temperature in formic acid.

Infrared spectroscopy. A portion of cleaved protein was placed in an Eppendorf tube and 90% formic acid was added thereto so that 1 μL of solution would contain 100 μg of solid. The solution was kept at room temperature until use. After an appropriate time period, a portion of the solution was spread on a NaCl plate and air dried.

Computer graphics. Molecular modeling was performed using Biograf version 2.2 (BioDesign, Inc.) running on a Silicon Graphics Iris work station.

NMR spectroscopy. NMR analyses were conducted at room temperature on Varian XL-300, Varian 500 MHz Unity, and Bruker 200 AF, 300 MSL and 500 AMX spectrometers. Formic acid formyl-d_1 was used as solvent.

RESULTS and DISCUSSION

Protein expression. The expression strain, BL21(DE3)pLysS, carries a chromosomal gene encoding bacteriophage T7 RNA polymerase under *lacUV5* control [5]. The pLysS plasmid produces a low level of T7 lysozyme, which suppresses leaky T7 RNA polymerase activity prior to induction with IPTG. Each of the proteins **1a-g** was expressed in *E. coli* successfully. None of these proteins stained well with the conventional dye Coomassie Blue, so *in vivo* labelling techniques were used to monitor accumulation.

Purification. Contaminating proteins were removed readily from the product by stepwise acidification of whole cell lysates, owing to the fact that the target proteins remain soluble in mildly acidic solutions that precipitate native *E. coli* proteins. Purification leads to products of general sequence **3**, in which the repetitive oligopeptide building blocks are flanked by leader and trailer sequences derived from the cloning and expression vectors. Typical yields of purified protein were 20-70 mg/L, decreasing slightly with increased spacing between

glutamic acid residues. The leader and trailer sequences were removed by cyanogen bromide digestion prior to structural analysis by infrared and NMR methods.

MASMTGGQQMGRDPMFKYSRDPM[(GA)$_x$GE]$_n$ **3**
GARMHIRPGRYQLDPAANKARKEAELAAATAEG

Infrared spectroscopy. Figure 2 shows IR absorption spectra of films of polymer **1c** cast from formic acid after aging of the casting solution for various times. The broad band in the amide I region is apparently composed of two main peaks, one centered near 1660 cm^{-1} and the other around 1625 cm^{-1}. The former band decreased in intensity as the solution aged, while the intensity of the latter band increased. The rate of change in the relative intensities of these two bands was found to depend on the sample concentration, and was reduced in more dilute solutions. Gelation of each solution was observed concurrently with the rise in intensity at 1625 cm^{-1}. We attribute the 1625 cm^{-1} band to an antiparallel β-sheet structure and the higher frequency absorption to a disordered conformation.

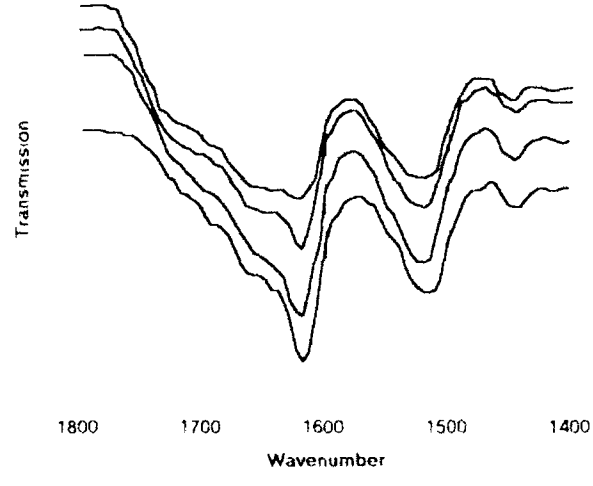

Figure 2. Infrared spectra of cast films. Cleaved **1c** protein was dissolved in formic acid and films were cast on NaCl. From the top, curves correspond to 5 min, 2 hr, 8 hr, and 26 hr of solution aging prior to film casting.

NMR spectroscopy. The infrared results discussed above, coupled with the observed gelation of the formic acid solutions upon aging, suggest that an ordered β-structure develops with time in these polymer solutions. This structure was probed more fully in preliminary high-field NMR experiments. Of special interest were questions of: i). whether or not the chain folds in regular fashion in solution, and ii). if regular folding does occur, what the local structure of the fold may be.

The ^{13}C NMR spectrum of polymer **1c** dissolved in formic acid-d_1 is shown in Figure 3. Chemical shifts relative to formic acid (δ166.31 ppm) and peak assignments are listed in Table I. Assignments were made on the basis of repeating unit sequence **4**, in which the designation of 3 distinct glycyl units and 2 distinct alanyl units is suggested by the appearance of multiple carbonyl resonances for each of these residues.

—(GlyAla)$_3$Gly*GluGly**Ala*— **4**

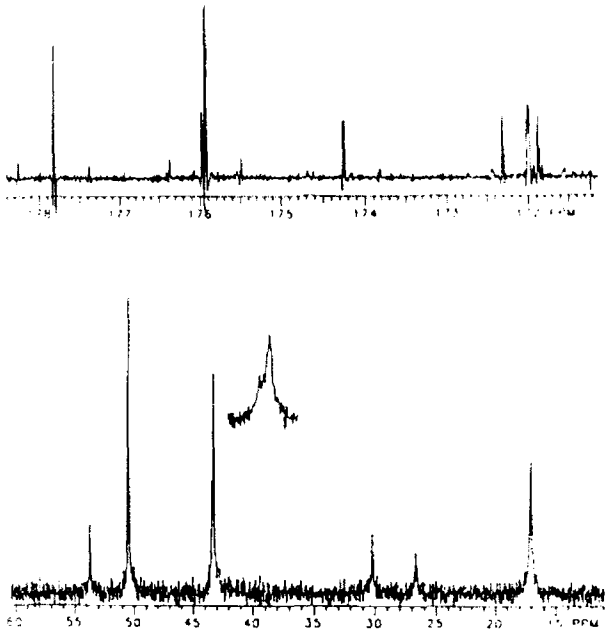

Figure 3. ^{13}C NMR spectra of cleaved 1c. Upper: carbonyl carbons; lower: aliphatic carbons.

Table I. Assignment of ^{13}C NMR Spectrum of Polymer 1c

δ in ppm	*Assignment*
17.03	β-CH_3 of all Ala residues
26.63	β-CH_2 of Glu
30.21	γ-CH_2 of Glu
43.28	α-CH_2 of Gly
43.33	α-CH_2 of Gly* or Gly**
43.37	α-CH_2 of Gly* or Gly**
50.51	α-CH of Ala and Ala*
53.76	α-CH of Glu
171.88	Carbonyl of Gly*
172.00	Carbonyl of Gly
172.31	Carbonyl of Gly**
174.26	Carbonyl of Glu
175.94	Carbonyl of Ala
175.98	Carbonyl of Ala*
177.83	Side chain carboxyl group of Glu

The relative intensities of the carbonyl signals are consistent with this assignment, and the presence of sharp resonances suggests that the chain adopts a limited set of conformations in formic acid solution. In contrast, the ^{13}C NMR spectrum obtained in HFIP-d_2 solution shows very broad carbonyl peaks, suggesting that in HFIP the polypeptide chain exists as a random coil.

Figure 4 shows a partial NOESY spectrum of **1c** taken in formic acid solution. The observation of strong sequential α-proton-NH NOEs and absence of amide-amide NOEs suggest that pleated β-sheets are present. This is supported by the appearance of H_α-H_α and H_α-H_β NOEs which are to be expected in a regular antiparallel β-pleated sheet, in which the interstrand H_α-H_α distance is approximately 2.4 Å. Furthermore, the NH peak of Gly** indicates a short interresidue interaction with the α-CH and a weak interaction with the β-CH_2 of Glu. This observation is consistent with the occurrence of a β-turn. The very strong correlation of Gly_i**NH $\rightarrow Glu_{i-1}$αCH suggests a turn of type II rather than type I or I'.

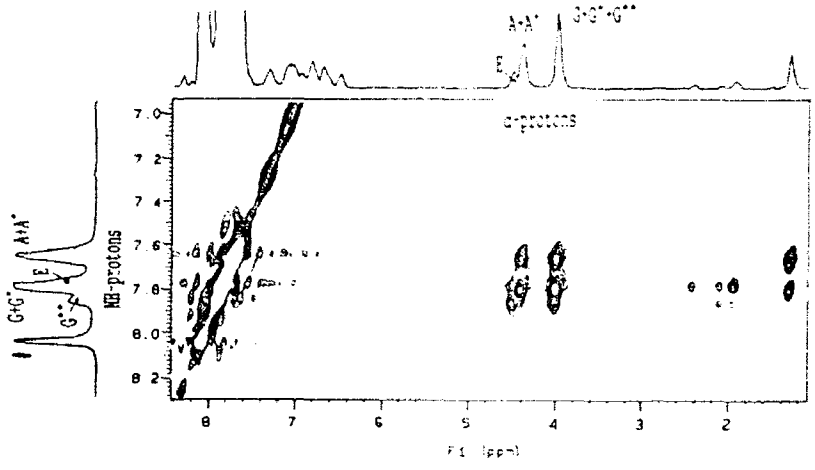

Figure 4. Partial NOESY spectrum of cleaved **1c**.

CONCLUSIONS

Although this is a preliminary analysis, the ^1H and ^{13}C NMR data obtained in formic acid are consistent with a chain conformation characterized by a predominance of β-strands interrupted by reverse turns. In contrast, the polymer in HFIP appears to be a statistical coil, giving rise to broad resonances in the ^{13}C NMR spectrum. Given these differences, it is intriguing that polymer films cast from formic acid exhibit infrared spectra characteristic of β-sheet structure, while those from HFIP are disordered. We are pursuing refinement of the solution structure of **1c** and related polymers, with the objective of understanding the mechanism of structure formation during solidification.

ACKNOWLEDGMENT

This work was supported by a grant from the Polymers and Genetics Programs of the National Science Foundation (DMR-8914359) and by the Materials Research Laboratory at the University of Massachusetts. J. Borbély thanks the Fulbright Foundation for financial support. Dr. Borbély is on leave from the Department of Applied Chemistry, Kossuth Lajos University, H-4010 Debrecen, Hungary. Yoshikuni Deguchi was on leave from Central Research Laboratories, Kaneka Corporation, 1-2-80, Yoshida-cho, Hyogo-ku, Kobe 652, JAPAN.

REFERENCES

1. D.A. Tirrell, M.J. Fournier and T.L. Mason, *MRS Bulletin* **16(7)**, 23 (1991).
2. R.D.B. Fraser, T.P. MacRae, F.H.C. Stewart and E. Suzuki, *J. Mol. Biol.* **11**, 706 (1965).
3. K.P. McGrath, M.J. Fournier, T.L. Mason and D.A. Tirrell, *J. Am. Chem. Soc.* **114**, 727 (1992).
4. Y. Deguchi, M.J. Fournier, T.L. Mason and D.A. Tirrell, in preparation.
5. F.W. Studier, A.H. Rosenberg and J.J. Dunn, *Methods Enzymol.* **185**, 60 (1990).
6. P.Y. Chou and G.D. Fasman, *J. Mol. Biol.* **115**, 135 (1977).

PROCESSING NATURAL AND RECONSTITUTED SILK SOLUTIONS UNDER EQUILIBRIUM AND NON-EQUILIBRIUM CONDITIONS

CHRISTOPHER VINEY*, ANNE E. HUBER*, DWAYNE L. DUNAWAY*, STEVEN T. CASE§ AND DAVID L. KAPLAN‡

*Molecular Bioengineering Program, Center for Bioengineering WD-12, Univ. of Washington, Seattle, WA 98195, USA

§Dept. of Biochemistry, Univ. of Mississippi Medical Center, 2500 North State Street, Jackson, MS 39216, USA

‡US Army Research, Development & Engineering Center, Natick, MA 01760, USA

ABSTRACT

A variety of natural silk secretions (from spiders, silkworms and aquatic insect larvae), and also reconstituted silk solutions, are able to form a nematic liquid crystalline phase. The anisotropic structures that self-assemble in this phase are formed from the isotropic phase by aggregation of molecules, rather than by individual molecules undergoing a conformational change to a rod-like form. This enables the molecules to retain their solubility in water while, simultaneously, the viscosity of the solution is reduced. The liquid crystalline phase is stable under a wide range of equilibrium conditions, but its ability to form *is* sensitive to the rate at which the initially isotropic solution is allowed to dry. The kinetics of phase transitions exhibited by solutions of silk proteins must be taken into account if solutions of silk fibroin are to be successfully processed *in vitro*.

BACKGROUND

Several biosynthesized polymers and their derivatives are useful as engineering materials. While unaltered or transgenic organisms therefore can play an important role as sources of chemical feedstock in materials synthesis, the subsequent processing steps needed to manufacture useful objects are still conducted *in vitro*. There are many benefits of carrying out processing operations (fiber drawing, film forming, injection molding) on polymers in the nematic liquid crystalline state, and of retaining nematic order in the solid product [1-5]. In the case of both liquid crystalline solutions and liquid crystalline melts, these benefits include:

- the low viscosity and therefore easy processability of the liquid crystalline state, compared to isotropic fluids having the same concentration of polymer;
- facilitated production of microstructures in which molecules are extended and globally aligned, leading to enhanced uniaxial stiffness and strength in the solid product;
- the low thermal expansion coefficient of the product;
- reduced susceptibility of the product to retraction (dimensional change arising from randomization of molecular orientational order) when annealed at temperatures above the glass transition but below the melting point;
- the ability to orient non-liquid crystalline materials through guest-host interactions.

In addition, liquid crystalline melts (but not solutions) exhibit relatively low solidification shrinkage compared to conventional melts, and so can be used to obtain moldings with more precise dimensional tolerances. These properties of liquid crystalline polymers are the result of spontaneous local alignment of extended molecules that characterizes the (fluid) liquid crystalline state, reducing the contributions of entanglements to fluid viscosities, and reducing the extent to which molecular re-ordering must occur during solidification.

Examples from all the major classes of biological macromolecule (proteins [6-10], polysaccharides [11-13], glycoproteins [13], nucleic acids [14-16] and lipids [17-19]) are known to form liquid crystalline phases in water. Of particular interest here are macromolecules that form liquid crystalline phases under physiological conditions, so that the liquid crystalline state plays a direct role in the *in vivo* assembly of these molecules into more complex structures, and thus is directly responsible for their function. Then, *in vitro* processing of these materials and their analogs in the liquid crystalline state is an obvious approach towards duplicating the microstructures and properties inspired by the natural materials.

Mat. Res. Soc. Symp. Proc. Vol. 292. ©1993 Materials Research Society

LIQUID CRYSTALLINITY AND SILK

The silk fibers produced by spiders and the larvae of some insects exhibit a variety of impressive engineering properties; some significant ones are summarized in Table I.

Table I Some Sophisticated Properties of Silk

PROPERTY	COMMENTS	REFERENCE
Mechanical		[20-23]
strength	up to 2 $GN.m^{-2}$ for spider drag line	
stiffness	up to 30 $GN.m^{-2}$ for spider drag line	
toughness	elongation to failure can be greater than 30% for spider drag line	
Processing		[23-25]
solvent	silk fiber is spun from aqueous solution, but will not subsequently dissolve in water (compare Kevlar®, which is spun from a solution in concentrated sulfuric acid)	
processing temperature	silk fiber is spun at ambient temperature	
processing environment	in air or under water	
fiber thickness	fibers may be as fine as 0.01μm	
Environmental		[26, 27]
durability	resists degradation in a wide variety of outdoor and chemical environments	
biodegradability	degradation to the level of amino acids by specific proteolytic enzymes allows spiders to recycle their web silk	

We are especially interested in the *in vivo* processing characteristics of silk secretions. Apart from seeking to reproduce *in vitro* the spinning of fibers from solutions of silk fibroin and similar molecules (regardless of their source), we note the generic usefulness of a room-temperature processing route that converts water-soluble polymer to insoluble high-performance fiber by physical rather than chemical means.

Both as-secreted and reconstituted silk solutions may form a nematic liquid crystalline phase

Qualitatively, we have observed the formation of liquid crystalline order in the silk secretions from diverse organisms and glands:

- silk glands from *Bombyx mori* silkworms;
- drag line, capture thread and cocoon silk secretions from *Nephila clavipes* (golden orb weaver) spiders;
- salivary glands of *Chironomus tentans* (midge) larvae.

Liquid crystalline microstructures of silkworm and spider silk secretions are shown elsewhere. In those cases [10, 28, 29], liquid crystalline microstructures were seen to develop in the viscous secretion recovered by allowing dissected silk glands to leak onto a glass microscope slide.

Microstructures of *Chironomus* silk secretions are shown in Figure 1. Salivary glands were manually dissected from larvae and placed in a droplet of deionized water (@ 20 glands/50 μl droplet) on a siliconized coverslip on the thermostated stage (4 °C) of a dissecting microscope. The lumens were punctured with a needle; secretion was allowed to leak out for about 10 minutes. The glands were removed with dissecting needles, and the extract was transferred to a

microfuge tube and centrifuged at 12,000 x *g*. Supernatants from five extracts were combined; the final sample volume after further concentration was ~50 µl. This solution was initially fluid, compared to undiluted secretion obtained directly from silkworms and spiders. Samples were examined by transmitted polarized light microscopy within 48 hours of preparation. They were allowed to dry slowly between a glass microscope slide and coverslip (Figure 1, left), or rapidly on a microscope slide with no coverslip (Figure 1, right). The phase changes of *Chironomus* silk are of particular interest because the natural silk fibers are produced entirely under water.

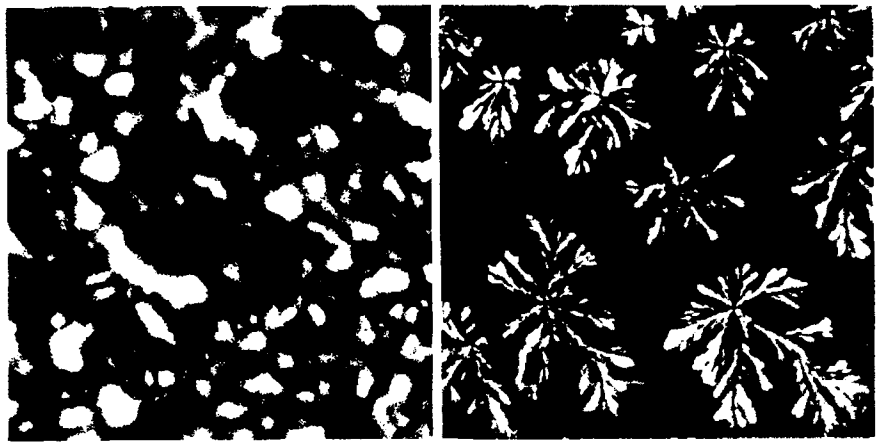

Figure 1 Microstructures of *C. tentans* silk secretion: (left) liquid crystalline order after partial drying under a coverslip; (right) crystalline order after partial drying with no coverslip. Specimens viewed in transmission between crossed polars. 10µm ———

Figure 2 Microstructure of reconstituted *B. mori* silk. Specimen viewed in transmission between crossed polars. 10µm ———

We have also observed that liquid crystalline phases can form in reconstituted silk solutions (Figure 2). The broad range of solution compositions (silk : water : chaotropic salt) over which this occurs has not yet been quantified. The microstructure in Figure 2 is representative of material with the following history: *B. mori* cocoons (with the pupae excised) were boiled in 0.065% NaOH for 2-3 minutes and then in tap water for another 20 minutes, to remove the sericin coating. After drying in a desiccator, silk was dissolved at a concentration of 7.5% by weight in 9.3M LiBr [30]. Approx. 10 grams of the solution were placed in a 10-inch length of cellulose dialysis tubing (Spectra/Por; MWCO 12,000 - 14,000; previously de-sulfurized by

treatment for 30 minutes in 1500 ml water + 30 g sodium bicarbonate + 0.618 g EDTA) and dialyzed against ~200 ml tap water for 2 days.

The liquid crystalline state of silk is assembled from supermolecular anisotropic structures

Several observations imply consistently that the "rods" constituting the liquid crystalline phase of silk are not individual molecules or molecular segments, but instead arise at the supermolecular level:

- silk proteins from different organisms have very different primary structures (none of which is recognizably nematogenic) in solution;
- the phase behavior of silkworm and spider silk secretions implies the existence of rigid rods that have an axial ratio of approximately 30 [13, 29, 31]; however, individual solubilized molecules are flexible and have no significant amounts of secondary structure [32, 33];
- microstructural observations imply that the rods are polydisperse [29].

By aggregating into rod-like structures, silk fibroin molecules with an essentially random coil conformation can form a liquid crystalline phase without having to first undergo a change in conformation. Thus, the fibroin can retain its solubility in water, while at the same time the solution becomes more easily processable because its viscosity is lowered. Fiber spinning is accompanied by a shear-induced conformational change [34]; the molecules then form a stable crystalline structure that is no longer water-soluble. This mechanism may serve as the basis for developing synthetic polymer processing routes that enable the fabrication of durable, water-insoluble fibers from molecules initially in aqueous solution.

Conditions that favor the formation of liquid crystalline order in silk solutions

Because of the experimental difficulties of accurately measuring protein and salt concentration in small samples used for microscopy, reliable quantitative information about the concentration range of liquid crystalline stability is limited. Yet, even qualitative observations show that the nematic phase forms under a wide range of conditions:

- the ability to form a liquid crystalline phase is exhibited by silks of widely differing compositions, i.e it is not sensitive to the sequence of monomers; indeed, in the case of *Chironomus* silk, one is dealing with a mixture of proteins whose apparent molecular weights span two orders of magnitude [25];
- silk can form liquid crystalline phases in substantially different environments – in the natural secreted state (containing only a trace of dissolved components that are not fibroin [22]) as well as in the presence of significant concentrations of LiBr (the material shown in Figure 2 contains LiBr at a concentration of approximately 0.5M);
- in specimens of silkworm and spider silk secretion (initial concentration ~26 vol.% or ~30 wt.% protein) that are maintained between a glass microscope slide and cover slip, a liquid crystalline phase can be recognized within minutes, i.e. after only a small change in concentration due to evaporation; a more ordered phase typically does not occur until after 2-3 days of slow drying.

However, whether or not a continuously drying silk solution exhibits liquid crystalline order does appear to be *sensitive to the initial concentration and the rate at which water is lost.* Fluid solutions, such as water-diluted *Chironomus* silk secretions, initially form liquid crystalline phases if allowed to dry slowly between a glass slide and cover slip. If no cover slip is used, then crystalline phases are formed. Viscous solutions, such as the undiluted silk secretions from silkworms and spiders, form a liquid crystalline phase whether or not a cover slip is present. A similar dependence of microstructure on initial concentration and subsequent drying rate is exhibited by other types of biological macromolecule [13].

REPRESENTING PHASE TRANSITION KINETICS ON TRANSFORMATION DIAGRAMS

Phase diagrams display the phases that occur under equilibrium conditions in a given system. In an open system in which equilibrium is not reached, the phases obtained depend on the driving force for transformation (how far is the system from equilibrium?) and on the extent to which the microstructure is able to rearrange in response to this driving force.

An established representation of the kinetics of temperature induced phase transformations in multi-component metals and ceramics is by means of Time-Temperature-Transformation (TTT) curves [35]. These curves (Figure 3a) illustrate the time dependence of the microstructural changes exhibited by a system *of fixed composition* at different temperatures. The characteristic "C" shape of the curves results from the fact that, at small supercoolings (close to equilibrium), there is little driving force for the phase change to occur. At large supercoolings, there is significant driving force for the system to convert to the new equilibrium phase, but the atoms or molecules now lack the mobility to achieve this transformation quickly. At intermediate supercoolings, the combination of driving force and mobility enables the transformation to occur at a maximum rate. Typically, TTT curves are drawn for 1% completion and 99% completion of the transformation, though a single curve is often adequate for illustrative purposes. The time difference between 1% completion and 99% completion is most significant for transformations that occur entirely in the solid state.

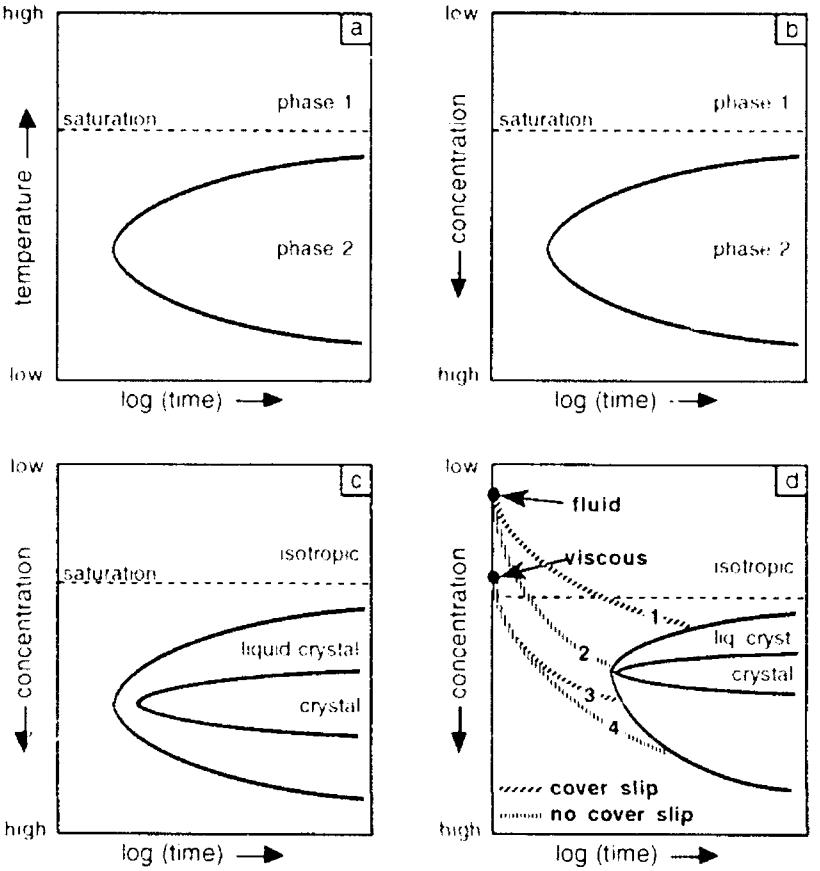

Figure 3 Transformation diagrams showing phase transition kinetics.
(a) Time-Temperature-Transformation relationship for temperature induced phase changes.
(b) Analogous Time-Concentration-Transformation relationship for concentration induced phase changes.
(c) Time-Concentration-Transformation curves for a system that forms both liquid crystalline and crystalline phases.
(d) Time-Concentration-Transformation curves schematically representing the behaviour of dilute and viscous solutions of silk.

We find that an analogous graphical device provides a useful intellectual framework for illustrating the kinetics of phase transformation in polymer solutions (Figure 3b). For transformations occurring in solutions of different concentration *at a fixed temperature*, the vertical axis is scaled in terms of concentration. The behavior of the system at varying levels of *supersaturation* is shown, rather than at varying degrees of supercooling. Transformations at low supersaturations would occur slowly, due to the system being close to equilibrium, and transformations at very high supersaturations would also occur slowly, since chain interactions would limit microstructural mobility. Again, therefore, a maximum transformation rate would be expected at intermediate supersaturations, where the combination of kinetic drive and molecular mobility would be optimized. Given that the transformation from isotropic material to a mesophase is kinetically easier (requires less microstructural rearrangement) than the precipitation of a three-dimensionally ordered crystalline phase, the transformation curves for mesophase formation and crystallization should be nested as shown (Figure 3c).

The format of these curves is qualitatively consistent with the observed behavior of silk solutions (Figure 3d). Dilute specimens maintained between glass slides (and thus losing water relatively slowly; curve 1) can form liquid crystalline phases, with the possibility of crystallizing at very long times. Dilute specimens without a cover slide will start at the same concentration as those maintained between glass surfaces, but will change in concentration more rapidly. Thus the "drying curve" of the specimen (curve 2) may be able to intercept the "nose" of the crystallization curve. Concentrated specimens with (curve 3) or without (curve 4) a cover slide do not have sufficient microstructural mobility to crystallize immediately after transformation to the liquid crystalline state. The smooth curves (1-4) showing concentration change with time are schematic in the present qualitative discussion; they are discontinuous at the "C" curve for transformation to the liquid crystalline state because the diffusion coefficients of solvent in liquid crystalline and crystalline material will be different

ACKNOWLEDGEMENTS

We have benefitted from several stimulating conversations with Dr Pedro Verdugo. Support was provided by the US Army Research, Development and Engineering Center (contract #DAAK60-91-K-005), the US Army Research Office (grant #DAAL03-91-G-0239), the Donors of the American Chemical Society Petroleum Research Fund (grant #25218-AC), the National Science Foundation (grant #BCS-9202007), the Whitaker Foundation, and the Washington Technology Center.

REFERENCES

1. M.K. Cox, Molecular Crystals and Liquid Crystals **153**, 415 (1987).
2. T.G. Ryan, Molecular Crystals and Liquid Crystals **157**, 577 (1988).
3. P.J. Collings, *Liquid Crystals: Nature's Delicate Phase of Matter* (Princeton Univ. Press, Princeton, NJ, 1990).
4. R.A. Weiss and C.K. Ober, eds, *Liquid-Crystalline Polymers* (American Chemical Society, Washington, DC, 1990).
5. A.M. Donald and A.H. Windle, *Liquid Crystalline Polymers* (Cambridge University Press, Cambridge, U.K., 1992).
6. A. Suzuki, T. Maeda and T. Ito, Biophysical Journal **59**, 25 (1991).
7. A. Kerst, C. Chmielewski, C. Livesay, R.E. Buxbaum and S.R. Heidemann, Proceedings of the National Academy of Sciences, USA **87**, 4241 (1990).
8. E.W. April, Nature **257**, 139 (1975).
9. M.-M. Giraud-Guille, Molecular Crystals and Liquid Crystals **153**, 15 (1987).
10. K. Kerkam, C. Viney, D.L. Kaplan and S.J. Lombardi, Nature **349**, 596 (1991).

11. D.G. Gray, Journal of Applied Polymer Science: Applied Polymer Symposia **37**, 179 (1983).

12. F. Livolant, Journal de Physique **47**, 1605 (1986).

13. C. Viney, A.E. Huber and P. Verdugo, in *Fundamentals of Biodegradable Materials and Packaging*, edited by D.L. Kaplan, E.L. Thomas, and C. Ching (Technomic, Lancaster, PA, 1992 in press).

14. T.E. Strzelecka, M.W. Davidson and R.L. Rill, Nature **331**, 457 (1988).

15. F. Livolant, A.M. Levelut, J. Doucet and J.P. Benoit, Nature **339**, 724 (1989).

16. R.L. Rill, F. Livolant, H.C. Aldrich and M.W. Davidson, Chromosoma **98**, 280 (1989).

17. J. Verhas, Liquid Crystals **3**, 1183 (1988).

18. D. Chapman, in *Liquid Crystals: Applications and Uses*, edited by B. Bahadur (World Scientific, Singapore, 1991) p. 185.

19. R. Lipowsky, Nature **349**, 475 (1991).

20. J.C. Zemlin, *A study of the mechanical behavior of spider silks*, Report No. 69-29-CM (AD 684333), U.S. Army Natick Laboratories, 1968.

21. J.M. Gosline, M.E. DeMont and M.W. Denny, Endeavour **10**, 37 (1986).

22. D.L. Kaplan, S.J. Lombardi, W.S. Muller and S.A. Fossey, in *Biomaterials: Novel Materials from Biological Sources*, edited by D. Byrom (Stockton Press, New York, 1991) p. 3.

23. D.L. Kaplan, S. Fossey, C.M. Mello, S. Arcidiacono, K. Senecal, W. Muller, S. Stockwell, R. Beckwitt, C. Viney and K. Kerkam, MRS Bulletin **17 (10)**, 41 (1992).

24. R.F. Foelix, *Biology of Spiders* (Harvard University Press, Cambridge, MA, 1982).

25. S.T. Case and L. Wieslander, in *Structure, Cellular Synthesis and Assembly of Biopolymers*, edited by S.T. Case (Springer-Verlag, Berlin, 1992) p. 187.

26. F. Lucas, J.T.B. Shaw and S.G. Smith, in *Advances in Protein Chemistry*, edited by C.B. Anfinsen, M.L. Anson, K. Bailey and J.T. Edsall (Academic Press, New York, 1958) p. 107.

27. D.B. Peakall, Journal of Experimental Zoology **176**, 257 (1971).

28. K. Kerkam, D.L. Kaplan, S.J. Lombardi and C. Viney, in *Materials Synthesis Based on Biological Processes*, edited by M. Alper, P.D. Calvert, R. Frankel, P.C. Rieke and D.A. Tirrell (Materials Research Society, Pittsburgh, 1991) p. 239.

29. C. Viney, K. Kerkam, L.K. Gilliland, D.L. Kaplan and S. Fossey, in *Complex Fluids*, edited by E.B. Sirota, D. Weitz, T. Witten and J. Israelachvili (Materials Research Society, Pittsburgh, 1992) p. 89.

30. K. Yamaura, Y. Okumura, A. Ozaki and S. Matsuzawa, Journal of Applied Polymer Science: Applied Polymer Symposium **41**, 205 (1985).

31. C. Viney, in *Structure, Cellular Synthesis and Assembly of Biopolymers*, edited by S.T. Case (Springer Verlag, Heidelberg, 1992) p. 255.

32. T. Asakura, Makromoleculare Chemie, Rapid Communications **7**, 755 (1986).

33. S. Zheng, G. Li, W. Yao and T. Yu, Applied Spectroscopy **43**, 1269 (1989).

34. E. Iizuka, Journal of Applied Polymer Science: Applied Polymer Symposia **41**, 163 (1985).

35. D.A. Porter and K.E. Easterling, *Phase Transformations in Metals and Alloys* (Van Nostrand Reinhold, Wokingham, U.K., 1984).

DECALCIFICATION STUDIES ON AVIAN EGGSHELL

M. Agarwal, S.Q. Xiao and A.H. Heuer
Department of Materials Science and Engineering, Case Western Reserve University, Cleveland, OH 44106

ABSTRACT

Avian eggshells are one of the most rapidly calcifying systems known. Although the entire shell contains ~ 97 weight % $CaCO_3$, etching in EDTA reveals great spatial variability in etching rate. A correlation between the etching rate of various regions and the relative positions of the different parts in the calcium reserve assembly (CRA) has been made; the CRA is the source of calcium during natural decalcification by chick embryos.

INTRODUCTION

Nature produces many biological ceramics (mineralized or hard tissues) at ambient temperature. These *biological* ceramics are biominerals reinforced with biopolymers. The ceramic phase provides the structural integrity (strength and hardness), whereas the polymer gives the structures the required toughness. The nucleation and growth morphology of the ceramic is regulated by the biopolymeric organic matrix [1-4], which acts as a substrate.

The avian eggshell is a useful model system for understanding biomineralization. A cross section of the eggshell is shown in Fig.1. The eggshell assembly is about 300-400 μm thick [5-7]. The shell has a 5 μm thick layer on the outside, known as the cuticle. The shell itself, which is known as the palisade layer and is mainly calcitic $CaCO_3$ with approximately 3% organic matrix, is about 250 μm thick. The mammillary or cone layer is about 50 μm thick. The shell membrane, which serves as the substrate for the calcification of the shell proper, is about 70-100 μm thick. The membrane is composed of a woven mat of collagen fibers which are about 2-10 μm in diameter. Partial etching studies on eggshells were performed in an attempt to mimic natural calcification.

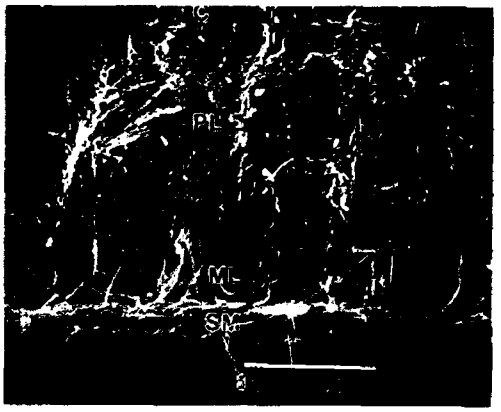

Figure 1 : Cross section of the eggshell showing distinct regions : cuticle (C), palisade layer (PL), mammillary layer (ML) and the shell membrane (SM).

EXPERIMENTAL PROCEDURE

Eggs from White Leghorn hens were used. The membrane was separated from the shell by soaking it in 15% (weight/volume) ethylene diamine tetraacetic acid (EDTA) solution for 60 minutes and then mechanically stripping it away from the shell. EDTA is a Ca^{+2} - binding chelator and therefore dissolves some of the $CaCO_3$ at the interface of the shell and the membrane, thus loosening the contact between the two [8-10]. The membrane was then rinsed in distilled water.

For etching experiments, small pieces of the fractured eggshell were kept in EDTA solution for 1 hour, 2 hours and 9 hours.

The membrane after EDTA treatment and the partially etched cross sections of the shells were studied by scanning electron microscopy (SEM) and the local microchemistries determined qualitatively using X-ray energy dispersive spectroscopy (EDS). For SEM , the samples were coated with a 90Å thick Pd film.

RESULTS

Membrane after separation from the shell

Figure 2 is a micrograph of the outer eggshell membrane after mechanical separation from the shell proper. The collagen fibers form a dense network. At certain places, darker regions, 10-20 µm in diameter, are present. These darker regions are known as the mammillae; these were believed in the past to be initial *in vivo* calcification sites. These knobs are elevated by 10-20 µm above the woven structure [11-13] and have a higher content of sulfur than the collagen fibers.

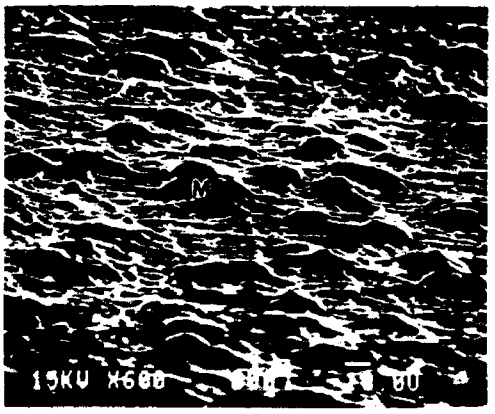

Figure 2 : Membrane after 1 hour soaking in EDTA and mechanical stripping from the shell. The darker regions are the mammillae (M).

Partial etching of the eggshell assembly

Figure 3 is a micrograph of the cross section of the shell, etched in EDTA for 1 hour. On the basis of the etching rates, the shell can be divided into distinct regions, numbered 1 through 5.

Region 1 was almost completely etched away in this case, and, therefore, was most susceptible to demineralization. The second most susceptible region is region 4, in the upper half of the palisade. Region 2 is most resistant to demineralization. Cavities are formed in the lower part of region 3 (i.e. region 3a), after prolonged exposure to EDTA (as in Fig.4) indicating that this region is also susceptible to demineralization.

Figure 3 : Cross section of the shell etched for 1 hour. Five distinct regions (1,2,3,4 and 5) can be identified.

Figure 4 : Cross section of the shell etched for 2 hours. Cavities are formed in region 3a.

A higher magnification micrograph of the broad interface between the palisade layer and the membrane, after 2 hours etching in EDTA solution, is shown in Fig.5. It can be clearly seen that the organic sheets protrude from the shell membrane in the mammillary zone. Their morphology and that of the crystalline fragments still present in this figure suggest that the knob-like morphology of the mammillae in Fig.2 is an artifact of EDTA demineralization. This view is strengthened by Fig.6, which shows a view of the broad interface after prolonged demineralization; it appears that the vertical organic sheets collapse upon demineralization to form the mammillary "knobs", which we now believe to be a misnomer.

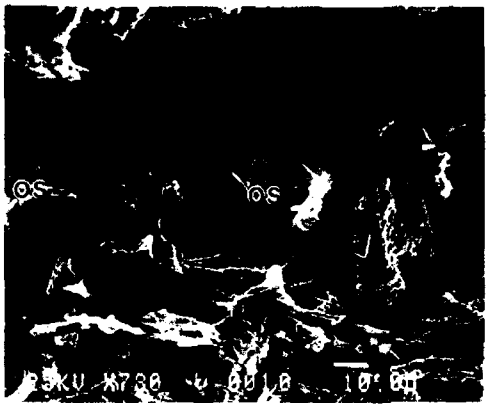

Figure 5 : Cross section of the lower part of the shell after 2 hours in EDTA. Organic sheet clusters (OS) can be seen, as well as some crystalline remnants (arrowed).

Figure 6 : Cross section of the lower part of the shell after 9 hours in EDTA. Organic sheets (OS) collapse to form mammillae (M).

DISCUSSION

From the above observations, one can draw an inference that the mammillae comprise discrete aggregates of fine organic sheets, mixed with calcite crystals. However, because of the mechanical forces arising during extensive decalcification of the shell, these organic sheets collapse to form the so - called mammillary knobs, which are apparently artifacts of *in vitro* demineralization. Careful demineralization shows the true nature of the calcification sites to be

fine organic sheets. In a separate paper in this proceedings the ultrastructure of eggshell has been studied by transmission electron microscopy and the aggregation of organic sheets and calcite crystals in the mammillary zone is further confirmed [14].

A one to one relationship between the regions of rapid demineralization and the calcium reserve assembly (CRA) [15] apparently exists. A CRA consists of three distinct regions, namely the *baseplate* (BP) which is partially integrated into the outer membrane, a *calcium reserve body* (CRB), attached to the BP, and a distinct CRB *cover*. Another structure, the *crown*, is present on top of the CRA. The relative positions and the sizes of the various regions of the CRA and the crown are shown in Fig.7. On the basis of this correlation, regions 1 and 2 in Fig.3 comprise the BP and CRB, which are about 70-100 μm in thickness; part of region 3 forms the crown, which is 40 μm thick. The crown region and the CRB are most susceptible to decalcification, providing further evidence that during natural decalcification of the shell, the growing embryo draws its calcium from the CRB.

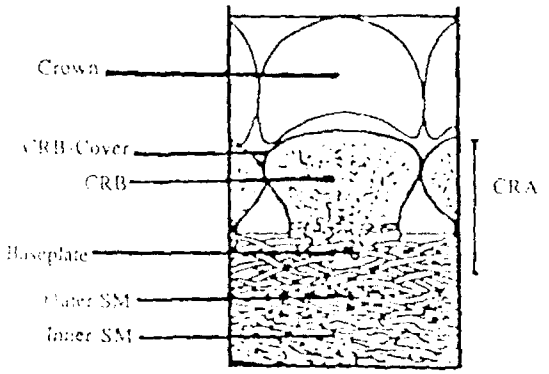

Figure 7 : The calcium reserve assembly (CRA) and the crown . CRB = calcium reserve body; SM = shell membrane. [Ref. 15]

CONCLUSION

The eggshell assembly can be used as a model system for studying and understanding the complexities of biomineralization. Preferential etching occurs in the eggshell assembly, although the entire shell is mainly calcitic in nature; this spatial variation in decalcification has implications involving differences in the microstructure of calcite, as well as the differences in the organic matrix, along the entire length of the palisade. Complete EDTA demineralization of the organic sheet - calcite aggregates leads to the collapse of the sheets, forming artifactual knob-like structures on the shell membrane.

ACKNOWLEDGMENTS

This work was supported by the Basic Energy Sciences Division, Department of Energy through a grant to Battelle Pacific Northwest Laboratories.

REFERENCES

1. H.A.Lowenstam, S.Weiner, in *On Biomineralization*, (Oxford: Oxford University Press, 1989).
2. S.Mann, J.Webb, R.J.P.Williams, editors, in *Chemical and Biological Perspectives*, (Weinheim: VCH Publishers, 1989).
3. S.Weiner, Amer. Zool., **24**, 945-951 (1984).
4. P.Calvert, S.Mann, Journal of Materials Science, **23**, 3801-3815 (1988).
5. C.Tyler, in *Wilhelm von Nathusius on Avian eggshells : A translated and edited version of his work*, (University Reading, Reading, England, 1964).
6. A.H.Parsons, Poultry Science, **61**, 2013-2021 (1982).
7. A.S.Poole, in *Scanning Electron Microscopy II* , edited by O.Johari and R.P.Becker, (SEM Inc., AMF O'Hare, 1979) pp475-482.
8. J.L.Arias, O.Nakamura, M.S.Fernandez, J.P.Rodriguez, V.J.Laraia, J.J.Wu, P.Knigge, D.R.Eyre, A.I.Caplan, Unpublished data.
9. J.L.Arias, M.S.Fernandez, V.J.Laraia, J.Janicki, A.H.Heuer, A.I.Caplan, in *Materials Synthesis based on Biological Processes*, edited by M.Alper et al., (Materials Research Society Proc., 1991) pp193-201.
10. T.M.Wu, D.J.Fink, J.L.Arias, J.P.Rodriguez, A.H.Heuer, A.I.Caplan, in *Chemistry and Biology of Mineralized Tissues*, edited by P.Price and H.C.Slavkin, (Elsevier Sci. Publishers, 1992) pp133-141.
11. C.R.Greger, H.Phillips, J.J.Scott, Poultry Science, **55**, 1717-1723 (1976).
12. B.H.Stemberger, W.J.Mueller, R.M.Jr Leach, Poultry Sci., **56**, 537-543 (1977).
13. S.Baumgartner, D.J.Brown, E.Slaevsky, R.M.Jr Leach, J. Nutr., **108**, 804-811 (1978).
14. S.Q.Xiao, M.Agarwal and A.H.Heuer, in Mater. Res. Soc. Proc. (this volume).
15. J.W.Dieckert, M.C.Dieckert, C.R.Creger, Poultry Science, **68**, 1569-1584 (1989).

SUB-MICROMETER HYDROXYAPATITE BIOCERAMICS

ZENG SHAOXIAN, GUO JINGKUN, YANG ZHIXIONG, CAI JIE, AND CAO WANPENG
Shanghai Institute of Ceramics, Academia Sinica, 1295 Ding-xi Road, Shanghai 200050, People's Republic of China

ABSTRACT

We studied the microstructures of hydroxyapatite (HA) ceramics which were sintered under three different conditions. It was found that all the ceramics were of sub-micrometer structure. The synthetic HA ceramics were also compared with human enamel. It is concluded that human enamel has higher strength because of its unique microstructure.

INTRODUCTION

Human hard tissues are composed of living cells and bone matrix. The main components of the bone matrix are organic collagen and inorganic hydroxyapatite (HA). HA occupies nearly 69 wt% of bone [1]. Extensive study by many researchers has shown that HA ceramic is a bioactive material, with good biocompatibility in the biological environment and the ability to bond with the body's hard and soft tissues. However, the poor sintering properties of HA, and especially its bad fracture strength and fatigue resistance, restrict its applications. Human enamel is a natural nanometer HA ceramic with a high strength. Promoting the powder sintering properties of HA, and increasing the strength and fatigue resistance of synthetic HA ceramic, is now an important subject in the biomaterials field. In this paper, the submicrometer structure of HA ceramic is reported and discussed.

EXPERIMENT

Materials

High-purity HA powder, and a small amount of glass as sintering aid, were sufficiently mixed. The glass must be wetting to HA and must cause no structure change of HA in the sintering process. The melting point of the glass must be lower than 1200 °C, because when the temperature is higher than 1200°C, HA will lose OH^- groups. In this paper, the glass that we chose was based on Si_2O_3 and B_2O_3.

The mixed powder was sintered in the following different ways to obtain samples:

1. in Ar under hot pressure (100 kg/cm^2 at 1100°C) for 1 hr
2. in air under hot pressure (300 kg/cm^2 at 1100°C) for 0.5 hr
3. in a microwave furnace at 1000-1050°C for 2 min.

Measurements

The sample was characterized by various experimental techniques. Density measurements were made by the displacement method using doubly distilled water. Electron micrographs of samples were obtained by high-resolution electron microscopy at the level of grains and at the atomic level. The grain and pore sizes of samples were estimated from the micrographs. Bars of 2mm x 3mm x 26mm were cut from the samples with a diamond saw. The fracture strengths of the HA ceramics were measured with these unpolished bars in three-point bending.

RESULTS

Physical and mechanical properties

Fig.1. Electron micrograph of HA sintered under hot pressure (100 kg/cm^2 at 1100°C) for 1 hr.

Fig.2. Electron micrograph of HA sintered under hot pressure (300 kg/cm^2 at 1100°C) for 0.5 hr.

Fig.3. Electron micrograph of HA sintered in microwave at 1000-1050°C for 2 min.

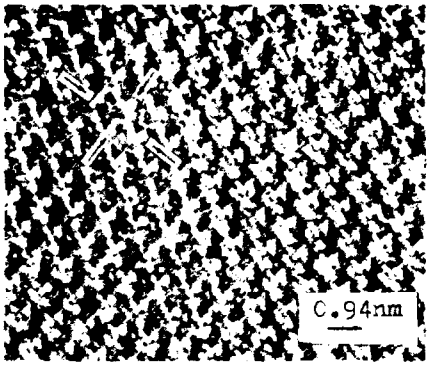

Fig.4. Structure image of HA along [0001] zone. OH (white spots marked by arrow) and Ca (black spots around OH)

Sintering was complete under all three sets of conditions. The sample sintered under the first set of conditions (sample A) was translucent, with a density of 3.127 g/cm^3, a fracture strength of 115 MPa, and an average grain size of 0.46 μm (Fig.1). The sample sintered under the second set of conditions (sample B) was opaque, with a density 3.107 g/cm^3, a fracture strength of 140 MPa, and an average grain size of 0.35 μm (Fig.2). For the third set of conditions (sample C), the density was 3.10 g/cm^3, and he grain size was smaller, ranging from 0.2 to 0.3 μm (Fig.3). The maximum grain size of all sintered samples was below 0.8 μm. The results of measurements are shown in Table I.

Table I. Physical and mechanical properties of the sintered HA ceramics

	Density (g/cm^3)	Grain size (μm)	Fracture strength (MPa)	Transparency
Sample A	3.127	0.46	115	translucent
Sample B	3.107	0.35	140	opaque
Sample C	3.100	0.2-0.3	1	opaque

Microstructure

The structure of samples was observed by high resolution electron microscopy at atomic level. It was found that all the samples had the same structure image. Fig.4 shows the structure image along the [0001] zone. From the image, it is found that the structure is hexagonal, having space group $P6_3/m$ with a = 9.42 Å and b = 5.8 Å. This result indicates that all the samples are HA. In Fig.4, OH and Ca in a unit cell can be seen clearly.

DISCUSSION

Relationship between structure and strength

Samples A were translucent, indicating that there was some light scattering from the grain boundaries; compared to samples B, considerable grain growth occurred. Long sintering time results in increased grain and pore sizes. For the microwave sintering, the sintering time was much shorter, so much smaller grains are obtained. Theoretically, the sample with higher density has higher fracture strength. In this paper, all samples had similar densities, regardless of how they were prepared. Comparing sample A and sample B, it is found that the second one has a fracture strength (140 MPa) which is higher than that of the first (115 MPa). This is because of their different microstructures. Sample B shows more micro-pores. These pores can relax stress to enhance the strength of the sample. Furthermore, cracks in ceramics occur and propagate along grain boundaries. In the ceramic with smaller grains, crack growth needs to cover a longer route and expend more energy. This is also a reason why sample B has a higher strength. Bars characterized in the experiments were not polished; otherwise, the strengths would be much higher.

Comparison between enamel and sintered HA ceramic

Human enamel is a nanometer HA ceramic with a high fracture strength. Its grains are small (20 x 50 x 200nm) and have a prior arrangement direction along the [0001] zone. The grain boundaries of human enamel are wide, with many dislocations [2]. These dislocations can disperse stress concentration to increase the bonding strength of the grain boundary. Compared to human enamel, the synthetic HA ceramic is composed of larger grains; these grains are irregular in shape and arrangement. The grain boundaries in synthetic HA are more narrow, and there are fewer dislocations at the grain boundaries (Fig.5). So, the fracture strength of the enamel is much higher than that of synthetic HA ceramic.

Fig.5. Electron micrograph of a grain boundary in synthetic HA ceramic. The boundary is very clean, with few dislocations at the boundary.

From the comparison above, it is found that there are significant microstructural differences between the synthetic HA ceramic and human enamel. Human enamel has a much higher fracture strength because of its unique microstructure. In order to promote the strength of synthetic HA ceramic, we must pay attention to the following factors:

1. The grains of human enamel are much smaller than those of HA ceramic. Limiting grain growth in the sintering process, to obtain HA ceramic with smaller grains, is helpful to enhancing material's strength.
2. The significant differences between the grain boundaries of human enamel and synthetic HA ceramic show that it is important to improve the grain boundaries of synthetic HA ceramic, to increase the bonding strength of the boundaries.
3. The shape and arrangement of the grains also influence the material strength. How to control the grain shape and arrangement in the sintering process needs further research.

CONCLUSIONS

We obtained sub-micrometer HA ceramics by hot-pressure sintering. Those sintered under higher hot pressure for shorter sintering times had higher fracture strength. Human enamel has higher strength because of its unique microstructure.

REFERENCES

1. R.W. Davidge, G. Tappin, Proc. Brit. Ceram. Soc., No. 15, 47 (1975).
2. Wen Shulin, Electron Microsc. Res., vol. 2, 1-16 (1989).

CRYSTALLINE STRUCTURE AND MOISTURE EFFECTS ON DEFORMATION MECHANISMS OF GELATIN FILMS UNDER MODE I STRESS FIELD

BETA YUHONG NI AND ANNE LE FAOU
Materials Science and Engineering Division, Eastman Kodak Company, Rochester, NY 14652-3701.

ABSTRACT

Crazing and shear-deformation phenomena are found in thin gelatin films. The gelatin crystallinity and relative humidity affect these deformation mechanisms significantly. A deformation map of gelatin films at low strain rate is established.

INTRODUCTION

The mechanical failure behaviors of polymeric materials are governed to a large extent by their deformation modes before final fracture. These deformation modes are brittle failure which is determined by material surface energy, semibrittle failure which is characterized by crazing phenomena, and ductile failure which is associated with a shear yielding mechanism. Brittle to ductile transitions and crazing to shear deformation transitions have been observed in many polymers [1-3]. These transitions actually determine polymer failure behavior in terms of fracture toughness, impact strength, and even fatigue characteristics.

The microscopic molecular textures such as entanglement density (aging history), crosslinking density, crystallinity, and the morphology of secondary phases determine when such transitions occur. Furthermore, it is well known that all the plastic deformations such as crazing and shearing are thermal activation processes [4]. So temperature has a large impact on brittle to ductile and crazing to shear deformation transitions. In general, for a given applied stress field, a given strain rate, and a given temperature, the material's response to that stress field depends on the microstructure of the material. Once such a structure-properties relation is established, it opens many possibilities to tailor material structures to meet specific product requirements for practical use.

Gelatin is a biopolymer and serves as a primary photographic binder. Its mechanical properties are essential to the end use of photographic films. Since water is a good solvent to gelatin, moisture has a severe plasticizing effect which lowers gelatin's glass transition temperature T_g and melting temperature T_m significantly [5]. Therefore, the moisture effect to some extent can be considered as a temperature effect for gelatin. It is well known that the Young's modulus, break stress, yield stress and viscoelastic properties of gelatin are strong functions of relative humidity. However, little is

Mat. Res. Soc. Symp. Proc. Vol. 292. 1993 Materials Research Society

known about the nature of deformation phenomena of gelatin. Our objective is to investigate how gelatin fails under stress and what materials (crystallinity, morphology, aging history) and environmental (relative humidity, temperature, strain rate) parameters control that failure process. Ultimately we should relate the results to the failure behavior of gelatin films.

In this study, we investigate the brittle to ductile and crazing to shear deformation transitions by examining the plastic deformation zones in front of a Mode I crack in gelatin coatings.

EXPERIMENTS

Since gelatin is a fragile material, pure Kodak type IV gelatin coatings (coated on a polymer support) were deformed with polymer support at different relative humidities in order to minimize further deformation during handling. The specimen geometry is shown in Fig.1. The bare polymer supports were deformed at various humidities too and they showed no apparent plastic deformation. So whatever was observed in gelatin coatings on the support is attributed to the deformation of gelatin. These specimens of various degrees of crystallinity with Mode I precracks (cut with a razor blade) were deformed with an Instron tester at cross-head speed of 0.5 mm/min to a maximum load of 15 lb. Also some of the coatings were peeled away from the support and tensile tests were performed on these free-standing films. The plastic deformations in all these samples were observed using optical microscopy. In addition, x-ray diffraction patterns were collected for some of the deformed tensile samples.

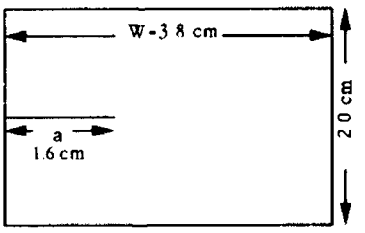

Fig. 1 The geometry of Mode I specimens.

The glass transition temperature, melting temperature, and degree of crystallinity of gelatin films were measured using a Perkin-Elmer DSC 7 with temperature rate of 10°C/min. These gelatin coatings have crystallinities ΔH of 0.0, 0.6, 1.9, and 3.2 cal/gram respectively. Fig. 2 shows a typical DSC scan of a gelatin film with an apparent glass transition and a melting peak. The scan also shows a aging peak, but the variation of aging peaks among the

samples is not significant; for simplicity these coatings can be considered as having similar relaxation enthalpy or aging history. Fig. 3 shows T_g and T_m as function of relative humidity for the samples that were examined. Noticeably, the glass transition temperature T_g at 80% RH is very close to room temperature.

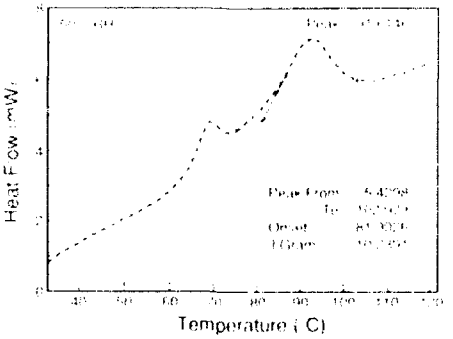

Fig. 2 A typical DSC scan of a gelatin film at 50% RH.

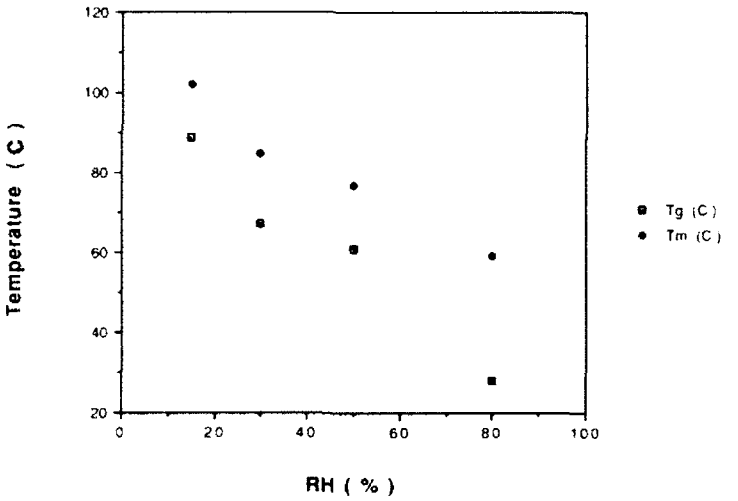

Fig. 3 T_g and T_m as function of relative humidity.

RESULTS

Figs. 4 & 5 show the typical crazing and shear deformation in gelatin, respectively. As seen in Fig. 6, x-ray diffraction (100) peak of the gelatin triple helix structure indicates decreasing gelatin crystallinity due to deformation. Three deformation transitions, brittle (no deformation) to crazing, crazing to shear deformation, shear deformation to crazing again, were observed as relative humidity increased. The transition relative humidities at which such

transitions occur are strongly dependent on the degree of crystallinity of a film at humidities below 65% RH. There is a certain margin around a transition relative humidity within which both crazing and shear deformation coexist. Therefore the final judgement of transition relative humidity is based on the dominant deformation feature at the close vicinity of a crack tip. Fig. 7 summarizes these results (at Instron crosshead speed of 0.5 mm/min) into a deformation map where the deformation mode can be determined at given crystallinity and relative humidity.

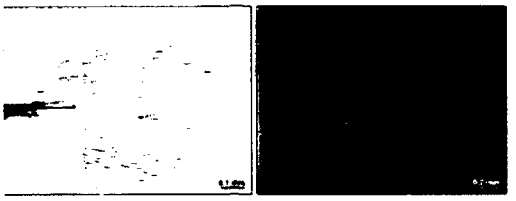

(a) (b)

Fig.4 Typical crazing phenomena of gelatin: (a) in front of a Mode I crack; (b) in a deformed tensile sample.

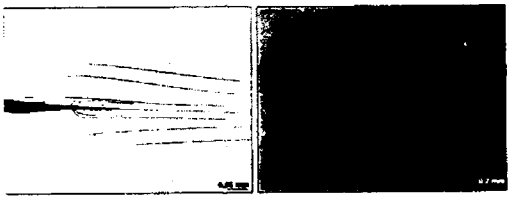

(a) (b)

Fig. 5 Typical shearing phenomena of gelatin: (a) in front of a Mode I crack; (b) in a deformed tensile sample.

DISCUSSIONS

The features of two typical plastic deformations observed in broken tensile samples shown in Figs. 4 & 5 agree well with the general descriptions of crazing and shearing in literature [1,6]. The crazes (Fig. 4) lay perpendicular to the direction of tensile stress, and the shear bands (Fig. 5) approximately develop along the direction of maximum shear stress which is 45° off the direction of tensile stress. The crazing zone in front of a Mode I crack (Fig. 4) in gelatin strongly resembles the craze distribution around a Mode I crack in polystyrene [7]. The shear deformation zone in front of a Mode I crack (Fig. 5) can be described using a Mode I plane stress slip line field [8] (see Fig.8) which is generated based on a perfect plastic material model obeying the Von Mises or Tresca shearing criterion.

The moisture effect on these deformation transitions can be understood as the temperature effect. Both shear yielding stress and crazing stress are functions of temperature; which stress is lower at a given temperature or relative humidity decides the mode of deformation.

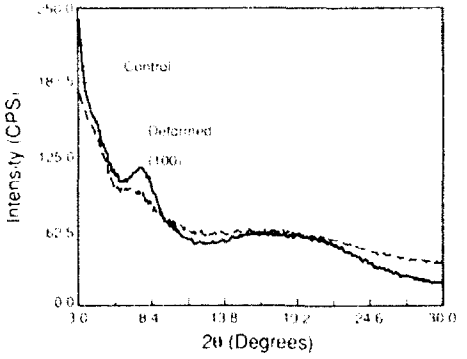

Fig. 6 Wide-angle x-ray diffraction of (100) peak of triple helix structure in gelatin. The sample was deformed at 80% RH.

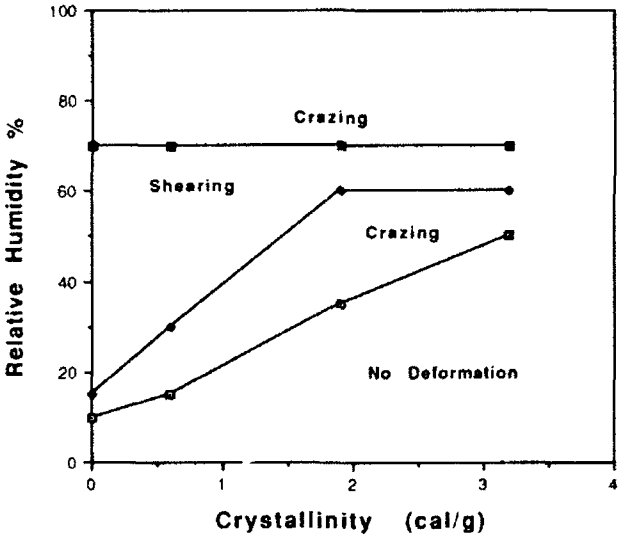

Fig. 7 The deformation map of gelatin at 70°F, displacement rate of 0.5 mm/min.

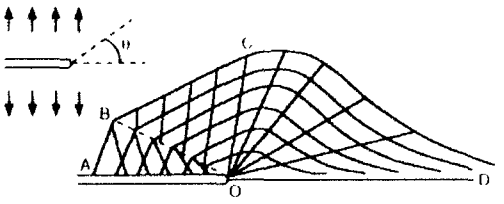

Fig. 8 The slip-line field in front of a plane stress Mode I crack.

The x-ray diffraction data provide the evidence that the crystalline structure of a gelatin film is disturbed after deformation. The explanation of this decreasing (100) peak needs further study. However, it implies that both crystalline domains and amorphous regions of a gelatin film are involved in a deformation process. Therefore, the shear yielding stress and crazing stress should depend on the crystallinity of gelatin. Experimental results (see Fig. 7) do show that gelatin crystallinity strongly affects the deformation mechanisms at relative humidities below 65% RH. Further experiments and detailed analysis of each transition will be published elsewhere.

CONCLUSIONS

There are three deformation transitions in gelatin films, they are brittle (no deformation) to crazing, crazing to shear deformation, shear deformation to crazing. The transitions are achieved as relative humidity increases. The crystallinity of gelatin strongly affects the transition relative humidities at which such transitions occur.

ACKNOWLEDGEMENT

We want to thank Mr. T. Blanton for performing the x-ray diffraction experiments.

REFERENCES

[1] I. M. Ward, Mechanical Properties of Solid Polymers, 2nd ed. (John Wiley & Sons 1990), p. 424.

[2] E. Kramer, in Advances in Polymer Science, 52/53, 1984.

[3] E. Kramer, in Advances in Polymer Science, 91/92, 1990.

[4] J. C. M. Li, C. A. Pampillo and L. A. Davis, in Deformation and Fracture of High Polymers, Edited by H. H. Kausch (Plenum Publishing).

[5] P. I. Rose, in The Theory of the Photographic Process, 4th Edition, Ed. by T. H. James, Macmillan Publishing Co., Inc.

[6] J. C. M. Li, Poly. Eng. & Sci., **24**, 750 (1984).

[7] M. Bevis, D. Hull, J. Mater. Sci., **5**, 983 (1970).

[8] J. W. Hutchinson, J. Mech. Phys. Solids, **16**, 337 (1968).

CHIRAL SYMMETRY BREAKING AND PATTERN FORMATION IN TWO-DIMENSIONAL FILMS

JONATHAN V. SELINGER,[1,2,3] ZHEN-GANG WANG,[2] AND ROBIJN F. BRUINSMA[1]
[1]Department of Physics, University of California, Los Angeles, CA 90024
[2]Department of Chemical Engineering, California Institute of Technology, Pasadena, CA 91125
[3]Current Address: Center for Bio/Molecular Science and Engineering, Naval Research Laboratory, Code 6900, 4555 Overlook Avenue, SW, Washington, DC 20375

ABSTRACT

Thin films of organic molecules, such as Langmuir monolayers and freely suspended smectic films, can exhibit a spontaneous breaking of chiral symmetry. This chiral symmetry breaking can occur through at least three possible mechanisms: (1) the relation between tilt order and bond-orientational order in a tilted hexatic phase, (2) a special packing of non-chiral molecules on a two-dimensional surface, and (3) phase separation of a racemic mixture. Because the chiral order parameter is coupled to variations in the direction of molecular tilt, chiral symmetry breaking leads to the formation of patterns in the tilt direction with one-dimensional or two-dimensional order. Using a Landau theory, we investigate these patterns and predict the critical behavior near the chiral symmetry breaking transition.

INTRODUCTION

There is a very general connection between molecular chirality and pattern formation in liquid-crystalline systems. On a molecular scale, the fundamental basis of this connection is that chiral molecules do not pack parallel to their nearest neighbors. Rather, there is some finite displacement angle between each molecule and its nearest neighbors. On a more macroscopic scale, molecular chirality leads to a continuum free energy that favors a finite twist in the director field [1]. In a bulk three-dimensional (3D) system, this finite twist leads to a cholesteric phase, with a helical pattern in the molecular director, and a smectic-C* phase, in which the director rotates from each layer to the next. In thin films, the molecules are frustrated, because it is impossible to accommodate a uniform twist in a 2D system. As a result, in thin films, chiral molecules form a striped pattern of parallel defect walls separating regions with the favored twist [2]. Furthermore, in the specific case of tilted hexatic films, chiral molecules form star defects with spiral arms [3]. The spiral form of the defect arms is a direct result of the chirality of the molecules.

In recent experiments on Langmuir monolayers [4-5] and freely suspended smectic films [6], striped patterns and spiral star defects have been found in 2D systems of *non-chiral* molecules. Because of the observation of spiral star defects, these systems have been identified as chiral phases of non-chiral molecules. The chiral symmetry of the molecules is spontaneously broken in the macroscopic phase. These experimental results lead to two general questions: (1) What is the mechanism for breaking chiral symmetry? (2) How is chiral symmetry breaking related to pattern formation in these 2D systems?

In this paper, we address both of those questions. We first discuss the mechanism for chiral symmetry breaking, and propose three specific mechanisms. We then use a Landau theory to investigate the connection between chiral symmetry breaking (through any mechanism) and pattern formation. We find a general phase diagram that exhibits a uniform non-chiral phase, a striped pattern, a square lattice, and a uniform chiral phase.

Mat. Res. Soc. Symp. Proc. Vol. 292. 1993 Materials Research Society

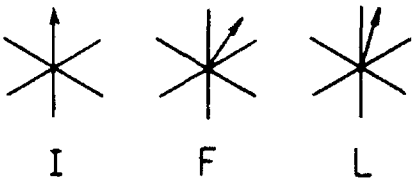

Fig. 1. The tilt and bond directions in the hexatic-I, F, and L phases of Langmuir monolayers of non-chiral molecules. Note that the hexatic-L phase is chiral while the I and F phases are non-chiral.

We also discuss the critical behavior at the transition from the uniform non-chiral phase to the striped phase. This paper reviews work from Refs. [7-8], and further details can be found in those references.

MECHANISMS FOR CHIRAL SYMMETRY BREAKING

There are several possible mechanisms for breaking chiral symmetry in a Langmuir monolayer. First, Langmuir monolayers are believed to exhibit tilted hexatic phases in a large region of the phase diagram [4-5]. In a tilted hexatic phase, chiral symmetry can be broken by the relation between tilt order and bond-orientational order. As indicated in Fig. 1, there are three different tilted hexatic phases, in which the tilt direction is locked in different ways with respect to the bond directions. The tilt direction (projected into the layer plane) can be locked along one of the six local intermolecular bonds (hexatic-I), halfway between two intermolecular bonds (hexatic-F), or at an intermediate direction, between 0° and 30° from a local bond (hexatic-L). All three of these phases have been identified in x-ray scattering experiments on lyotropic lamellar systems [9]. Note that the hexatic-I and F phases have a reflection symmetry, but the hexatic-L phase does not, and hence it is a chiral phase. The chiral order parameter is $\psi(\mathbf{r}) = \sin[6(\phi(\mathbf{r}) - \theta(\mathbf{r}))]$, where ϕ is the azimuthal angle of the tilt and θ is the orientation of the bonds relative to the x-axis.

A second possible mechanism for chiral symmetry breaking in a Langmuir monolayer is the packing of non-chiral molecules on a 2D surface. This mechanism depends on the symmetry of the molecules themselves. If the molecules have the symmetry of a cylinder with a single side group (like an ordinary pen with a clip), then they can pack on the surface in two inequivalent ways that are mirror images of each other, with the side groups extending to the right or to the left of the molecules. The chiral order parameter is then the difference in the densities of the two packings. By contrast, if the molecules have perfect cylindrical symmetry, then this mechanism for chiral symmetry breaking is not possible. Note that this mechanism does not depend on the presence of hexatic order in the monolayer.

Finally, a third possible mechanism for chiral symmetry breaking in a Langmuir monolayer is phase separation of a racemic mixture. If the monolayer is composed of a racemic mixture of two opposite enantiomers, the mixture can separate to form chiral domains. In this case, the chiral order parameter is simply the difference in densities of the two enantiomers. This mechanism does not occur in the experiments of Refs. [4-5], because the molecules used in those experiments are non-chiral, but it could occur in other systems.

In a freely suspended smectic film, chiral symmetry can be broken by the second and third mechanisms described above—either packing of molecules in the film or phase

separation of a racemic mixture. However, chiral symmetry breaking through the relation between tilt order and bond-orientational order is more subtle. This mechanism depends on the thickness of the film relative to the director correlation length. In a thin film, the 3D molecular director $\hat{\mathbf{n}}$ is uniform across the thickness of film. If the top and bottom surfaces are equivalent, as is normally the case, then $\hat{\mathbf{n}}$ is equivalent to $-\hat{\mathbf{n}}$. For that reason, all three of the tilted hexatic phases have an inversion symmetry, and hence $\sin[6(\phi-\theta)]$ is not a chiral order parameter for a thin smectic film. By contrast, in a thick film, $\hat{\mathbf{n}}$ is not uniform across the thickness of the film. As a result, the top and bottom layers are individually equivalent to Langmuir monolayers, and hence the hexatic-L phase does break chiral symmetry.

PATTERN FORMATION

To investigate the connection between chiral symmetry breaking and pattern formation, we have developed a Landau theory in terms of a general chiral order parameter $\psi(\mathbf{r})$ and the 2D tilt director field $\hat{\mathbf{c}}(\mathbf{r}) = (\cos\phi(\mathbf{r}), \sin\phi(\mathbf{r}))$. Here, $\hat{\mathbf{c}}$ is the (normalized) projection of the 3D molecular director $\hat{\mathbf{n}}$ into the xy plane. The general free energy can be written as

$$F = \int d^2\mathbf{r} \left[\frac{1}{2}\kappa(\nabla\psi)^2 + \frac{1}{2}t\psi^2 + \frac{1}{4}u\psi^4 + \frac{1}{2}K_1(\nabla\cdot\hat{\mathbf{c}})^2 + \frac{1}{2}K_3(\nabla\times\hat{\mathbf{c}})^2 - \lambda\psi\hat{\mathbf{z}}\cdot\nabla\times\hat{\mathbf{c}} \right].$$

In this expression, the first three terms are the Ginzburg-Landau expansion in powers of ψ, with the coefficient t passing through 0 as a function of temperature. The next two terms are the Frank free energy for variations in $\hat{\mathbf{c}}$. For simplicity, we make the single-Frank-constant approximation $K_1 = K_3 \equiv K$. The final term is the coupling between chiral symmetry breaking and variations in the director field. It corresponds to the $\nabla\times\hat{\mathbf{c}}$ term that has been considered in earlier theories of striped phases of chiral molecules [9-12], but here chiral symmetry is broken by the order parameter $\psi(\mathbf{r})$, which can itself vary across the monolayer.

Through a combination of analytic calculations and numerical minimization of the free energy, we have derived the mean-field phase diagram of Fig. 2. It is shown schematically in terms of the temperature t and the coupling λ for fixed K, κ, and u. At high temperature, the system is in the uniform non-chiral phase. From this uniform non-chiral phase, there is a second-order transition into the striped phase. The nature of the striped pattern changes continuously as the temperature decreases, as shown in Fig. 3. Just below the transition, the system is in the sinusoidal-stripe regime, in which both ψ and ϕ vary sinusoidally as functions of position. In this regime, the wavelength of the striped pattern decreases as the temperature decreases. At lower temperature, the system crosses over into the soliton-stripe regime, which consists of domains of constant ψ and linear variation of ϕ, separated by solitons (sharp domain walls) in which ψ changes sign. In this regime, the width of the stripes *increases* as the temperature decreases. When the stripe width diverges, there is a transition to the uniform chiral phase.

For small coupling λ, there is a smooth evolution from the sinusoidal-stripe regime to the soliton-stripe regime. For larger values of λ, these two regimes are separated by a two-dimensionally ordered phase, illustrated in Fig. 4. This phase consists of a square lattice of cells with alternating positive and negative chirality, separated by sharp walls across which ψ changes sign. Because of this lattice of alternating chirality, there is a tilt vortex at the center of each cell and an antivortex at each corner where four cells meet.

Most of our quantitative results for this model have been discussed in detail in Ref. [8]. However, it is useful to emphasize the critical behavior near the transition from

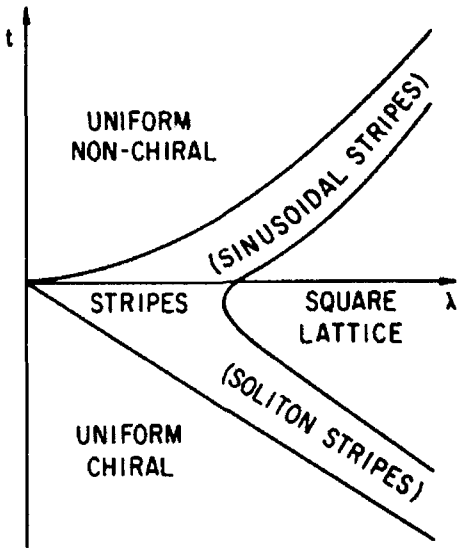

Fig. 2. Schematic view of the mean-field phase diagram. Here, t is temperature and λ is the coupling between the chiral order parameter and the curl of the tilt director field.

---

the uniform non-chiral phase to the striped phase. To understand the mean-field critical behavior of ψ and ϕ, we make the variational ansatz $\psi(\mathbf{r}) = \psi_0 \cos qx$, $\phi(\mathbf{r}) = \phi_0 \sin qx$. By minimizing the free energy over the amplitudes ψ_0 and ϕ_0 and the wavevector q, we find a second-order transition from the uniform non-chiral phase to the striped phase at the critical temperature $t_c = \lambda^2/K$. Just below the transition, the amplitudes and wavevector scale as $\psi_0 \propto (t_c - t)$, $\phi_0 \propto q \propto (t_c - t)^{1/2}$. The critical exponent $\beta = 1$ for the amplitude ψ_0 is surprising because it is not equal to the mean-field Ising critical exponent $\beta = 1/2$.

If we apply a magnetic or electric field that couples to the tilt director $\hat{\mathbf{c}}$, the nature of this phase transition changes significantly. A field h in the x-direction leads to an additional term of $-h \cos\phi \approx -h + \frac{1}{2}h\phi^2$ in the free energy. As a result, the transition from the uniform non-chiral phase to the striped phase is depressed to the critical temperature $t_c = (\lambda - (h\kappa)^{1/2})^2/K$. Furthermore, the striped pattern sets in at the finite wavevector $q = (ht_c/K\kappa)^{1/4}$ rather than at $q = 0$. In this case, the amplitudes ψ_0 and ϕ_0 of the sinusoidal modulation both scale as $\psi_0 \propto \phi_0 \propto (t_c - t)^{1/2}$, just as in mean-field theory for the Ising model. Thus, a finite field suppresses the anomalous critical exponent for ψ_0 found in the zero-field case.

In Ref. [8], we go beyond mean-field theory in the zero-field case by considering how thermal fluctuations in the director field affect the transition from the uniform non-chiral phase to the striped phase. We find that these fluctuations lead to a finite-wavevector instability in the chiral order parameter. Because of this instability, we expect the transition to be driven weakly first-order. In the presence of a finite field h, thermal fluctuations in the director field are suppressed, and hence they should not have a significant effect on the transition from the uniform non-chiral phase to the striped phase.

ACKNOWLEDGMENTS

We thank C. M. Knobler, J. Maclennan, D. R. Nelson, J. M. Schnur, and M. Seul for

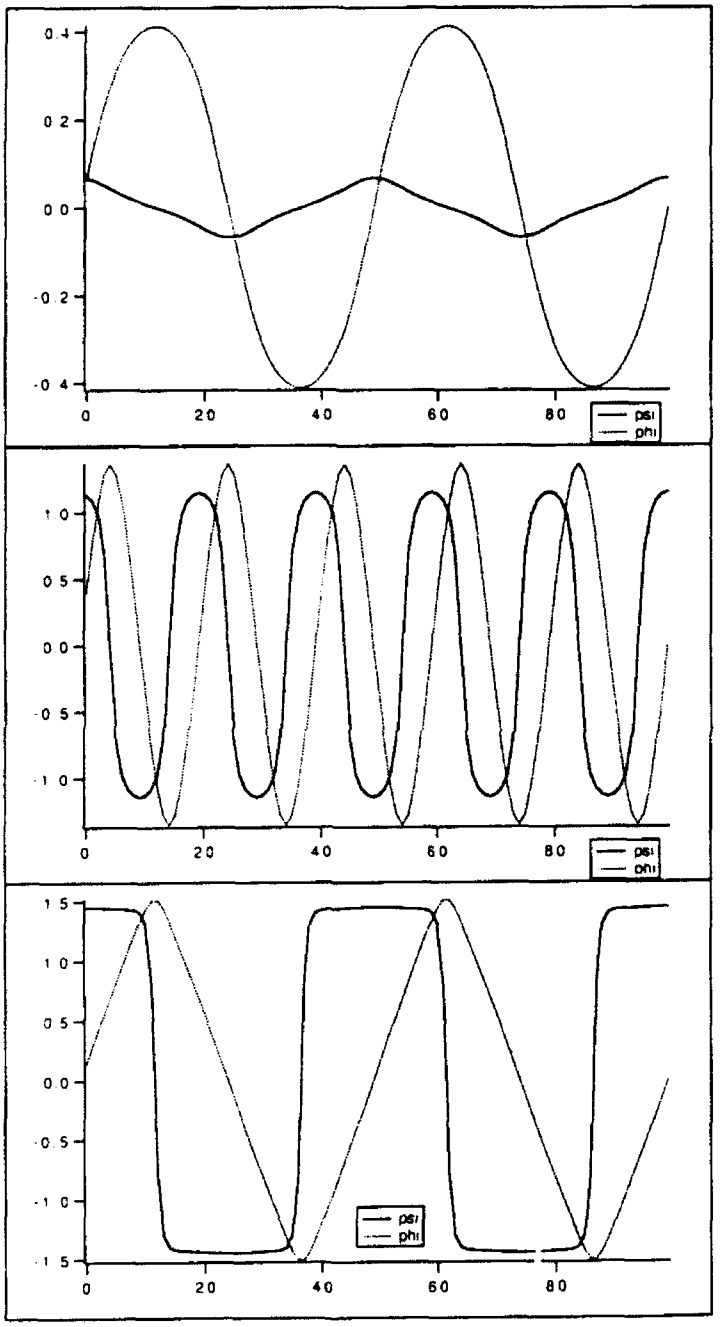

Fig. 3. The modulation in the chiral order parameter $\psi(\mathbf{r})$ and the tilt direction $\phi(\mathbf{r})$, at three temperatures in the striped phase: (a) $t = 0.9$. (b) $t = -1$. (c) $t = -2$. In all three plots, $\lambda = K = \kappa = u = 1$. Note the evolution from the sinusoidal-stripe regime to the soliton-stripe regime.

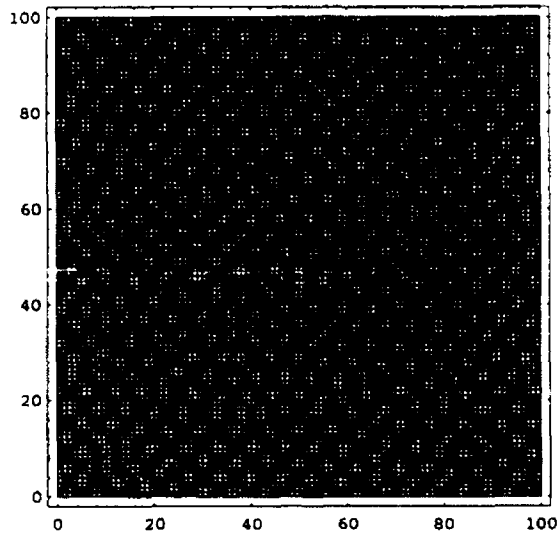

Fig. 4. The modulation in the chiral order parameter $\psi(\mathbf{r})$ in the square-lattice phase, at $t = -1$, $\lambda = 4$, $K = \kappa = u = 1$. The grey scale represents the magnitude of ψ, with black representing positive values and white negative values.

many helpful discussions. This research was supported by the Donors of The Petroleum Research Fund, administered by the American Chemical Society, and by the Caltech Consortium in Chemistry and Chemical Engineering; founding members: E. I. Du Pont de Nemours and Company, Inc., Eastman Kodak Company, and Minnesota Mining and Manufacturing Company.

REFERENCES

[1] P. G. de Gennes, *The Physics of Liquid Crystals* (Oxford University Press, London, 1974).
[2] N. A. Clark, D. H. Van Winkle, and C. Muzny (unpublished); see Ref. [9].
[3] S. B. Dierker, R. Pindak, and R. B. Meyer, Phys. Rev. Lett. **56**, 1819 (1986).
[4] X. Qiu, J. Ruiz-Garcia, K. J. Stine, C. M. Knobler, and J. V. Selinger, Phys. Rev. Lett. **67**, 703 (1991).
[5] X. Qiu, J. Ruiz-Garcia, and C. M. Knobler, in *Interface Dynamics and Growth*, edited by K. S. Liang, M. P. Anderson, R. F. Bruinsma, and G. Scoles (Mat. Res. Soc., Pittsburgh, 1992), p. 263.
[6] J. Maclennan and M. Seul, Phys. Rev. Lett. **69**, 2082 (1992).
[7] J. V. Selinger, in *Complex Fluids*, edited by E. B. Sirota, D. Weitz, T. Witten, and J. Israelachvili (Mat. Res. Soc., Pittsburgh, 1992), p. 29.
[8] J. V. Selinger, Z.-G. Wang, and R. F. Bruinsma, Phys. Rev. Lett., in press (1993).
[9] S. A. Langer and J. P. Sethna, Phys. Rev. A **34**, 5035 (1986).
[10] G. A. Hinshaw, R. G. Petschek, and R. A. Pelcovits, Phys. Rev. Lett. **60**, 1864 (1988).
[11] G. A. Hinshaw and R. G. Petschek, Phys. Rev. A **39**, 5914 (1989).
[12] A. E. Jacobs, G. Goldner, and D. Mukamel, Phys. Rev. A **45**, 5783 (1992).

PART V

Applications

ASSEMBLY OF α-HEMOLYSIN: A PROTEINACEOUS PORE WITH POTENTIAL APPLICATIONS IN MATERIALS SYNTHESIS

HAGAN BAYLEY*, MUSTI KRISHNASASTRY*, BARbARA WALKER* and JOHN KASIANOWICZ**
* Worcester Foundation for Experimental Biology, 222 Maple Ave., Shrewsbury, MA 01545
** National Institute of Standards and Technology, Bldg. 222-A353, Gaithersburg MD 20899

ABSTRACT

α-Hemolysin (αHL) is secreted by the bacterium *Staphylococcus aureus* as a water-soluble polypeptide of 293 amino acid residues. When presented with lipid bilayers or the detergent deoxycholate (DOC), αHL assembles into hexameric cylindrical pores that each contain one channel ~1 to 2 nm in internal diameter. A long-term goal of this laboratory is to use wild-type or re-engineered αHL pores as components of nanoscale materials: for example, to confer novel permeability properties upon thin films. The implementation of this concept would be facilitated by a better understanding of the mechanism by which the pore assembles. Reviewed here are findings that have given us insight into the assembly mechanism, including the results of recent mutagenesis experiments. A critical summary is given of knowledge about the conformation of the monomer in solution, the hexameric pore and two proposed intermediates in assembly (a membrane-bound monomer and an oligomeric pore precursor). Future directions are outlined including the prospects of obtaining three-dimensional structural data on the αHL pore or its precursors, methods for obtaining better monolayer sheets and new experiments on the topography of the pore and its precursors. The role of membrane receptors in facilitating the assembly of αHL is also discussed. Finally, it is demonstrated that despite our rather rudimentary knowledge of the assembly process, the information gained so far still allows the design of mutant αHL polypeptides with useful properties. For example, αHL mutants whose pore-forming ability is activated by proteases have been made.

STAPHYLOCOCCAL α-HEMOLYSIN AS A CANDIDATE FOR PROTEIN ENGINEERING

A long-term goal of this laboratory is to utilize α-hemolysin (αHL) as a building block in molecular devices (1,2). αHL is a hydrophilic 293 amino acid polypeptide (3-5), folded largely into β-sheet secondary structure (6), which is secreted by *Staphylococcus aureus*. The molecule binds to and forms pores in red blood cells (RBCs) (7), phospholipid vesicles (8,9) and planar bilayers (10). The diameter of the αHL pore is between 1.1 and 2.5 nm, as estimated from measurements of the single channel conductance (10) and of the permeability of the channel to nonelectrolytes (11). αHL pores are open in the absence of an applied electric field, but close when a transmembrane voltage of sufficient magnitude is applied (10).

αHL is particularly well suited for use as a component in nanoscale biomolecular devices (1,2). It is a robust polypeptide, with a sequence that is short enough to be conveniently manipulated with recombinant DNA technology. The pore can assemble without the participation of cellular organelles or enzymes. For example, the addition of deoxycholate, a mild detergent, initiates oligomerization (12). Further, unlike many biological channels (e.g. the acetylcholine receptor), the pore is formed by the assembly of identical subunits. In addition, a higher level of self assembly occurs: aggregates of the pores can form extended crystalline two-dimensional (2D) arrays (13,14).

Therefore, while αHL is certainly not the only pore-forming polypeptide that might be used in biotechnology, it is an attractive starting point.

POTENTIAL UTILITY OF PROTEINACEOUS NANOSCALE PORES

Nanoscale structures, ranging from optical and electronic devices (15,16) to tiny machines (17), are currently made from inorganic materials. Organic materials might also be used for such purposes (18). For example, molecules containing rings of atoms that slide along molecular wires have been synthesized (19). In addition to chemical synthesis, a plausible source of organic components is living cells, which have been producing nanoscale structures based on polypeptides and other macromolecules for billions of

years. Indeed, many biological molecules perform functions that parallel those of manufactured structures, including signal transduction (20,21), energy transduction (22), and force generation (23). The point of using polypeptides in molecular devices might be questioned since nanofabrication of inorganic materials is now being extended to the atomic level (15). But polypeptides, before or after rational chemical modification, are sophisticated molecules, which, in addition to their ability to self-assemble, can recognize other molecules. Ligands can be modified or translocated, or a function of the receptor can be activated by a ligand-induced conformational or organizational change. These properties of polypeptides emerge in the size range of a few nanometers and above.

Perhaps the most compelling proposed application (1,2) for αHL is in monolayer (or perhaps multilayer) lattices of pores bonded to support matrices for use in membrane separation systems, sensor technology and electronic devices. In sensor technology, a coating with an αHL lattice might be used to select species of predetermined size and charge for access to a surface such as an electrode. Pores gated by voltage, light or pressure might be incorporated into microelectronic devices (Fig. 1).

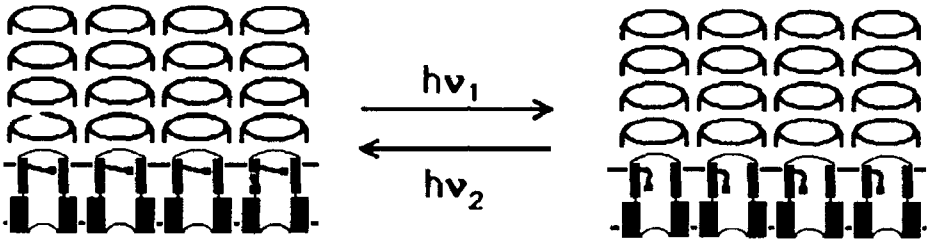

Fig. 1: Speculative depiction of a photogated monolayer of αHL pores. A photoisomerizable group, such as azobisbenzene, is linked to a cysteine residue that has been introduced into αHL at a single site by site-directed mutagenesis. On illumination the group, which blocks the pore in the dark, isomerizes and changes shape permitting ions to flow. The gate closes when illuminated with light of a different wavelength. Adapted from ref. (2).

Regular arrays of αHL might also be used as templates for metallic nanostructures (24) or as substrates to orient other proteins (25), which could be attached by cysteine residues introduced at selected sites by genetic engineering. Eventually it will be possible to alter side-chains that project into the channel. The secure identification of residues that control ion transport will allow the production of pores with a range of properties (e.g. different ion selectivities, pore diameters, and gating activities). More speculative is the possibilty of endowing pores in lipid bilayers or in lattices with catalytic properties, an idea that has proved successful with antibodies (26). It might even be possible to achieve active transport of selected molecules through modified αHL pores.

The implementation of these ideas would be facilitated by an understanding of the mechanism by which the αHL pore assembles. Experimental findings that bear on this are reviewed here. Information about the assembly of oligomeric membrane proteins also has implications in basic science: for understanding the biosynthesis of integral membrane proteins, the physiological effects of cytolytic toxins and immune proteins, and how receptors aggregate with each other or with regulatory proteins.

ASSEMBLY OF αHL- WHAT WE KNOW NOW

Recombinant αHL: Progress both in fundamental studies of αHL, such as those on assembly described below, and on potential applications of αHL in materials synthesis requires genetically engineered variants of the wild-type structure. Using recombinant DNA technology, we have overexpressed the αHL gene in *Escherichia coli* (27). Approximately 50% of the cellular protein is recombinant αHL. Recombinant and wild type αHL are virtually identical, as judged by several criteria based on protein chemistry, biological assays and electrical recordings (27). For example, they have the same apparent molecular weight, N-terminal sequence and peptide maps, they form hexameric structures either in DOC or when

bound to RBCs, and they are equally effective at lysing RBCs. Pores formed by recombinant and wild type αHL also exhibit very similar electrical properties when reconstituted into planar bilayer membranes. They have virtually the same conductances, and the pH-dependencies of the kinetics of pore formation, the conductance values, the gating kinetics and the ion selectivities are indistinguishable.

The ability to synthesize αHL and mutants thereof by in vitro transcription and translation (IVTT) from plasmid DNA has greatly facilitated our studies (27-29). This procedure can produce useful concentrations of αHL of up to 50 μg/ mL (αHL is hemolytic at ~30 ng/ mL). The polypeptide can be labeled, when necessary (e.g. for RBC binding), with ^{35}S of high specific radioactivity. Alterations in the central loop have been made by using an additional technique based on IVTT: complementation mutagenesis, in which αHL is expressed as two complementary chains from two plasmids (29). By this means αHL polypeptides have been made with nicks, overlaps and gaps in the loop (Fig. 2). This approach is superior to conventional deletion mutagenesis, which can result in malfolding of the mutant polypeptide (Fig. 2, *far right*).

Fig. 2: Complementation mutants of αHL. See refs. (29,30) for details.

Deletion mutagenesis has contributed to an understanding of pore assembly: Previous studies had suggested a model for the assembly of αHL in which a glycine-rich loop exists at the surface of the monomer, constituting a hinge about which the polypeptide opens up to form an amphipathic rod (6). The rod inserts into the lipid bilayer where, because of its exposed hydrophilic face, it aggregates into an oligomer, the hexameric nature of which has been confirmed by chemical crosslinking (6). To identify the regions of the molecule that are critical for assembly, a series of αHL truncation mutants was recently produced by IVTT in *E. coli* extracts (28). Three classes of mutants have been defined: those that bind to RBC membranes as monomers and fail to oligomerize or do so only slowly, those that bind and oligomerize but do not lyse the cells, and those that assemble into lytic pores. The earlier findings combined with the results from mutagenesis suggest the following revised minimal mechanism for assembly of the αHL pore, in which the central region is now regarded as a loop rather than a hinge (i.e. it has no active role in oligomerization) and in which oligomerization occurs before a final conformational change in which the transmembrane channel is formed (Fig. 3).

Let us examine critically the evidence for structures **1** through **4**. The proposed structures of **1** and **4** will be discussed first followed by a summary of the evidence for assembly intermediates **2** and **3**.

Monomeric αHL in solution (structure **1**): αHL as secreted by *S. aureus* or after expression in *E. coli* ((27); unpublished) is a water-soluble monomer as ascertained by gel filtration and sedimentation analysis (11,12). The monomer consists largely of β structure as determined from its circular dichroism (CD) (6,31). Monomeric αHL in solution contains protease-sensitive sites near the midpoint of the polypeptide chain that lie in a glycine-rich sequence (4,6). The two halves of the polypeptide chain formed by proteolysis in this central loop, or by complementation mutagenesis, are relatively resistant to further cleavage (6,30), suggesting that they are intimately associated as implied in Fig. 3. By contrast, individually synthesized N- or C-terminal domains of the polypeptide are highly susceptible to proteolysis (30). Therefore, these halves are either malfolded or protease sites occluded in the two chain complexes are exposed. Whatever the case, separately synthesized halves can be combined to form pore-forming αHL molecules with nicks in the central loop (29).

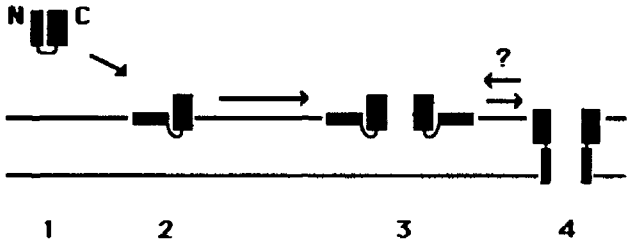

Fig. 3: Working model for assembly of the αHL pore. At this point, the model is intended to provide a succinct summary of experimental findings and not to be taken too literally. The monomer in solution (**1**) comprises two domains linked by a glycine-rich loop. The N-terminal (**N**) and C-terminal (**C**) domains are marked. αHL binds to the cell surface as a monomer in which the loop is occluded (**2**). A nonlytic oligomer consisting of up to six subunits is then formed (**3**). The subunits then further penetrate the membrane to form the lytic pore (**4**). The interconversion of **3** and **4** may be reversible and correspond to certain gating transitions of the pore seen in planar bilayers (see the text). Adapted from ref. (28).

The αHL pore (structure **4**): On contact with membranes or the detergent DOC, αHL forms sodium dodecyl sulfate (SDS)-resistant oligomeric structures that are most probably hexamers. Evidence for the stoichiometry of the oligomers was originally obtained by electron microscopy (EM), which detected 5 to 7 subunits per oligomer (32). More recent application of a rotational averaging technique to views of single particles in membranes yielded a structure with six symmetrically arranged peaks (33). By contrast, image reconstruction from 2D tetragonal crystalline arrays of αHL oligomers suggests that each oligomer in an array contains four subunits, each with two domains (perhaps the N and C termini) (14,34). Additional evidence, including results from freeze-fracture EM, suggests that this form of αHL is attached to the outer leaflet of the lipid bilayer and therefore may represent a pore precursor such as **3**, but, surprisingly, tetrameric. This view is supported by the finding that oligomers formed by nonlytic trypsin-treated αHL have a similar projection structure (34). Experiments based on gel electrophoresis and sedimentation analysis indicated that the oligomer formed on RBCs or in detergent was likely to be a hexamer (11,12). These hydrodynamic methods are subject to systematic errors and therefore the nature of the oligomer was later re-evaluated by chemical crosslinking, which produces a ladder of crosslinked forms, the steps of which are easily counted. By this method the αHL oligomer in DOC was found to be a hexamer (6). Although αHL in DOC is identical to wild-type oligomers extracted from RBCs (12), it is not certain whether the pore (**4**) or its precursor (**3**) was examined (see below). Further, in retrospect, the evidence from crosslinking does not unequivocally demonstrate that the αHL oligomer is not a heptamer, which would have migrated with only a slightly reduced mobility compared to a hexamer. This rumination has emerged because of a surprising new finding: the oligomeric form of the functionally-related aerolysin, which has an unrelated primary sequence, is indeed a heptamer (35).

Another striking feature of the oligomeric form of αHL is that its circular dichroism (in detergent) is very similar to that of the monomer in solution (6,31), although subtle differences in the spectra are seen, indicative of a conformational change that involves little reorganization of the polypeptide backbone. Of course, CD cannot reveal where these changes are located. The calculated secondary structure contents of the monomer and oligomer hardly differ. Both are largely β sheet and the α-helical content is unlikely to exceed ~10% (6,31). Therefore, it is quite likely that the channel is formed by β structure as is the case for the porins (36) and perhaps for both voltage-gated (37) and ligand-gated (38) eukaryotic ion channels. Nevertheless, the existence of a single α helix capable of spanning the lipid bilayer is not inconsistent with the CD measurements, although a helical hairpin as suggested for colicins E1 and A (39) is less likely. These considerations are important because six α helices (one per αHL chain) are capable of forming the walls of a channel ~1 nm (10,40) but not 2 nm (6,11) in diameter. The polypeptide sequence is rather hydrophilic (3) and there are no extended hydrophobic sequences that might penetrate the lipid bilayer. Nevertheless, a

candidate amphipathic α helix has been identified by computer analysis (40). Interestingly, it contains a central proline, a common feature of helices in ion channels, and it is immediately C-terminal of the central glycine-rich loop. However, there is no experimental evidence that this region of αHL is either helical or that it spans the lipid bilayer.

By contrast with **1**, the glycine-rich central loop is not available to proteases in **4** (28). As yet, it cannot be ascertained whether this means that the αHL polypeptide has undergone a conformational change or whether the loop is involved in subunit-subunit interactions, buried in the lipid bilayer or perhaps bound to a receptor. The involvement of the loop in subunit-subunit or αHL-receptor interactions that are necessary for oligomerization appears to be ruled out by the finding that complementation mutants of αHL missing large parts of the loop are able to assemble into hexamers (29). Many of these mutants are unable to form functional pores suggesting that the **3** -> **4** transition is blocked, or that **4** is formed but alteration of the loop results in a defective channel (29).

Remarkably, below 65°C, αHL oligomers are resistant to the detergent SDS, which is generally denaturing at room temperature. Furthermore, oligomers of αHL made from complementation mutants that have breaks in the central loop (Fig. 3) are also stable to SDS, whether or not the mutants are lytic. Because the two chains that constitute these mutants do dissociate when the non-oligomerized polypeptides are treated with SDS, the interaction between the N- and C-terminal domains of the protein must be strengthened by oligomerization as early as the formation of **3**. Unless the interaction between the two halves is strengthened by a change of environment (e.g. immersion in the bilayer as suggested in Fig. 3), this rules out models in which only one half of the polypeptide chain is involved in oligomerization, because, in this case, the other half would be free to dissociate upon the addition of SDS.

While αHL mutants with drastically altered loop regions will oligomerize, only those nicked at the center but not the edges of the loop lyse RBCs efficiently (Fig. 4). It will be interesting to look at the properties of single channels formed by the active nicked molecules in planar bilayers to see if the lesions lie close to the conductive pathway.

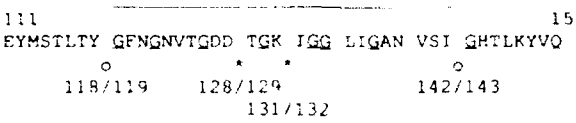

Fig. 4: Schematic of the glycine-rich loop region of αHL. Glycine residues are underlined. Gaps in the sequence mark nicks in the polypeptide chain generated by complementation mutagenesis. The following phenotypes were observed: o, oligomerization but no lysis; *, oligomerization and lysis. From ref. (29).

Membrane-bound monomer (structure **2**): Of the proposed structures in Fig. 3, the evidence for a membrane-bound monomeric intermediate in assembly is the weakest. However, unless oligomerization occurs in solution, and there is no evidence that this happens at a relevant rate, monomer adsorbed at the membrane surface must be at least a transient intermediate. In favor of this, C-terminal truncation (ΔC) mutants missing 3 or 5 amino acids have greatly reduced hemolytic activity and appear to be retarded as monomers at the cell surface (28). The ΔC mutants do lyse RBCs at a rate 100 times slower than wild-type αHL when applied at a 100 times higher concentration, which we interpret as the very slow formation of a hexameric pore. Further, the central loop in the membrane-bound mutant monomers is protected from proteolytic cleavage, just as it is in the assembled wild-type pore, while the loop in the monomer in solution is exposed. One interpretation of this is a conformational change as depicted in Fig. 3, although other possibilities cannot be eliminated as summarized in the discussion of **4**. In the case of the ΔC mutants, an additional possibility is that the polypeptides do oligomerize on the membrane but that the oligomers are labile in SDS because of a weakened subunit-subunit interaction. This seems unlikely because a small fraction of SDS-stable oligomers can be observed that are thought to account for the slow lysis. Because the ΔC mutants are largely monomeric when membrane-bound, it is likely that the C terminus is involved in the contacts made during assembly. It is not claimed that the deleted residues themselves are at the contact site

because a small truncation might cause malfolding of an extended domain of the polypeptide

Nonlytic, oligomeric pore precursor (structure **3**): Nonlytic oligomeric structures, stable in SDS, are a common phenotype among αHL mutants. They are seen when N-terminal truncations are made (28), when overlaps, nicks and gaps are made in the central loop (29), with various point mutants (e.g. H35N; unpublished) and with certain chemically modified single-cysteine mutants (unpublished). As judged by proteolysis, the central loop of N-terminal truncation (ΔN) mutants missing 2 to 22 amino acids is occluded after they have formed oligomers on RBCs. Unlike the ΔC mutants, the ΔN mutants are nonlytic at the highest concentrations tested (4000 times greater than wild-type).

This phenotype suggests that, while the C terminus is involved in the initial aggregation of αHL on the membrane surface (**2** -> **3**), the N terminus plays a role in the final step in pore assembly (**3** -> **4**). One possibility, depicted in Fig. 3, is that the N terminus itself inserts into the lipid bilayer. In support of this, a proteolytic site at the N terminus is exposed on the RBC surface in monomeric ΔC truncation mutants and the oligomerized ΔN deletion mutant αHL(A3-293), but occluded in the wild-type hexameric pore (28). Of course this is hardly conclusive evidence, for example, the rate of proteolysis at the N terminus is likely to be affected by mutations in this region. Further, the result cannot show that a large volume of the N-terminal domain becomes buried as depicted in the working model (Fig. 3).

Of course, there must be other intermediates in assembly. Six-way collisions are undoubtedly rare events, even when a polypeptide is constrained to move on a surface. However, there is little concrete evidence for intermediates containing between 2 and 5 subunits. Tetramers have been tentatively detected on SDS gels (6), by single channel recording (10) and in 2D crystals (14,34). ΔN mutants missing 2 or 11 residues form pentamers more readily than hexamers, indicating that the pore stoichiometry may be rather finely balanced (28). This is reminiscent of the structure of the pore formed by the C9 polypeptide of complement, which has a broad size distribution and contains up to 20 subunits (41). An important question is whether the assembly of αHL is ordered or random, e.g. can the final step be either $\alpha5 + \alpha1$, $\alpha4 + \alpha2$ or $\alpha3 + \alpha3$ or only one of the possibilities. While, no data is available pertaining to this, the sequence of the potential intermediates **2** and **3** in the assembly pathway has at least been confirmed by using dominant negative mutations, in vitro. The weak hemolytic activity of ΔC deletion mutants is inhibited by subequimolar amounts of nonlytic ΔN truncation mutants, suggesting that the ΔC mutants become trapped with the ΔN mutants as nonlytic hetero-oligomers (28).

One further unresolved issue is whether **3** and **4** are interconvertible. If they are the interconversion might reflect the gating of the pore that is seen under certain conditions in planar bilayers. This is an important question because it places in doubt the identity of the structure seen in detergent, and assumed to be **4**, upon which the CD measurements on the "pore" were performed. It seems likely that the wild-type pore on RBC membranes, as examined for example by limited proteolysis, is largely the open form as the resting potential of these cells is virtually zero and divalent metal ions are absent, conditions which mitigate channel closure (10). Although gating might well involve a step distinct from **3** <-> **4**, it is unlikely to involve the dissociation of hexamers as they are rather stable.

SELF-ASSEMBLY OF αHL- WHAT WE NEED TO KNOW

Structural analysis: Low resolution techniques might yet yield additional information about the structure of αHL and its assembly intermediates. For example, Fourier-transform infrared spectroscopy could reveal the orientation of β sheets with respect to the lipid bilayer. Naturally, a three dimensional structure of αHL in monomeric or hexameric form would be more informative. Of course, it might not tell the whole story. For example, if hexamers are seen it might not be clear whether they represent the proposed structure **3** or **4**. Such problems emphasize the need for complementary biochemical data in interpreting structures. Dr. Eric Gouaux (U. Chicago) has obtained crystals beginning with αHL monomer and our groups are collaborating on structure determination and interpretation. αHL is too large for high resolution nuclear magnetic resonance (NMR) in solution, and there is no evidence that the individually expressed N- or C-terminal domains, which fall into the mass range appropriate for NMR analysis, are correctly folded.

How might the formation of 2D sheets be improved Besides their utility for structure determination (14,34,42), 2D sheets of the αHL pore might be useful for applications in materials science (1,2). The most readily formed lattices of αHL are tetragonal and appear to contain αHL tetramers lying on the surface of a lipid bilayer. The tetramers are probably inactive pore precursors (see above). Hexagonal arrays are harder to obtain and although they are suspected to contain hexamers, this has not been conclusively demonstrated by image analysis (42). Therefore, Langmuir-Blodgett techniques may be required to make films from hexameric pores preformed by DOC treatment or isolated from RBC membranes. In a further improvement the sheets might be covalently crosslinked using chemical reagents that react either with the wild-type polypeptide or with sulfhydryl groups placed at selected sites in the polypeptide by cysteine mutagenesis.

The RBC receptor- what does it do? While the oligomerization of αHL is facilitated by receptors on susceptible cells, such as rabbit RBCs (43,44), apparently identical oligomers are generated by treatment of monomeric αHL with heat (32), deoxycholate (12) or lipids (31), or by treatment of resistant cells with high concentrations of αHL (44). This raises the question of whether receptors on susceptible cells play an active role in triggering assembly or whether they merely serve to concentrate αHL at the cell surface.

Let us first consider the concentration effect. αHL lyses rabbit RBCs when presented at ~1 nM or ~30 ng/mL. At 1 nM the mean intermolecular separation in solution is ~1.2 μm. Because there are at least 1500 receptors for αHL per RBC (43,44), at saturation the mean intermolecular separation on the surface of the cell will be ~0.4 μm, assuming a surface area of 200 μm^2 per RBC. Using the expressions of Hardt (45) for estimating the rates of diffusion controlled reactions in two and three dimensions, it can be shown that attachment to receptors expressed at such low density cannot offer a significant kinetic advantage even if the diffusion coefficient of the membrane-bound αHL monomer is very high (e.g. 0.01 times that in solution). Therefore, it is likely that additional effects come into play such as orientation at the cell surface, a conformational change induced by the lipid bilayer or the stabilization of assembly intermediates. The bilayer itself plays a rate-determining role when αHL assembles on liposomes. In this case, the presence of high mole fractions of cholesterol greatly enhance both the rate and extent of marker release (46). At present, there is no evidence to suggest that receptors for αHL play an active role for example, by inducing a conformational change.

How the detergent DOC stimulates the formation of hexamer in solution as demonstrated by Bhakdi et al. (12) remains a mystery. No other detergents tested are capable of causing efficient oligomerization ((12), unpublished); indeed, the effect may be specific for DOC. Perhaps an impurity in the commercial detergent is responsible, but this is improbable as recrystallized DOC works just as well. Further, oligomerization is optimal at around the critical micelle concentration, which also indicates that DOC is the causal agent. Incidentally, whether bile salt detergents form true micelles is debatable. DOC forms small clusters of 10 to 20 molecules far too small a structure to envelop an αHL hexamer. Because the bile salts are related in structure to cholesterol and because cholesterol-containing bilayers are more susceptible than others to damage by αHL (46), we have examined the effects of cholesterol on αHL assembly in solution. Cholesterol was solubilized in octyl glucoside, a detergent that does not cause oligomerization, or solubilized by covalent modification (polyoxyethanyl-cholesteryl sebacate). In preliminary experiments, a wide range of concentrations of these materials did not mediate oligomerization.

Thermodynamics and kinetics: There is no reason why an assembly process such as that presented by αHL cannot be studied using the thermodynamic and kinetic analyses that are applied to chemical reactions in solution or on surfaces. Nevertheless, relatively little work has been done in this area, perhaps because the assembly process is more complex than it appears at first glance. With regard to thermodynamic parameters, transition enthalpies might be obtained by comparing heating curves for monomeric and hexameric samples of αHL by using differential scanning calorimetry. Even irreversible processes can yield useful information (47). Ultimately, it might be possible to place restraints on models for αHL folding and oligomerization based on such data (48).

Even though there is only one reactant, the kinetic analysis of αHL assembly is complicated because the reaction is initiated by binding to a surface and by the potentially

high overall order of the reaction. The lysis of RBCs is a complex process involving osmotic lysis preceded and caused by the leakage of ions. The efficiency of binding of αHL to RBCs and RBC lysis decrease above 10 to 20°C (43,44,49). For this reason, the kinetics of lysis of liposomes or the penetration of planar lipid bilayers are more readily interpreted, but even here there is a lengthy lag period before lysis begins and lysis itself is multiphasic. A useful start has been made by Menestrina and his collaborators, who have determined the dependence of the lag period, pore formation and pore conductance on temperature and αHL concentration by using electric recordings from planar bilayers and marker release from liposomes (50). From concentration dependences, they conclude that reversible formation of small aggregates α_2 and α_3 (the lag phase) is followed by the irreversible formation of higher lytic oligomers α_4, α_5 and α_6. From Arrhenius plots, which are linear up to 50°C, they further deduce that the activation energy for the lag phase is comparable to that required for diffusion in the plane of the bilayer. Their data is consistent with earlier, less readily analyzed, findings using RBCs. One hopes is that future kinetic studies will be facilitated by using mutants that are arrested at various stages of assembly.

WHAT ARE WE DOING NOW?

To address some of the questions posed in this review, this laboratory is focusing on the application of mutagenesis to studies of αHL assembly. For example, a series of single-cysteine mutants is being constructed to obtain information about the topography of the polypeptide with respect to the lipid bilayer and the conformational changes it undergoes during assembly. Topological questions can be addressed by using chemical modification reagents to ask whether cysteine residues introduced at selected positions in the chain can be modified, after assembly, from one side of the bilayer or the other. Biotinylation of selected residues followed by the investigation of topography with EM, utilizing avidin conjugated to colloidal gold, is a useful adjunct to chemical modification. To further characterize the conformational changes that occur during assembly, fluorescence techniques are being employed. For example, using separately synthesized N- and C-terminal domains, it is possible to label each half of the molecule with different fluorescent groups and then reconstitute active αHL. The distances between the fluorescent groups can then be determined by energy transfer measurements.

WHAT USE IS IT ALL?

Even though there is much more to learn, the process of accumulating information about the assembly of αHL has made us familiar with many aspects of what can and cannot be done with the polypeptide. This has allowed us to re-engineer the molecule for specific purposes based on predictions made without the help of a three-dimensional structure. For example, the analysis of complementation mutants indicated that the integrity of the central loop is relatively unimportant for oligomerization but crucial for pore formation (29). Based on this, we have now been able to re-engineer the protease-sensitive wild-type αHL into a protease-activated form that contains two non-covalently attached chains (Fig. 5) (30).

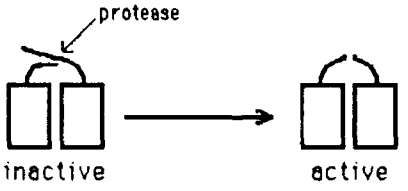

Fig. 5. Activation of an overlap mutant of αHL by proteolysis. Wild-type αHL was rendered insensitive to the protease endo C by removing a protease site near the N terminus by site-directed mutagenesis. An inactive overlap mutant was then generated in vitro by complementation mutagenesis. The pore-forming activity of this mutant can be activated by endo C, which removes the redundant peptide in the central loop (30).

Based on these findings we are now designing "proimmunolysins", modified αHL molecules that bind to malignant cells. There they will be activated by cell surface proteases and damage the plasma membrane. Given this success in modifying the properties of the wild-type polypeptide, αHL molecules activated by other means such as light (Fig. 1) or metal ions should soon be available, for which we have projected several applications in biotechnology, including materials science.

ACKNOWLEDGEMENTS

Supported by a grant from the DOE. JK is supported by a fellowship from the NRC.

REFERENCES

1. H. Bayley, MRS Symp. Proc. **218**, 69 (1991).

2. M. Krishnasastry, B. Walker, L. Zorn, J. Kasianowicz and H. Bayley, in *Synthetic microstructures in biological research*, J. Schnur, J. and M. Peckerar, eds. New York: Plenum, 1992, pp. 41-51.

3. G.S. Gray and M. Kehoe, Infect. Immun. **46**, 615 (1984).

4. M. Thelestam and L. Blomqvist, Toxicon **26**, 51 (1988).

5. S. Bhakdi and J. Tranum-Jensen, Microbiol. Rev. **55**, 733 (1991).

6. N. Tobkes, B.A. Wallace and H. Bayley, Biochemistry **24**, 1915 (1985).

7. S. Bhakdi and J. Tranum-Jensen, Trends Biochem. Sci. **8**, 134 (1983).

8. H. Ikigai and T. Nakae, J. Biol. Chem. **262**, 2150 (1987).

9. H. Ikigai and T. Nakae, J. Biol. Chem. **262**, 2156 (1987).

10. G. Menestrina, J. Membrane Biol. **90**, 177 (1986).

11. R. Fussle, S. Bhakdi, A. Sziegoleit, J. Tranum-Jensen, T. Kranz and H.J. Wellensiek, J. Cell Biol. **91**, 83 (1981).

12. S. Bhakdi, R. Fussle and J. Tranum-Jensen, Proc. Natl. Acad. Sci. USA **78**, 5475 (1981).

13. A.W. Bernheimer, K.S. Kim, C.C. Remsen, J. Antanavage and S.W. Watson, Infect. Immun. **6**, 636 (1972).

14. A. Grafsson, B. Kavéus, I. Hackse, M. Thelestam and H. Hebert, J. Mol. Biol. **214**, 299 (1990).

15. M. Sundaram, S.A. Chalmers, P.F. Hopkins and A.C. Gossard, Science **254**, 1326 (1991).

16. J.L. Jewell, J.P. Harbison and A. Scherer, Sci. Am. **265 (5)**, 86 (1991).

17. K.D. Wise and K. Najafi, Science **254**, 1335 (1991).

18. G.M. Whitesides, J.P. Mathias and C.T. Seto, Science **254**, 1312 (1991).

19. D. Philp and J.F. Stoddart, Synlett 445 (1991).

20. G.M. Shepherd, Cell **67**, 845 (1991).

21. H. Bayley, MRS Symp. Proc. **255**, 269 (1992).

22. W.A. Cramer and D.B. Knaff, *Energy transduction in biological membranes*, New York: Springer-Verlag, 1989.

23. H.E. Huxley, J. Biol. Chem. **265**, 8347 (1990).

24. S. Douglas, N.A. Clark and K.J. Rothschild, Appl. Phys. Lett. **48**, 676 (1986).

25. E.L. Uzgiris and R.D. Kornberg, Nature **301**, 125 (1983).

26. R.A. Lerner, S.J. Benkovic and P.G. Schultz, Science **252**, 659 (1991).

27. B.J. Walker, M. Krishnasastry, L. Zorn, J.J. Kasianowicz and H. Bayley, J. Biol. Chem. **267**, 10902 (1992).
28. B.J. Walker, M. Krishnasastry, L. Zorn and H. Bayley, J. Biol. Chem. **267**, 21782 (1992)
29. B.J. Walker, M. Krishnasastry and H. Bayley, J. Biol. Chem. **268**, in press (1993)
30. B.J. Walker and H. Bayley, submitted (1993).
31. H. Ikigai and T. Nakae, Biochem. Biophys. Res. Commun. **130**, 175 (1985)
32. J.P. Arbuthnott, J.H. Freer and A.W. Bernheimer, J. Bacteriol. **94**, 1170 (1967)
33. A. Olofsson, U. Kavéus, M. Thelestam and H. Hebert, J. Ultrastruct. Mol. Struct. Res. **100**, 194 (1988).
34. A. Olofsson, U. Kavéus, M. Thelestam and H. Hebert, J. Struct. Biol. **108**, 238 (1992)
35. H.U. Wilmsen, K.R. Leonard, W. Tichelaar, J.T. Buckley and F. Pattus, EMBO J. **11**, 2457 (1992).
36. S.W. Cowan, T. Schirmer, G. Rummel, M. Steiert, R. Ghosh, R.A. Pauptit, J.N. Jansonius and J.P. Rosenbusch, Nature **358**, 727 (1992).
37. G. Yellen, M.E. Jurman, T. Abramson and R. MacKinnon, Science **251**, 939 (1991)
38. M.H. Akabas, D.A. Stauffer, M. Xu and A. Karlin, Science **258**, 307 (1992)
39. A.R. Merrill and W.A. Cramer, Biochemistry **29**, 8529 (1990).
40. G. Menestrina, G. Belmonte, V. Parisi and S. Morante, FEMS Microbiol. Immunol. **105**, 19 (1992).
41. M.C. Peitsch and J. Tschopp, Curr. Opinion Cell Biol. **3**, 710 (1991).
42. H. Hebert, A. Olofsson, M. Thelestam and E. Skriver, FEMS Microbiol. Immunol. **105**, 5 (1992)
43. P. Cassidy and S. Harshman, Biochemistry **15**, 2348 (1976).
44. A. Hildebrand, M. Pohl and S. Bhakdi, J. Biol. Chem. **266**, 17195 (1991).
45. S.L. Hardt, Biophysical Chem. **10**, 239 (1979).
46. S. Forti and G. Menestrina, Eur. J. Biochem. **181**, 767 (1989).
47. J.M. Sturtevant, Ann. Rev. Phys. Chem. **38**, 463 (1987).
48. J.-L. Popot and D.M. Engelman, Biochemistry **29**, 4031 (1990).
49. H. Ikigai and T. Nakae, FEMS Microbiol. Lett. **24**, 319 (1984)
50. G. Belmonte, L. Cescatti, B. Ferrari, T. Nicolussi, M. Ropele and G. Menestrina, Eur. Biophys. J. **14**, 349 (1987).

PROPERTIES AND PREVENTION OF ADHESIONS APPLICATIONS OF BIOELASTIC MATERIALS

D. W. URRY*, D. CHANNE GOWDA**, BETTY A. COX**, LYNNE D. HOBAN***, ADAM McKEE*** and TAFFY WILLIAMS***

*The University of Alabama at Birmingham, Laboratory of Molecular Biophysics, VH300, Birmingham, AL 35294-0019

**Bioelastics Research, Ltd., 1075 South 13th Street, Birmingham, AL 35205

***United States Department of the Navy, Naval Medical Research, Bethesda, MD 20889-5055.

ABSTRACT

The origins, syntheses, variable composition and physical properties of bioelastic materials are discussed. The latter includes their capacity to undergo inverse temperature transitions to increased order on raising the temperature and to be designable to interconvert free energies involving the intensive variables of mechanical force, temperature, pressure, chemical potential, electrochemical potential and light.

Bioelastic materials include analogues and other chemical variations of the viscoelastic polypeptide, poly(Val-Pro-Gly-Val-Gly), and cross-linked elastomeric matrices thereof. This parent material has been shown to be remarkably biocompatible; it can be minimally modified to vary the rate of hydrolytic breakdown; it can contain enzymatically reactive sites; and it can have cell attachment sites included which promote excellent cell adhesion, spreading and growth to confluence.

One specific application is in the prevention of postoperative adhesion. There are some 30,000,000 per year surgical procedures in this country and a large portion of these would benefit if a suitable material were available for preventing adhesions. Bioelastic materials have been tested in a contaminated peritoneal model, and promising preliminary studies have been carried out in the rabbit eye model for strabismus surgery. In the peritoneal model, 90% of the 29 control animals exhibited significant adhesions; whereas, only 20% of the 29 animals using gas sterilized matrices had significant adhesions. On the basis of this data, it appears that cross-linked poly(VPGVG) is an effective physical barrier to adhesion formation in a trauma model with resulting hemorrhage and contamination.

The potential use of bioelastic materials as a pericardial substitute following the more than 400,000 open heart surgeries per year in the U.S. is under development beginning with the use of bioelastic matrices to prevent adhesions to the total artificial heart being used as a bridge to heart transplantation such that the site will be less compromised when receiving the donor heart.

BIOELASTIC MATERIALS

Origins of Bioelastic Materials

Bioelastic materials have their origins in repeating sequences of the mammalian elastic protein, elastin[1,2]. The most prominent repeating sequence occurs in bovine elastin; it can be written $(Val^1\text{-}Pro^2\text{-}Gly^3\text{-}Val^4\text{-}Gly^5)_n$ where n is eleven without a single substitution. Another repeat first found in porcine elastin is $(Val^1\text{-}Pro^2\text{-}Gly^3\text{-}Gly^4)_n$ but this repeat has not been found to occur with n greater than 2 without substitution[3]. High polymers of both of these repeats, written as poly(VPGVG) and poly(VPGG) or equivalently as poly(GVGVP) and poly(GGVP), form viscoelastic phases in water and when γ-irradiation cross-linked form elastic matrices[4,5].

Mat. Res. Soc. Symp. Proc. Vol. 292. © 1993 Materials Research Society

Compositions of Bioelastic Materials

A wide range of compositions of bioelastic materials becomes possible when substitutions are carried out in a way that does not disrupt higher order structure formation and elastic function[6,7]. For the series of primary structures that have been considered in the prevention of adhesions applications the following general structural formula may be written for the polypentapeptides as

$$\text{poly}[f_V(\text{VPGVG}), f_X(\text{VPGXG}), f_I(\text{IPGVG})] \quad [1]$$

and for the polytetrapeptides as

$$\text{poly}[f_V(\text{VPGG}), f_X(\text{XPGG})] \quad [2]$$

where the f_i are mole fractions such that in each formula the sum of f_i is equal to one and where V = Val, P = Pro, G = Gly, I = Ile and X can be any naturally occurring amino acid or a chemical modification thereof.

The compositions may be further modified to contain enzymatically reactive sites or cell attachment sites. An example of the former is poly[30(IPGVG)(RGYSLG)] where (RGYSLG), i.e., Arg-Gly-Tyr-Ser-Leu-Gly, is a specific kinase site wherein a cardiac cyclic AMP dependent kinase can phosphorylate the Ser residue and the phosphate can be removed by intestinal alkaline phosphatase[8]. An example of inclusion of a cell attachment site is poly[40(GVGVP),(GRGDSP)] where (GRGDSP), i.e., Gly-Arg-Gly-Asp-Ser-Pro, is a cell attachment sequence from fibronectin. Whereas in a standard culture medium cells do not adhere to the matrix comprised of poly(GVGVP), they do adhere, spread and grow to confluence when GRGDSP is within the elastic matrix[9].

A further modification could be the introduction of a site for proteolytic cleavage by enzymes in the milieu of interest or by enzymes doped in the matrix for the purpose of controlling rate of degradation. The matrices can be used for releasing therapeutic agents whether being employed in the prevention of adhesions or in other drug delivery contexts. Also, the chemical synthesis wherein glycolic acid residues, Glc, replaced either of the Gly residues can provide a means of controlling rate of degradation for removal and/or for release of drugs[10].

Preparation of Bioelastic Matrices

Polymers based on the repeating elastin sequences and their amino acid analogues can be synthesized microbially by using genetic engineering[11] and they can be synthesized chemically by using classical solution and/or solid phase peptide synthesis methods or by using a combination of microbial and chemical means[11,12]. For poly(GVGVP) an estimate of the cost for large scale chemical synthesis is of the order of $20.00/gram and for large scale microbial synthesis of less than $1.00/gram.

For many applications elastomeric sheets or matrices are desired. While there are many chemical and enzymatic means of achieving cross-linking to form elastic matrices, a particularly convenient method is by γ-irradiation. An effective dose is 20 Mrads with the resulting elastic matrix being designated for example as X^{20}-poly(GVGVP). One gram of poly(GVGVP) can result in a matrix 7 cm x 7 cm x 0.4 mm when contracted and 15 cm x 15 cm x 1 cm when swollen in water. Interestingly, for protein-based polymers of Formula [1] above, nuclear magnetic resonance (even using nitrogen-15 and carbon-13 enrichment)[13,14] and amino acid analyses (in preparation) before and after 20 Mrad γ-irradiation cross-linking indicate amino acid destruction to be below detectable levels.

Physical Properties of Bioelastic Materials

Inverse Temperature Transitions: Protein-based polymers of Formulae [1] and [2] as well as a number of other compositions such as poly(APGVGV) and poly(VPGFGVGAG) are

soluble in water at low enough temperatures but on raising the temperature they self-associate with clear examples of unambiguous increase in order. This increase in order on increasing the temperature is called an inverse temperature transition[15].

T_t-based Hydrophobicity Scale: On introduction of a more hydrophobic residue, e.g., Val → Ile, the temperature of the transition, T_t, is lowered and on introduction of a less hydrophobic residue, e.g., Val → Ala, the temperature of the transition, T_t, is raised. In fact, a hydrophobicity scale has been developed for all of the naturally occurring amino acid residues, their different states of ionization when relevant, chemical modifications, and biologically relevant prosthetic groups[7]. This is referred to as the T_t-based hydrophobicity scale; it provides the molecular engineer with the capacity to design materials of desired properties.

Elasticity: The elastic (Young's) modulus for X^{20}-poly(GVGVP) is about 1 x 10^6 dynes/cm^2 (10^5 N/m^2 /tons/m^2) with little or no hysteresis and with extensions of up to 200% having been observed. The elastic modulus is proportional to the square of the γ-irradiation dose; for example, a doubling of the dose quadruples the elastic modulus. Depending on the composition the elastic modulus for a 20 Mrad dose can vary from 10^5 dynes/cm^2 to 10^9 dynes/cm^2. When determining the temperature, T, dependence of force, f, at fixed length, a plot of ln (f/T) versus T approximates a zero slope when above the transition temperature range such that by classical arguments X^{20}-poly(GVGVP) is a dominantly entropic (ideal) elastomer[6] as is natural elastin with the potential for the remarkable durability exhibited by natural elastin which appears to be capable of sustaining billions of demanding stretch/relaxation cycles in the aortic arch.

Thermomechanical Transduction: For those compositions such as Formulae [1] and [2] that form viscoelastic phases above the temperature, T_t, of the inverse temperature transition, they may be shaped as desired, e.g., as sheets, and γ-irradiation cross-linked to form the elastic matrices described above. These matrices exhibit reversible contraction and relaxation, i.e., de-swelling and swelling, on passing through the inverse temperature transition. On raising the temperature from below to above T_t the elastic matrices can contract and perform the mechanical work of lifting a weight. They can perform thermomechanical transduction[15,16].

The ΔT_t-Mechanism of Free Energy Transduction: Now instead of raising the temperature from below to above T_t to drive contraction, it has been shown that there are many ways to lower the value of T_t from above to below a working temperature to achieve contraction and the performance of mechanical work. This is called the ΔT_t-mechanism of free energy transduction[15,16]. Decreasing the degree of ionization of a Glu(E) residue, for example, is a dramatic means of lowering the value of T_t and addition of protons to a Glu-containing matrix has been shown isothermally to drive contraction. This is referred to as intrinsic chemo-mechanical transduction. As increasing salt (NaCl)

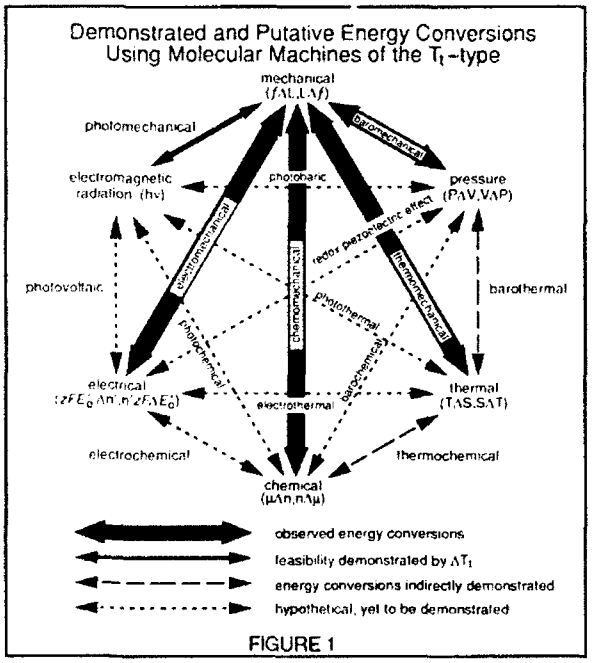

FIGURE 1

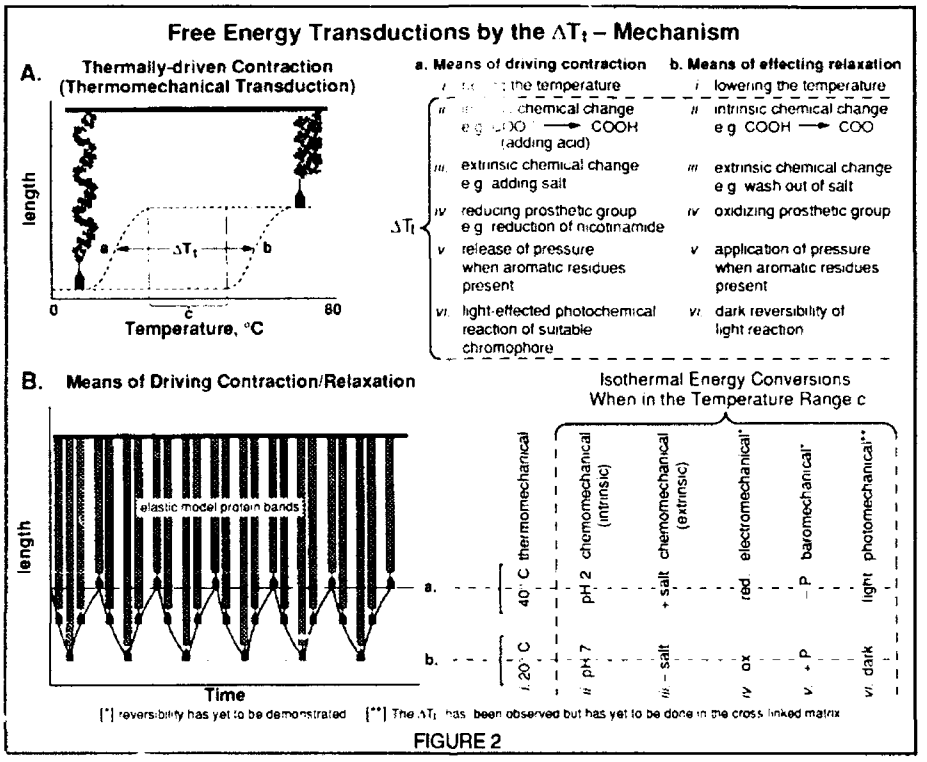

FIGURE 2

concentration lowers T_t, this too becomes a means of driving contraction referred to as extrinsic chemomechanical transduction.

Energy Conversions Possible by the ΔT_t-mechanism: In fact, the bioelastic matrices can be designed for many forms of free energy conversion involving the intensive variables of temperature, pressure, chemical potential, electrochemical potential, light and mechanical force as depicted in Figure 1. A summary of the ΔT_t-mechanism is given in Figure 2[16].

Biocompatibility of Bioelastic Materials

With the mammalian origin and nature (dynamic with a dominantly hydrophobic structure) of the bioelastic materials, it had been anticipated that these materials would be biocompatible. Following the recommendations for the set of generic biological tests required to establish biocompatibility for materials in contact with tissues, tissue fluids and blood, eleven tests were performed on poly(GVGVP) and the elastic matrix, X^{20}-poly(GVGVP). With the results following in parenthesis, these were: "(1) the Ames mutagenicity test (non-mutagenic), (2) cytotoxicity-agarose overlay (non-toxic), (3) acute systemic toxicity (non-toxic), (4) intracutaneous toxicity (non-toxic), (5) muscle implantation (favorable), (6) acute intraperitoneal toxicity (non-toxic), (7) systemic antigenicity (non-antigenic), (8) dermal sensitization—the Magnusson and Kligman maximization method (non-sensitizing), (9) pyrogenicity (non-pyrogenic), (10) Lee-White clotting study (normal clotting time), and (11) *in vitro* hemolysis test (non-hemolytic)"[17]. The result is a remarkable biocompatibility.

In addition, biocompatibility tests are underway on a member of the polytetrapeptide series, namely poly(GGAP) and X^{20}-poly(GGAP). To date the series of tests—the Ames mutagenicity test, cytotoxicity-agarose overlay, systemic toxicity, Kligman sensitization and hemolysis—also underscore good biocompatibility. Further information is available from peritoneal implants in the rat where numerous additional compositions of the Formulae [1] and [2] class of bioelastic materials all appeared to be biocompatible with X = Phe(F), Ala(A), Glu(E), and Ile(I).

Cell Attachment to Bioelastic Matrices

The bioelastic matrices—X^{20}-poly(GVGVP), X^{20}-poly(GGIP), X^{20}-poly(GGVP) and X^{20}-poly(GGAP)—do not result in cell adhesion by fibroblasts and vascular endothelial cells in appropriate cell culture media. When 10% fetal bovine serum is used in place of 0.1% bovine serum albumin, cell adhesion is observed with bovine ligamentum nuchae fibroblasts adhering better than human umbilical vein endothelial cells and with the order of decreasing cell adhesion being X^{20}-poly(GGIP) > X^{20}-poly(GGVP) > X^{20}-poly(GVGVP) but with no cell adhesion even in the presence of serum for X^{20}-poly(GGAP)[18].

On introduction of the GRGDSP cell attachment sequence[19], as in X^{20}-poly[40(GVGVP),(GRGDSP)], the bioelastic matrix presents a surface on which cells will attach and spread and grow to confluence[9]. The cells include bovine ligamentum nuchae fibroblasts, bovine aortic endothelial cells, human umbilical vein endothelial cells, and a human A375 malignant melanoma cell line[9,18,20].

Interestingly, the GRGDSP sequence as presented at the surface of this bioelastic matrix has been shown to be an attachment site for the vitronectin cell membrane receptor[20] rather than the fibronectin cell membrane receptor as might have been expected, as GRGDSP is the sequence in fibronectin that binds to the fibronectin cell membrane receptor[19]. Since blood platelets contain the fibronectin cell membrane receptor, this surface has the advantage of being very favorable for vascular endothelial cell attachment without favoring unwanted blood platelet adhesion and activation.

Another advantage of the bioelastic matrix designed for cell attachment arises because of its inherent elasticity and the capacity to vary the stiffness (the elastic modulus) of the matrix over a wide range of values from 10^5 dynes/cm^2 to 10^9 dynes/cm^2 ranging from a gelatin-like substance to a plastic-like material. Importantly, cells attached to a bioelastic matrix, as to the natural extracellular matrix, could sense deformations to which the matrix may be subjected in its role as a prosthesis, i.e., as a tissue substitute or replacement. Cells capable of sensing the tensional forces to which a tissue or a prosthesis is subjected function as mechanochemical transducers with the release of intracellular chemical signals that turn on genes for producing protein necessary for maintaining or reconstructing the extracellular matrix[21-23]. In this way a biodegradable bioelastic matrix could act as a temporary functional scaffolding which would have the potential to be remodeled into a natural tissue.

PREVENTION OF ADHESIONS APPLICATIONS

More than 30 million surgical procedures are performed annually in the U. S. with an equivalent number in Europe. In most of these adhesions, the formation of unwanted fibrous scar tissue binding tissues and organs together that should otherwise be separated, are a significant, and too often a severe, complication. An interesting example of a growing subset of these surgical procedures are the more than 400,000 open heart surgeries performed annually in the U. S. which require cardiopulmonary bypass (CPB) with the attending CPB-induced swelling of the heart which in turn commonly necessitates leaving open the pericardial sac which normally surrounds the heart. The result can be adhesion of

heart to the sternum, as well as other adhesions, with great danger of lacerating the heart on repeat sternotomy. A substantial number, approaching 20% at some centers, of the open heart procedures are reoperations with far greater risk due to the adhesions. In the abdominal cavity, post-operative and trauma-induced adhesions cause great discomfort and even intestinal blockage requiring reoperation with again increased risk in part due to adhesions obscuring the usual anatomical landmarks which guide the surgeon.

A Contaminated Peritoneal Model in the Rat[25]

Bioelastic materials have been tested in an abdominal cavity model where, as depicted in Figure 3A, the abdominal wall is scraped with a scalpel until bleeding; a loop of intestine is repeatedly punctured with a hypodermic needle until bleeding and bowel contents can be extruded; and the injured contaminated intestine is held in apposition to the injured wall by a loose loop of suture accessible without reopening the cavity. At seven days the suture loop is removed and at two weeks the abdominal cavity is reopened and examined. This results in the intestine being bound to the wall by adhesions in 100% of the cases (29 animals) with adhesions being significant in 90% of the animals[25]. Seen in Figures 4A and B for these control animals and identified by the arrows are adhesions binding loop of bowel to abdominal wall.

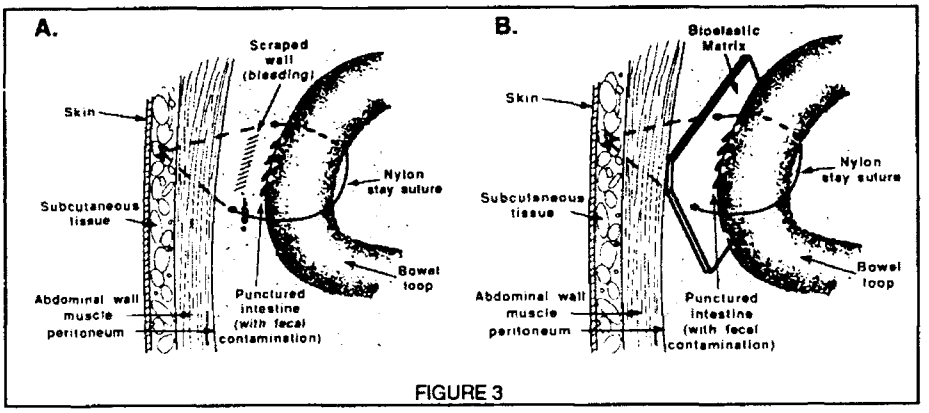

FIGURE 3

When the gas sterilized bioelastic sheet is interposed between injured wall and injured intestine as schematically shown in Figure 3B and photographed in Figure 4C, significant adhesions were prevented in 80% of 29 animals[25]. What is not apparent in the black and white print of Figure 4C is the presence of blood. In Figure 4D is the re-opened abdominal cavity showing the scarred region of the abdominal wall and the absence of any adhesions. Thus, even with the presence of blood and with frank contamination, this bioelastic matrix, X^{20}-poly(GVGVP), provided in this model an effective barrier to adhesion formation.

An instructive example is seen in Figure 4E where the vertical arrows indicate the bioelastic matrix and the horizontal arrow identifies a small loop of adhesion that has grown around the sheet of X^{20}-poly(GVGVP). The matrix is seen to have remained transparent; no fibrous coating had encapsulated the matrix in the two-week period; in fact, the matrix remains uncoated and transparent for months, seemingly ignored by the host. Through the transparent matrix it is seen that there is no sign of inflammation of the abdominal wall against which the matrix has been in contact for two weeks. Seen in Figure 4F are two bands of adhesion having grown through a break in the matrix indicated by the arrow. This occurred approximately 10% of the time, such that if this were overcome, the matrix might be expected to prevent significant adhesions some 90% of the time in this model. While other barrier materials that have been proposed for the prevention of adhesions have not

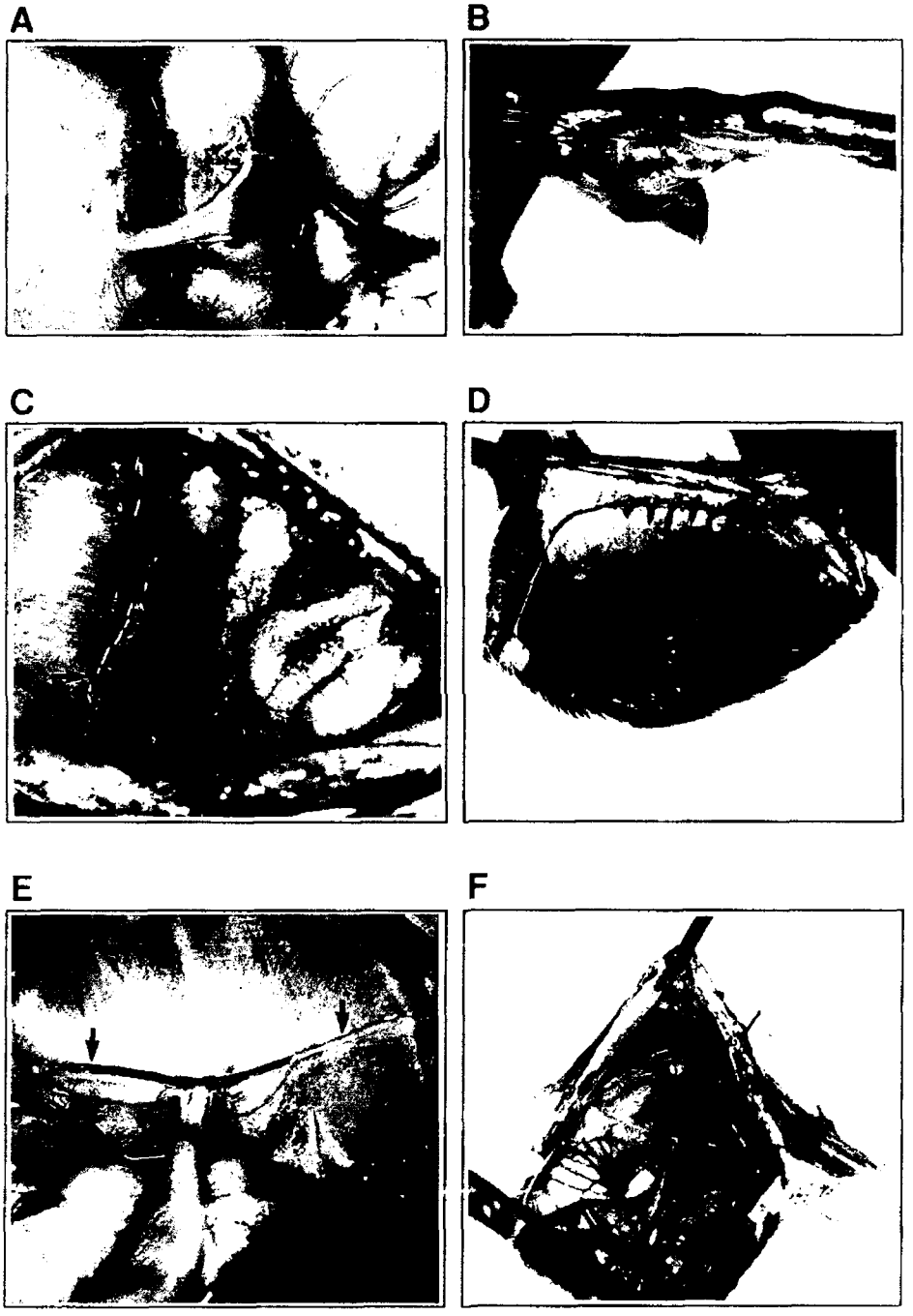

FIGURE 4

been compared in this model, this degree of efficacy has yet to be demonstrated by other materials or therapies.

These favorable findings for the X^{20}-poly(GVGVP) composition of bioelastic matrix may be obtainable by additional compositions. While there are as yet an inadequate number of animals tested for the other compositions, two were particularly promising. With four animals tested for each composition, X^{20}-poly(GGIP) was effective 100% of the time, and X^{20}-poly(GVGIP) was effective 75% of the time. Also appearing effective were X^{20}-poly[0.45(GVGVP),0.55(GAGVP)] and X^{20}-poly[0.75(GVGVP),0.25(GFGVP)]. Less effective was X^{20}-poly[0.67(GGVP),0.33(GGFP)]; with 6 animals this material was effective 50% of the time, but with the other three animals the matrix was entirely encapsulated. Exhibiting the poorest performance, but still appearing to be biocompatible, was X^{20}-poly(AVGVP) where with but three animals the material was effective 33% of the time. These additional compositions provide the opportunity for a range of physical properties; for example, they encompass the full range of elastic moduli noted above.

The serous membrane lining which covers the abdominal wall is called the parietal peritoneum, and that continuous part that is reflected over the internal organs is the visceral peritoneum. In the contaminated peritoneal model in the rat utilized above, both parietal and visceral peritoneal surfaces are injured and contaminated, and the injured sites are held in juxtaposition. This is a severe challenge to the fundamental problem of achieving repair of the serous membrane by regeneration of the mesothelial cell lining without resulting in the fibrotic response giving rise to adhesions.

Many adjunctive chemical therapies have been attempted for promoting mesothelial regeneration while limiting fibrosis resulting from surgical procedures. These include[25] heparin[26], corticosteroids[27], antihistamines[28], non-steroidal anti-inflammatory drugs[29], fibrinolytics[30], sodium carboxy methyl cellulose[31], chondroitin sulfate[32], proteolytics[33] and dextran[34,35]. Quoting from Jansen[36] in his review of "The First International Symposium for the Treatment of Post-Surgical Adhesions" held in Phoenix, Arizona September 1989, "Adjunctive therapy to promote mesothelial healing over fibrosis and formation of adhesions has a tenuous basis in the clinical practice of preventing adhesions[37-39]. Corticosteroids, antihistamines, antiprostaglandins and anticoagulants have all been used to aid healing, but properly controlled clinical studies are few and the evidence is against their use around the time of operation making a material difference to the eventual outcome."

The use of bioelastic matrices for the prevention of adhesions involves the physical barrier approach. There are many materials that have been considered as physical barriers principally as pericardial substitutes as considered further below. As recently reviewed by Gabbay[40], "These have included silicone membranes[41], polyurethane[42], fascia lata[43,44], polytetrafluoroethylene (Gore-Tex) patches[45,46], bovine and porcine pericardium xenografts (PXs) treated with glutaraldehyde[47-50], siliconized Dacron[51,52] and dura mater[53]".

Soules, et al.[54], in a comparison of the available physical barrier materials for the prevention of adhesions in the pelvic cavity, tested Gelfilm, Surgicel, Silastic, Gelfoam paste, amnion, peritoneum and omentum and concluded "The data suggest that the barrier methods actually promote the formation of adhesions...". By further designing Surgicel, specifically as a material for the prevention of adhesions, the resulting oxidized, regenerated cellulose, called Interceed (TC7), was tested in the rabbit uterine horn model[55]. Those results led to a multicenter clinical study where good surgical technique was the control with a 28% absence of adhesions and where use of Interceed and good surgical technique was the test with a 54% absence of adhesions[56]. In the Japanese multicenter clinical study for infertility and endometriosis surgery, adhesions were reduced from 76% in the controls to 41% when Interceed was used[57].

Interceed has now been approved for use in the pelvic region by the U. S. Food and Drug Administration. Even in this favorable, approved, limited anatomical use, 41% to 46% of the cases resulted in adhesion formation. In addition, Interceed is considered to promote adhesion when saturated with blood[36] and it is contra-indicated when there is

frank infection. Thus, the need for a material or therapy to prevent adhesions remains critical to improve the outcome of surgeries in general, to prevent the chronic pain and discomfort that follow abdominal surgery, to decrease the incidence of bowel obstruction following abdominal surgery, to decrease the incidence of infertility in women due to surgical procedures in the pelvic region, and to decrease risk and improve the outcome of reoperations.

Strabismus Surgery Model in the Rabbit Eye[58]

Strabismus is a disorder of the rectus muscles of the eye which prevents both eyes from simultaneously focusing on the same point, as in crossed eyes. Corrective surgery attempts to alleviate this disorder by detachment of one of the four rectus muscles that orient the eye and reattachment in order to bring the eyes into better alignment. The complication is that the repositioned muscle can adhere (become reattached due to scarring), for example, to the old insertion site, thereby defeating attempts to achieve accurate alignment.

A number of materials—silicone[59]; a polyglactin 910 mesh[60], Supramid Extra®—have been used in the form of tubes or sleeves to improve the outcome of this surgical procedure[61,62], but these efforts have now been largely discontinued. It becomes of interest therefore to determine the possible effectiveness of bioelastic materials.

In the rabbit eye model following a modification of Sondhi's method[60], the superior rectus muscle is detached at its insertion site on the sclera; a patch of sclera 3 mm x 3 mm is removed underlying the muscle; the muscle capsule overlying the scleral injury is removed, and the muscle is reattached at its original site. At one week the muscle is tightly adherent to the scleral injury site and at eight weeks histological examination demonstrated a dense fibrovascular scar. For the test animals two compositions of bioelastic materials were used, X^{20}-poly(GVGVP) with three animals and X^{20}-poly[0.75(GVGVP),0.25(GFGVP)] with two animals. Both compositions were well tolerated by the eye with no inflammation evident after the mild inflammation of the procedure subsided within a few days. In both cases adhesion of the muscle to the overlying conjunctiva and the muscle to the sclera did not occur. A glistening fibrous capsule formed around X^{20}-poly[0.75(GVGVP),0.25(GFGVP)] within two weeks whereas no capsule formed around X^{20}-poly(GVGVP) in a two-month period. Both materials ultimately extruded through the conjunctiva of the small rabbit eye. The latter material holds promise for use in strabismus surgery, particularly if the matrix can be designed to degrade within a period of a month or two in order to prevent limiting of eye movement, and possible extrusion.

Total Artificial Heart Model in the Calf (Toward an Artificial Pericardium)

Use with the Total Artificial Heart: The properties of the bioelastic materials considered in the peritoneal model appear to be appropriate for use with the total artificial heart (TAH) as a bridge to heart transplantation. When the TAH is emplaced even for a short time, adhesions form to the surface of the device. Removal of the TAH prior to placement of the donor heart requires dissection of the adhesions which presents a compromised site for the donor heart. Work is presently underway to make sheets of X^{20}-poly(GVGVP) of appropriate size which are to be utilized by the University of Utah group under the direction of D. B. Olsen in the calf model. The periods of placement are to vary from one to six months.

Toward an Artificial Pericardium: In the more than 400,000 open heart surgeries performed per year in the U. S. , the chest is opened by splitting the sternum; the pericardial sac in which the heart resides is opened and cardiopulmonary bypass (CPB) is instituted. When the procedure, which may be the emplacement of coronary artery bypass

grafts (CABG), valve replacement or correction of congenital defects, is completed, the issue of closure is addressed. It is preferred if the pericardium can be closed, but it is often necessary to leave the pericardial sac open for several reasons[45,50,63,64]. During cardiopulmonary bypass the heart can become distended and the compression due to closure can lower the performance of the heart; compression due to closure can also compress, distort or kink the aorta-coronary bypass grafts compromising their function; the pericardium can be left open to permit drainage, and shrinkage of the pericardium may have occurred following a previous operation.

There are many conditions necessitating reoperation[50,65]: "intimal hyperplasia of saphenous vein bypass grafts, graft atherosclerosis, progression of underlying coronary artery disease[65]", prosthetic valve failure, perivalvular leakage, infection on prosthetic valves and conduits, progression of coronary artery disease necessitating repeat CABG, and congenital heart disease requiring a definitive operation following a palliative surgical procedure[50]

The increased risks on reoperation are many. Perhaps most striking are the danger of rupturing the heart as the sternum is reopened due to severe adhesions between heart and sternum resulting from having left the pericardial sac open and the danger of severing an aorta-coronary graft buried within an adhesion[66]. There is increased reoperation time, excessive bleeding due to dissection of adhesions, and degeneration of pericardial substitutes that may have been tried and adhesion of the pericardial substitute to the heart[60].

Gabbay[40] has listed desirable properties for a pericardial substitute as "(1) nonadherence to the heart and easy separability upon reoperation; (2) nonadherance to the sternum upon reoperation, so that repeat sternotomy is technically no different from the original procedure; (3) capability of mechanical attributes, and maintenance of the barrier integrity of the native pericardial sac; (4) freedom from dimensional distortion or shrinkage upon prolonged implantation; (5) convenience and technical ease of handling; (6) immunologic inertia, so as not to provoke inflammatory host response; and (7) capability of acquiring fibronolytic activity similar to nature pericardial tissue".

The consideration of bioelastic materials as a pericardial substitute presents a challenge to which these new materials are well-suited. While it would be possible to discuss bioelastic matrices in terms of each of the desired properties noted above, only three aspects will be briefly noted. One is the capacity to design bioelastic matrices to have an elastic modulus in the range exhibited by the pericardial sac; the second is the demonstrated capacity in the peritoneal and eye models noted above not to adhere to tissues undergoing repair; and the third is the capacity to introduce cell attachment sequences and to provide a matrix on which those cells can function. Thus, identification and incorporation of cell attachment sequences for the mesothelial cells that line the pericardium and for the underlying mesenchymal cells could provide for a pericardial substitute that could be remodeled to form a functional pericardium with, among other properties, a fibrinolytic activity.

ACKNOWLEDGMENT

This work was supported in part by Contract Nos. N00014-89-C-0282 and N00014-90-C-0265 from the Department of the Navy, Office of Naval Research, Naval Medical Research and Development Command; Grant No. R43-HL-47955 from the National Institutes of Health; and Office of Naval Research Contract No. N00014-89-J-1970.

REFERENCES

1. L. B. Sandberg, J. G. Leslie, C. T. Leach, V. L. Torres, A. R. Smith and D. W. Smith, Pathol. Biol. **33**, 266-274 (1985).
2. H. Yeh, N. Ornstein-Goldstein, Z. Indik, P. Sheppard, N. Anderson, J. C. Rosenbloom, G. Cicila, K. Yoon and J. Rosenbloom, Collagen and Related Res. **7**, 235-247 (1987).
3. L. B. Sandberg, N. T. Soskel and J. B. Leslie, N. Engl. J. Med **304**, 566-579 (1981).
4. D. W. Urry, M. M. Long, R. D. Harris and K. U. Prasad, Biopolymers **25**, 1939-1953 (1986).

5. D. W. Urry, R D. Harris, M. M. Long and K. U. Prasad, Int. J. Pept. Protein Res. **28**, 649-660 (1986).
6. D. W. Urry, in Mol. Conformation and Biol. Interactions, edited by P. Balaram and S. Ramaseshan (Indian Acad. of Sci., Bangalore, India, 1991) pp. 555-583.
7. D. W. Urry, D. C. Gowda, T. M. Parker, C-H. Luan, M. C. Reid, C. M. Harris, A. Pattanaik and R. D. Harris, Biopolymers **32**, 1243-1250 (1992).
8. A. Pattanaik, D. C. Gowda and D. W. Urry, Biochem. Biophys. Res. Comm. **178**, 539-545 (1991).
9. A. Nicol, D. C. Gowda and D. W. Urry, J. Biomed. Mater. Res. **26**, 393-413 (1992).
10. D. W. Urry, D. C. Gowda, C. Harris, R. D. Harris and B. A. Cox, Polym. Preprints, Div. Polym. Chem., Am. Chem. Soc. **33** (2) 84-85 (1992).
11. D. T. McPherson, C. Morrow, D. S. Minehan, J. Wu, E. Hunter and D. W. Urry, Biotechnol. Prog. **8**, 347-352 (1992).
12. D. W. Urry and K. U. Prasad, in Biocompatibility of Tissue Analogues, edited by D. F. Williams (CRC Press, Inc., Boca Raton, Florida, 1985), pp. 89-116.
13. D. W. Urry, T. L. Trapane, R. B. McMichens, M. Iqbal, R. D. Harris and K. U. Prasad, Biopolymers **25**, S209-S228 (1986).
14. D. W. Urry, T. L. Trapane, M. Iqbal, C. M. Venkatachalam and K. U. Prasad, Biochemistry **24**, 5182-5189 (1985).
15. D. W. Urry, Prog. Biophys. molec. Biol. **57**, 23-57 (1992).
16. D. W. Urry, Angew. Chem. Int. Ed. Engl. (1993) (in press).
17. D. W. Urry, T. M. Parker, M. C. Reid and D. C. Gowda, J. Bioactive Compatible Polym. **6**, 263-282 (1991).
18. A. Nicol, D. C. Gowda, T. M. Parker and D. W. Urry (1992) (submitted).
19. E. Ruoslahti, M. D. Pierschbacher, Science **238**, 491-497 (1987).
20. A. Nicol, D. C. Gowda, T. M. Parker and D. W. Urry, in Biotechnol. Bioactive Polym., edited by C. G. Gebelein and C. E. Carraher (Plenum Press, New York, 1993) (in press).
21. D. Ingber, Current Opinion in Cell Biology **3**, 841-848 (1991).
22. B. van der Lei, C. R. H. Wildevuur, P. Nieuwenhuis, E. H. Blaauw, F. Dijk, C. E. Hulstaert and I. Molenaar, Cell Tissue Res. **242**, 569-578 (1985).
23. D. Y. M. Leung, S. Glagov and M. B. Mathews, Science **191**, 475-477 (1976).
24. D. Y. M. Leung, S. Glagov and M. B. Mathews, Exp. Cell Res **109**, 285-298 (1977).
25. L. D. Hoban, M. Pierce, J. Quance, I. Hayward, A. McKee, D. C. Gowda, D. W. Urry and T. Williams, J. Surgical Res (1993) (in press).
26. M. M. Davidson, Arch. Surg. **59**, 300 (1979).
27. R. L. Replogle, R. Johnson and R. E. Gross, Ann. Surg. **163**, 580 (1966).
28. H. W. Horne, M. Clyman, C. Debrovner, G. Griggs, R. Kistner, T. Kosasa, C. Stevenson and M. Taymor, Int. J. Fertil. **18**, 109 (1973).
29. G. diZerega and G. Hodgen, Am. J. Obstet. Gynecol. **136**, 173 (1980).
30. J. L. Koltai and A. Gerhard, Prog. Ped. Surg. **25**, 71 (1990).
31. T. E. Elkins, R. J. Bury, J. L. Ritter, F. W. Ling, R. A. Ahokas, C. A. Homsey and L. R. Malinak, Fertility and Sterility. **41**, 926 (1984).
32. G. Oelsner, R. A. Graebe, S-B. Pan, F. P. Haseltine, E. R. Barnea, H. Fakih, and A. H. DeCherney, J. Repro. Med. **32**, 812 (1987).
33. D. C. O. James, H. Ellis and T. B. Hugh, J. Pathol. Bact. **90**, 279 (1965).
34. M. J. N. Weinans, F. M. Kauer, I. J. Klompmaker and J. Weijma Fertil. Steril. **53**, 159-160 (1990).
35. M. R. Soules, L. Dennis, A. Bosarge and D. E. Moore, Amer. J. Obstet. Gynecol. **143**, 829 (1982).
36. R. Jansen, Med. J. Australia **152**, 305-306 (1989).
37. W. H. Pfeffer, Fertil. Steril. **33**, 245-256 (1980).
38. R. P. S. Jansen, Am. J. Obstet. Gynecol. **153**, 363-371 (1985).
39. R. P. S. Jansen, Surg. Gynecol. Obstet. **166**, 154-160 (1988).
40. S. Gabbay, Trans. Am. Soc. Artif. Intern. Organs **36**, 789-791 (1990).
41. H. Laks, G. Hammond, A. S. Geha, J. Thorac. Cardiovasc. Surg. **82**, 88-92 (1981).
42. C. A. Mester, J. V. Comas, S. Ninot et al., Thai. J. Surg **17**, 125-128 (1986).
43. F. H. Kohanna, P. X. Adams, J. N. Cunningham, Jr. and F. C. Spencer, J. Thorac Cardiovasc. Surg. **74**, 14-19 (1977).
44. K. Yu-Chin, Chin. Med. J. **78**, 210-213 (1959).

45. J. M. Revuelta, P. Gracia-Rinaldi, F. Val., R. Crego and C. M. G. Duran, J. Thorac. Cardiovasc. Surg. **89**, 451-455 (1985).
46. C. Minale, G. Hollweg, S. Nikol, Ch. Mittermayer and B. J. Messmer, J. Thorac. Cardiovasc. Surg. **35**, 312-315 (1987).
47. J. I. Gallo, J. L. Pomar, E. Artinano, F. Val and C. M. G. Duran, Ann. Thorac. Surg. **26**, 149-154 (1978).
48. I. Gallo, E. Artinano and C. G. Duran, J. Thorac. Cardiovasc. Surg. **89**, 709-712 (1985).
49. R. H. Dietzman, A. R. Hotler, M. F. Lynch et al., Contemp. Surg. **24**, 35-39 (1984).
50. V. S. Vakirevich, S. A. Abdulali, C. R. Abbott and M. I. Ionescu, Tex. Heart Inst. **11**, 238-242 (1984).
51. C. R. Youmans, J. White and J. R. Derrick, J. Thorac. Cardiovasc. Surg **55**, 383-388 (1968).
52. M. K. Mazuji and J. C. Lett, Arch. Surg. **87**, 104-107 (1963).
53. R. C. Bonnabeau, Jr., A. W. Armanious and T. J. Tarnay, J. Thorac. Cardiovasc. Surg. **66**, 196-201 (1973).
54. M. R. Soules, L. Dennis, A. Bosarge and D. F. Moore, Am. J. Obstet. Gynecol. **143**, 829-834 (1982).
55. C. B. Linsky, M. P. Diamond, T. Cunningham, B. Constantine, A. H. DeCherney and G. S. di Zerega, J. Reproductive Medicine **32**, 17-20 (1987).
56. S. M. Cohen, R. R. Franklin, A. F. Haney, L. R. Molinak, G. W. Patton, J. A. Rock, S. M. Rosenberg, B. W. Webster and A. A. Yuzpe, Fertil. Seril. **51**, 933-938 (1989).
57. K. Sekiba, T. Fukaya, T. Ono, H. Mizunuma, H. Osada, N. Mitsuhashi, K. Sugimura, H. Awaji, T. Sawada, Y. Noda, K. Miyazaki and F. Saji, Obstet. Gynecol. **79**, 518-522 (1992).
58. F. J. Elsas, D. C. Gowda and D. W. Urry, J. Ped. Ophtha. and Strab. **29**, 284-286 (1992).
59. A. G. Morales, F. M. Polack, A. F. Arata, Br. J. Ophthalmol. **50**, 235-244 (1966).
60. N. Sondhi., F. D. Ellis, L. M. Hamed, E. M. Helveston, Ophthalmic Surg. **18**, 441-443 (1987).
61. E. A. Dunlap, Trans. Am. Ophthalmol. Soc. **65**, 393-410 (1967).
62. E. A. Dunlap, Br. J. Ophthalmol. **58**, 307-312 (1974).
63. J. N. Cunningham, F. C. Spencer, R. Zeff, C. D. Williams, R. Cukingnan and M. Mullin, J. Thorac. Cardiovasc. Surg. **70**, 119-125 (1975).
64. S. Gabbay, A. M. Guindy, J. F. Andrews, J. J. Amoto, P. Seaver and M. Y. Khan, Ann. Thorac. Surg. **48**, 803-812 (1989).
65. R. M Ungerleider, N. L. Mills and A. S. Wechsler, Ann. Thorac. Surg. **40**, 11-15 (1985).
66. R. DePaulis, J. B. Riebman, P. Deleuze, F. S. Mohammed, G. L. Burns, M. Morea and D. B. Olsen, J. Cardiovasc. Surg. **31**, 202-208 (1990).
67. W. H. Heydorn, J. S. Daniel and C. E. Wade, J. Thorac. Cardiovasc. Surg. **94**, 291-296 (1987).

THE PHYSICAL PROPERTIES OF A HYALURONIC ACID BASED BIORESORBABLE MEMBRANE FOR THE PREVENTION OF POST-SURGICAL ADHESIONS

K. Greenawalt, L. Masi, C. Muir, and J. Burns
Biopolymers Department, Genzyme Corporation, Cambridge, MA 02139

ABSTRACT

We have evaluated the physical properties and animal efficacy of a hyaluronic acid (HA) based bioresorbable membrane for the prevention of post-surgical adhesions. Test methods were developed to measure the dry and wet tensile properties and in vitro tissue adhesiveness of the membranes. The thin membranes were found to have sufficient strength and flexibility in the dry state for surgical handling. When hydrated in buffered saline, the membranes became weaker and more elastic. The membranes exhibited a high degree of tissue adhesiveness and significantly reduced adhesion formation in a rat cecal abrasion model.

INTRODUCTION

Surgical adhesions are unnatural joinings of normally separate tissue surfaces which may form as a consequence of the normal wound healing response to injury. Adhesions can result in bowel obstruction and pain following abdominal surgery, limited range of motion following orthopedic surgery, and infertility following gynecological surgery. Various methods, including pharmacological agents, solutions, and physical barriers, have been evaluated for adhesion prevention with limited success. The barrier materials that are currently available have definite limitations. For example, the only FDA approved product for adhesion prevention is the Interceed™-TC7 barrier composed of oxidized regenerated cellulose. However this product is contraindicated in the presence of blood [1]. The GORE-TEX® Surgical Membrane barrier, made from expanded Teflon®, is currently under investigation in human gynecologic surgery but must be sutured in place and removed at a second operation [2].

We have developed a bioresorbable membrane for the prevention of post-surgical adhesions based on sodium hyaluronate, the sodium salt of hyaluronic acid (HA). HA is a naturally occurring biopolymer found in the synovial fluid, vitreous humor, and extracellular matrix of humans. It is a polyanionic polysaccharide with glucuronic acid and N-acetylglucosamine repeating units (Structure 1) that can be modified to reduce its solubility and degradation rate in physiological environments and thereby enhance its utility as a biomaterial. Our studies in animal models have shown significant reduction of adhesion formation with the use of HA based bioresorbable membranes [3,4]. The membranes reduce adhesion formation by providing a protective barrier at the specific sites of tissue injury that occur during surgery.

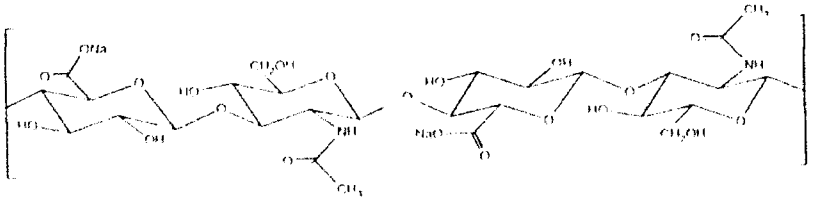

Structure 1. Sodium Hyaluronate

Mat. Res. Soc. Symp. Proc. Vol. 292. © 1993 Materials Research Society

The physical properties of an adhesion barrier are critical to the product's performance. The barrier must have sufficient strength and flexibility to provide the surgeon with good handling properties in both a dry and wet environment and it must be readily resorbed during the normal wound healing process. The barrier must also possess a certain degree of tissue adhesiveness to prevent product migration after placement on the injured site, but must not adhere to surgical instruments and gloves. Finally, the barrier must be able to withstand terminal sterilization.

The goals of this study were to: (1) develop methods to analyze the dry and wet tensile properties and tissue adhesiveness of HA based bioresorbable membranes in order to assess their suitability for in vivo studies; (2) determine the effects of gamma irradiation on the mechanical properties of the membranes; and (3) confirm effective adhesion reduction with the membranes in an animal model.

MATERIALS AND METHODS

The bioresorbable membranes were manufactured from modified HA based formulations made by a proprietary method [5]. An Instron Universal Testing System Model 4201 was used for all of the tensile and tissue adhesiveness tests. The membranes were gamma irradiated at six doses, including nonirradiated controls.

Dry Tensile Tests

The dry tensile properties of the membranes were determined according to ASTM Standard Test Method D882. Test samples were cut into strips 1 cm wide and the cross-sectional area of each sample was measured. The test specimens were placed in air-actuated, flat-faced grips with an initial separation of 25 mm. A constant crosshead speed of 2 mm/min was used to determine the ultimate tensile strength, elastic modulus, and percent elongation at break.

Wet Tensile Tests

Samples were prepared as above. A test chamber was specifically designed for measuring the mechanical properties of the membranes in a physiological environment. In this testing system, the entire sample was immersed in a phosphate buffered saline solution (pH 7.2) at room temperature during mechanical testing. The initial grip separation was 25 mm and the crosshead speed was 5 mm/min. The test was performed immediately after immersing the membrane in saline. The ultimate tensile strength, elastic modulus, and percent elongation at break were determined.

Tissue Adhesion Tests

A method for measuring the tissue adhesiveness of membranes in vitro was modified from the literature [6]. The energy required to break the bond between the membrane and biological tissue (skinless chicken breast) was measured and related to the energy required to break the bond between a Teflon® reference membrane and tissue. A schematic diagram of the test apparatus is shown in Figure 1. The membrane was brought in contact with moist tissue under a constant compressive load for 30 seconds. Then the membrane was pulled off the tissue at a speed of 1 mm/min and the energy was recorded. A stainless steel substrate was used to simulate the adhesiveness of the membranes to surgical instruments.

Animal Efficacy Study

Eighty female Sprague-Dawley rats (225-250 gm) were anesthetized with an intramuscular injection of ketamine and xylazine. A midline incision was made and the cecum was isolated and abraded by a previously described method [4]. Animals were randomized to test (membrane) or control (no membrane) groups after abrasion. For animals in the test group, a 2 in. x 2 in. piece of sterile HA based bioresorbable membrane

was wrapped completely around the cecum. The incision was closed and the animals were allowed to recover. Seven days after surgery, the animals were sacrificed and graded for the number and severity of cecal adhesions by a blinded evaluator. The severity of adhesions was scored on a scale of 0 to 4 with a grade of 2 or higher considered clinically significant.

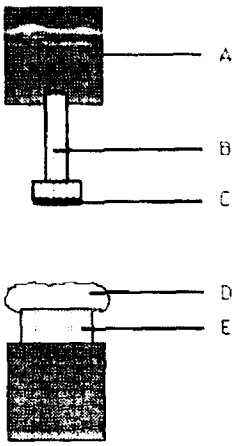

Figure 1. Tissue Adhesiveness Test Apparatus
A: Instron test system; B: Membrane sample holder;
C: Test membrane; D: Tissue substrate; E: Substrate holder

RESULTS

Mechanical Tests

The dry HA based bioresorbable membranes were very strong and stiff. The mean dry nominal tensile strength of the membranes was 72 MPa, the mean elastic modulus was 4.5 GPa, and the mean elongation at break was 2.6% (Table I). When immersed in saline, the membranes became weaker and more elastic. The mean wet nominal tensile strength was 1.5 MPa, the mean elastic modulus was 3.3 MPa, and the mean elongation at break was 63%. We believe the change in properties is due to the rapid hydration of the membrane, which occurs within 30 seconds, and the inherent hydrophilic property of HA based materials.

There was no change in the dry properties of the membranes with gamma irradiation dosage as compared to non-irradiated controls. However, gamma irradiation reduced the wet strength of the HA based membranes (Figure 2). The membranes lost 50% of their initial wet strength after irradiation at 1.6 Mrad and 76% at 2.5 Mrad.

Table I. Dry and Wet Tensile Properties of
HAL-F™ Bioresorbable Membrane

	Tensile Strength(MPa)	Elongation at Break (%)	Elastic Modulus(MPa)
DRY	71.7 ± 6.9	2.6 ± 0.4	4,490 ± 400
WET	1.5 ± 0.3	63.2 ± 2.0	3.3 ± 0.6

Values expressed as the mean ± standard error of the mean
n=6 for dry tests; n=4 for wet tests

Tissue Adhesiveness Tests

During preliminary test method development, in vivo tissue adherence of the membranes correlated well with the in vitro test results. A subsequent study showed that HA based bioresorbable membranes had similar or greater tissue adherence properties when compared to Interceed (TC-7)™ and Teflon® (Figure 3).

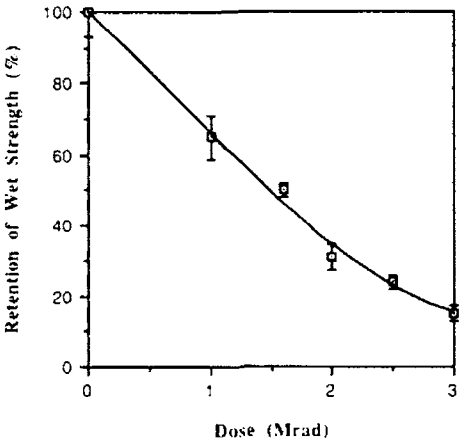

Figure 2. Effect of Gamma Irradiation on Retention of Wet Strength of HA Based Membrane

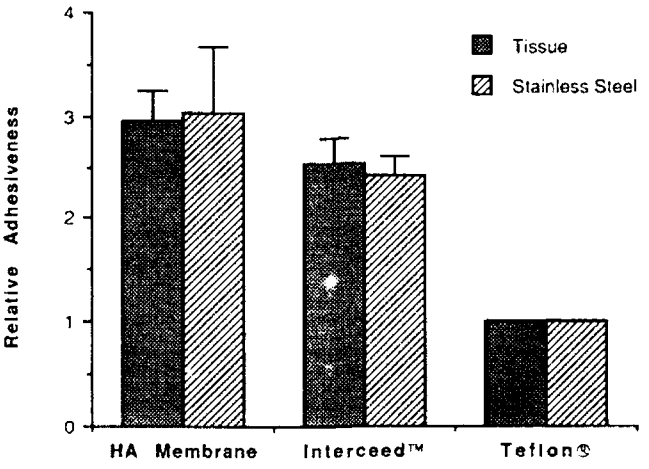

Figure 3. Relative Adhesiveness of HA Based Membrane and Interceed (TC7)™ to Teflon®

Relative Adhesiveness is the square root of the energy to break for the sample divided by the energy to break for Teflon® reference. Values expressed as the mean ± standard error of the mean (n=6)

Animal Efficacy Study

Grade 2 or higher adhesions were found in 20% (8/40) of the animals in the HA based membrane group compared to 92% (36/39) in the control group. This represents a 78% reduction of significant adhesions with HA based membrane treatment. Additionally, the mean incidence of all cecal adhesions was significantly lower in the HA based membrane group (0.2 ± 0.1) when compared to the control group (1.9 ± 0.4).

SUMMARY

We have developed test methods to evaluate the physical properties of HA based bioresorbable membranes for adhesion prevention. Results from these tests have aided in the selection of materials for manufacturing development and animal efficacy studies. The membranes had sufficient tensile strength in the dry state for surgical handling and placement. Upon hydration, the strength of the membranes decreased due to the rapid hydration of the HA based material. The membranes were able to be gamma irradiated at low doses and possessed a high degree of tissue adhesiveness to prevent product migration after surgery. The wet strength of the membranes, even after gamma irradiation, was sufficient to ensure the membranes remained intact to act effectively as an adhesion barrier.

REFERENCES

1. Linsky, C.B. et al., Infert. **11**, 273 (1988).
2. Boyers, S.P. et al., Fertil. Steril. **49**, 1066 (1988).
3. Burns, J.W., et al., Trans. Soc. Biomat., 17th Annual Meeting of the Society for Biomaterials 1991, 251.
4. Skinner, K., et al., J. Invest. Surg., 7th Annual Meeting of Academy of Surgical Research 1991, 381.
5. Burns, J.W., et al., U.S. Patent No. 5,017,229.
6. Robert C., et al., Acta. Pharm. Technol., **34**(2), 95 (1988).

HYDROXYAPATITE/Al_2O_3 COMPOSITE BIOMATERIAL IMPLANT

ZENG SHAOXIAN, YANG ZHIXIONG, LING PING, XU GUANGHONG, AND CAO WANPENG
Shanghai Institute of Ceramics, Academia Sinica, 1295 Dingxi Road, Shanghai 200050, People's Republic of China

ABSTRACT

A new type of composite biomaterial was developed and is described in this paper. The composite is based on a high strength Al_2O_3 ceramic substrate, sintered with a layer of hydroxyapatite. The layer was examined by x-ray diffraction and infrared spectroscopy. Animal experiment showed that the composite has good biocompatibility, and can form tight osteo-integration with bone in 12 weeks. It is a bioactive material with a high strength.

INTRODUCTION

Alumina was the first bioceramic to achieve wide clinical applications [1]. It has high wear resistance, high strength, good biocompatibility and very stable chemical properties in the physiological environment. Alumina is an example of a nearly inert bioceramic which forms no chemical or biological bond at the material-tissue interface, but instead leads to the formation of a nonadherent fibrous capsule. There is relative movement at the interface, which eventually leads to interfacial deterioration.

Hydroxyapatite (HA) has the same structure as the inorganic substance of human hard tissues. It is a bioactive material that elicits a direct chemical response at the interface and forms a very tight bond to the tissue. However, its poor sintering properties, low strength and limited fatigue resistance restrict its applications [2]. The present investigation developed a new type of biomaterial, that combines the virtues of alumina and HA.

EXPERIMENTAL PROCEDURE

Materials

Alumina powder with an average grain size of < 0.1 μm and > 99.99% purity was mixed with a small amount of magnesia (0.x%), then shaped in the form of φ4mm screws, and sintered in air or H_2 at 1600-1700 °C for 2-5 hr to obtain the Al_2O_3 substrates.

A solution of $Ca(NO_3)_2$ and a solution of $(NH_4)_2HPO_4$ were brought to pH 11 to 12 with concentrated NH_4OH, then the ammonium hydrogen phosphate solution was added dropwise into stirred calcium nitrate solution at a proper speed to produce a milky precipitate, which was then stirred for 24 hr. HA is formed via the following reaction:

$$Ca(NO_3)_2 + (NH_4)_2HPO_4 \rightarrow Ca_{10}(PO_4)_6(OH)_2 + NH_4NO_3$$

The reaction mixture was washed with distilled water and centrifuged to get pure HA powder.

In accordance with phase equilibrium diagrams, a glass with a melting point of < 1000 °C was chosen as the sintering aid. This aid must be wetting to HA and Al_2O_3. An appropriate amount of the sintering aid and HA powder were mixed efficiently in distilled water or alcohol. Then the mixture was coated on the Al_2O_3 ceramic substrates and sintered in air at a temperature < 1000°C to obtain the composites (Fig. 1).

Mat. Res. Soc. Symp. Proc. Vol. 292. ©1993 Materials Research Society

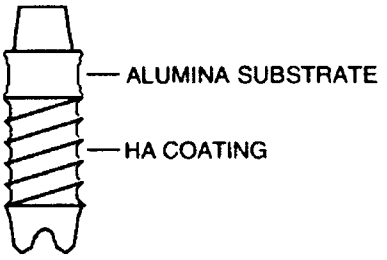

Fig. 1. Shape of the composite implant

Measurements

The Al_2O_3 substrate of the Al_2O_3/HA composite was characterized by mechanical testing and physical analysis.

The surface of the composite was examined by the techniques of x-ray diffraction (XRD) and infrared (IR) spectroscopy.

Dogs weighing between 15 and 20 kilograms were chosen as the experimental animal. The composite implants were implanted in the dogs' mandibles. Dogs were sacrificed after 2, 4, 8 and 12 weeks implantation respectively to prepare sections. The sections were observed by light microscopy and electron microscopy. The Ca^{2+} content at the implant-bone interface was determined by energy-dispersion spectroscopic analysis.

RESULTS AND DISCUSSION

Characterization of the implant

The properties of HA ceramic, Al_2O_3 ceramic and Al_2O_3/HA composite are shown in Table I. The HA coating of the composite is about 60 μm in thickness. The composite maintains the good mechanical properties of Al_2O_3 ceramic, so it can be used for large load-bearing clinical applications.

Surface structure of the composite

HA begins to lose OH^- groups when the temperature is over 1200°C. In order to maintain the structure of HA in the sintering process, a sintering aid with a melting point below 1000°C was chosen. Light microscopy showed that the coating was porous; small undeveloped HA grains were united by the glass. An XRD pattern of the surface is shown in Fig.2. Diffraction peaks were correlated with ASTM data for HA (Fig.2). Further analysis by IR verified the existence of absorption at 650 cm^{-1}, which characterizes OH^- groups (Fig.3). XRD and IR results therefore indicate that there is no structure change of HA in the sintering process.

Table I. The properties of HA ceramic, Al_2O_3 ceramic and Al_2O_3/HA composite

	HA	Al_2O_3	Al_2O_3/HA
Fracture strength (MPa)	130	440	440
Bulk density (g/cm^3)	3.13	3.89	
Bond	osteointegration	fibrous capsule	osteointegration

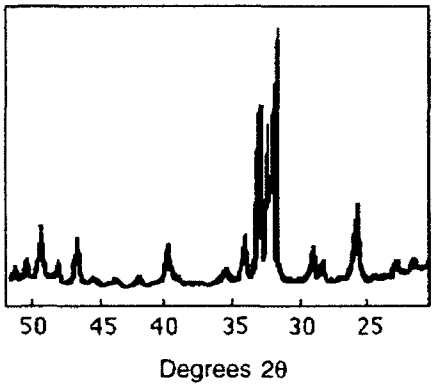

Fig.2. X-ray diffraction pattern of sintered coating

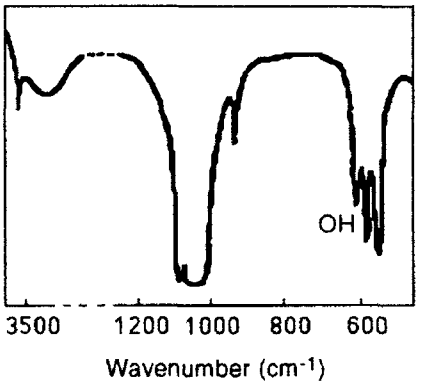

Fig.3. Infrared spectrum of sintered coating

Composite-bone interface

After 2 weeks, granulations were found at the composite-bone interface. Typical fibroblasts could be identified clearly (Fig.4). After 4 weeks implantation, a number of new trabeculae formed at the composite-bone interface. The trabeculae were surrounded by osteoblasts. In this earlier period, osteoblasts, blood capillary and mesenchymal cells at the interface increased rapidly. Collagen fibers began to mineralize (Fig.5). After 8 weeks, trabeculae at the interface were larger and more regular in arrangement than those at 4 weeks postimplantation, forming new bone. The new bone connected with the base bone and began to mineralize. There were Haversian canals forming (Fig.6). After 12 weeks, the new bone matured primarily and merged with the base bone (Fig.7).

The calcium content of the implant-bone interface was determined at 2, 4, 8, 12 weeks postimplantation. The results are shown in Table II. From the results, we conclude that the calcium content of the interface after 8 weeks implantation was close to that of the normal bone, and that these two quantities were the same after 12 weeks. This result agreed with histological observation.

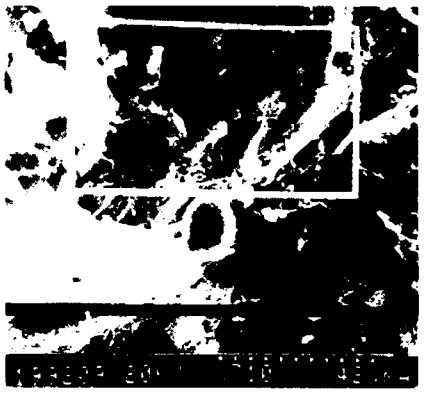

Fig.4. Electron micrograph of the interface after 2 weeks implantation (Fibroblasts could be identified)

Fig.5. Electron micrograph of the interface after 4 weeks implantation (Collagen fibers began to mineralize)

Fig.6. Electron micrograph of the interface after 8 weeks implantation (Haversian canals can be seen)

Fig.7. Electron micrograph of the interface after 12 weeks implantation (The bond has matured)

Table. II. Ca^{2+} content of the interface at different weeks postimplantation X+SE

Weeks	2	4	8	12
Composite	43.76±0.67	54.19±0.76	64.56±1.04	68.04±0.49
Normal bone	58.87±0.21	67.84±0.17	67.69±0.3	68.81±0.9

Mechanism of implant-tissue attachment

In the biological environment, HA ceramic and bioglasses form bonds with bone in different ways. When the bioactive glass is implanted in the bone, a series of complicated interfacial chemical reactions will take place at first. These reactions result in a layer of apatite on the surface. The glass bonds with the bone through this layer eventually. HA has the same structure as the inorganic substance of bone tissues. Compared with the bioglasses, HA ceramic has better affinity for bone. When HA ceramic is implanted in bone, it can bond with bone directly. The diffusion of ion is very important to the bond forming and developing.

The coating of the composite consisted of small undeveloped HA grains, and glass that contained Ca^{2+} and PO_4^{3-}. The small grains had high activity, and Ca^{2+} and PO_4^{3-} in the glass migrate easily to the surface to promote the growth of new bone. The coating was porous; along with degeneration of the glass, the pores became larger. Ingrowth of collagen and new bone into the surface pores could increase the attachment area, promoting interfacial bonding strength.

CONCLUSIONS

Al_2O_3/HA composite is a bioactive material with a high strength. It maintains the high strength of the Al_2O_3 substrate, and can achieve larger load-bearing applications. Animal experiment shows that it has very good biocompatibility and forms tight osteointegration with bone in 12 weeks. The composite is also very easy to process into ideal desired shapes.

REFERENCES

1. S.F. Hulbert, L.L. Hench, in High Tech. Ceramics, edited by P. Vincenzini (Elsevier Science Publishers, Amsterdam, 1987) pp.3-24.

2. J.W. Boretos, Adv. Cer. Mater. 2(1), (1987) 15.

LARGE SCALE THERMALLY SYNTHESIZED POLYASPARTATE AS A BIODEGRADABLE SUBSTITUTE IN POLYMER APPLICATIONS

A.P. WHEELER* AND L.P. KOSKAN**
*Dept. of Biological Sciences, Clemson Univ., Clemson, SC 29634
**Donlar Corp., Bedford Park, IL 60501

ABSTRACT

Polyanionic proteins isolated from biominerals serve as models for the development of biodegradable surface-reactive commercial polymers. A simple model for the natural polyanions is polyaspartic acid. This polymer may be made on a large scale using thermal polymerization of dry aspartic acid. The immediate result of the reaction is polysuccinimide which is hydrolyzed with base to form the polypeptide. The overall process yields up to 99% conversion of aspartic acid to polyaspartate. The thermal polyaspartate (TPA) is a copolymer having 70% of the amide bonds formed from β-carboxyl groups and 30% from α-carboxyl groups. TPA is as effective as the commercial polyanion polyacrylate in mineral dispersion and growth inhibition assays. Biodegradation of the TPA has been established using standard BOD and CO_2 evolution assays. In contrast, polyacrylates appear to be non-degradable. Modifications of the TPA have been made by reacting the succinimide with nucleophiles. Crosslinking of the polymer has been achieved, a process which results in absorbent gels. Because TPA can be produced in large scale, has similar activity to polyacrylate and is biodegradable, it seems a likely candidate for use in numerous applications in which non-degradable polyanions are employed. These applications include use as detergent additives, water treatment chemicals, dispersants for the paint and paper industry and as superabsorbents in health and sanitary products.

INTRODUCTION

The search for degradable materials has led workers to consider using biopolymers as components of new or existing technologies. However, in many cases the supply of the polymer is limiting or the cost of obtaining the material is excessive for the application under consideration.

An example of a class of biopolymers having numerous theoretical applications but available in only small quantities is the matrix polyanionic protein extracted from various biominerals such as teeth, bone and mollusc shell. It has been demonstrated that these charged proteins can readily adsorb to crystals and in so doing inhibit their growth [1]. In the context of biomineralization, the adsorption may be crystal face or site-specific and thus the inhibition may occur for growth along specific axes [2]. It is in this fashion that matrix proteins may control crystal growth leading to the conserved and sometimes unusual microstructures typical of biominerals.

Some of the properties of polyanionic proteins that lead to control of biomineral formation may also make them candidates for a number of commercial applications. For example, numerous commercial polyanions which are produced in 100's of millions of pound quantities are used to inhibit the growth of various minerals (anti-scalants) or act as dispersants of particles [3]. Like the matrix proteins, these activities result largely from the capacity of the polymers to adsorb to particle surfaces.

Having identified a natural material that is analogous to commercial polymers, the process of evaluating the feasibility of adapting the biopolymer to technology begins. As mentioned above, in the case of these polymers from biominerals there is no opportunity to directly utilize the polymer. Rather, the strategy is to identify the characteristics of the biopolymer that make it effective and then proceed to evaluate what approaches might be taken to cost-effectively synthesize an appropriate analog.

MATRIX PROTEINS AND THEIR ANALOGS

We have focused our attention on proteins from one particular system, the $CaCO_3$ shell of

Mat. Res. Soc. Symp. Proc. Vol. 292. © 1993 Materials Research Society

the Eastern oyster. The proteins of this system appear to exist in a series of molecular weights including soluble proteins ranging from 50 to thousands of kDa and insoluble (possibly cross-linked) proteins [4]. What is somewhat unusual about these molecules is that all the size classes are polyanionic, containing nearly 60% aspartic acid (Asp) and phosphoserine PSer, two anionic amino acids. Further, it appears that Asp may be largely distributed in runs or domains of polyaspartate [5]. Other domains, such as regions enriched in PSer, may exist as well.

Having identified some of the major domains of the natural proteins, it was important to produce selected analogs to better evaluate minimum structural requirements for activity. A variety of small molecular weight polymers with specific sequences were synthesized using solid phase chemistry and tested for their ability to adsorb to and inhibit the nucleation and growth of $CaCO_3$ [6]. From these studies it was clear that peptides with continuous runs of anionic residues were most effective in all categories. In particular, polyaspartate with a degree of polymerization of approximately 20 adsorbed to $CaCO_3$ with a high capacity and could completely inhibit growth of $CaCO_3$ crystals. Although the efficacy of polyaspartate could be enhanced against crystal nucleation if it had a higher degree of polymerization, or had a hydrophobic or PSer terminus, low molecular weight polyaspartate emerged from these studies as a very simple model for larger scale synthesis.

In retrospect, it is perhaps not surprising that polyaspartate is such an effective surface-reactive polymer given that polyacrylate, also a polycarboxylate (Fig. 1), is no doubt one of the most common commercial polymers used in many of the aforementioned applications. Ultimately one of the important differences between the two polymers resides in the fact that polyaspartate is at least theoretically biodegradable and polyacrylates are, at best, poorly degradable [7].

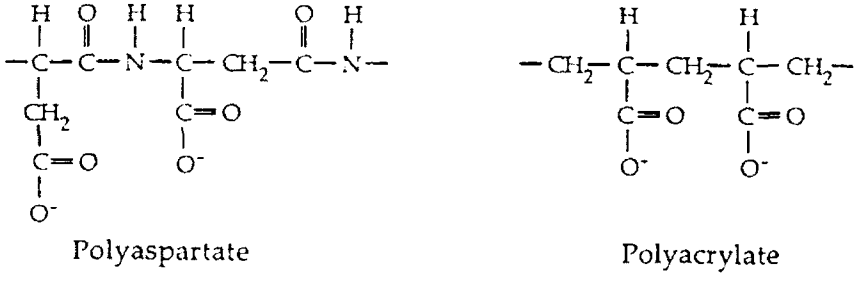

Figure 1. Comparison of the molecular structures of thermal polyaspartate and polyacrylate.

SYNTHESIS AND CHARACTERISTICS OF THERMAL POLYASPARTATE

Although polyaspartate appears to be a suitable analog of both the natural proteins and commercial polymers, several questions must be addressed before one assumes that any new polymer is an ideal candidate for development (Table 1). The first question is whether or not it can be made on a large enough scale to suit the requirements of a market the size of that for polyacrylates.

Synthesis of a polypeptide can be done by a number of methods, including those that utilize solid phase or solution chemistry and genetically engineered microbes. These methods have advantages in allowing control of composition and even sequence of amino acids. However, they fail on the basis of other criteria, such as cost of producing large quantities or the requirement for the use of undesirable reactants.

An alternative synthetic method, dry thermal polymerization, has been studied on a small scale for a number of years [8] and has the advantages of not utilizing any additional reagents other than amino acids and has water as its primary by-product. The disadvantages of the technique are that it is difficult to control the exact composition of peptides and nearly impossible to control

peptide sequence. These disadvantages, for a simple polymer such as polyaspartate, are outweighed by the fact that we have shown the synthesis can be readily scaled-up [9]. If temperature and mixing during reaction are carefully controlled, quantities of aspartic acid as large as 100's of kg can be reacted using either batch or continuous feed commercial reactors. It is projected that the requisite quantities of aspartic acid to be used in the polymer synthesis processes can be produced by either fermentation or immobilized enzyme processes.

Table 1. Selected Criteria for New Polymer Technology

1. Can polymer be produced in industrial scale?
2. Does synthesis result in a high yield of polymer?
3. Does the polymer have consistent characteristics?
4. Does the polymer demonstrate competitive performance?
5. Is the polymer biodegradable?
6. Is the polymer amenable to modification?

The reaction for thermal polymerization of crystalline aspartic acid is shown in Figure 2. The actual product is a powdered polysuccinimide [10]. The time for reaction is dependent on the temperature of the mixture. A typical reaction is performed at 240° C. Below a certain temperature the reaction is too slow to be practical and will result in poor yields.

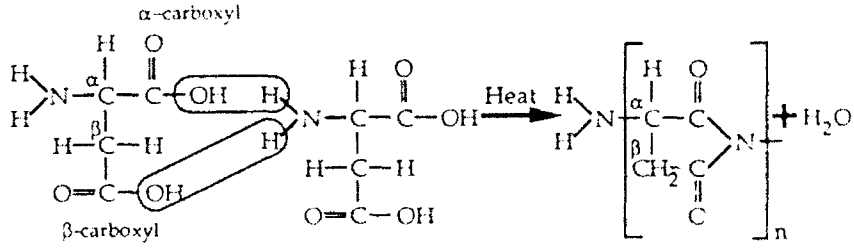

Figure 2. Thermal polycondensation of aspartic acid to polysuccinimide.

The succinimide ring is readily opened with base to form the polyaspartate (Fig. 3). The rate of hydrolysis is dependent on hydroxide ion concentration [11,12] and temperature [12]. Very rapid rates can be achieved at pH 9-10 and 60° C without danger of side reactions or hydrolysis of the polymer backbone [12].

It should be noted that upon hydrolysis the imide ring can open on either side resulting in a form of co-polymer. One of the monomers involves the normal (α) carbon in the backbone of the polymer whereas for the other the β-carbon is involved. The fraction of β formed in the thermal polymerization we perform is approximately 70%. In addition, at the normal temperature of synthesis, the polymer is made up of a racemic mixture of D- and L- aspartic acid despite the fact that synthesis utilizes optically pure L-Asp. The characteristics of the thermal polyaspartate (TPA) and its synthesis are summarized in Table 2. These characteristics of the polymer are highly repeatable from batch to batch, which is one of the principal criteria to be met by a polymer in order for it to be commercially viable (Table 1).

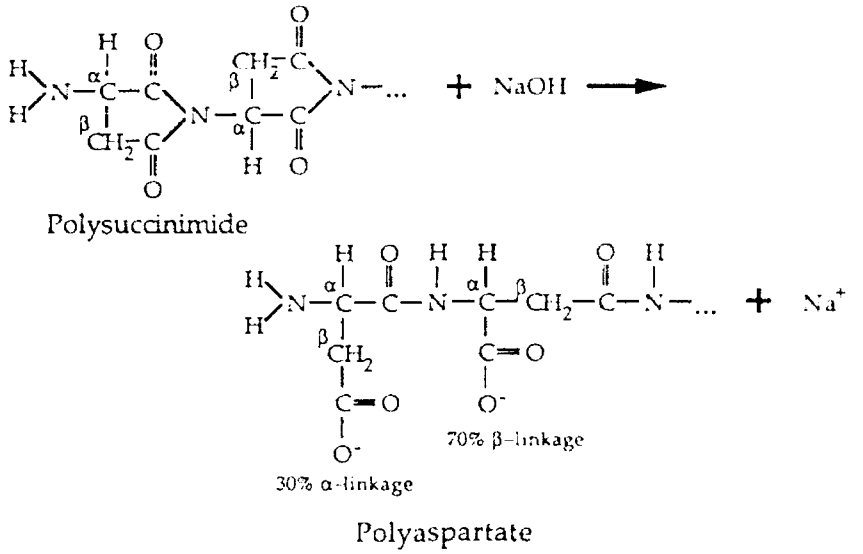

Figure 3. Hydrolysis of polysuccinimide.

Table 2. Typical Selected Characteristics of Thermal Polyaspartate (TPA) and TPA Synthesis

Characteristic	Analysis	Method
α/β amide bonds[a]	0.4	C-13 NMR[b]
D/L aspartic acid[c]	1.0	Acid hydrolysis and polarimetry
Molecular weight	Polydisperse Ave ≅ 2000 Da	Size exclusion - HPLC
Amine composition	>99% aspartic acid	Amino acid analysis
Carboxylate yield	>90%	pH titration
Primary structure	Amide backbone	FTIR
Yield (% conversion)	>98%	Direct amine titration

[a]May vary slightly with pH of hydrolysis.
[b]Performed according to [13]
[c]May vary with temperature of synthesis [14,15]

ACTIVITY OF THERMAL POLYASPARTATE

The thermally produced polyaspartate has been tested in numerous activity assays, the majority of which are designed to test the efficacy of the polymer as a dispersant, an anti-scalant, and a metal-binding substance. These assays are designed to reflect the viability of the polymer in numerous commercial applications including use in water treatment formulas, paper processing, paints and detergents to name a few. As a detergent additive, the dispersant capability would serve to prevent redeposition of soil on surfaces [7]. Any capability of the polymers to prevent insoluble minerals from forming or for "softening" the water, although not the principal functions of polyanionic additives in detergents, would be beneficial as well [7,16].

To date, the activity of polyaspartate in the various bench assays has been comparable, and in some cases superior, to commercial polyacrylates, one of the principal polymers manufactured for many of the above-mentioned applications. A specific example of comparative activity is given in Table 3. This data shows that TPA is as effective as an inhibitor of calcium carbonate as commercial polymers. It is interesting to note that the estimated average degree of polymerization of TPA (approx. 20, based on average MW in Table 2) is about that which was determined previously as optimal for inhibition of carbonate [6].

Table 3. Inhibition of Calcium Carbonate Crystal Growth by Various Polymers and Aspartic Acid

Inhibitor	I_{50}[a]	N[b]
Thermal Polyaspartate[c]	0.57 μg ml^{-1}	5
Asp15[d]	0.68	4
Belclene 500[e]	0.60	5
Acrysol-20[f]	0.51	4
Acrysol-45[f]	0.58	3
Aspartate[g]	>40	3
BS Albumin[h]	>10	3

[a]The concentration of polymer required to achieve 50% inhibition of carbonate crystal growth in a pH stat assay [4].

[b]Number of data sets used to determine I_{50}.

[c]Polyaspartate produced by a process described in the text and having a mean molecular weight of approx. 2000.

[d]A polyaspartate made by solid phase synthesis.

[e]A phosphinocarboxylic acid water treatment polymer produced by Ciba-Geigy.

[f]Acrysol-20 and -45 are two polyacrylates produced by Rhom and Haas having mean molecular weights of approx. 2000 and 4500 respectively.

[g]Monomeric L-aspartic acid. Note that a non polymeric anion is not necessarily an effective inhibitor.

[h]Bovine serum albumin. Note that proteins per se are not necessarily good inhibitors.

Table 4 shows a number of additional assays in which polyaspartate has been compared to polyacrylate. In each case the activity of TPA is similar to or exceeds that of polyacrylate. These findings give additional support to the earlier observations that TPA may fulfill the activity criteria of Table 1 for continued development as a new commercial polymer.

Table 4. Assays for Which Activity of Thermal Polyaspartate has been Identified as Comparable to Polyacrylate

Inhibition of Crystallization	Dispersion
calcium phosphate	ferric oxide
calcium sulfate	calcium carbonate
calcium carbonate	zinc hydroxide
barium sulfate	titanium dioxide
	kaolin
	soil

Ion Binding

Ca^{2+}, Mg^{2+}, Cu^{2+}, Co^{2+}, Ni^{2+}, Zn^{2+}, Fe^{3+}

BIODEGRADABILITY OF THERMAL POLYASPARTATE

There are two obvious reasons to choose biopolymers for commercialization: (1) the advantage one might gain from evolutionary design processes, and (2) the inherent biodegradability of the polymers. Although one might assume a priori that any polypeptide would be biodegradable, the actual demonstration of degradability is necessitated by the atypical peptide structure of TPA.

Results to date suggest that TPA is in fact degradable. This was demonstrated initially using standard biochemical oxygen demand (BOD) tests with diluted secondary effluent from a sewage treatment plant as a source of flora. These tests demonstrate approximately 40% of theoretical oxygen demand by 3 ppm TPA samples in a 3 week incubation period. In comparison both D- and L- aspartic acid or bovine serum albumin were nearly completely degraded in shorter incubation periods, whereas polyacrylate was not degraded at all in longer incubations. The slower rate of degradation of TPA compared to control molecules may be a function of the presence of β-linkages or D-amino acids or both, two structural aspects which may make the peptide a less than ideal substrate for microbial proteases.

Because of the low biomass used in BOD tests, these studies may represent relatively stringent conditions for determining degradation. Consequently, other tests are underway including CO_2 evolution studies with treatment plant sludge as the source of flora. These kinds of studies have been augmented by the use of ^{14}C-labelled TPA which allows the detection of degradation using much lower, more realistic concentrations of polymer. Depending on the exact conditions, it can be demonstrated that either the rate or the extent of degradation exceeds that demonstrated by the BOD tests.

SUMMARY AND PROSPECTS

At this time it appears that TPA can be made in large scale, is significantly biodegradable and has activity much like a non-degradable analog currently used in numerous commerical applications. These characteristics in themselves warrant continued development. However, the last property listed in Table 1 warrants attention. That is, how readily can the polymer be modified to either increase its efficacy or expand its uses. In partial answer to this, it should be pointed out that many nucleophiles can react with the succinimide. Therefore, when NH_3 is added to the base hydrolysis medium, a mixture of amide and carboxylate groups is produced. This is not purely an academic exercise in that it has been noted that acrylamide-acrylic acid copolymers have improved activity in certain water-treatment applications [17]. Using the same strategy, cross-linked gels have been produced. This opens the door for the production of biodegradable superabsorbents for the sanitary, health and agricultural markets. The development of this kind of product would parallel that for the soluble polyaspartates in that many of the superabsorbents on the market today

are cross-linked polyacrylates. Further, the insoluble polyanions from oyster shell have superabsorbent properties and thus can serve as examples that absorbent polypeptides can be made.

ACKNOWLEGEMENTS

Support for much of the work reviewed here was provided by grants from NSF and the South Carolina Sea Grant Consortium.

REFERENCES

1. A.P. Wheeler and C.S. Sikes, in Biomineralization: Chemical and Biochemical perspectives, edited by S. Mann, J. Webb and R.J.P. Williams (VCH, Weinheim, 1989), p. 95.

2. L. Addadi, J. Moradian-Oldak, and S. Weiner, in Surface Reactive Peptides and Polymers, edited by C.S. Sikes and A.P. Wheeler (ACS, Washington DC, 1991), p. 13.

3. C.S. Sikes and A.P. Wheeler, CHEMTECH 18, 620 (1988).

4. J.E. Borbas, A.P. Wheeler and C.S. Sikes, J. Exp. Zool. 258, 1 (1991).

5. K.W. Rusenko, J.E. Donachy and A.P. Wheeler, in Surface Reactive Peptides and Polymers, edited by C.S. Sikes and A.P. Wheeler (ACS, Washington DC, 1991), p. 107.

6. A.P. Wheeler and C.S. Sikes, in Materials Synthesis Utilizing Biological Processes, edited by P.C. Rieke, P.D. Calvert, and M. Alper (MRS, Pittsburgh, 1990), p. 69.

7. G. Chiaudani and P. Poltronien, Ingegneria Ambientale, No. 11 (1990).

8. S.W. Fox and K. Harada, in A Laboratory Manual of Analytical Methods of Protein Chemistry, Vol. 4, edited by P. Alexander and H.P. Lundgren (Pergamon Press, Oxford, 1966), p. 127.

9. L.P. Koskan and K.C. Low. U.S. Patent No. 5057597 (1991).

10. A. Vegotsky, K. Harada and S.W. Fox. J. Am. Chem. Soc. 80, 3361 (1958).

11. P.D. Hoagland and S.W. Fox, Experientia 29, 962 (1973).

12. J. Mosig, A.P. Wheeler and C.H. Gooding unpublished data.

13. H. Pivcova, V. Saudek and H. Drobnik. Polymer 23, 1237 (1982).

14. E. Kokufuta, S. Suzuki and K. Harada, Bull. Chem. Soc. Jap. 51, 1555 (1978).

15. A.P. Wheeler, unpublished data.

16. B.F. Greek. Chem Eng. News. Jan 25, (1988) p. 21.

17. C.C. Pierce and J.E. Hoots, in Chemical Aspects of Regulation of Mineralization, edited by C.S. Sikes and A.P. Wheeler (Univ. of South Alabama Publication Services, Mobile, AL, 1988), p. 53.

Author Index

Subject Index